An Analysis of the Hadronic Final State and Jets in Deep Inelastic $e\gamma$ Scattering Events using the OPAL Detector at LEP

Anthony Michael Rooke

Department of Physics and Astronomy
University College London

Submitted for the degree of
Doctor of Philosophy
September 1998

Abstract

The hadronic final state of deep inelastic $e\gamma$ scattering events are studied and comparisons are made with predictions from the general purpose QCD–based Monte Carlo generators, HERWIG and PYTHIA, and from the two–photon event generator F2GEN. The data was collected using the OPAL detector at LEP from 1994 to 1996 with a total luminosity 109.48 pb^{-1} and divided into three samples in terms of beam energy: $44.6 - 46.6$ GeV, 80.5 GeV and $85.0 - 86.0$ GeV. The complete data sample covers the Q^2 region of $1.1 - 220.0$ GeV^2 with the energy and angle of the scattered electron or positron measured in one of three OPAL subdetectors with different polar angle ranges: the Silicon–Tungsten luminosity calorimeters (27–55 milliradians), the Forward Detector calorimeters (60–120 milliradians), or the main OPAL electromagnetic endcap calorimeters (200–550 milliradians). Discrepancies in hadronic energy flow are highlighted using a classification of events in terms of jet multiplicities. A first estimation of energy flow and jet multiplicity in events with the photon–gluon fusion subprocess is made using a development of the F2GEN event generator. Suggestions are made for improvements to the modelling of the hadronic final state in the HERWIG and PYTHIA generators.

Acknowledgements

I would like to thank David Miller and Jan Lauber for their wisdom and advice during the last four years. They have managed to keep me on the straight and narrow (ish), especially in pointing out when I am talking rubbish. Particular thanks go to Mike Seymour for helping me understand the mysteries of HERWIG and PYTHIA, Jeff Forshaw for advice with the photon–gluon fusion model and to Jason Ward for his insights (and for putting up with my questions). Stefan Söldner–Rembold, Richard Nisius, Jon Butterworth, Bruce Kennedy and Roland Bürgin also contributed a great deal to helping me understand the pointlike (not pointless) and peripheral world of two–photon physics. I would like to extend my gratitude to PPARC for their sponsorship in this work, to summer schools (I thoroughly recommend St. Croix, US Virgin Islands) and to work with kids in schools which I enjoyed thoroughly.

My most special thanks goes to my family and friends. I have been exceptionally lucky to have had a great deal of love and support from my mother, Eileen, as well as from my brother Andrew (plus wife Amelia), my sister Helen, my grandfather Reg (Butch, Bob, Buddha, SOS, etc...) and my late grandmother Joan. They have contributed to my education (especially card playing) and development in many indescribable ways that are best left unmentioned[1] [2] over the last (nearly) 28 years. For their friendship, kindness[3] and generosity, I would especially like to thank[4] Simon and Emma, as well as the other "members" of the **S.W.A.** - Dave (co–founder) and Alice (honorary member), Mack (co–founder) and Lizzie (honorary member) - Cecile (French...), Dr. Bob, Irish Peter, Stu (Cardboard) and Wendy (L.B.W.), Gillian (Smelly–Feet), (Mad–Cow) Danny, (Kneeling) James.

There are many others who I would like to add my thanks for the odd tipple (and quite a few not so "odd"): Neil, Nobby and Sam (Tone Deafs); Diane, Bob H., Paul (the Irish Setter), Rod, (Chubby Cheeks) Rosa and Geordie Helen (Edinburgh Knights); Dorris McSquirter, Fi, Diamond Dan, Dougal, Rhona, Tim, Xavier, Stephanie, Kate (cake), Max, Peter S., Theresa, Olivier, Mette, Lisa, and Dr.'s Barney

[1] Except for the card playing.
[2] ...and drinking games.
[3] i.e. Mickey-taking
[4] And in some cases do something only a few of letters away from "thank".

and Barney (Geneva punters); Antony, Sexy Legs, Nils, Yvonne, Silvia Buzz, Boden's Senior and Junior, Kathleen, Lorenzo, Mariella, Vivien, Sophie and Hoanh (UCL volley–jollies and dollies); Lucy M, Heather, Christina, Heather, Amy, Jo, Mungo and Ed (Cambridge Wasters); the Andersons (great accommodation at low prices), Parul, Glen, Helen, (Whiplash) Debora, Kate, Kate, Kate, Lu, Alison (underneath the) Archer, (Smoking) Alison J., Roberta, and Mark H. (PhD...drinks a lot) (London Lovvies); and Ivan, Brian, Martin, Sophie, Baljeet, Theo, Neil, Ari, Will, Chris, Mark, John, Ramon, Matt, Nigel, Simone, Roy, Tim, Simon, Gareth, William B., Eleanor, Ewan, James, Tony, Julia and all the rest (Logibods). Thanks also go to friends past and present whom I have not mentioned (no room....honest!!!!).

Cheers and beers,
Tony (the Tiger) Rooke,
September, 1998.

Dedication

To my mother, Eileen, my grandfather, Reg,

and my grandmother, Joan.

For their love, support and for being great fun.

''What're are quantum mechanics?''

''.... People who repair quantums, I suppose.''

Eric,

Terry Pratchett

''...while I am describing *how* Nature works, you won't understand *why* Nature works that way. But you see, nobody understands that.''

QED, The strange theory of light,

Richard Feynman

''More light and light: more dark and dark our woes!''

Act 3, Scene V, Romeo and Juliet,

William Shakespeare

''Newton believed light behaved ... as if it were a stream of tiny particles. Huygens argued that ... light behaved as if it were a wave... Modern quantum mechanics combines both ideas... There is something mysterious and stirring in this marriage of opposites.''

Cosmos,

Carl Sagan

Contents

List of Figures

List of Tables

Chapter 1

Introduction

The photon is considered to be a fundamental particle in current theories of elementary particle physics and is a central part of the Standard Model. In Quantum Electrodynamics (QED), the photon is the carrier of the electromagnetic force between two charges. No experimental evidence exists to suggest that the photon is a composite of more elementary particles. In quantum theory, however, a photon can fluctuate briefly into a charged particle–antiparticle pair and, while it is in one of these virtual states, it can be said to have "structure" [1]. By convention, this structure is called "leptonic" when the virtual state is a lepton–antilepton pair and "hadronic" when the virtual state is a quark–antiquark pair. Deep inelastic electron–photon ($e\gamma$) scattering events are used to study photon structure at e^+e^- colliders such as LEP. A lepton from one beam scatters off a nearly–real photon emitted by a lepton in the other beam. Analyses [2, 3, 4, 5, 6] of the hadronic photon structure function, F_2^γ, are subject to large systematic errors due to the poor descriptions of the hadronic final state by the Monte Carlo models used.

This thesis uses LEP data to study the deficiencies of the models in the QCD–based Monte Carlo generators HERWIG [7, 8] and PYTHIA [7, 9] for describing the hadronic final state in deep inelastic $e\gamma$ scattering events. Data samples over the Q^2 range $\sim 1 - 220$ GeV^2 are compared with Monte Carlo samples from the HERWIG, PYTHIA and F2GEN [10] generators. Emphasis is placed upon comparisons of hadronic final state variables such as energy flow and cone jet multiplicity where discrepancies between data and Monte Carlo distributions are marked. I have written

an algorithm for a simple model of the photon–gluon subprocess into the F2GEN generator and the samples generated using this algorithm are compared for the first time with the data and other Monte Carlo samples to aid the interpretation of the limitations of the HERWIG and PYTHIA generators.

The data samples are subsets of the data collected in 1994, 1995 and 1996 using the OPAL (**O**mni–**P**urpose **A**pparatus for **L**EP) detector [11] at the LEP (**L**arge **E**lectron–**P**ositron) collider [12] at CERN (**C**entre **E**uropean de la **R**echerche **N**ucleaire) near Geneva, Switzerland. The total e^+e^- integrated luminosity over this period of time is 109.48 pb^{-1}.

In this chapter, a simple introduction to photon structure is given along with results from analyses of the structure function of the photon, $F_2^\gamma(x, Q^2)$. This picture of photon structure is expanded upon in Chapter 2 along with a description of the HERWIG, PYTHIA, F2GEN and VERMASEREN event generation algorithms. Details of the OPAL detector are given 3. The selection criteria of the data and Monte Carlo samples are described in Chapter 4 along with the trigger efficiencies and the estimation of the background in each of the data samples. A comparison of data and Monte Carlo distributions for selected global event quantities are made in Chapter 5. In Chapter 6, comparisons of hadronic energy flow and transverse energy distributions are made with particular reference to the regions where the Monte Carlo distributions disagree with the data distributions. The cone jet algorithm [13, 14] is used to identify subsets of events sensitive to these disagreements as an extension of work I have contributed to OPAL publications [15, 16] and interpretation of the possible origins of these discrepancies is given. Comparisons of the photon–gluon fusion samples are shown in Chapter 7 and are used as additional evidence for proposed improvements to the final state models used in the HERWIG and PYTHIA generators. A discussion and summary of the findings of this thesis is given in Chapter 8.

1.1 What is Photon Structure

The photon is a fundamental particle. So how can it be said to have structure? In classical mechanics, the photon is described by the linear Maxwell equations. However, this picture of the photon makes no allowance for quantum effects where it

is possible for the photon to fluctuate into a charged particle pair with mass m_{pair} for a period of time, Δt, given by the uncertainty principle [2]:

$$\Delta t \leq \frac{2E_\gamma}{m_{pair}^2} \tag{1.1}$$

It is assumed that the energy of the photon, E_γ, is such that $E_\gamma \gg m_{pair}^2$ and that $\hbar = c = 1$. Eqn. 1.1 shows that the amount of time that a photon can be described as such a virtual state increases with the E_γ. The charged particle pair could be of light mass, such as a quark–antiquark ($q\bar{q}$) pair or a charged lepton–antilepton pair (l^+l^-), or could be heavy such as a W^+W^- pair. In all cases, there will be further complications of the structure due to higher order effects involving emission of extra photons and/or gluons

Fluctuations into a $q\bar{q}$ pair can be divided into low and high virtuality states using a cut–off parameter, p_o, for the transverse momentum of the $q\bar{q}$ pair relative to the photon momentum direction. Below p_o, the $q\bar{q}$ pair is described by non-perturbative QCD models such as the **V**ector **M**eson **D**ominance (VMD) model. This approximates the $q\bar{q}$ pair using a sum over low–mass vector meson states, $|V\rangle$. Above p_o, the $q\bar{q}$ pair is described by a $|q\bar{q}\rangle$ virtual state calculated using perturbative QCD. The cut–off p_o is interpreted as the lowest allowable transverse momentum for the $|q\bar{q}\rangle$ state. The wave-function of the photon, $|\gamma\rangle$, can be considered for low–mass states as a sum [17]:

$$|\gamma\rangle = c_{bare}|\gamma_{bare}\rangle + \sum_{V=\rho_o,\omega,\phi,..} c_V|V\rangle + \sum_q c_q|q\bar{q}\rangle + \sum_l |l^+l^-\rangle \tag{1.2}$$

where $|\gamma_{bare}\rangle$ represents the bare photon state and $|l^+l^-\rangle$ represents lepton–antilepton virtual states.

1.2 Two–Photon Interactions at an e^+e^- Collider

Two–photon interactions occur when one photon couples to one of the charged particles of the virtual state of another photon. At an e^+e^- collider, this interaction takes place when the two photons are emitted by one electron (positron[1]) from each of the beams.

[1]Electron is used throughout the rest of the text to denote either an electron or positron in the beam or that is scattered out of the beam. This is done to avoid unnecessary duplication.

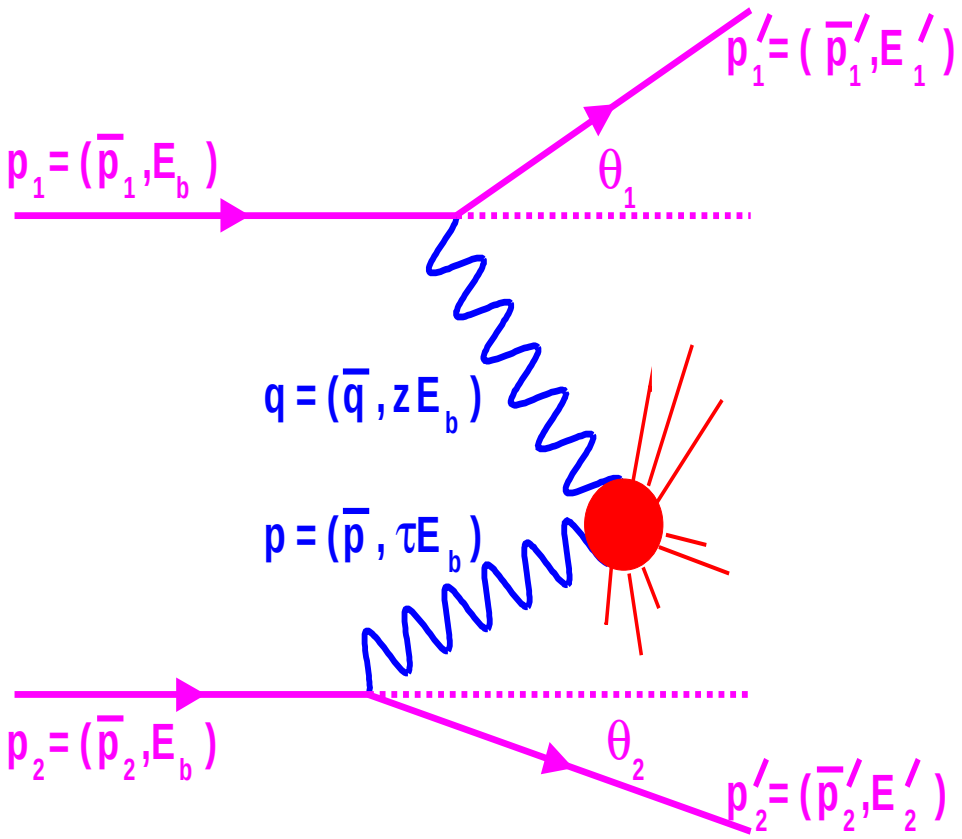

Figure 1.1: The kinematics of the multi–peripheral two–photon process at an e^+e^- collider where hadrons are produced in the final state. In the multi–peripheral process, a photon is emitted by a lepton in each of the beams and these photons interact to produce final state hadrons.

The flux for the photon emission by a beam electron is given approximately by [18]:

$$, _t(x, Q^2) = \frac{\alpha_{em}}{2\pi^2}\frac{E_1^{'}}{Q^2}\frac{1+(1-z)^2}{z} \tag{1.3}$$

where z is the fraction of the electron beam energy, $E_{\rm b}$, carried by the photon, $E_1^{'}$ is the energy of the scattered electron, α_{em} is the electromagnetic coupling constant, and Q^2 is defined as the negative square of the photon four–momentum:

$$Q^2 \equiv -q^2 \simeq 2E_{\rm b}E_1^{'}(1-\cos\theta_1) \tag{1.4}$$

The electron mass is neglected in deriving the right–hand side of Eqn. 1.4. The flux factor, $, _t$, peaks at small Q^2 and small z.

1.2.1 Two–Photon Interactions with a Hadronic Final State

Currently, the best way to study the hadronic structure of the photon at e^+e^- colliders is to use two–photon events such as that of the multi–peripheral process shown schematically in Fig. 1.1. A photon of high virtuality is used to probe the hadronic structure of a quasi–real photon. The probe photon couples directly to a quark within the target quasi–real photon giving rise to a hadronic final state. It is customary to label the four–momenta of the photons as q and p for the virtual and quasi–real photons respectively. The highly virtual photon is often denoted as γ^* to distinguish it from the quasi–real photon, γ. The invariant kinematic variables for the two–photon interaction in Fig. 1.1 are:

$$x = \frac{Q^2}{2p.q} = \frac{Q^2}{Q^2+P^2+W^2} \tag{1.5}$$

$$y = \frac{p.q}{p.p_1} \tag{1.6}$$

where W is the invariant mass of the two–photon system and P^2 is defined similarly to Q^2 for the quasi–real photon:

$$P^2 \equiv -p^2. \tag{1.7}$$

1.2.2 Experimental Kinematical Variables and Deep Inelastic Scattering

A two–photon interaction can be regarded as a deep inelastic $e\gamma$ scattering process for $Q^2 \gtrsim 4$ GeV^2 and $P^2 \approx 0$ GeV^2. This process is measured experimentally by observing the hadronic final state particles and the electron scattered into the detector after emitting the probe photon. An "antitag" condition that the other scattered electron is not detected ensures that the target photon is quasi–real ($P^2 \approx 0$). The detected electron is called the "tag" and the Q^2 for the event is calculated by substituting the measured values for $E_1' = E_{\rm tag}$ and $\theta_1 = \theta_{\rm tag}$ into Eqn. 1.4.

For $P^2 \approx 0$, the invariant variables x and y become

$$x = \frac{Q^2}{Q^2 + W^2} \tag{1.8}$$

$$y = 1 - \frac{E_{\rm tag}}{E_{\rm b}} \cos^2\left(\frac{\theta_{\rm tag}}{2}\right). \tag{1.9}$$

The variable x is called "Bjorken x" and can be interpreted as the fraction of the four–momentum of the quasi–real photon carried by the struck quark. The quasi–real photon has low transverse momentum compared to its longitudinal momentum due to its low virtuality and hence is approximately collinear with the beam.

1.2.3 The Total Differential Two–Photon Cross–Section and $F_2^\gamma(x, Q^2)$

A photon emitted from a electron beam can be in one of two polarisations: longitudinal (L) or transverse (T). This means that there are four contributions ($\sigma_{\rm TT}$, $\sigma_{\rm LT}$, $\sigma_{\rm TL}$ and $\sigma_{\rm LL}$) to the total $\gamma\gamma$ differential cross–section for unpolarised e^+e^- beams, as well as two interference terms ($\tau_{\rm TT}$ and $\tau_{\rm TL}$) [19]:

$$\frac{d\sigma}{d,} = \mathcal{L}_{\rm TT}\Big\{\sigma_{\rm TT} + \epsilon_1\sigma_{\rm LT} + \epsilon_2\sigma_{\rm TL} + \epsilon_1\epsilon_2\sigma_{\rm LL} + \frac{1}{2}\epsilon_1\epsilon_2\tau_{\rm TT}\cos 2\phi \\ +2\sqrt{\epsilon_1(1+\epsilon_1)}\sqrt{\epsilon_2(1+\epsilon_2)}\tau_{\rm TL}\cos\phi\Big\} \tag{1.10}$$

where ϕ is the angle between the scattered lepton planes in the two–photon centre–of–mass frame and

$$d, = \frac{dp_1^{'} dp_2^{'}}{E_1^{'} E_2^{'}} \tag{1.11}$$

The luminosity function $\mathcal{L}_{\mathrm{TT}}$ and ϵ_1,ϵ_2 are calculable using QED. The interference terms τ_{TL} and τ_{TT} disappear in the integration over ϕ. By considering only deep inelastic $e\gamma$ scattering, then the cross–sections σ_{TL} and σ_{LL} disappear since the target photon is considered real ($P^2 = 0$).

The total differential cross–section is more usually written in terms of structure functions of the photon. The cross–sections σ_{TT} and σ_{LT} are used to define the longitudinal and transverse structure functions:

$$F_{\mathrm{T}}^{\gamma}(x, Q^2) = \frac{Q^2}{4\pi^2 \alpha_{em}} \frac{1}{2x} \sigma_{\mathrm{TT}} \tag{1.12}$$

$$F_{\mathrm{L}}^{\gamma}(x, Q^2) = \frac{Q^2}{4\pi^2 \alpha_{em}} \sigma_{\mathrm{LT}} \tag{1.13}$$

These are sometimes expressed in terms of the structure functions F_1^{γ} and F_2^{γ}:

$$F_1^{\gamma}(x, Q^2) = F_{\mathrm{T}}^{\gamma}(x, Q^2) \tag{1.14}$$

$$F_2^{\gamma}(x, Q^2) = 2x F_{\mathrm{T}}^{\gamma}(x, Q^2) + F_{\mathrm{L}}^{\gamma}(x, Q^2) \tag{1.15}$$

so that the differential cross–section can be written as:

$$\frac{d\sigma_{e\gamma \to eX}}{dxdy} = \frac{16\pi \alpha_{em}^2 {E_{\mathrm{b}}}^2 \tau}{Q^4} \Big[(1-y) F_2^{\gamma}(x, Q^2) + xy^2 F_1^{\gamma}(x, Q^2) \Big] \tag{1.16}$$

This can be further simplified by considering some of the characteristics of deep inelastic $e\gamma$ scattering events. From Eqn. 1.3, it can be seen that such events are heavily peaked towards high E_{tag} and low θ_{tag}. This, together with Eqn. 1.9, means that y is small and hence $y^2 \ll (1-y)$. Additionally, from Eqn.'s 1.14 and 1.15, $F_2^{\gamma} > F_1^{\gamma}$ so that Eqn. 1.16 reduces to:

$$\frac{d\sigma_{e\gamma \to eX}}{dxdy} = \frac{16\pi \alpha_{em}^2 {E_{\mathrm{b}}}^2 \tau}{Q^4} \Big[(1-y) F_2^{\gamma}(x, Q^2) \Big] \tag{1.17}$$

This equation applies to events where the two photons interact to produce hadrons or to produce a lepton pair (l^+l^-). Measurements of the leptonic photon structure function, $F_{2,\mu}^{\gamma}$, [20, 21, 22, 23, 24, 25, 26, 27] agree well with QED predictions. This analysis is a study of two–photon events which have hadronic final states only.

1.3 Interest in Deep Inelastic $e\gamma$ Scattering

The analysis of hadronic two–photon events is motivated because it gives:

- tests of perturbative QCD and phenomenological models;
- comparisons with proton structure;
- background studies to other processes at LEP.

Deep inelastic $e\gamma$ scattering events test both non–perturbative and perturbative models of the strong interaction. For $Q^2 < 1$ GeV^2, phenomenological models are needed to describe the photon structure as two photons interact as if they were hadrons. At scales $Q^2 > 5$ GeV^2, photon structure functions are best described by perturbative QCD models, whilst the transition region, $Q^2 = 1 - 5$ GeV^2, between these two extremes is poorly understood.

1.3.1 High Q^2

An important test of QCD is the effect on the structure function, $F_2^\gamma(x, Q^2)$, due to the behaviour of strong coupling constant, α_s, with the scale Q^2. For an α_s independent of Q^2, $F_2^\gamma(x, Q^2)$ tends to an asymptotic value with increasing Q^2 [28]. For a running coupling constant, $\alpha_s = \alpha_s(Q^2)$, $F_2^\gamma(x, Q^2)$ is expected to rise linearly with $\log Q^2$. Measurements of $F_2^\gamma(x, Q^2)$ at high Q^2 should give an indication as to whether an asymptotic limit to $F_2^\gamma(x, Q^2)$ is reached.

The upper limit in Q^2 at LEP2 is expected to be extended up to scales of $Q^2 \approx 500$ GeV^2 to make measurements into the kinematical areas where the proton structure function, F_2^{P}, begins to rise for low x (see Fig. 1.2 [29]). This rise was first reported [30] by the ZEUS and H1 experimental collaborations at the HERA ep collider over a wide range of Q^2 values.

1.3.2 Low x

One of the current areas of interest is the low x behaviour of F_2^γ. This is motivated by theoretical models and experimental results. Theoretically, both the DGLAP equations [31] for parton density functions with Q^2 evolution and the BFKL

equation [32] for $F_2^\gamma(x,Q^2)$ with $1/x$ evolution predict an increase in $F_2^\gamma(x,Q^2)$ with decreasing x below 0.1. This corresponds to a large rise in the gluon content of the photon at low x. Experimentally, interest has been further heightened by the observation of such a low x rise in the structure function of the proton, F_2^{P}. A low x rise in the photon structure function F_2^γ has not yet been observed. The measurements at LEP1 are hampered by not being able to extend down as low in x and as high in Q^2 as at HERA. The low x limit is not expected to be improved upon at LEP2 due to higher Q^2 values measured in each tagging detector than at LEP1.

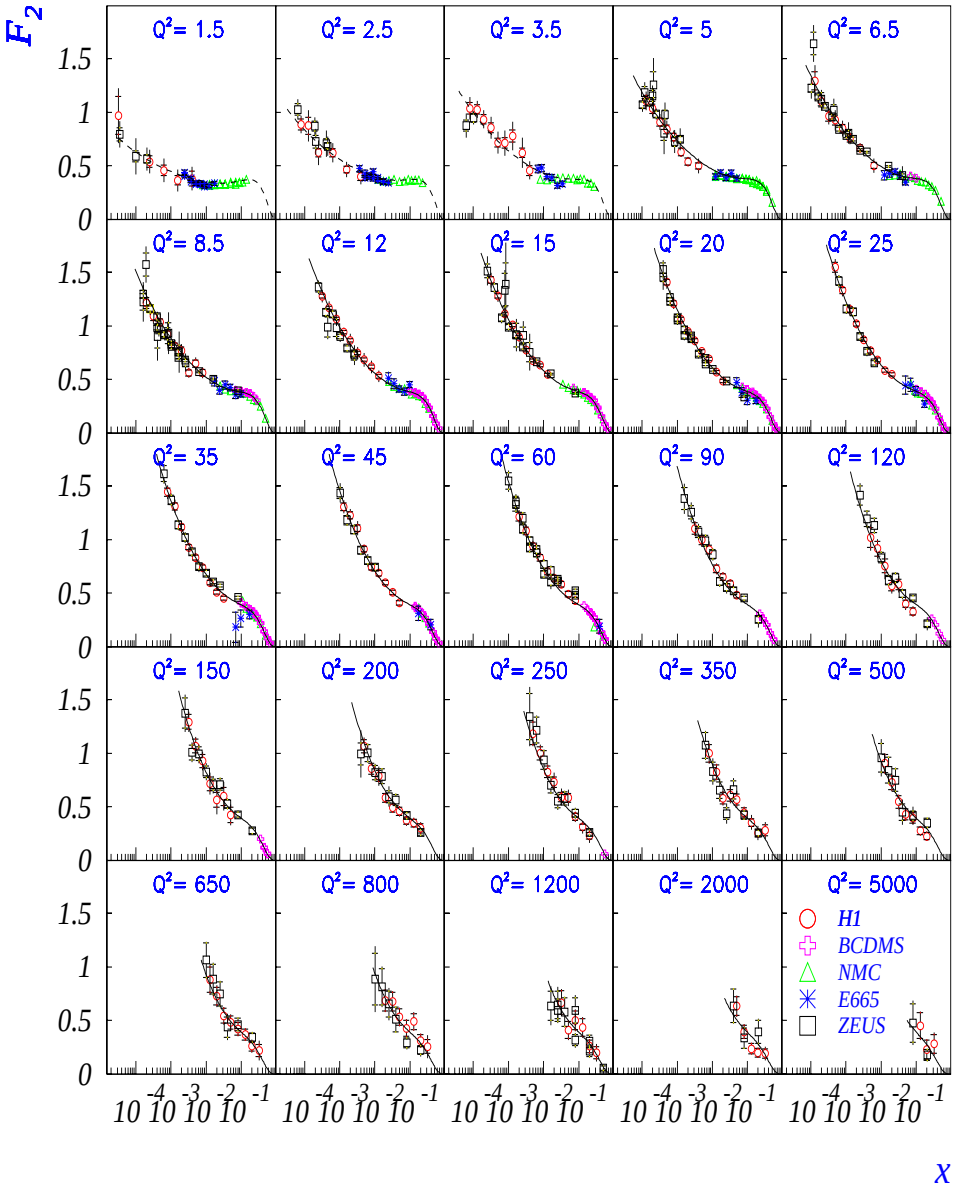

Figure 1.2: Diagrams showing the rise in the proton structure function F_2^{P}.

1.4 Background Studies at LEP

An important issue for experimentalists who are performing analyses in other areas at LEP is to be able to accurately calculate the background from two–photon interactions in their data samples. This is particularly acute for searches for new particles such as the Higgs boson and supersymmetric particles. I have generated samples of events using the F2GEN generator for background processes at both LEP1 and LEP2.

The cross–sections for hadronic and muonic two–photon processes are shown as a function of e^+e^- centre–of–mass energy in Fig. 1.3. At LEP1, the hadron production via e^+e^- annihilation shows a sharp peak at the Z^0 mass and dominates over the hadronic two–photon cross–sections. For LEP2, the hadronic two–photon cross–section is at least three orders of magnitude larger than those for hadron production, Z^0 pair production and W pair production. It is worth noting that both of the two–photon cross–sections are dominated by events where neither photon is tagged in the detector, i.e. untagged events. The cross–section for singly–tagged analyses is about two orders of magnitude smaller than that for untagged analyses. However, this still means that singly–tagged events form a significant background when compared with the other processes shown in Fig. 1.3 and so it is extremely important to be able to model these processes well.

1.5 Experimental Measurements of $F_2^\gamma(x, Q^2)$

Measurements of the hadronic structure function of the photon, $F_2^\gamma(x, Q^2)$, have been made by several experimental collaborations at e^+e^- colliders. These are listed in Table 1.1 with corresponding Q^2 and x ranges.

Fig. 1.4 [27] shows the results for $F_2^\gamma(x, Q^2)$ from the LEP experiments. These measurements are made by analysing events where only one of the scattered beam electrons is detected so that x has to be determined from the hadronic final state. The measured invariant mass, $W_{\rm vis}$, of the detected (or "visible") hadronic final state is used to make an estimate $x_{\rm vis}$ for the true x distribution for the event samples.

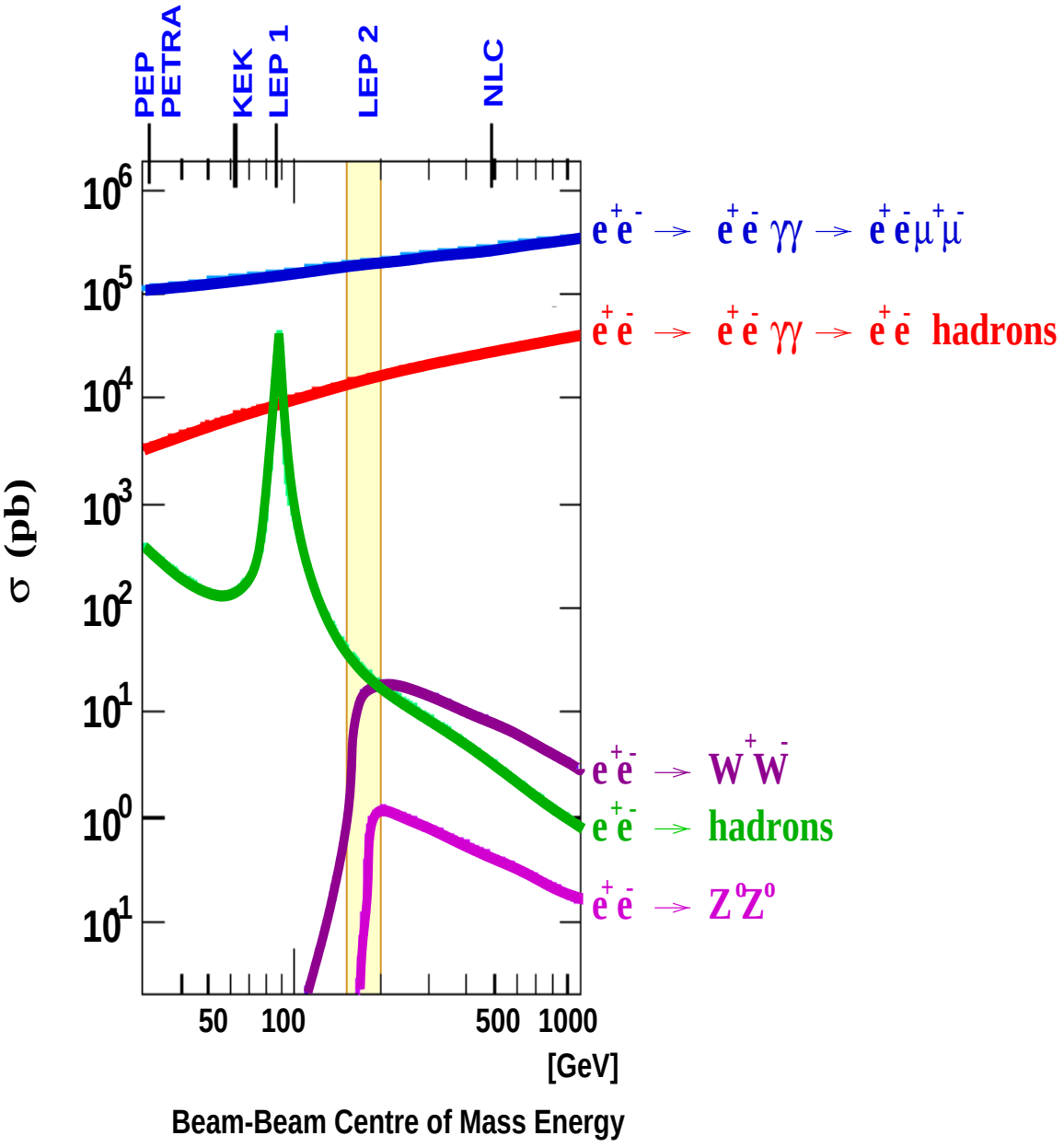

Figure 1.3: Cross–section of various processes at LEP as a function of the centre–of–mass energy of the electron and position beams

This reliance on the final state has forced experimentalists to use unfolding methods [33, 34] to correct for detector inefficiency. Unfolding methods rely in turn upon estimations of the detector efficiency for measuring hadrons by using Monte Carlo simulations of two–photon events. As a result, this can cause large systematic errors in the distributions for $F_2^\gamma(x,Q^2)$ where the Monte Carlo generators model the hadronic final state poorly. These errors on F_2^γ are particularly large for the two most interesting regions: high Q^2 (Fig. 1.5) and low x (Fig. 1.6) [35]. The large systematic and statistical errors make it difficult to perform any precision tests on the evolution of the structure function into the high Q^2 region, whilst in the low x region, they reduce greatly any sensitivity to a low x rise.

Clearly, the modelling of the hadronic final state must be improved for a reduction in the size of the systematic errors. In Chapters 6 and 7, comparisons of the energy flow in the hadronic final state are made and changes to the modelling in the HERWIG and PYTHIA Monte Carlo programs are proposed to aid the reduction of these systematic errors.

Collider	Coll.	$\langle Q^2 \rangle (\mathrm{GeV}^2)$	x range (No. of bins)	Reference
PETRA	PLUTO	2.4	0.016–0.700 (3)	[36]
		4.3	0.03–0.80 (3)	[36]
		9.2	0.06–0.90 (3)	[36]
		5.3	0.035–0.840 (6)	[36]
		45.0	0.1–0.9 (4)	[37]
	TASSO	23.0	0.02–0.98 (5)	[38]
	JADE	24.0	0.10–0.90 (4)	[39]
		100.0	0.1–0.9 (3)	[39]
PEP	TPC/2γ	0.7	0.014–0.105 (4)	[40]
		1.3	0.025–0.146 (4)	[40]
		5.1	0.02–0.74 (3)	[40]
		20.0	0.196–0.963 (3)	[41]
TRISTAN	AMY	73.0	0.2–0.9 (3)	[42]
		160.0	0.2–0.9 (3)	[42]
		390.0	0.2–0.9 (2)	[42]
		73.0	0.3–0.8 (3)	[43]
		390.0	0.3–0.8 (2)	[43]
	TOPAZ	5.1	0.01–0.20 (2)	[44]
		16.0	0.20–0.78 (3)	[44]
		80.0	0.06–0.98 (3)	[44]
	VENUS	40.0	0.09–0.81 (4)	[45]
		90.0	0.19–0.91 (4)	[45]
LEP	OPAL	1.86	0.0025–0.10 (4)	[4]
		3.76	0.0063–0.10 (4)	[4]
		5.9	0.001–0.649 (3)	[2, 46, 47]
		14.7	0.006–0.836 (4)	[2, 46, 47]
		7.5	0.001–0.649 (3)	[3]
		14.7	0.006–0.836 (4)	[3]
		135.0	0.1–0.8 (3)	[3]
		9.0	0.02–0.60 (3)	[5]
		14.5	0.02–0.60 (3)	[5]
		30.0	0.05–0.80 (4)	[5]
		59.0	0.05–0.08 (4)	[5]
		11.0	0.02–0.06 (3)	[5]
		41.0	0.05–0.80 (4)	[5]
	ALEPH	8.9	0.002–0.729 (4)	[6]
		19.1	0.005–0.900 (4)	[6]
		279.0	0.3–0.8 (4)	[27]
	DELPHI	12.0	0.001–0.847 (4)	[48]
		12.0	0.001–0.350 (3)	[48]
		6.3	0.3–0.8 (4)	[49]
		13.0	0.3–0.8 (4)	[49]
		22.0	0.3–0.8 (3)	[49]

Table 1.1: Experimental measurements of hadronic F_2^γ.

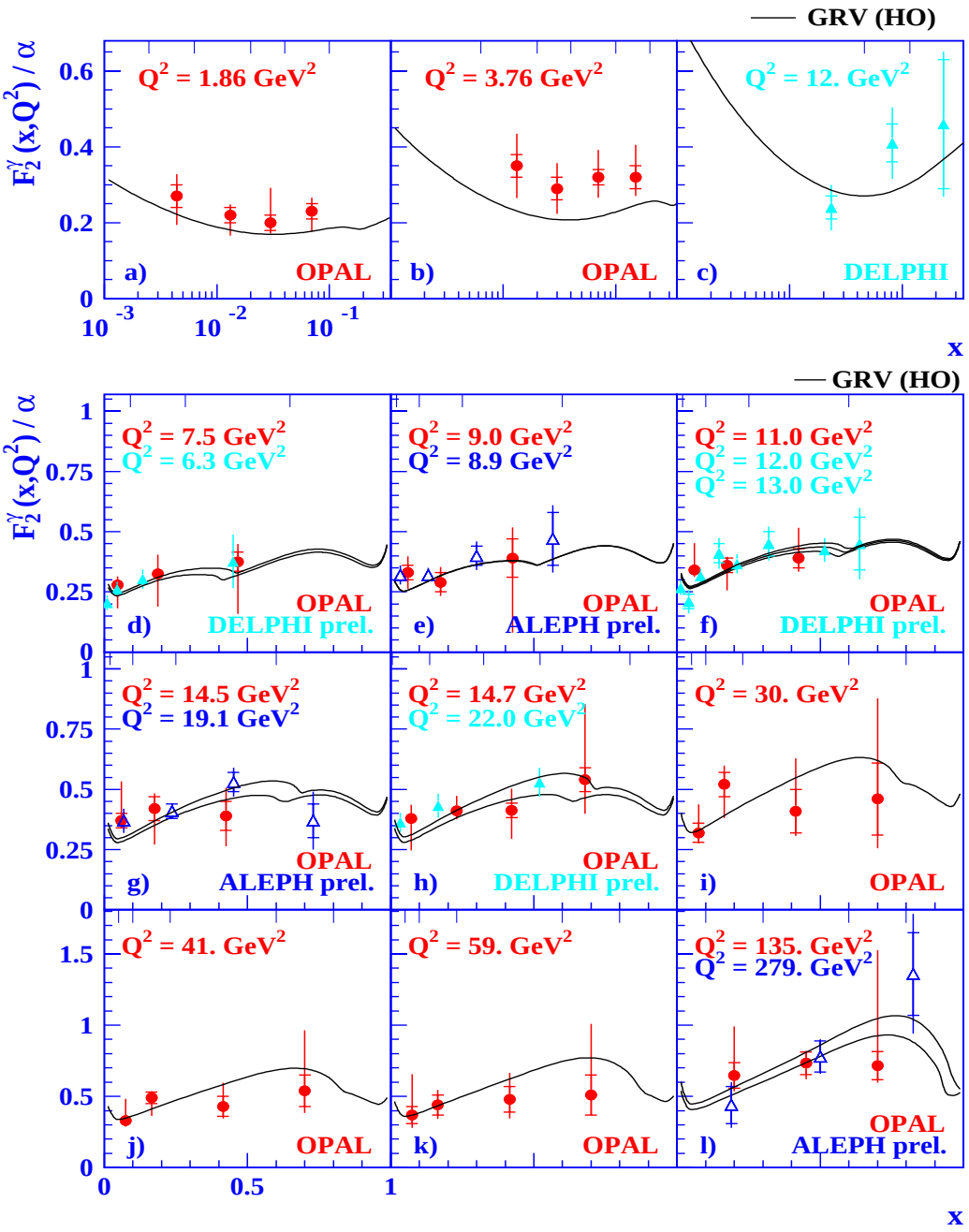

Figure 1.4: Measurements of F_2^γ at LEP. The theoretical curves shown are from the parameterisation of $F_2^\gamma(x,Q^2)$ by Glück, Reya and Vogt (GRV) and discussed in section 2.6.1.

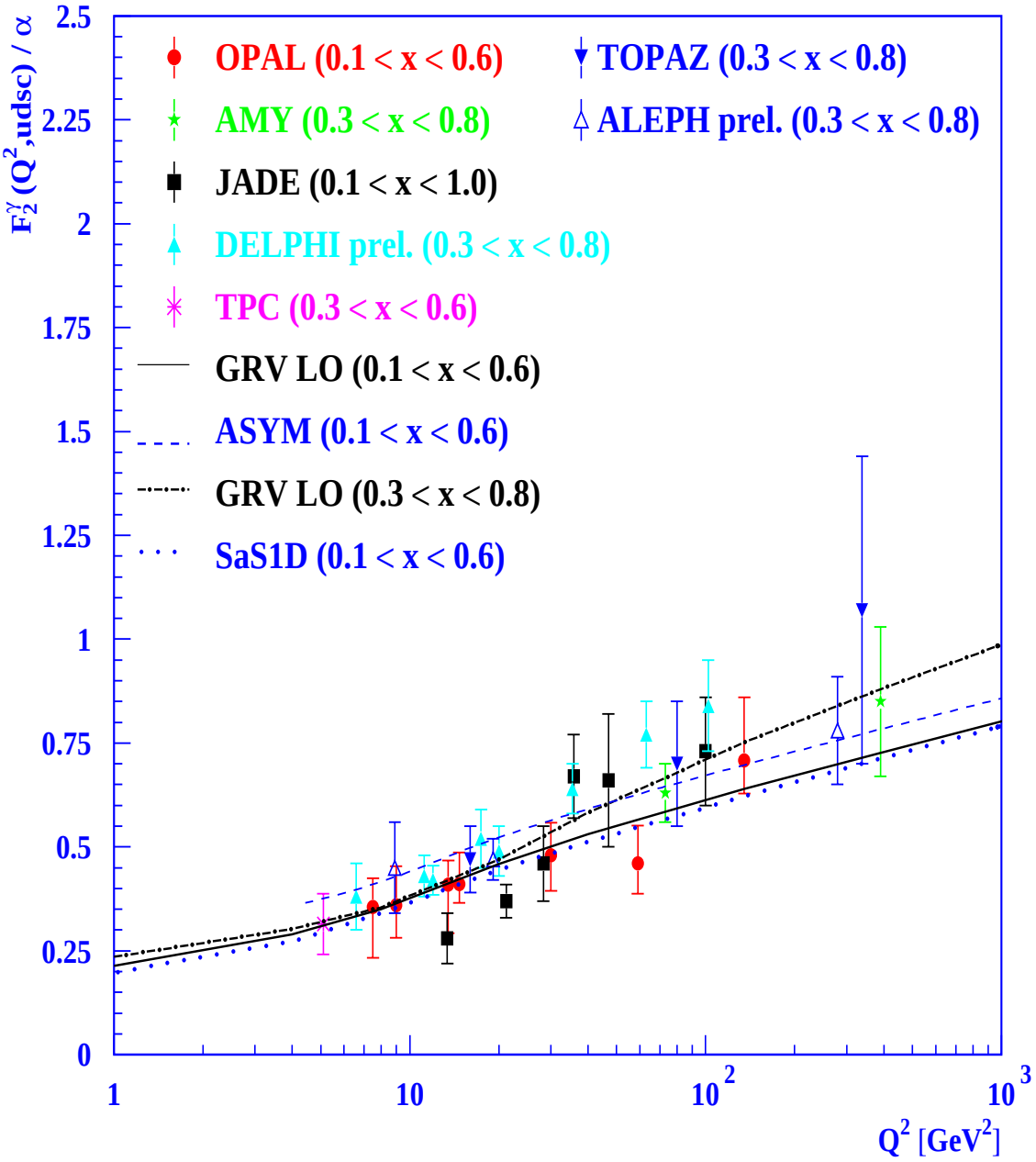

Figure 1.5: Q^2 evolution of F_2^γ. The theoretical models for the GRV and SaS1D parameterisations of $F_2^\gamma(x, Q^2)$ are discussed in sections 2.6.1 and 2.6.3

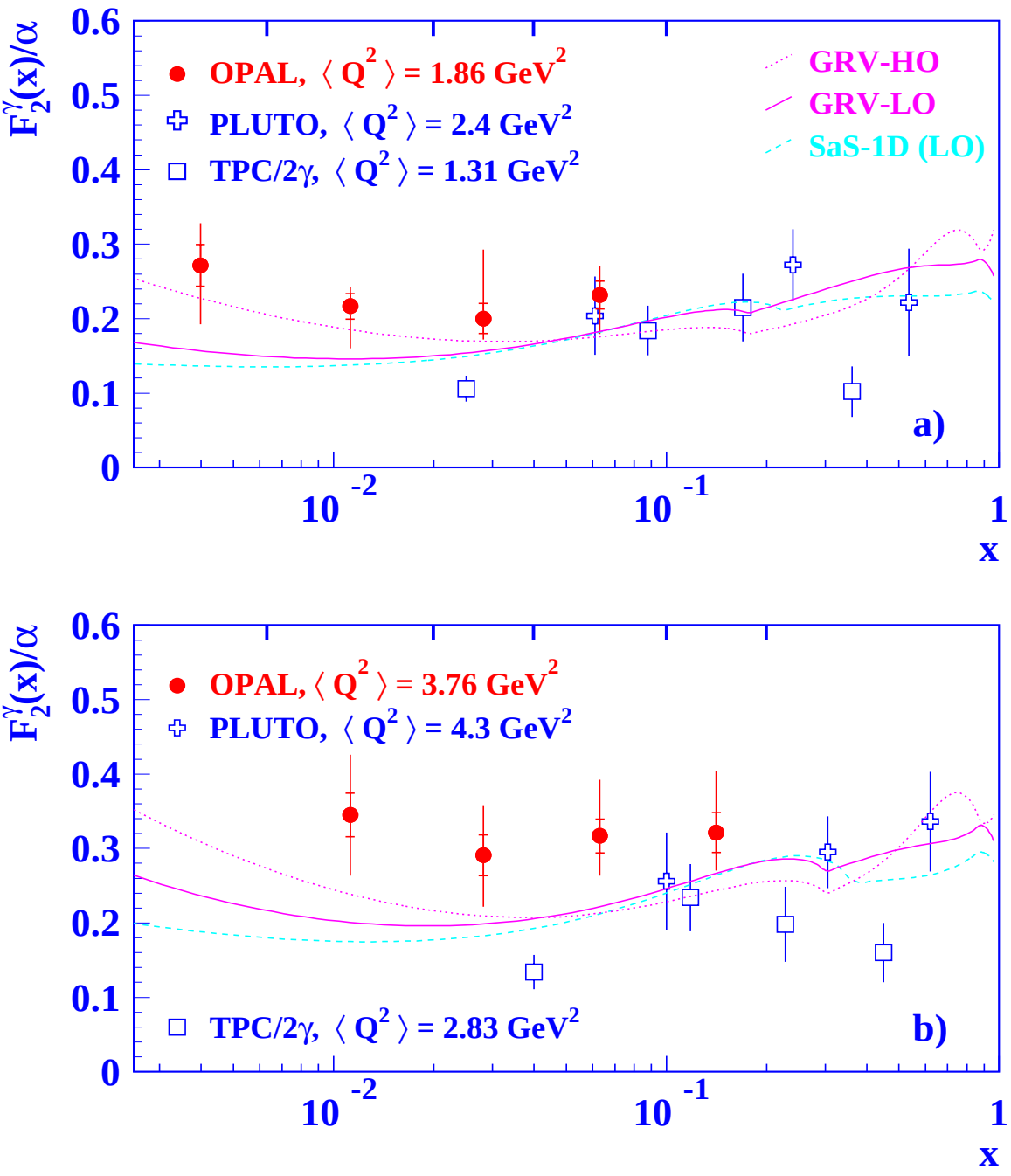

Figure 1.6: Measurements of F_2^γ at low x and Q^2.The theoretical models for the GRV and SaS1D parameterisations of $F_2^\gamma(x,Q^2)$ are discussed in sections 2.6.1 and 2.6.3

Chapter 2

Theory

The core of this thesis is comparing measured hadronic final state distributions with those predicted by the QCD–based Monte Carlo generators HERWIG and PYTHIA. The theory presented in this chapter attempts to explain the models used to describe the photonic structure in the language of QCD and deals with the regions of phase space where non–perturbative and perturbative models are needed.

2.1 Parton Distributions of the Photon

The photon can be considered sometimes to consist of partons (the set of all virtual fermions and gauge bosons produced by quantum fluctuations). It is natural to think of the structure function, $F_2^\gamma(x,Q^2)$, describing the cross–section (see section 1.2.3) for deep inelastic $e\gamma$ scattering, as a sum of parton density distributions, $q_i^\gamma(x,Q^2)$ and $\bar{q}_i^\gamma(x,Q^2)$ within the probed photon. To **L**eading **O**rder (LO):

$$F_2^\gamma(x,Q^2) = x\sum_{i=1}^{n_f} e_i^2\left[q_i^\gamma(x,Q^2)+\bar{q}_i^\gamma(x,Q^2)\right] + F_{2,he}^\gamma(x,Q^2) \quad (2.1)$$

$$= 2x\sum_{i=1}^{n_f} e_i^2\left[q_i^\gamma(x,Q^2)\right] + F_{2,he}^\gamma(x,Q^2) \quad (2.2)$$

where n_f is the number of active light quark flavours (u, d, s), e_i is the parton charge, $q_i^\gamma(x,Q^2)=\bar{q}_i^\gamma(x,Q^2)$ is assumed to hold and $F_{2,he}^\gamma(x,Q^2)$ is the calculated contribution of heavy quark flavours [50]. In most parameterisations for F_2^γ, bottom and top flavour

contributions to $F_{2,he}^\gamma$ are small at the presently achievable scales so that only the charm contribution to $F_{2,he}^\gamma$ is calculated.

At **N**ext–to–**L**eading **O**rder (NLO), there are additional contributions from gluons and the bare photon:

$$F_2^\gamma(x,Q^2) = \sum_{i=1}^{n_f} 2xe_i^2\Big[q_i^\gamma(x,Q^2) + \frac{\alpha_s}{2\pi}\Big(C_q \otimes q_i^\gamma(x,Q^2) + C_g \otimes g^\gamma(x,Q^2)\Big) + \frac{\alpha}{2\pi}e_i^2 C_\gamma\Big] + F_{2,he}^\gamma(x,Q^2) + \mathcal{O}\Big(1/Q^2\Big) \quad (2.3)$$

where $g^\gamma(x,Q^2)$ is the gluon density distribution in the photon, C_q, C_g are (factorisation scheme–dependent) hadronic NLO coefficient functions of x for the quark and the gluon densities respectively, and C_γ is a term for the 'direct' contribution of the bare photon. For the $\overline{MS}$ factorisation scheme, $C_\gamma = 6C_g$ [51], whilst for the DIS$_\gamma$ scheme [52], $C_\gamma = 0$. The symbol $\otimes$ represents the Mellin convolution of two functions, e.g. $a(x)$ and $b(x)$:

$$a(x) \otimes b(x) = \int_x^1 \frac{dy}{y} a\left(\frac{x}{y}\right) b(y) \quad (2.4)$$

Theoretical parameterisations of F_2^γ (see section 2.6) are calculated using the singlet and non–singlet representations, $q_S^\gamma(x,Q^2)$ and $q_{NS}^\gamma(x,Q^2)$ respectively, of the parton densities:

$$q_S^\gamma(x,Q^2) = 2\sum_{i=1}^{n_f} q_i^\gamma(x,Q^2) \quad (2.5)$$

$$q_{NS}^\gamma(x,Q^2) = 2\sum_{i=1}^{n_f}\Big[e_i^2 - \langle e^2\rangle\Big] q_i^\gamma(x,Q^2) \quad (2.6)$$

where

$$\langle e^2\rangle \equiv \frac{1}{n_f}\sum_i^{n_f} e_i^2. \quad (2.7)$$

2.2 Components of $F_2^\gamma(x,Q^2)$

It is desirable to be able to calculate the parton distributions of the photon from first principles. However, it is only in the asymptotic limit of $Q^2 \to \infty$ that it is possible to probe structure at distances much smaller than the confinement distance of ~ 1 fm, and hence use perturbative QCD calculations only. At low Q^2, the target

photon behaves as if it were a hadron [53] and a phenomenological treatment of its structure is needed. In deep inelastic $e\gamma$ scattering, it is conventional for calculations of the structure function, $F_2^\gamma(x,Q^2)$, to be made by separation of $F_2^\gamma(x,Q^2)$ into a "hadronic" component $F_{2,\mathrm{had}}^\gamma$ and a "pointlike" component $F_{2,\mathrm{pl}}^\gamma$:

$$F_2^\gamma(x,Q^2) = F_{2,\mathrm{had}}^\gamma + F_{2,\mathrm{pl}}^\gamma. \tag{2.8}$$

The hadronic component corresponds to considering the target photon as a hadron and calculations assume the hadronic photon can be described using the **V**ector **M**eson **D**ominance model. For the pointlike component, the scattering can be calculated using QCD corrections to the **Q**uark **P**arton **M**odel (QPM).

2.3 Vector Meson Dominance (VMD) and $F_{2,\mathrm{had}}^\gamma$

In the Vector Meson Dominance model, the photon is pictured as fluctuating into a vector meson with the same quantum numbers as the photon and hence VMD is often used to describe $F_{2,\mathrm{had}}^\gamma$. Since the quantum numbers of the meson, V, and the photon are the required to be the same, photon couplings to the ρ^0, ω, ϕ and J/ψ vector mesons form the basis of the VMD model for $F_{2,\mathrm{had}}^\gamma$:

$$F_{2,\mathrm{had}}^\gamma = F_{2,\mathrm{VMD}}^\gamma = \sum_V \left(\frac{4\pi\alpha_{em}}{f_V^2}\right) F_2^{\mathrm{V}} \tag{2.9}$$

where F_2^{V} is the structure function for the meson V and the values of $f_V^2/4\pi$ from data [53] are 2.20 for ρ^0, 23.6 for ω, 18.4 for ϕ and 11.5 for J/ψ. None of the vector meson structure functions F_2^{V} have been measured experimentally but are estimated using the measurements of the pion structure function [54].

There are several parameterisations of the VMD model. The simplest formula derived from the pion structure function data is [1, 19, 28]:

$$F_{2,\mathrm{VMD}}^\gamma = 0.2\alpha_{em}(1-x). \tag{2.10}$$

A second approach used in [55] is to construct the parton distributions of the photon, $f^\gamma = q^\gamma (= \bar{q}^\gamma)$ or g^γ, using the pionic parton distributions [56], f_π:

$$f^\gamma(x,\mu^2) = \kappa\left(\frac{4\pi\alpha_{em}}{f_\rho^2}\right) f_\pi(x,\mu^2) \tag{2.11}$$

where $\mu^2 \sim 0.3\text{GeV}^2$ is a low scale at which the vector meson input information applies and where $1 \lesssim \kappa \lesssim 2$ is a parameter related to ambiguities from the inclusion of the mesons into the VMD model.

A third approach is to use the low Q^2 data fit for $F^{\gamma}_{2,\text{VMD}}$ from the TPC/2γ experiment [40]:

$$F^{\gamma}_{2,\text{VMD}}(x, Q^2 = 0.7\ \text{GeV}^2) = \alpha_{em} A x^a (1-x)^{0.95} + B(1-x)^b \tag{2.12}$$

where $A = 0.22$, $B = 0.06$, $a = 0.31$ and $b = 2.5$. The limitations of this approach were discussed by Schuler and Sjöstrand in [57]. They pointed out that the analysis was conducted with a small number of data points in a limited x range. They offer an alternative approach where the non–perturbative VMD parton distribution functions are obtained using all available data for $F^{\gamma}_2(x, Q^2)$.

2.4 Quark Parton Model (QPM)

The Quark Parton Model is a simple model, predating QCD, for describing the structure of hadrons with the assumption that the pointlike quark constituents are free particles. This assumption does not account for gluon interactions between the quark constituents and so QCD corrections are needed.

Without QCD corrections and for light quarks ($m_i/Q^2 \ll 1$), the QPM structure function for the photon, $F^{\gamma}_{2,\text{QPM}}$, is given by [58]:

$$F^{\gamma}_{2,\text{QPM}}(x, Q^2, P^2, m_i^2) = \frac{3\alpha}{\pi} \sum_{i=1}^{n_f} e_i^4 x \left[(1 + 2x + 2x^2) \log\left(\frac{Q^2(1-x)}{x(m_i^2 - P^2 x(1-x))} \right) \right. \tag{2.13}$$
$$\left. + \frac{m_i^2(1 - 2x + 2x^2)}{(m_i^2 - P^2 x(1-x))} - 2(1 - 3x - 3x^2) \right].$$

In the case of deep inelastic $e\gamma$ scattering of an electron off a real photon, $P^2 \equiv 0$, Eqn. 2.13 simplifies to:

$$\begin{aligned} F^{\gamma}_{2,\text{QPM}}(x, Q^2, P^2 = 0, m_i^2) &= F^{\gamma}_{2,\text{QPM}}(x, Q^2, m_i^2) \\ &= \frac{3\alpha}{\pi} \sum_{i=1}^{n_f} e_i^4 x \left[(1 + 2x + 2x^2) \log\left(\frac{Q^2(1-x)}{x m_i^2} \right) + 8x(1-x) - 1 \right] \end{aligned} \tag{2.14}$$

In both Eqn.'s 2.13 and 2.14, there is a $\log Q^2$ dependence such that Bjorken x scaling is broken.

The picture that QPM gives is clearly incomplete. Eqn. 2.14 does not include QCD effects, the gluon content of the photon, and contributions from heavy flavour quarks, principally charm quarks at the energies and scales of current experimental measurements.

2.5 QCD and Heavy Flavour Effects

2.5.1 The Gluon Content of the Photon $g^\gamma(x, Q^2)$

In QCD, the strong interactions between quarks and antiquarks are mediated by gluon exchange. A gluon emitted by a quark (or antiquark) can be absorbed again by the quarks (antiquarks) within the photon structure, or can split into either a quark–antiquark pair or into two gluons. The gluon distribution $g^\gamma(x, Q^2)$ is concentrated at lower x than the quark distributions $q_i^\gamma(x, Q^2)$ (see Fig. 2.1), since an emitted gluon has a lower fraction of the photon's momentum than the emitting quark (antiquark).

2.5.2 The DGLAP Evolution Equations

There are several ways of incorporating gluons into predictions of $q_i^\gamma(x, Q^2)$ and $F_2^\gamma(x, Q^2)$. One method is the operator product expansion and renormalisation group equations (OPERGE) [51, 59], and another is to use Feynman diagrams in the leading log approximation [60, 61, 62]. The most common method of calculating $F_2^\gamma(x, Q^2)$ [55, 63, 64, 65, 66, 67, 68] is via the use of evolution equations [69, 70] upon an initial parameterisation for $q_i^\gamma(x, Q^2)$ and $g^\gamma(x, Q^2)$.

In general and for massless quarks, the evolution of $q_i^\gamma(x, Q^2)$ and $g^\gamma(x, Q^2)$ with the scale Q^2 is described by the **D**okshitzer–**G**ribov–**L**ipatov–**A**ltarelli–**P**arisi (DGLAP) [31, 71] evolution equations. These can be written as [70]:

$$\frac{dq_i^\gamma}{d\ln Q^2} = \frac{\alpha_{em}}{2\pi}\bar{P}_{q_i\gamma} \otimes 1^\gamma + \frac{\alpha_s}{2\pi}(Q^2)\left(2\sum_{k=1}^{n_f}\bar{P}_{q_iq_k} \otimes q_k^\gamma + \bar{P}_{q_ig} \otimes g^\gamma\right) \qquad (2.15)$$

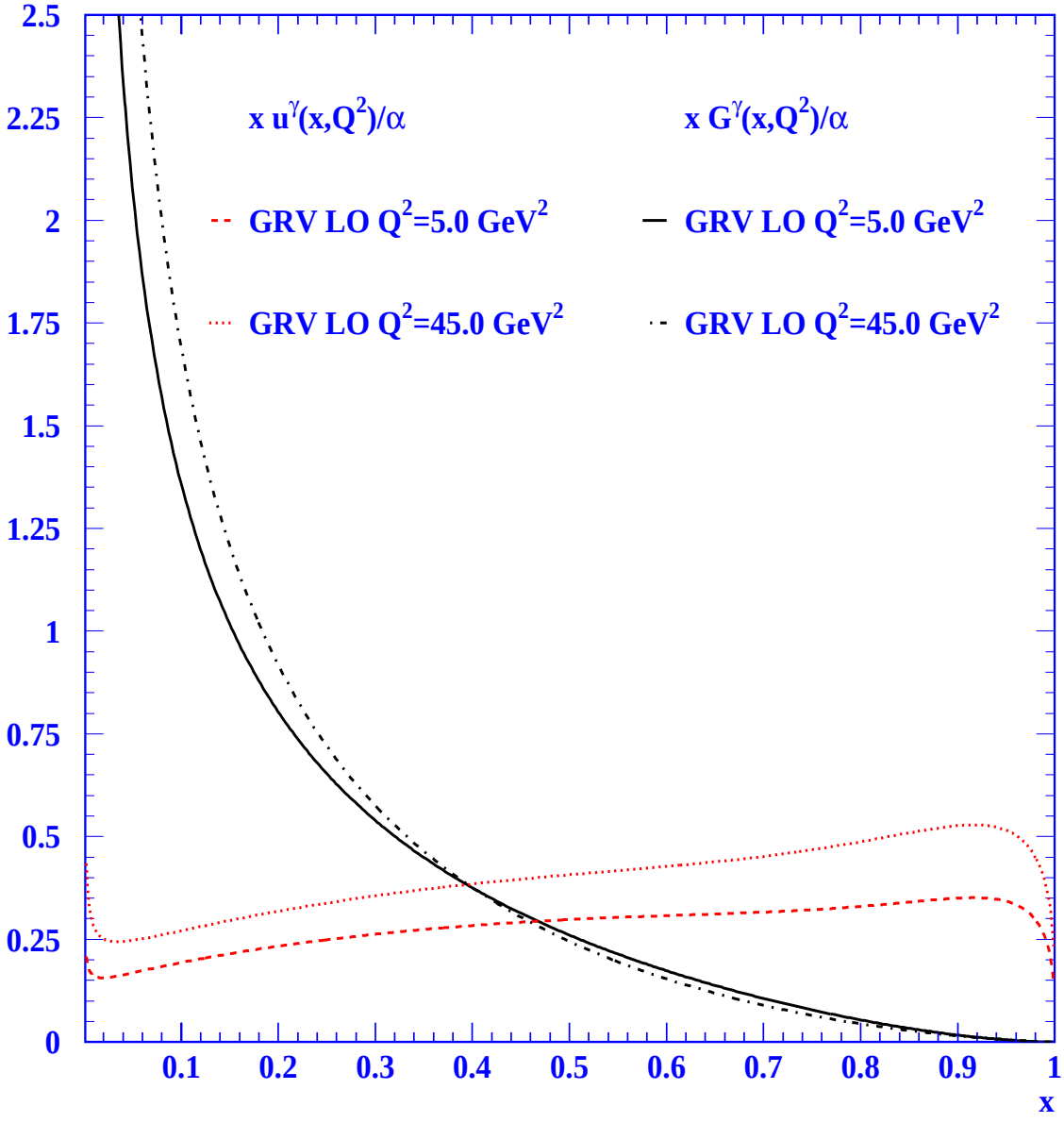

Figure 2.1: The GRV **L**eading **O**rder $u(x,Q^2)$ and $G^\gamma(x,Q^2)$ distributions calculated at $Q^2 = 5$ GeV^2 and $Q^2 = 45$ GeV^2.

$$\frac{dg^\gamma}{d\ln Q^2} = \frac{\alpha_{em}}{2\pi}\bar{P}_{g\gamma} \otimes , ^\gamma + \frac{\alpha_s}{2\pi}(Q^2)\left(2\sum_{k=1}^{n_f}\bar{P}_{gq_k} \otimes q_k^\gamma + \bar{P}_{gg} \otimes g^\gamma\right) \quad (2.16)$$

$$\frac{d, ^\gamma}{d\ln Q^2} = \frac{\alpha_{em}}{2\pi}\bar{P}_{\gamma\gamma} \otimes , ^\gamma + \frac{\alpha_s}{2\pi}(Q^2)\left(2\sum_{k=1}^{n_f}\bar{P}_{\gamma q_k} \otimes q_k^\gamma + \bar{P}_{\gamma g} \otimes g^\gamma\right) \quad (2.17)$$

where $, ^\gamma(x, Q^2)$ represents the "bare" photon distribution within the photon (see also section 2.1), $\otimes$ is the Mellin convolution (Eqn. 2.4), $n_f = 3$ is the number of active flavours (u,d,s), $\bar{P}_{ij}$ are the generalised splitting functions:

$$\bar{P}_{ij}(x, \alpha_{em}, \alpha_{Q^2}) = \sum_{l,m=0} \frac{\alpha_{em}^l \alpha_s^m}{(2\pi)^{l+m}} \bar{P}_{ij}^{l,m}(x) \quad (2.18)$$

and $\bar{P}_{q_i q_k}$ are the average of the quark–quark and quark–antiquark splitting functions. As for Eqn. 2.2, $q_i^\gamma(x, Q^2) \equiv \bar{q}_i^\gamma(x, Q^2)$ is assumed to hold.

Most calculations of the evolution of the parton distributions are performed to $\mathcal{O}(\alpha_{\rm em})$ where $\alpha_{em} \ll 1$ and so the $l \neq 0$ terms of Eqn. 2.18 can be neglected. To leading order (LO) in α_s, $\bar{P}_{ij} \equiv P_{ij}$ where P_{ij} are physically interpreted as the probability of finding a parton i in a parton j with a fraction x of the parent parton momentum. Eqns 2.15 and 2.16 can be simplified then to:

$$\frac{dq_i^\gamma}{d\ln Q^2} = \frac{\alpha_{em}}{2\pi}P_{q_i\gamma} + \frac{\alpha_s}{2\pi}(Q^2)\left(2\sum_{k=1}^{n_f}\bar{P}_{q_i q_k} \otimes q_k^\gamma + \bar{P}_{q_i g} \otimes g^\gamma\right) \quad (2.19)$$

$$\frac{dg^\gamma}{d\ln Q^2} = \frac{\alpha_{em}}{2\pi}P_{g\gamma} + \frac{\alpha_s}{2\pi}(Q^2)\left(2\sum_{k=1}^{n_f}\bar{P}_{q_i q_k} \otimes q_k^\gamma + \bar{P}_{q_i g} \otimes g^\gamma\right) \quad (2.20)$$

for $n_f = 3$ quark flavours and where the various splitting functions are [71]:

$$P_{qq}(z) = C_F\left[\frac{1+z^2}{(1-z)_+} + \frac{3}{2}\delta(1-z)\right] \quad (2.21)$$

$$P_{qg}(z) = C_F\left[z^2 + (1-z^2)\right] \quad (2.22)$$

$$P_{gq}(z) = T_R\left[\frac{1+(1-z^2)^2}{z}\right] \quad (2.23)$$

$$P_{gg}(z) = 2C_A\left[\frac{z}{(1-z)_+} + \frac{1-z}{z} + z(1-z)\right] + \frac{1}{6}(11C_A - 4n_f T_R)\delta(1-z) \quad (2.24)$$

with $C_F = 4/3$, $T_R = 1/2$ and $C_A = 3$. The "+" subscript is used to remove the singular terms from the calculation of the integrals in Eqns. 2.19 and 2.20 using:

$$\int_0^1 dx f(x)[g(x)]_+ = \int_0^1 dx(f(x) - f(1))g(x) \tag{2.25}$$

The singularities at $z = 1$ correspond to the emission of soft gluons whilst the remaining singularities at $z = 0$ lie outside the limits of integration.

2.5.3 Charm Quark Contributions to $F_2^\gamma(x, Q^2)$

For large scales ($Q^2 > 100$ GeV^2), the charm quark would also be considered light and hence could be included into the calculation of Eqn. 2.14 with $n_f = 4$. However, most measurements of F_2^γ are made at scales $Q^2 \lesssim 100$ GeV^2 where it is inappropriate to use the massless DGLAP evolution equations for calculating the charm parton distributions. Instead, to take into account the mass of the charm quark, m_c, the evolution of the parton distributions should be performed using the massive quark DGLAP equations [72], or, more accurately, the calculations of the charm content should incorporate the full next–to–leading order corrections [50].

In many of the available parameterisations [55, 63, 64, 68], a minimum threshold of $W^2 = Q^2(1/x - 1) = 4m_c^2$ is required for the charm contribution to be added into F_2^γ. Below this threshold, the charm contribution is set to zero. This gives rise to a discontinuity in the shape of F_2^γ as illustrated for the GRV, LAC1 and SaS1D parameterisations in Fig. 2.2 (see also section 2.6).

In [64], the sum of the two leading order QPM processes, $\gamma\gamma^* \to c\bar{c}$ and $g\gamma^* \to c\bar{c}$, were found to be a good approximation of the charm contribution to $F_2^\gamma(x, Q^2)$ for $Q^2 \leqslant 100$ GeV^2. The process $\gamma\gamma^* \to c\bar{c}$ is called the "direct" process whilst $g\gamma^* \to c\bar{c}$ is called the "resolved" process. Above $Q^2 = 100$ GeV^2, the gluon emissions of the quark and antiquark cannot be ignored and the evolution equations are needed.

The Direct QPM Process

The direct QPM process is used in the calculations of some F_2^γ parameterisations [55, 64, 66]. The charm contribution to F_2^γ is calculated using the lowest order Bethe–Heitler process [73, 74] and is [55, 64]:

$$F_{2,c}^\gamma(x, Q^2) \Big|_{\text{direct}} = 3xe_c^4 \frac{\alpha_{em}}{\pi} \omega\Big(x, \frac{m_c^2}{Q^2}\Big) \tag{2.26}$$

where $e_c = 2/3$ is the charm–quark electric charge and

$$\omega(z,r) = z\Big[\beta\Big\{-1+8z(1-z)-4rz(1-z)\Big\} + \Big\{z^2+(1-z^2)+4rz(1-3z)-8r^2z^2\Big\}\ln\Big(\frac{1+\beta}{1-\beta}\Big)\Big] \quad (2.27)$$

$$\beta = \sqrt{1-\frac{4rz}{1-z}} \quad (2.28)$$

The Resolved QPM Process

The contribution of the resolved QPM process ($g\gamma^* \to c\bar{c}$) to F_2^γ is given by [64] as

$$F_{2,c}^\gamma(x,Q^2)\Big|_{resolved} = e_c^2\frac{\alpha_s(Q^2)}{2\pi}\int_{ax}^1 dy\ \omega\Big(\frac{x}{y},\frac{m_c^2}{Q^2}\Big)g^\gamma(y,Q^2) \quad (2.29)$$

where $a = 1+4m_c^2/Q^2$, $g^\gamma(x,Q^2)$ is obtained by solving Eqn. 2.16 or Eqn. 2.20 and the function ω is given in Eqn. 2.27.

2.5.4 Low x

Much of the current interest in F_2^γ is in the low x region and stems from the HERA findings of the rise in the proton structure function, $F_2^{\rm P}$, as $x \to 0$. So far, no corresponding rise in F_2^γ has been reported. The rise in $F_2^{\rm P}$ implies that the sea quark distribution grows rapidly as $x \to 0$. In terms of the parton distributions at low Q^2, the increase in quark density is driven by the much larger and increasing gluon density at low x.

Two ways of calculating parton distributions for low x are:

1. the use of the DGLAP equations (see section 2.5.2);
2. the use of the **B**alitsky–**F**adin–**K**uraev–**L**ipatov (BFKL) equation.

The DGLAP equations describe the evolution of parton distributions with the scale Q^2. Only leading log terms in Q^2 are kept in the derivation whilst terms proportional to $\ln 1/x$ are taken to be negligible. This assumption holds only for $\ln 1/x \ll \ln Q^2$.

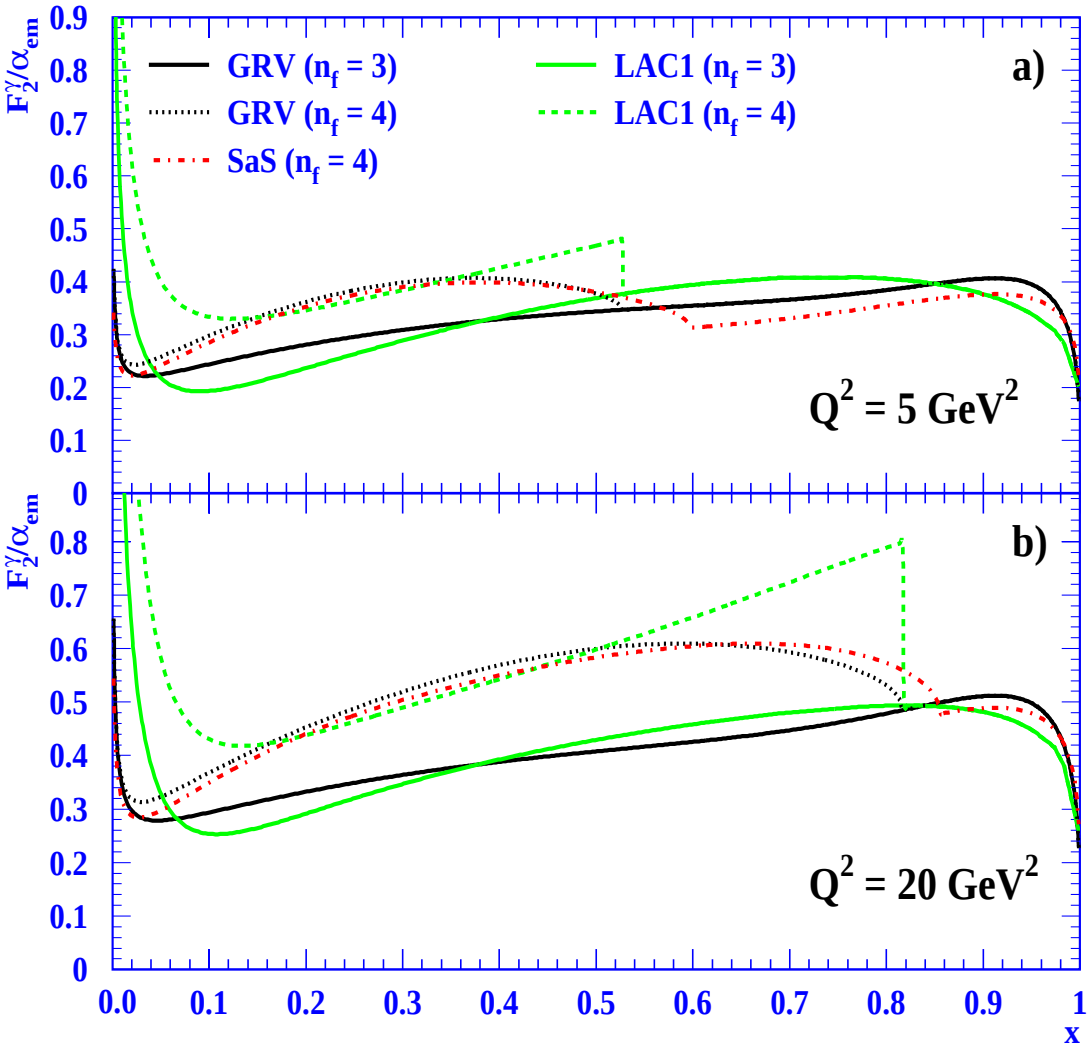

Figure 2.2: The GRV, LAC1 and SaS1D **L**eading **O**rder parameterisations of F_2^γ for 4 flavours and 3 flavours calculated at a) $Q^2 = 5$ GeV^2 and b) $Q^2 = 20$ GeV^2.

In the low x region, the DGLAP calculations correspond to a resummation of terms proportional to $\alpha_s \ln Q^2$ to all orders in perturbation theory. A solution for the gluon distribution g^γ has been calculated [75] in terms of x and the virtuality phase space, t, of the gluon evolution:

$$g^\gamma(x,t) \sim \frac{1}{x} \exp \sqrt{\frac{12}{\pi b} \ln \frac{\ln t/\Lambda^2}{\ln t_o/\Lambda^2} \ln \frac{1}{x}} \tag{2.30}$$

where

$$b = \frac{11C_A - 2n_f}{12\pi}; \quad C_A = 3. \tag{2.31}$$

The initial virtuality t_o of the gluon corresponds to a starting point for the evolution. For $t < t_o$, the gluon is assumed to form part of the hadron–like photon which is modelled as a vector meson (see section 2.3) and is thus not calculable in perturbative QCD.

The BFKL equation describes the evolution of parton densities with $1/x$, with particular application in the low x region (i.e. where Q^2 is not large). The BFKL equation includes the resummation of $\alpha_s \ln 1/x$ terms to all orders and retaining the full Q^2 dependence. A simple derivation of the BFKL equation is performed by Mueller [76] in terms of the wave-function of a heavy flavour quark–antiquark pair (quarkonium). The result for the gluon distribution g at small x in terms of the transverse momentum k_T of the gluons is:

$$xg(x,Q^2) \sim \int^{Q^2} dk_T^2 h(k_T^2) x^{-\lambda} \tag{2.32}$$

where $h \sim (k_T^2)^{-\frac{1}{2}}$ for large k_T^2 and $\lambda = 12 \ln 2 \alpha_s/\pi \approx 0.5$.

2.6 Parameterisations of $F_2^\gamma(x,Q^2)$

There are many parameterisations of F_2^γ available e.g. [55, 62, 63, 64, 65, 66, 67, 68]. A common method of calculating F_2^γ parameterisations is to set parton distributions at some low resolution scale, Q_o, and use the DGLAP equations (Eqns. 2.15–2.17) to perform the Q^2 evolution of these distributions. $F_2^\gamma(x,Q^2)$ is then constructed using Eqn. 2.2 (LO) or Eqn. 2.4 (NLO). The parameterisations used to generate Monte Carlo samples for comparison with data samples (see chapters 5) are described below.

2.6.1 The Glück, Reya and Vogt Parameterisation: GRV

These authors have calculated parton distributions for the pion [56] and the proton [77]. The parton distributions of both were generated from a common valence–like structure at a common low resolution scale, Q_o. The choice of a similar approach for calculating the parton distributions of the photon is motivated by the good agreement of the proton and pion parameterisations with data from deep inelastic scattering experiments, especially those taken at HERA [30].

The GRV parton distributions for the photon [55] are given to LO and NLO, and are made for the DIS_γ factorisation scheme [52]. The input distributions to the evolution equations are purely VMD using Eqn. 2.11 where

$$x f_\pi(x,\mu^2) \sim x^a(1-x)^b \quad (a>0) \tag{2.33}$$

and are given by [56]. The evolution begins at the scales ${Q^2}_o = 0.25$ GeV^2 (LO) and ${Q^2}_o = 0.3$ GeV^2 (NLO). Only one free parameter, κ, remains to be fixed and is calculated to be $\kappa_{\mathrm{LO}} = 2$ (LO) and $\kappa_{NLO} = 1.6$ (NLO) using the best fits to the available data [36, 37, 38, 39, 40, 40, 42]. The partonic distributions $q_i^\gamma(x,Q^2)$ are calculated from the evolution equations by differentiating each $q_i^\gamma(x,Q^2)$ into two components: a "hadronic" part q_{had}^γ and a "pointlike" part q_{PL}^γ where

$$q_i^\gamma(x,Q^2) = q_{\mathrm{had}}^\gamma + q_{\mathrm{PL}}^\gamma \tag{2.34}$$

(see section 2.2). The low Q^2, high x points from the TPC/2γ measurements [40] were excluded as they lie within the resonance region ($W < 2$ GeV) which are argued to be poorly measured [55, 78]. The contribution from charm quarks is modelled using the direct QPM process described in section 2.5.3 and is calculated for a charm quark mass, $m_c = 1.5$ GeV.

Only the LO parameterisation is used in the generation of Monte Carlo samples for comparison with data (see chapters 5). Fig. 2.2 shows the predictions of $F_2^\gamma(x,Q^2)/\alpha$ from the GRV LO parameterisation for $n_f = 3$ and $n_f = 4$ flavours and for $Q^2 = 5.0$ GeV^2 and $Q^2 = 20$ GeV^2.

2.6.2 The Levy, Abaramowicz and Charchula Parameterisations: LAC

Levy, Abaramowicz and Charchula adopted the same approach as that of Drees and Grassie [66] by not splitting F_2^γ into perturbative and non–perturbative components as in Eqn. 2.8. They presented [68] a set of three LO parameterisations (LAC1, LAC2 and LAC3) derived by choosing quark and gluon distributions at a starting low resolution scale ${Q^2}_0$. The free parameters in these initial distributions were set by fitting the evolution of these distributions to a larger number of data points [20, 36, 37, 38, 39, 40, 42] than the 7 data points available to Drees and Grassie.

The quark distributions used in the fit are of the functional form:

$$xq_i^\gamma(x) = Ae_q^2 x\frac{x^2+(1-x)^2}{1-B\ln(1-x)} + C_i x^{D_i}(1-x)^{E_i} \tag{2.35}$$

where A and B are the same for all flavours $i = u, d, s, c$. The parameters C_i, D_i and E_i are the same for u and d quarks and D_i and E_i are the same for s and c quarks. The remaining two C_i parameters are different for s and c quarks. The charm contribution was included only for $W^2 \geqslant 4m_c^2$ where $m_c = 1.5$ GeV. The gluon distribution takes the form:

$$xg^\gamma(x) = C_g x^{D_g}(1-x)^{E_g} \tag{2.36}$$

This gives a total of 12 free parameters for which three fits were performed:

1. **LAC1**: for all data points with $Q^2 > {Q^2}_o = 4$ GeV^2;
2. **LAC2**: for all data points with $Q^2 > {Q^2}_o = 4$ GeV^2 and where the parameter $D_g \equiv 0$ was kept fixed;
3. **LAC3**: for all data points with $Q^2 > {Q^2}_o = 1$ GeV^2.

Additionally, the parameter Λ in the evolution equations was set at 0.2 GeV.

The calculated $F_2^\gamma(x, Q^2)$ for the LAC1 parameterisation are shown in Fig. 2.2 for $n_f = 3$ and $n_f = 4$ quark flavours at $Q^2 = 5.0$ GeV^2 and $Q^2 = 20.0$ GeV^2. In [79], Vogt argues that the lack of physical constraints on the quark flavour decomposition and on the gluon density lead to unphysical results (e.g. $s(x, Q^2) > d(x, Q^2)$ in some regions).

2.6.3 The Schuler and Sjöstrand Parameterisations: SaS

The set of F_2^γ parameterisations proposed by Schuler and Sjöstrand [63] were calculated using a decomposition of the parton distributions into three components (compare with Eqns. 2.8 and 2.11)

$$f^\gamma(x,Q^2) = f^{\gamma,anom}(x,Q^2) + f^{\gamma,hadronic}(x,Q^2) + f^{\gamma,direct}(x,Q^2). \tag{2.37}$$

$f^{\gamma,anom}(x,Q^2)$ is the perturbatively calculable ("anomalous") contribution, $f^{\gamma,had}(x,Q^2)$ is the non–perturbative ("hadronic") contribution, and $f^{\gamma,direct}(x,Q^2)$ is a direct contribution from the bare photon to f^γ. The major difference between the GRV and SaS parameterisations is in the treatment of the hadronic component, $f^{\gamma,had}$. In GRV, it was assumed that this can be modelled using the parton distributions for the pion. In SaS, $f^{\gamma,had}$ was calculated by performing a fit to all of the available data [20, 36, 37, 38, 39, 40, 42, 44, 47].

There are four sets of parton distributions presented, corresponding to the permutations of two different starting scales, Q_o, for the evolution with the DIS and $\overline{MS}$ factorisation schemes:

1. **SaS1D** : $Q_o = 0.6$ GeV, DIS_γ factorisation;
2. **SaS1M** : $Q_o = 0.6$ GeV, $\overline{MS}$ factorisation;
3. **SaS2D** : $Q_o = 2.0$ GeV, DIS_γ factorisation;
4. **SaS2M** : $Q_o = 2.0$ GeV, $\overline{MS}$ factorisation;

The evolution is carried out with $\Lambda = 0.23$ GeV for $n_f = 3$ quark flavours and $\Lambda = 0.2$ GeV for $n_f = 4$ quark flavours. Charm contributions are included for both direct and resolved processes (see section 2.5.3) with $m_c = 1.3$ GeV.

2.7 QCD–Based Monte Carlo Generators

Two QCD–based Monte Carlo generators are used here in the analysis of two–photon events. The first of these is the general purpose **HERWIG** [7, 8] event generator which simulates **H**adron **E**mission **R**eactions **W**ith **I**nterfering **G**luons. It was designed with the philosophy of providing as complete as possible an implementation of perturbative QCD, combined with a simple model of non–perturbative QCD,

in a wide range of processes. The second generator used is called **PYTHIA** [7, 9] and, like HERWIG, is designed to simulate a wide variety of physics processes using a combination of perturbative and non–perturbative QCD models.

The method of two–photon event generation employed by HERWIG and PYTHIA can be divided into four stages:

1. photon emission from the incoming e^+e^- beams;
2. simulation of a hard sub–process using partonic $2 \rightarrow 2$ matrix elements along with partonic densities of the photon;
3. emission of additional partons using parton showering of initial and final parton states;
4. hadronisation of all final state partons and photon remnants.

The main differences between the HERWIG and PYTHIA Monte Carlo programs lies in the treatment of the parton showers before and after the hard scattering subprocess. Both programs use parton showers to cover approximately 90% of the parton emission phase space. However, there is no attempt in the PYTHIA generator to cover the remaining phase space whilst full matrix elements to order α_s are used by HERWIG in this region.

2.7.1 Photon Generation

There are two methods available in HERWIG for photon radiation from the incoming e^+e^- beam particles. The first method makes use of the **E**quivalent **P**hoton **A**pproximation (EPA) [80] to generate both of the radiated photons, with the limits of photon transverse energy and virtuality (via the negative square of the photon invariant mass) set by the user. The second method is the deep inelastic lepton–photon ($e\gamma$) treatment of the two–photon interaction. A quasi–real photon (γ) is generated using the EPA from the incoming beam electron. The interaction with a virtual photon radiated by the other electron is simulated in the hard sub–process using a chosen partonic distribution for the photon. In principle, it is possible to generate single–tagged two–photon events using the first method but the second method is recommended by the authors and is adopted for the generation of all the HERWIG samples presented.

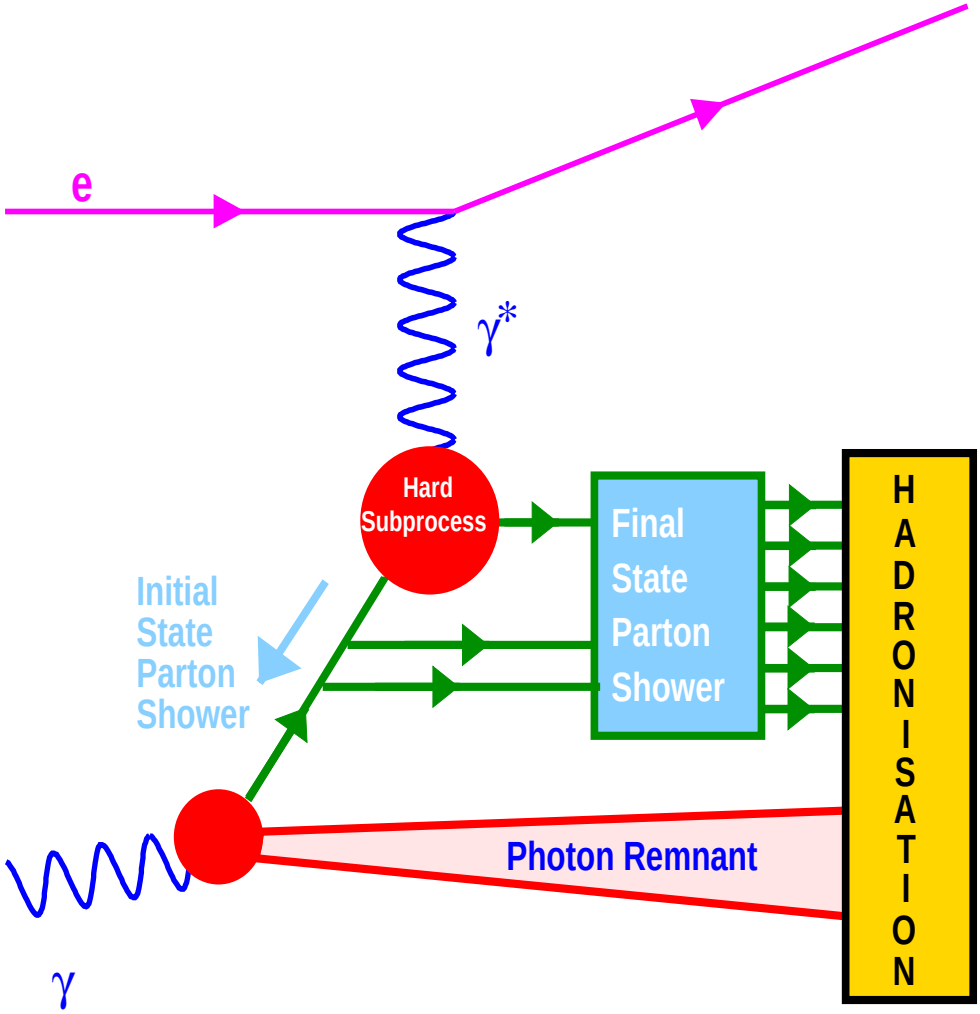

Figure 2.3: A representation of the deep inelastic $e\gamma$ scattering model used in the HERWIG and PYTHIA Monte Carlo generators.

The PYTHIA samples used in this analysis are generated using the deep inelastic $e\gamma$ scattering treatment of the two–photon interaction. The vertex involving the emission of the probe photon ($Q^2 \gg 0$) is simulated using a chosen parton distribution of the photon. In contrast to the HERWIG samples, the generated target photons are real ($P^2 \equiv 0$). The sampled photon energy spectrum is approximated by using the varying–energy and weighted–events options available.

2.7.2 Hard Subprocess

The generation of singly–tagged two–photon events is modelled using the deep inelastic $e\gamma$ scattering process (see Fig. 2.3). This means that the (exchanged) probe photon is usually more virtual than the struck parton. In principle, the simulation of the scattering process would use the full matrix elements describing the higher order $2 \rightarrow 3$ subprocesses $eq \rightarrow eqg$, $eg \rightarrow eq\bar{q}$ and $e\gamma \rightarrow eq\bar{q}$. However, when the photon virtuality is much larger than the quark virtuality, the DGLAP probability distributions of the chosen parameterisation of $F_2^\gamma(x, Q^2)$ (see section 2.5.2) are used as approximations to the chance of finding the struck quark inside a higher–x quark ($q \rightarrow qg$), gluon ($g \rightarrow q\bar{q}$) or photon ($\gamma \rightarrow q\bar{q}$). This approximation leads to the incorporation of the $2 \rightarrow 3$ processes into the evolution of the photon distribution functions using parton showering. However, it is acknowledged [81, 82] that this approach does not apply to the whole region of emission phase space covered by the full matrix elements and that it is based upon expansions around the soft and collinear limits which dominate the emission phase space. In versions of the HERWIG generator later than 5.7, matrix elements to first order in α_s are used to generate hard emission subprocesses outside the region covered by the parton shower method. The matrix element regions and the parton shower regions of the emission phase space are matched at the boundary of these two regions of phase space.

2.7.3 Parton Showering

The incoming parton to the hard scattering process undergoes inital state parton showering. Fig 2.4 shows the model used for the initial state parton shower

where the shower is evolved backwards in virtuality from the hard subprocess to the incoming target photon. Any partons radiated by the incoming parton, along with the outgoing parton from the hard subprocess, undergo further showering as part of the final state parton shower. Unlike the initial state shower, the evolution of the final state shower is forward in direction away from the hard subprocess.

The showering algorithms used in HERWIG and PYTHIA differ in the generation of each branching, $a \rightarrow bc$, in the shower, where the possible branching processes are $q \rightarrow qg$, $q \rightarrow q\gamma$, $g \rightarrow gg$ and $g \rightarrow q\bar{q}$ along with the corresponding processes for antiquarks. The PYTHIA algorithm orders the branching by decreasing the virtuality of the partons along the shower whilst HERWIG achieves a similar result by ordering of the branchings in terms of decreasing emission angle at each branching point. A shower is terminated when a minimum parton virtuality of 1 GeV is reached for PYTHIA, whilst the corresponding termination parameter for HERWIG is a minimum emission angle.

2.7.4 Hadronisation

All partons remaining after the termination of the final state parton shower, as well as the target photon remnant, are converted into particles using a hadronisation model.

The cluster model [83] is adopted in HERWIG. In this model, partons from the hard subprocess undergo the perturbatively–described parton showering and then form into colour–singlet *clusters* of partons which then decay into the observed hadrons.

In PYTHIA, the Lund string model from JETSET [84] is used. The outgoing partons from the hard subprocess are colour connected. As they move away from each other, they lose energy to the surrounding colour field which supposedly collapses into a string configuration between them. The string has a uniform energy per unit length which is consistent with quarkonium spectroscopy. The string breaks up into hadron–sized pieces through spontaneous $q\bar{q}$ pair production in the intense colour field of the string.

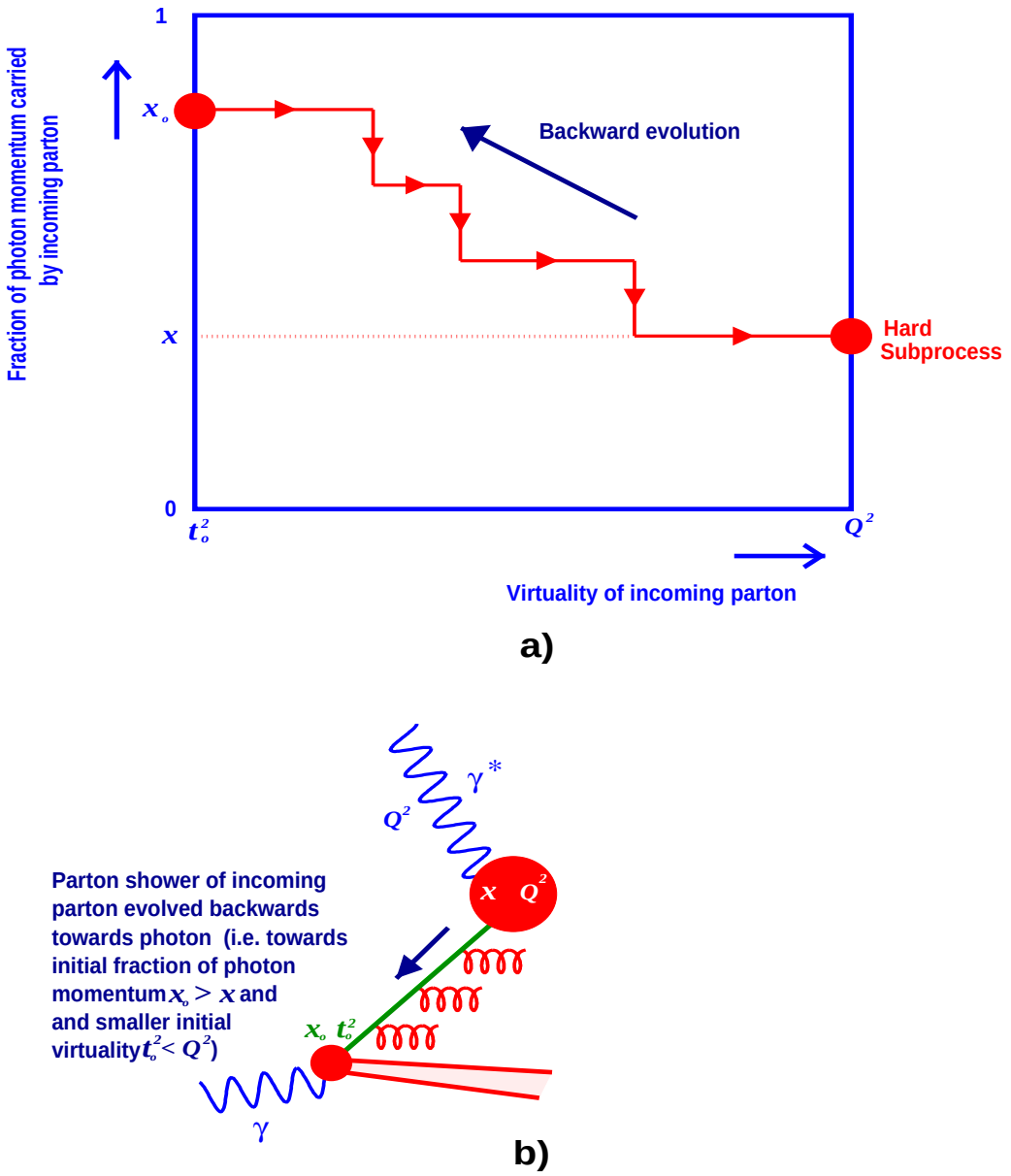

Figure 2.4: Diagrams illustrating the models of the initial state parton shower used in HERWIG and PYTHIA. Plot a) shows the direction of evolution in x and parton–virtuality space. Plot b) shows the schematics of this evolution from the hard subprocess back to the incoming target photon.

2.8 The VERMASEREN Monte Carlo Generator

The Vermaseren [85] Monte Carlo program (called VERMASEREN throughout the rest of the text) is used to generate fermion pair production events using exact QED matrix–elements for the multiperipheral two–photon process (Fig. 2.5a) and the t–channel Bremsstrahlung process (Fig. 2.5b). Hadronic final states can be generated when quark masses, charges and colour factors are also given, in which case VERMASEREN becomes a QPM generator.

This program is used to provide a comparison and check for the F2GEN program described briefly below and for background estimation in the data samples. For two–photon events where both the emitted photons have small virtualities, the Bremsstrahlung process has a contribution smaller than that of the multiperipheral process by a factor of roughly $\ln(E_{\rm b}/m_e)$ where $E_{\rm b}$ is beam energy and m_e is the mass of the electron. This corresponds to just over an order of magnitude at LEP beam energies. There is no interference between the Bremsstrahlung process and the multiperipheral process for both photons being real in Fig 2.5a). When one photon, γ^*, has a large virtuality, the Bremsstrahlung process is only significant for low invariant mass of the $\gamma\gamma^*$ and/or large scattering angles of the beam electron [1].

2.9 The F2GEN Monte Carlo Generator

The program F2GEN is used as a generator of singly–tagged, multiperipheral two–photon events (Fig. 2.5a). It was developed from the TWOGEN program [10] by the OPAL collaboration for use in measurements of $F_2^\gamma(x,Q^2)$ [47]. Events are generated by sampling:

1. the luminosity function for two–photon production from a lepton pair in colliding beams and

2. the cross–section, $\sigma(\gamma^*\gamma \rightarrow \text{hadrons})$, for the production of hadrons from the interaction of two photons.

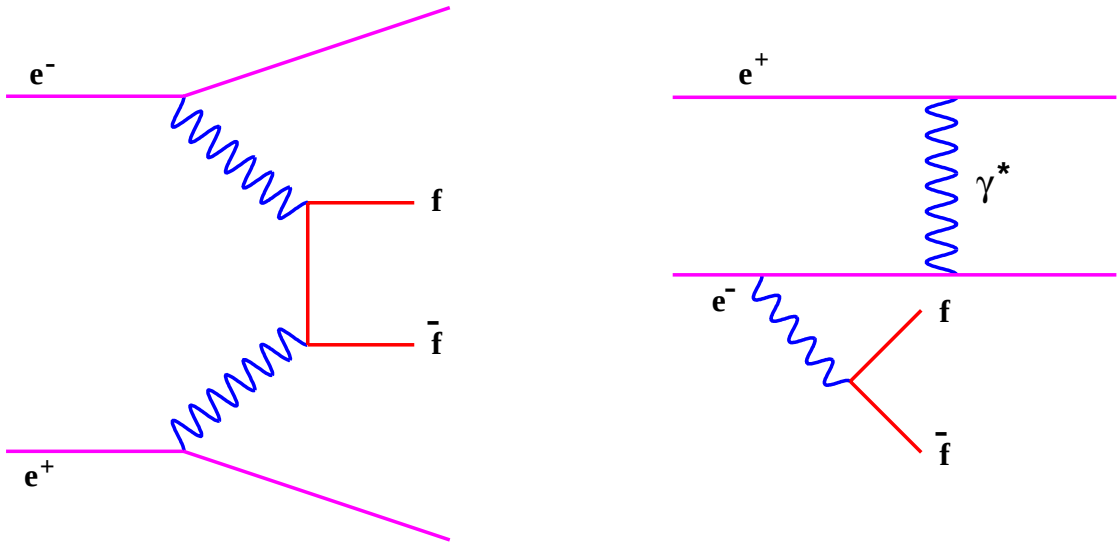

a) Fermion production in multiperipheral two-photon events

b) Fermion pair production via s-channel Bremsstrahlung

Figure 2.5: The two diagrams simulated in the Vermaseren Monte Carlo generator.

corresponding to a factorisation of the total cross–section into two parts. The chosen parameterisation for $F_2^\gamma(x,Q^2)$ is used to approximate for the cross–section $\sigma(\gamma^*\gamma \rightarrow$ hadrons):

$$\sigma(\gamma^*\gamma \rightarrow q\bar{q} \rightarrow \text{hadrons}) = \frac{8\pi^2\alpha}{Q^2} F_2^\gamma(x,Q^2). \tag{2.38}$$

The hadronic final state is simulated by generation of a quark–antiquark pair in the two–photon centre–of–mass frame and which are then hadronised using the JETSET string algorithm.

The algorithm used in F2GEN for event generation is more fully explained in chapter 7.

Chapter 3

LEP and OPAL

3.1 LEP

The Large Electron Positron (LEP) collider is an e^+e^- storage ring located at CERN, just outside Geneva, Switzerland (see Fig. 3.1). It has a circumference of 27 km, and is located underground at a depth of about 100 metres. It was first run in 1989, and until the latter part of 1995 was used to collide electron and positron beams with centre of mass energy around the mass of the Z^0 boson. At the end of October 1995, the LEP beams were run at the higher centre of mass energies (between 130 GeV and 140 GeV). This was increased to 161 GeV by using superconducting cavities with the start of the first LEP2 run in June 1996, and a further upgrade of LEP resulted in the 172 GeV running from October 1996. More upgrades are planned, with an aim to have LEP running at centre of mass energies of 192 GeV by 1998 and possibly 200 GeV by 1999.

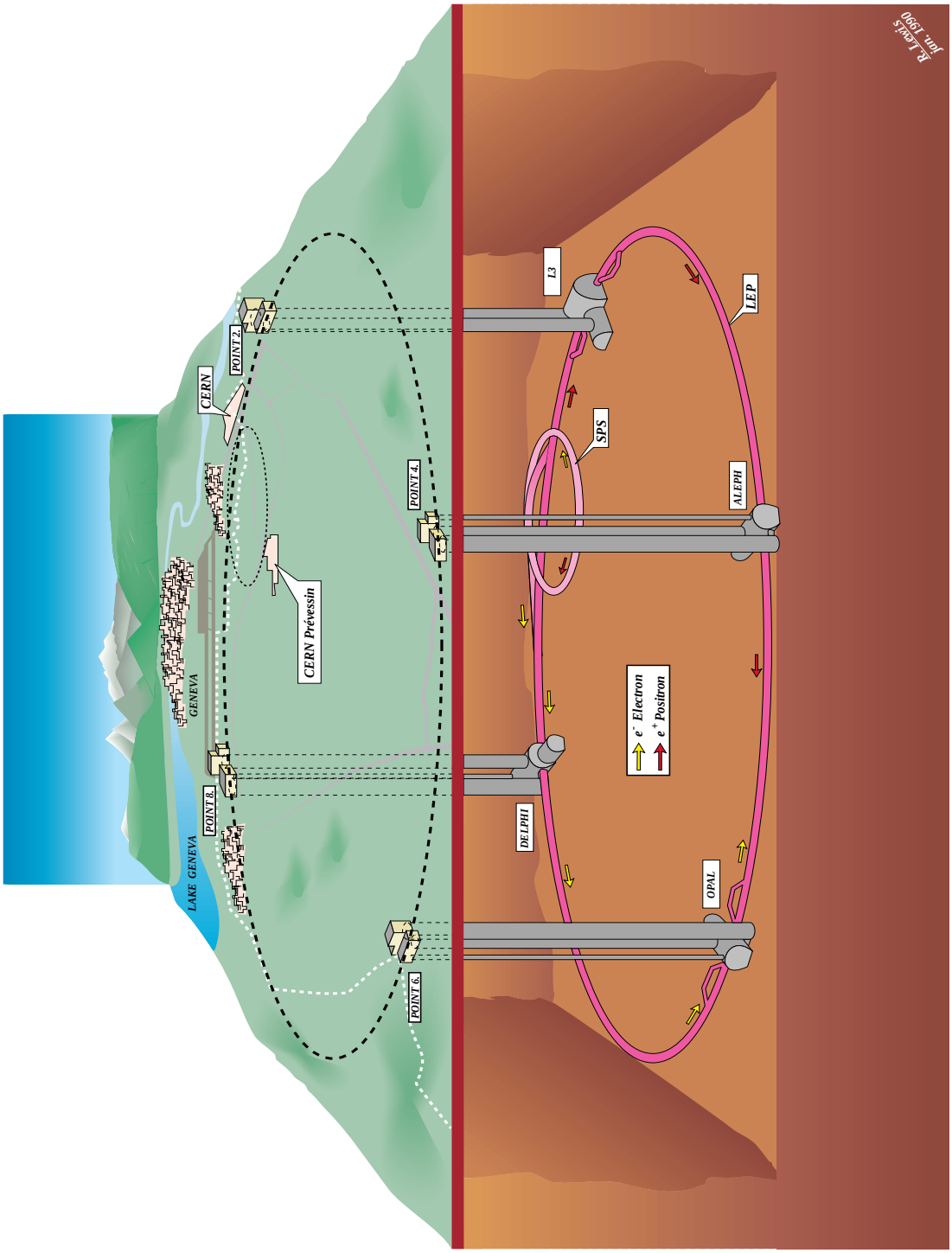

Figure 3.1: Schematic view of the LEP accelerator and the positions of the four LEP experiments around the ring

3.1.1 Obtaining Electron and Positron Beams in LEP

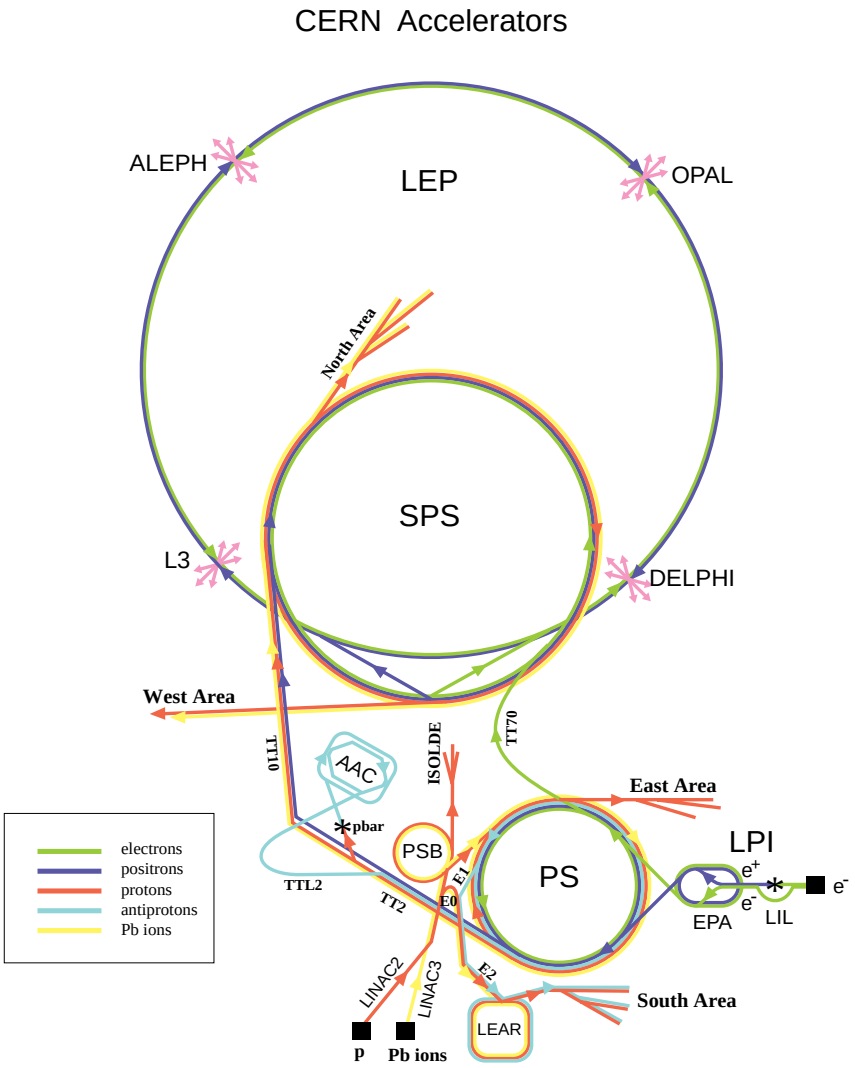

Figure 3.2: The various accelerators at CERN.

Fig. 3.2 shows the accelerators used at CERN. The LEP accelerator was designed to make use of the existing **P**roton **S**ynchrotron (PS) and **S**uper **P**roton **S**ynchrotron (SPS) to pre–accelerate electron and positron beams before they are put into the LEP ring and further accelerated. The sequence of beam generation is:

1. an electron gun is used to make bunches of electrons at a rate of about one hundred per second;

2. these electrons are focussed using magnets and accelerated to 600 MeV in the **L**EP **I**njector **L**inac. Some of the electron bunches are brought onto a fixed target to produce positrons via Bremsstrahlung and pair production. The bunches of positrons formed are focussed and accelerated to 600 MeV using the LIL;

3. approximately a thousand bunches from the LIL are amalgamated into 4 or more bunches of electrons and 4 or more bunches of positrons in the **E**lectron **P**ositron **A**ccumulator;

4. from the EPA, the electrons and positrons are injected into the PS and accelerated to 3.5 GeV ;

5. the beams from the PS are then fed into the SPS where they undergo a final pre-acceleration to 20 GeV ;

6. the beams are injected into LEP from the SPS and are accelerated up to the desired beam energy at which the beams are brought into collision at the the four experimental points around the LEP ring.

It takes 15–30 minutes for this repeated sequence to get $\sim 5 \times 10^9$ electrons and positrons in LEP. Such large numbers of electrons and positrons are needed to increase the probability of an interesting interaction taking place. This probability is directly related to the **luminosity** of the beams.

3.1.2 Beam Luminosity

The beam luminosity, $\mathcal{L}$, is an important quantity for measuring the cross–section, σ, of a physics process using

$$\mathcal{L} = \frac{\mathrm{N}}{\sigma} \tag{3.1}$$

where N is the number of events counted for this process in the detector. Hence, the beam luminosity is a measure of the particle density of the colliding beams in a unit

amount of time. Since the statistical error on this calculation decreases with $\sqrt{N}$, and hence with more beam–beam collisions, the beam luminosity is conventionally taken to mean the integrated luminosity over a period of time. The cross–section is conventionally quoted in units picobarns, pb, where

$$1\text{pb} = 10^{-12}\text{barn} = 10^{-36}\text{cm}^2$$

and as a result the (integrated) luminosity is given in terms of pb^{-1}. This convention is adopted throughout this thesis.

The luminosity received from LEP is measured by counting the number of events where a beam positron and a beam electron scatter elastically into the detector. These Bhabha events are characterised by two high energy back–to–back electromagnetic clusters with no other activity recorded in the detector. This process is used for calibrating the beam luminosity because the cross–section is well–known and large at low polar angles.

3.1.3 Bunch Modes and Bunch Trains in LEP

The electron and positron beams injected into LEP are not continuous beams but are comprised of a number of bunches of $< 2 \times 10^8$ electrons or positrons. For most of the running time at beam–beam centre of mass energies close to the Z^0 mass, LEP was operated with either 4 bunches ("4+4 bunch mode") or 8 bunches ("8+8 bunch mode") in each beam. Alternatively, it is possible to produce the two beams each composed of "bunchtrains". Each bunchtrain is in turn comprised of up to 4 separate bunchlets.

At the very start of running in 1989, LEP was operated in 4+4 bunch mode, switching to 8+8 bunches in 1992 until the end of data–taking in 1994. Since 1995, LEP has been operated with 4 bunchtrains in each beam with a varying number of bunchlets per bunchtrain. Both the "8+8 bunch" and the "4+4 bunchtrain" operating modes were used to increase the beam luminosity and hence the amount of data recorded by each experiment.

3.2 OPAL

The OPAL (**O**mni **P**urpose **A**pparatus for **L**EP) detector [11] is one of the four experiments collecting data at LEP and was first used in 1989. It is designed to study a wide variety of interactions occurring in e^+e^- collisions. Fig. 3.3 shows a diagram of the component subdetectors of OPAL. A description of their construction and function is given below.

There are five main types of subdetector, listed here in approximate order of increasing distance from the interaction region (see Fig 3.4):

- Vertex and tracking subdetectors to
  - → track positions and momenta of charged particles entering the central region of OPAL;
  - → provide dE/dx information for these charged particles which can be used for purposes of particle identification;
  - → reconstruct primary and secondary vertices of an event.
- Electromagnetic calorimetry for energy measurement of photons and electrons.
- Hadronic calorimetry for the energy measurement of hadrons.
- Muon detectors for muon identification.
- Forward luminosity monitors used for measuring the received LEP luminosity at OPAL, and for identification of scattered electrons necessary for selection of the events in this analysis.

Two–letter shorthand names are defined for easy labelling of data from each of the various subdetectors. This shorthand has been adopted in this thesis.

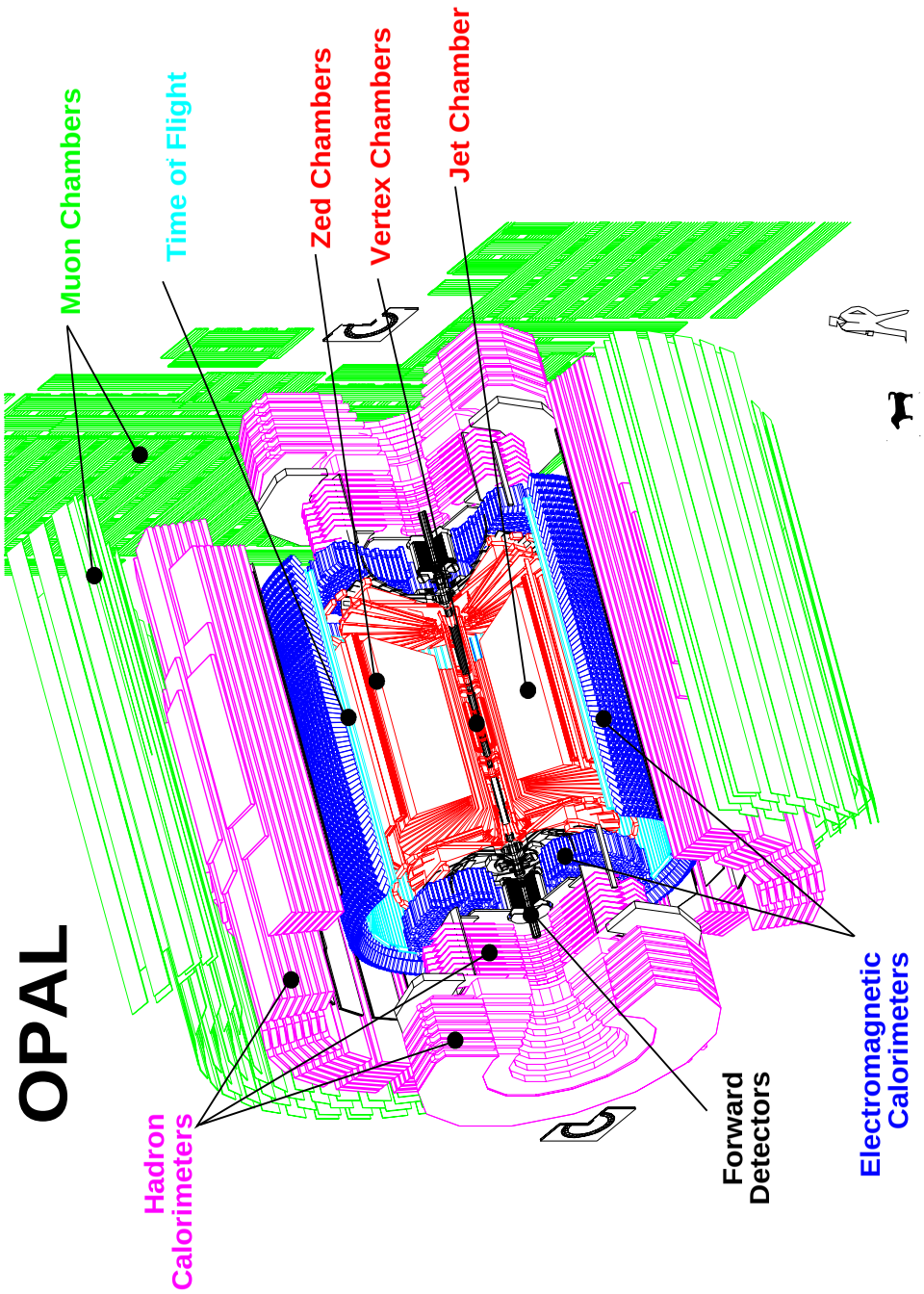

Figure 3.3: Cut away diagram showing the subdetectors of OPAL.

3.2.1 The OPAL Coordinate System

In the OPAL right–handed coordinate system, the x-axis points towards the centre of the LEP ring (see Fig. 3.1), the y-axis at a small angle to the vertical and the z-axis points in the direction of the electron beam. The polar angle θ and the azimuthal angle ϕ are defined with respect to the z-axis and x-axis, respectively.

3.2.2 The OPAL Magnet

The magnet consists of a water cooled solenoid and an iron yoke to provide the flux return. The solenoid was wound in one complete unit to prevent discontinuities causing non-uniformities in the magnetic field. The iron yoke also provides at least four interaction lengths for the sampling hadron calorimeter (see section 3.6).

The magnetic field in the central tracking region is 0.435 T and is uniform to within ± 0.5 %. The field between the solenoid and the iron yoke does not exceed a few tens of Gauss to allow the correct operation for the photomulitplier tubes of the time-of-flight system and lead–glass electromagnetic calorimeters.

3.3 Tracking Subdetectors (CT)

Tracking of charged particles in the OPAL detector is performed by the silicon microvertex detector (SI), the central vertex detector (CV), the central jet chamber (CJ) and the central Z chambers (CZ), given in order of increasing radial distance, r, from the interaction point. SI lies between the 1.1 mm thick beryllium beam pipe ($r =$ 54 mm) and the carbon fibre pressure tube ($r = 80$ mm). The pressure tube supports the 4 bar absolute pressure of gas in the central tracking region. The tracking detectors and gas pressure are enclosed by a pressure vessel closed off at each end by a pressure bell. The pressure vessel also provides inner mechanical support for the solenoid of the magnet surrounding it.

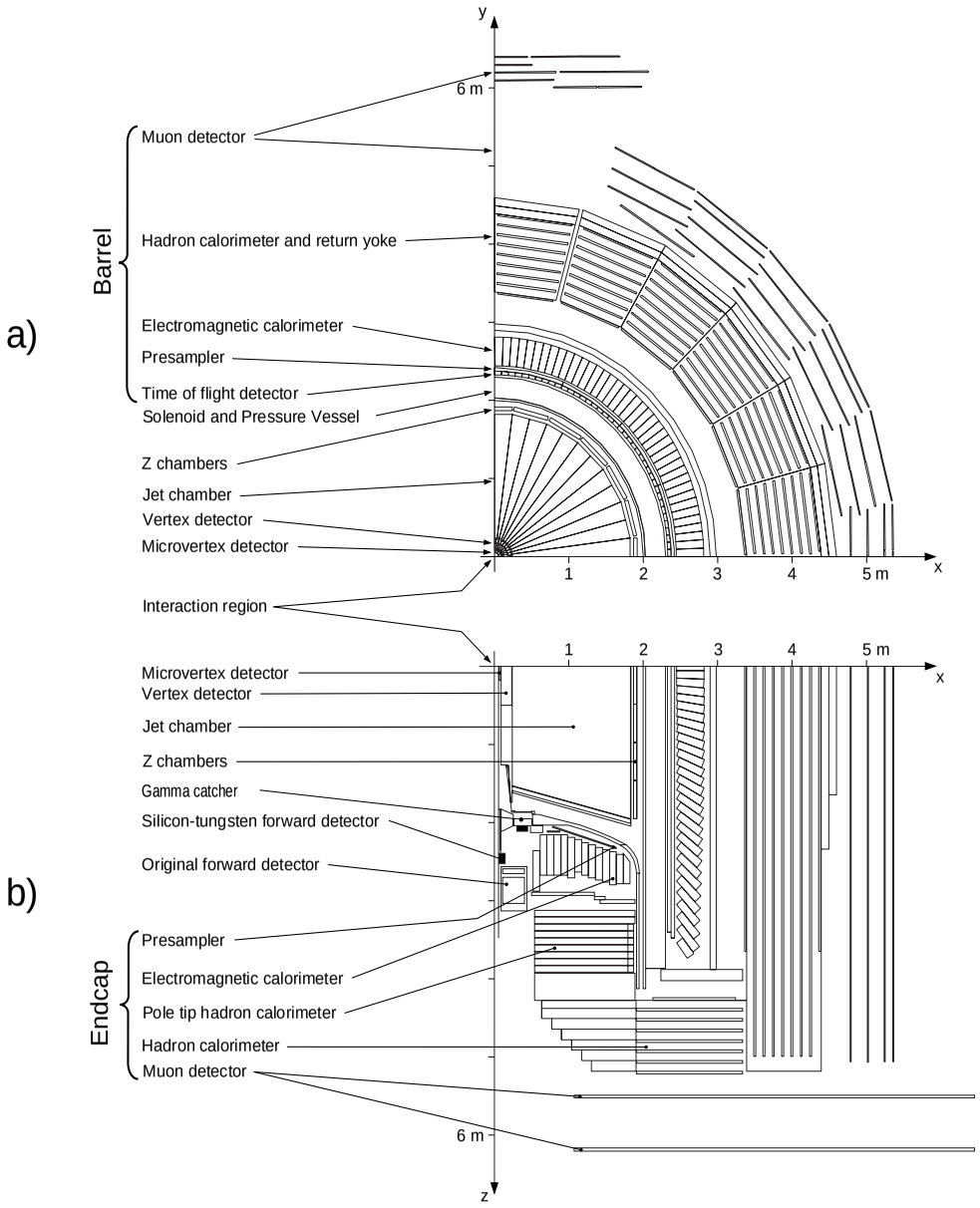

Figure 3.4: Positions of the subdetectors of OPAL in the a) $x-y$ and b) $x-z$ planes.

Between the 1995 and 1996 data taking, a low angle radiation shield was installed to protect the central tracking subdetectors from possible synchrotron radiation at higher beam energies. It consists of two parts on either side of OPAL, each forming a ring around the beam pipe and each located in front of the lower edge of the silicon–tungsten (SW) calorimeters (see section 3.8.1).

3.3.1 Silicon Microvertex Detector (SI)

SI is designed to locate accurately the primary vertices of interactions between beam particles, and to measure the positions of secondary vertices resulting from the decays of particles produced in the primary interaction (such as τ–leptons and heavy–flavour hadrons). It was added to the OPAL detector in 1991 to complement and improve vertex position measurements made using the CV subdetector.

SI consists of two concentric cylindrical layers of ladders of silicon wafers. Each ladder consists of three single–sided silicon wafers orientated for ϕ measurement back–to–back with three single–sided wafers orientated for z measurement. The inner cylindrical layer is made up of 11 ladders at a radius of 61 mm and the outer cylindrical layer consists of 14 ladders at a radius of 75 mm. The wafers for ϕ measurement have AC coupled strips at 50 μm pitch whilst the readout strips for z measurement are positioned every 100 μm.

The resolution in $r\phi$ is 5 μm and the resolution in z ranges from 13 μm for particles at normal incidence to 20 μm at 45^o incidence.

3.3.2 Central Vertex Detector (CV)

This detector is used to measure the vertex position of particle decays and to improve the momentum resolution for charged particles. It is a 1 m long cylindrical drift chamber with inner radius 0.235 m, surrounding the carbon fibre pressure pipe and is located inside the jet chamber (CJ).

The CV chamber consists of 2 layers: an inner layer of 36 cells of axial wires between radii 103 mm and 162 mm, and an outer layer of 36 small angle (4^o) stereo

cells between radii of 188 mm and 213 mm. The axial cells each contain 12 anode wires at 5.3 mm radial intervals and the stereo cells have 6 anode wires at 5.0 mm radial intervals, with each anode wire alternately staggered by ± 41 μm to resolve the left–right drift ambiguity.

The $r\phi$ resolution of the axial cells is $\sim$50 μm per wire and a coarse measurement of the z position along the wire is made by measuring the time difference between the signals at the two ends of the wire. This is used for quick track triggering and for offline track finding. A more accurate z position for charged tracks is obtained by combining the axial and stereo layer signals.

3.3.3 Central Jet Chamber (CJ)

CJ is designed to provide good spatial resolution of tracks and good resolution of track separation, and to allow the possibility of particle identification using $\mathrm{d}E/\mathrm{d}x$. By measuring the curvature of the track of a charged particle in the magnetic field, it is possible to calculate the momenta of the tracked particles.

The sensitive volume of the jet chamber is a cylinder 4 m long with an inner radius of 0.245 m and an outer radius of 1.85 m. It is divided into 24 identical segments in ϕ with a plane of wires at the segment boundary forming the cathode for the 159 anode sense wires in each segment. These wires are spaced at 10 mm intervals, lie parallel to the beam direction and form a plane in the radial direction (within a stagger of 100 μm either side of the plane to resolve the left-right drift ambiguities).

A maximum of 159 points on a track are measured for the range in polar angle $43^o < \theta < 137^o$, with at least 20 points measured for 98% of the 4π solid angle. The average spatial resolutions are 6 cm for z and for $r\phi$:

- beam energy = 45.6 GeV , $\sigma_{r\phi} \sim 129$ μm;
- beam energy = 80.5 GeV , $\sigma_{r\phi} \sim 117$ μm;
- beam energy = 86.0 GeV , $\sigma_{r\phi} \sim 142$ μm.

The momentum resolution in $r\phi$ is:

$$\frac{\sigma(p_t)}{p_t} = \sqrt{0.02^2 + (0.0015 p_t)^2} \tag{3.2}$$

3.3.4 Central Z Chambers (CZ)

The outermost of the central tracking detectors is CZ and is used to make precision measurements of the z position of charged particles. This leads to improvements in the resolution of polar angle, θ, and hence of the invariant mass of charged particles.

CZ is 4 m long and is divided into 24 drift chambers. Each drift chamber contains 8 drift cells of 6 sense wires laid perpendicular to the z direction and at a spacing of 4 mm (± 250 μm of stagger). A coarse measurement is also made in $r\phi$ using the time difference between the arrival of a signal at either ends of the sense wire.

CZ covers the polar angle region $44^o < \theta < 136^o$ and 94% of the azimuthal angle, ϕ. The resolution is 300 μm in z and 1.5 cm in $r\phi$.

3.4 Time-Of-Flight System

The time-of-flight system consists of a barrel of scintillation counters and two endcap scintillator detectors. It is designed to generate trigger signals and to aid in the rejection of cosmic rays. In the barrel region, it is designed to allow charged particle identification by measuring the time of flight particles from the interaction region.

3.4.1 Time-Of-Flight Barrel (TOF)

TOF consists of 160 scintillation counters, each 6.84 m long and individually wrapped in aluminised mylar foil and black PVC sheet. It forms a cylinder around the solenoid of the magnet at a mean radial distance of 2.36 m. Light is collected at both

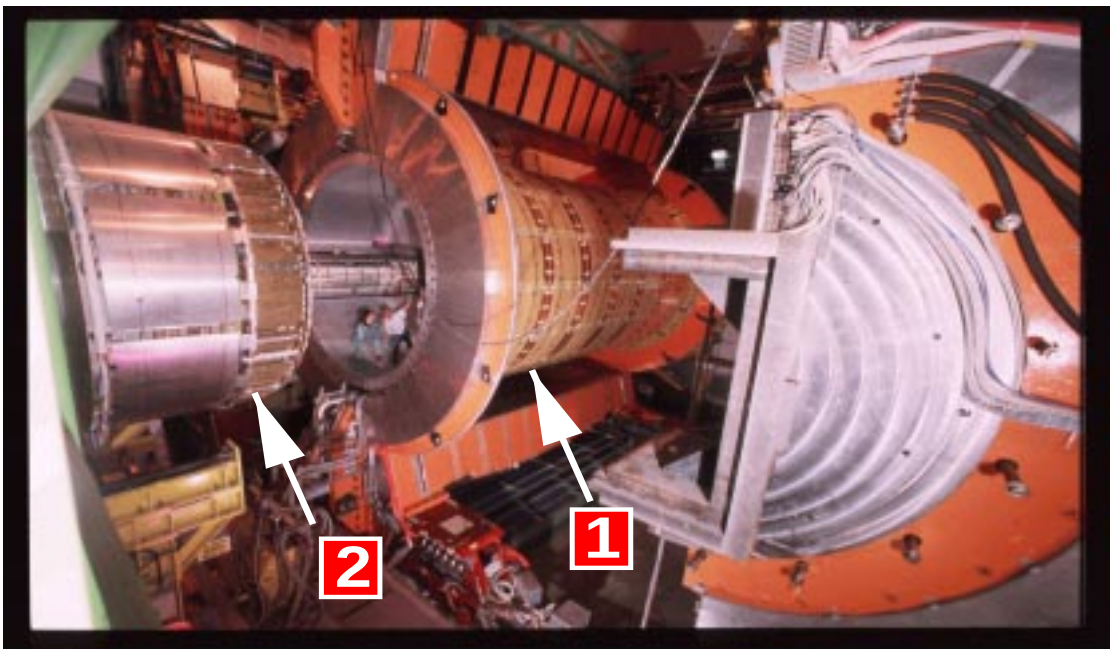

Figure 3.5: The OPAL central barrel region. Arrow 1 points to the electromagnetic presampler, inside of which lie the Time-of-flight counters, the solenoid of the OPAL magnet and the central tracking region. Arrow 2 points to one of the endcap electromagnetic calorimeters.

ends of the scintillator plexiglass light guides glued directly to phototubes. It has a timing precision of $\sim$ 300 ps, thus allowing the measurements of particle time-of-flight from the central region.

3.4.2 Tile Endcap (TE) and MIP Plug

Installed in 1996, TE is a layer of 10 mm thick scintillating plastic tiles designed to improve the triggering information in the forward regions of OPAL and thus to complement the use of the TOF system in the barrel region. Additionally, it allows an online determination of collision time for a given event and provide a correction for the signal in EE which is sensitive to timing. TE is located between the pressure bell and the endcap electromagnetic presampler (PE) at each end of OPAL.

TE consists of 3 radial sub-sectors of plastic scintillator tiles embedded with

wavelength shifting fibres and read out by phototubes. Each radial sub-sector is divided azimuthally into 24 segments. The outermost radial sub-sectors consist of 48 trapezoidal shaped tiles (2 per sub-sector) with edges of 225.3 mm and 168.5 mm and height 453.3 mm. The middle sub-sectors also have 48 trapezoidal tiles with edges 168.5 mm and 108.7 mm long and height 478.3 mm. Each of the innermost sub-sectors consists of only one trapezoidal tile of edges 232.3 mm and 171.2 mm long and height 232.4 mm. The timing precision for TE is $\sim$ 5 ns. This is good enough to be able to allow counting of the bunchtrains in the beam but is not precise enough for time of flight measurements.

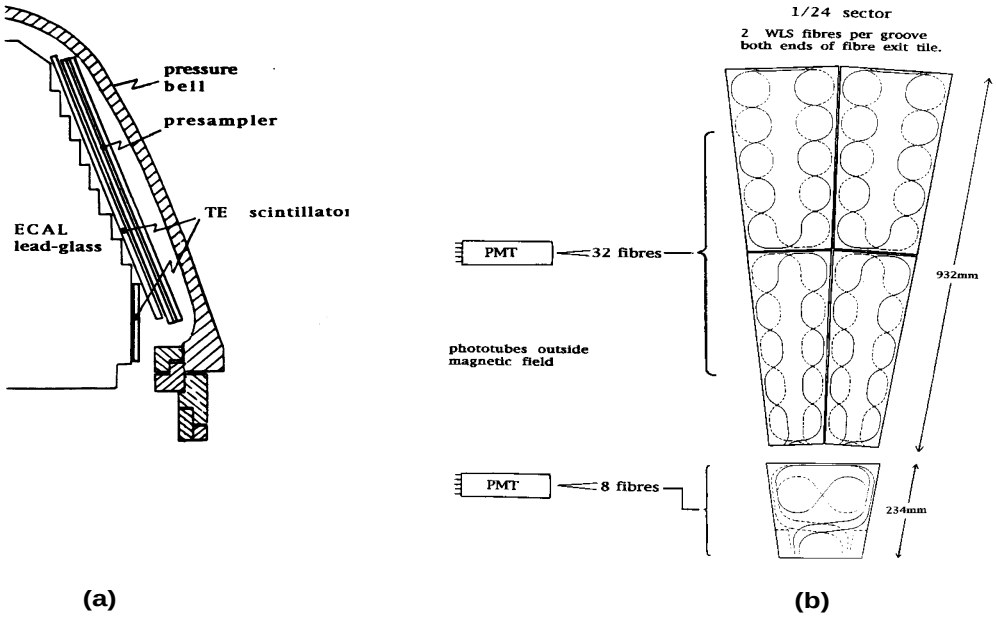

Figure 3.6: Diagram showing the position of the Time-of-Flight Endcap subdetector and the composition of $1/24^{th}$ of each of the radial sub-sectors.

An extension to TE, the **M**inimal **I**onising **P**article (MIP) plug, was added between the 1996 and 1997 running of LEP. It is designed to extend the region of acceptance for charged particles (and in particular muons) into the forward region.

The MIP plug uses the same scintillating technology as the rest of the TE and covers the polar angular region of 40–300 mrad from the beam pipe. It consists of two radial divisions, each divided into eight azimuthal sectors. Each azimuthal sector consists of two layers of scintillator in coincidence, separated by 5 mm of lead in the outer radial division and separated spatially by 246 mm in the inner division. The layers of the inner radial division are not separated by lead as they lie in front of the main calorimeter (FK) and tube chambers (FB) of the forward luminosity calorimeter (see section 3.8.2).

3.5 Electromagnetic Calorimeter (ECAL)

The energies and positions of electrons, positrons and photons are measured by the main electromagnetic calorimeter in OPAL. This calorimeter is designed to measure energies in the range of a few tens of MeV to 100 GeV. It is used to discriminate between the showers of neutral pions and photons, and between electrons and hadrons in conjunction with the central tracking regions.

ECAL covers 98% of the solid angle (including full azimuthal angle) and is divided into a barrel region and two endcap regions, each of which consists of a presampler in front of a lead–glass calorimeter. Since there are about two radiation lengths (2 X_o) of material between the interaction region and ECAL, most electromagnetic showers are initiated before reaching the lead–glass calorimeter. The use of presamplers to measure the position and to sample the energy of the shower improves neutral pion–photon and electron–hadron discriminations as well as increasing the energy resolution of the shower.

The lead–glass calorimetry gives an intrinsic energy resolution ($\frac{\sigma_E}{E} \sim \frac{5\%}{\sqrt{E}}$ with energy E measured in GeV) and a spatial resolution ($\sim$ 1 cm).

3.5.1 Barrel Electromagnetic Presampler (PB)

The barrel presampler covers the polar angle range $|\cos\theta| < 0.81$ and consists of 16 chambers forming a cylinder 6.623 m long and radius 2.388 m between the time-

of-flight system and the barrel lead–glass calorimeter. Each chamber contains two layers of limited streamer mode tubes with sense wires parallel to the beam axis. A measurement of z position is made by comparing the readouts of charge collected at both ends of the sense wires.

For a single charged particle, the $r\phi$ spatial resolution is $\sim$2 mm and the z resolution is $\sim$10 cm. Electromagnetic shower resolution is 6–4 mm for shower energy increasing from 6–50 GeV. The angular resolution for a photon is $\sim$2 mrad.

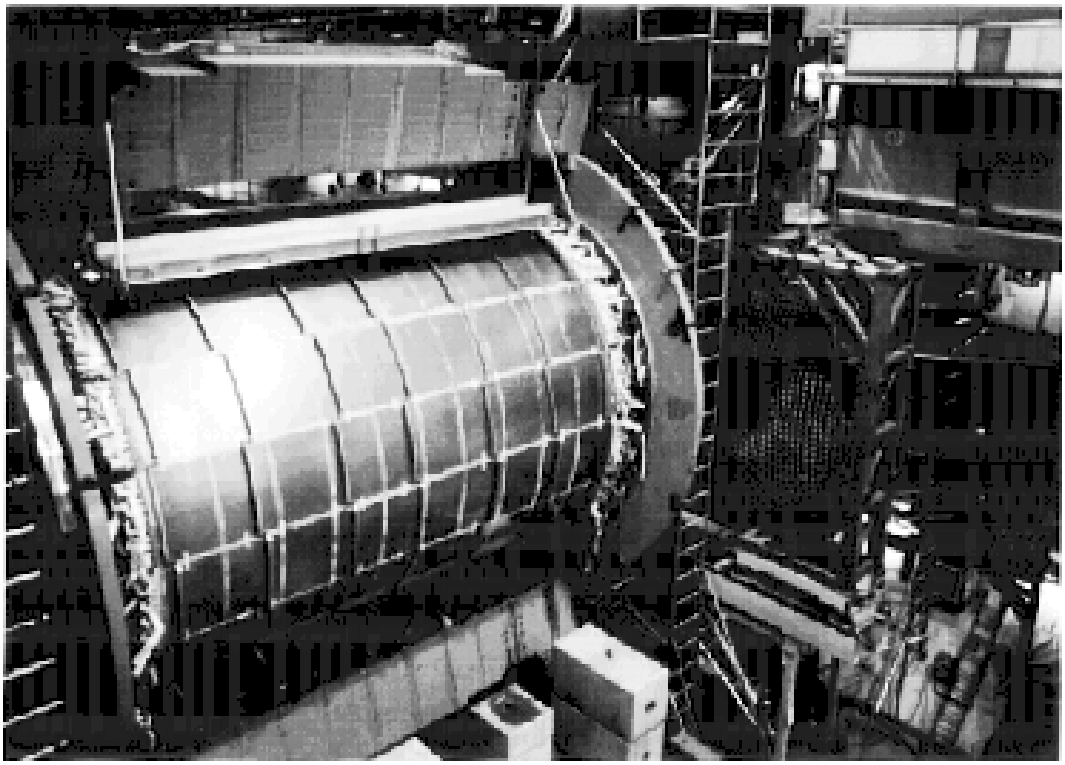

Figure 3.7: The barrel electromagnetic presampler.

3.5.2 Endcap Electromagnetic Presampler (PE)

The two endcap presamplers are located between the pressure bell for the central tracking and the endcap lead–glass calorimeters up to the end of 1995. During the winter break between 1995 and 1996, the time-of-flight endcap (TE) was sandwiched between PE and the pressure bell.

Each endcap presampler is divided into 16 azimuthally–arranged, overlapping wedges and covers the full azimuthal angle and the polar angle range $0.83 < |\cos\theta| <$

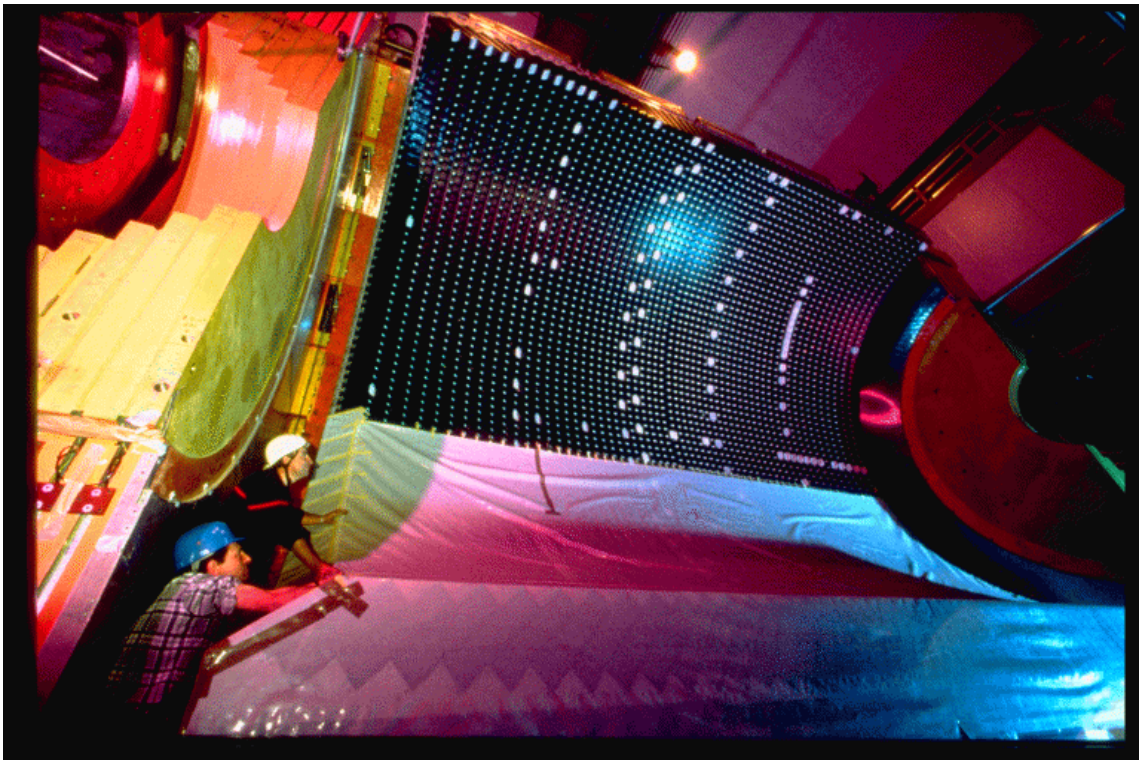

Figure 3.8: The barrel region of the electromagnetic lead–glass calorimeter.

0.95. Each wedge is made up of two trapezoidal multi-wire proportional counter chambers. The smaller of these two chambers is located in front of the other chamber and is orientated at 90^o to the beam axis, whilst the larger chamber is orientated at 18^o to the smaller chamber.

The $r\phi$ spatial resolution for a single charged particle is 2–4 mm and the angular resolution is $\sim$4.6 mrad.

3.5.3 Barrel Lead–Glass Calorimeter (EB)

EB is a cylindrical array of 9440 lead–glass scintillator blocks, each of 24.6 X_o, at 2.455 m radius from the interaction region. The scintillator blocks have dimensions of $\sim 10\times \sim 10\times 37.0\text{cm}^3$ and are made of material of density 5.54 g cm^{-3} and radiation length $X_o = 1.50$ cm. They are instrumented with magnetic field tolerant phototubes. To prevent neutral particles from being lost in the gaps between the blocks whilst simultaneously trying to prevent particles from traversing more than one block, the longitudinal axes of the blocks are pointed towards the interaction point but with a

slight tilt away from the perfect pointing geometry.

The azimuthal angle is fully covered and the polar angle is covered for the region $|\cos\theta| < 0.82$. The spatial resolution for a particle of 6 GeV is ~11 mm and the energy resolution is $\frac{\sigma_E}{E} \simeq 0.2\% + \frac{6.3\%}{\sqrt{E}}$.

3.5.4 Endcap Lead–Glass Calorimeters (EE)

Each of the two endcap electromagnetic calorimeters is a doughnut-shaped array of 1132 lead–glass scintillator blocks located at either end of OPAL between the pressure bell of the central tracking and the hadronic pole tip calorimeter (HP). The blocks are at least 20.5 X_o long and are mounted parallel to the beam axis. The material of these blocks is slightly different from that of the blocks in the barrel calorimeter: the EE blocks have a smaller density 4.06 g cm^{-3} and a longer interaction length (2.51 cm). The scintillation light is read out using single stage multipliers called vacuum phototriodes (VPT's).

At low energy, the energy resolution is $\frac{\sigma_E}{E} \sim \frac{5\%}{\sqrt{E}}$ at low energies with a spatial resolution of 8–14 mm for a 6 GeV electron incident at 15^o to the longitudinal block axes.

3.6 Hadronic Calorimeter (HCAL)

HCAL is a sampling calorimeter used to measure the energies of hadrons and assists in the identification of muons. It covers 97% of the solid angle and is divided into a barrel calorimeter, two endcap calorimeters and two pole tip calorimeters. Layers of the iron return yoke of the OPAL magnet are used as passive absorbing material and are sandwiched by planes of detectors. The main difference between the barrel, endcap and pole tip calorimeters is in the number of layers of detectors and iron. Due to the amount of material between the hadronic calorimetry (especially in the lead–glass calorimeters) and the interaction point, hadronic showers are likely to be initiated before reaching the HCAL and so hadronic energy measurement has to be made by adding energy from the ECAL to the from measurements in the HCAL.

The energy resolution is $\frac{\sigma_E}{E} \sim \frac{120\%}{\sqrt{E}}$ for all the calorimeters although there is more variation of this with energy E (in GeV) for the pole tip calorimeters.

3.6.1 Hadronic Barrel Calorimeter (HB)

The barrel calorimeter is cylindrical in shape with inner radius 3.39 m and outer radius 4.39 m. It consists of eight 100 mm thick layers of iron separated by gaps of 25 mm and between nine layers of detector. The detectors are limited streamer mode tubes with wires parallel to the beam axis.

3.6.2 Hadronic Endcap Calorimeters (HE)

HE consists of two doughnut-shaped calorimeters, located at either end of the OPAL detector (see Fig. 3.4). Seven layers of 100 mm thick iron are sandwiched by eight layers of the same type of detector used in HB with the tube sense wires arranged horizontally. The gap between the layers of iron is 35 mm.

3.6.3 Hadronic Pole Tip Calorimeters (HP)

The hadronic pole tip calorimeters lie behind the lead–glass endcap calorimeters. They consist of 10 layers of detectors separated by nine layers of 80 mm thick iron with a 10 mm gap between iron layers. The decrease in the distance between samplings is to improve the energy resolution with the decrease in the size of the gap between the iron layers made to avoid perturbing the magnetic field. Unlike HB and HE, the detectors used in the pole tip calorimeters are multi-wire chambers operating in high gain mode and similar to those used in the electromagnetic endcap presampler, PE, (see section 3.5.2).

3.7 Muon Chambers

The muon chambers are used to identify muons, particularly within a large hadronic background. This is particularly important as muons, like hadrons and unlike electrons, are likely to penetrate through the electromagnetic calorimetry. The chambers are divided up into a barrel region and two endcap regions which together provide 93% coverage of the full solid angle.

3.7.1 Muon Barrel (MB)

The muon barrel consists of 110 planar drift chambers with 44 chambers on each side, 12 chambers below and 10 chambers on top of OPAL. All of the chambers are 1.2 m wide and 90 mm thick but vary in length from 10 m long at the sides, 6 m long below and 8.4 m long on top.

3.7.2 Muon Endcaps (ME)

Each muon endcap subdetector consists of eight quadrant chambers (6 m by 6 m) and 4 patch chambers (3 m by 2.5 m). Each of these two types of chamber contains two layers of streamer tubes, separated by 19 mm, of which one layer has wires in the aligned horizontally and the other layer has wires aligned vertically.

3.8 The Electromagnetic Luminosity Calorimeters

The forward detectors are electromagnetic calorimeters used to measure the e^+e^- luminosity at the OPAL detector. This is done by counting the number of interactions where a beam positron and a beam electron scatter elastically. These events (called Bhabha events) are characterised by two back-to-back electromagnetic clusters with no other activity recorded in the detector. They are also used to measure the positions and energies of photons, candidate electron tags and to sample the hadronic energy in the region outside the acceptance of the ECAL and HCAL. The main subdetectors in place here are the silicon–tungsten calorimeter (SW), the far forward monitor (FF), the forward calorimeter (FK) the forward tube chambers (FB) and the gamma catcher (FE).

3.8.1 Silicon–Tungsten Calorimeter (SW)

Two identical silicon–tungsten electromagnetic calorimeters were installed in OPAL in 1993 at ± 2.389 m in z from the interaction point, covering the full azimuthal angle and the polar angle region of 25–59 mrad. The lower boundary for the clear acceptance of the calorimeters increased to 32 mrad at the start of 1996 following

the installation of a low angle shield to protect the central tracking detectors against possible synchrotron radiation.

Each calorimeter is divided azimuthally into 16 wedges and is made up 22 X_o of material in the form of 19 layers of sampling silicon wafers alternating with 18 layers of tungsten. Adjacent wedges are offset by 800 μm in z and overlap to prevent any gap in the acceptance of the active silicon. Each consecutive layer of silicon is offset by a half–wedge in ϕ ($\sim 11.5^o$). Each wedge is divided into 64 pads (32 in r and two in ϕ) giving a total of 38912 channels to be read out individually.

The spatial resolution in r is $\sim 10\mu$m and the energy resolution is $\frac{\sigma_E}{E} \sim \frac{28\%}{\sqrt{E}}$.

3.8.2 Forward Detector (FD)

There are two forward detectors, one on on each side of OPAL in z, and each comprising of four main components: the main calorimeter (FK), the forward tube chambers (FB), the γ–catcher (FE) and the far forward luminosity monitor (FF).

Main Calorimeter (FK)

The active region of the calorimeter covers the full azimuthal angle and the polar angle range 60–120 mrad. It is divided into 16 azimuthal segments of lead–scintillator sandwich, with each segment made up of a 4 X_o presampler and a 20 X_o main calorimeter. The scintillator is read out using wavelength shifter to vacuum phototetrodes. The presampler is read out on the outer edge only whilst the main calorimeter is read out on both inner and outer edges to give a measurement of θ. An electromagnetic cluster is made up from two adjacent segments with the ratio of the signals from these segments used to make a measurement of ϕ.

The FK has an energy resolution of $\frac{\sigma_E}{E} \sim \frac{18\%}{\sqrt{E}}$. The azimuthal angle resolution is $\pm 2^o$ whilst the polar angle resolution worsens from $\pm 4^o$ at the inner edge of the detector to $\pm 10^o$ at the outer edge. The minimum threshold energy for a cluster to be recorded is 2 GeV which is good for electrons and photons but is poor for hadrons as hadronic showers are not well contained within the calorimeter.

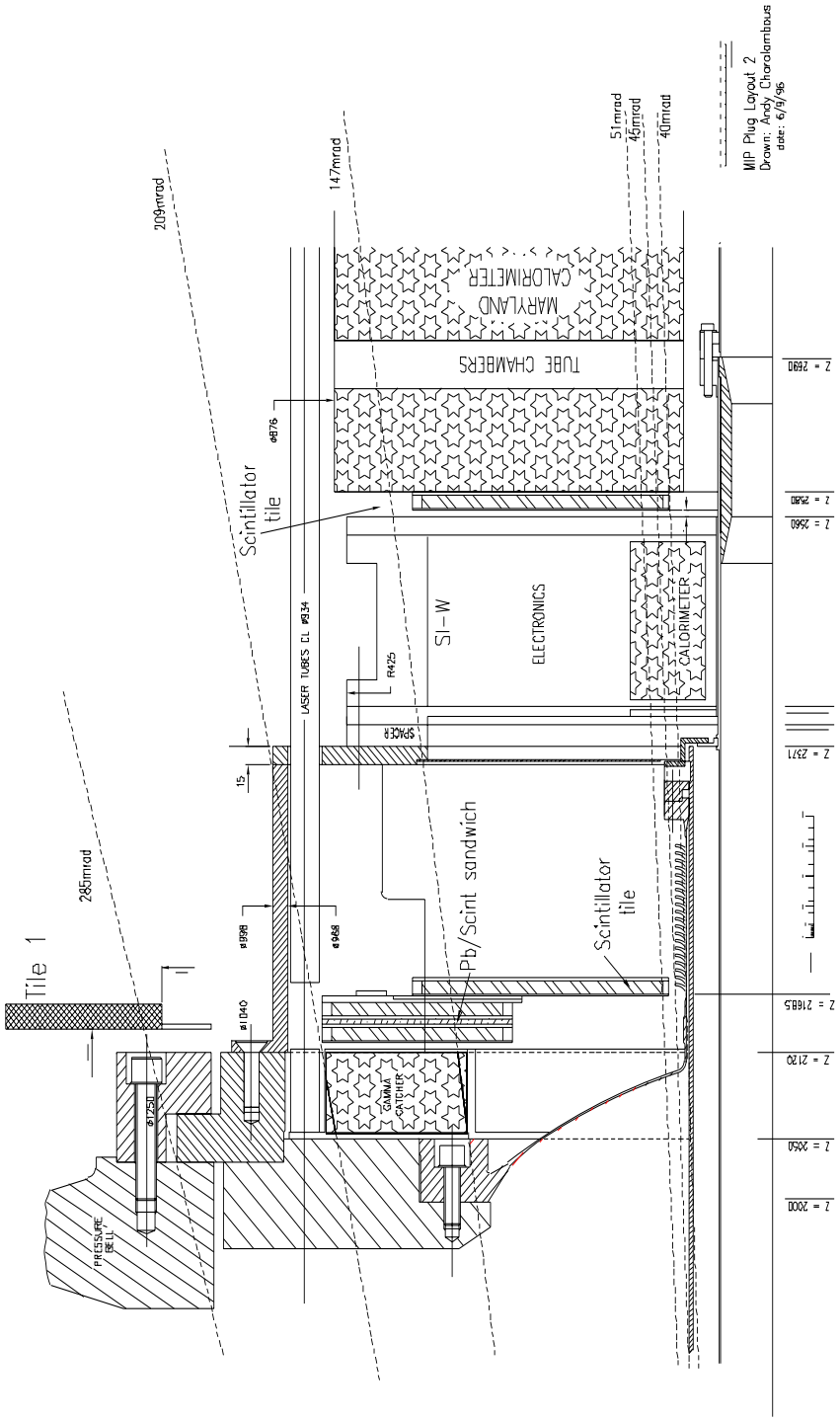

Figure 3.9: Cross–section of the luminosity calorimeters in the forward region taken in the $y - z$ plane. Note that the full extent of the forward calorimeter (FK) away from the interaction point is not shown here.

Tube Chambers (FB)

FB comprises of three planes of brass-walled proportional tube chambers sandwiched between the presampler and the main calorimeter of FK. It is used to give more precise position measurements when combined with the information from FK. The resolution in polar angle, θ, is ± 2 mrad and the position is given to an accuracy of ± 3 mm.

Gamma Catcher (FE)

Two small annular lead–scintillator (7 X_o) calorimeters are used to fill the gap in acceptance between the electromagnetic endcap and forward calorimeters. The active part of the calorimeter covers the polar region of 143–193 mrad and is divided into eight independent azimuthal segments to give a coarse ϕ determination. Since there are only 3 X_o of material in front of the gamma catcher, it is non–containing and so any measurement of a high energy cluster is shared either with EE or FK depending upon the θ.

The electromagnetic energy resolution of the gamma catcher is $\sim 20\%$.

Far Forward Monitor (FF)

Two small 50 mm by 150 mm by 20 X_o lead–scintillator calorimeters are positioned at ± 7.85 m from the interaction point in OPAL, beyond the low–β quadrupole magnets. They make up the far forward luminosity monitor and are used to measure positions and energies of showers from electrons and positrons in the 5–10 mrad region close to the horizontal plane and to measure the OPAL trigger rates during data taking. They are not used in this analysis.

3.9 OPAL Trigger System and Data Stream

At LEP, several bunches of electrons and of positrons circulate around the accelerator ring and data is taken when particles in two bunches are brought into collision. The OPAL detector is synchronised to become active as the bunches cross at its central point and a trigger system is used to decide if the detector should be read

out during this active time. If the detector is read out, then the raw electronic signals are processed to reconstruct the tracks and clusters observed in the detector.

3.9.1 The OPAL Trigger System

The OPAL trigger system is designed to select with high efficiency various physics processes taking place at each bunch crossing whilst maximising the rejection of background from cosmic rays, interactions of beam particles with gas in the beam pipe and with the walls, and noise.

Two types of trigger signal are used to decide whether to read out the whole detector: "$\theta - \phi$" and "stand–alone" signals. The $\theta - \phi$ signals are made by dividing the 4π solid angle into 144 overlapping bins, 6 in θ and 24 in ϕ. Trigger signals sent by combinations of subdetectors are matched to this spatial binning. Stand–alone signals are sent when higher thresholds of total energy sums, or of track counting, are surpassed in a subdetector than are needed for $\theta - \phi$ signals to be sent.

The trigger system is split into two main levels: the pretrigger and the trigger. Both the pretrigger and the trigger combine stand–alone and $\theta - \phi$ signals from the subdetector to determine if an event satisfies preliminary criteria to be selected and hence whether the OPAL subdetectors should be read out or cleared and reset. The time taken for a negative decision is 5.3 μs for the pretrigger and 14.5 μs for the trigger, and the reset of the subdetectors takes 4.5 μs. The pretrigger was important from 1992 to 1994 when LEP was operated in 8+8 bunch mode. The use of 4+4 bunchtrains after 1994 meant that the pretrigger was no longer necessary but was kept in place to minimise the number of changes needed during any switch back to 8+8 bunch running by LEP.

3.9.2 Tagging Triggers

Table 3.1 shows a list of trigger conditions used to select candidates of tagged two–photon events. The conditions necessary for OPAL to be read out can be either stand–alone signals from tag **or** hadronic activity, or can be logical combinations of signals of tag **and** hadronic activity.

Trigger Name	Subdetector	Trigger Condition
Tag candidates:		
SWHIOR	SW	$>$ 34 GeV energy in either end SW
SWSEGL	SW	$>$ 9 GeV energy in left SW segment
SWSEGR	SW	$>$ 9 GeV energy in right SW segment
LCALLO	FD	$>$ 15 GeV energy in left FK
RCALLO	FD	$>$ 15 GeV energy in right FK
FDHIOR	FD	$>$ 35 GeV energy in either end FK
FDGCLT	FD	$>$ 20 GeV energy in left FE
FDGCRT	FD	$>$ 20 GeV energy in right FE
Hadronic activity:		
TBM1	CT	$\geqslant$ 1 Barrel tracks
TM2	CT	$\geqslant$ 2 tracks
EBWEDGE	EB	$\geqslant$ 2 GeV energy in a 'wedge' of EB
EBTOTLO	EB	$\geqslant$ 1.8 GeV total energy in EB
EELLO	EE	$\geqslant$ 1.6 GeV energy in left EE
EERLO	EE	$\geqslant$ 1.6 GeV energy in right EE
TPEML	TP	$\geqslant$ 1 ECAL ϕ bin triggered in the $1^{st}\theta$ bin
TPEMR	TP	$\geqslant$ 1 ECAL ϕ bin triggered in the $6^{th}\theta$ bin

Table 3.1: Summary of the triggers used to identify candidate tagged two-photon events. The abbreviation **TP** is a classification of triggers in terms of its $\theta - \phi$ location.

3.9.3 Data Stream

Trigger signals from each of the subdetector local trigger units (LTU's) are received and logically combined in the central trigger logic. Each LTU is part of a VME local system crate (LSC) containing typically two CPU's and which is used to assemble and control the trigger and readout signals for a subdetector. The central trigger logic is housed in a dedicated Eurocrate with a standard VME/VSB bus plus an additional special "trigger bus". A trigger decision is made whether to read out OPAL or to reset the subdetectors from the signal combinations and this decision is passed back to the LTU's by the global trigger unit (GTU). A readout decision inhibits further triggering whilst measurement signals from the subdetectors are read out. The readout signals for each subdetector are combined and formatted in the LSC responsible for that subdetector. A single VME crate called the event builder is used to collect the sub-events from each subdetector and to reconstruct the full event measured in the

OPAL detector. The event builder then passes the event onto the filter VME crate which compresses the event and labels it as interesting or not, or discards the event if it is obviously junk. An accepted event is written to disk and displayed on the online event display. The last stage of online processing is performed by nine HP workstations running the full OPAL reconstruction code ROPE [86] to apply the calibrations of the signals from the various subdetectors, including those from the calorimeters. Any further processing or selection of events is then performed offline.

Chapter 4

Event Selection

This chapter covers the process of selecting singly–tagged two–photon events from the whole data sample, elaborating on the types of events that are the most difficult to separate from tagged two–photon events and finally checking for any differences between the data samples taken in different years.

4.1 Event Selection

There are three stages in the event selection:

1. a coarse preselection to discard events that are obviously not wanted;

2. a further selection to reduce the size of the data sample being analysed whilst simultaneously maintaining a high efficiency for passing singly–tagged two–photon events onto the last selection stage;

3. a final selection to make as pure as possible selection of singly–tagged events from background events.

Results are given in this document for the data sample passing the final selection stage.

4.1.1 Preselection

In ROPE, the preselection subroutine RTWOPH is used to flag events as possible tagged two–photon events. The preselection is made if a minimum number of good charged tracks and a candidate tag are present in the event. The minimum criteria for a track to be considered good are:

- number of hits in CJ and CV $\geqslant 30$;
- the nearest point of approach to the interaction point in $r\phi \leqslant 2$ cm;
- the nearest point of approach to the interaction point in $z \leqslant 50$ cm;
- the radius of the first CJ hit $\leqslant 75$ cm;
- the minimum transverse momentum $p_t \geqslant 0.1$ GeV .

Table 4.1 shows the conditions for an event to be flagged as a tagged two–photon event for tag candidates found in the SW, FD or EE calorimeters.

Tagging Subdetector	Condition For Candidate Tag	Condition For Tracks
SW	$\geqslant 1$ cluster with energy $\geqslant 10$ GeV	No. of tracks $\geqslant 2$
FD	$\geqslant 1$ cluster with energy $\geqslant 10$ GeV	No. of tracks $\geqslant 2$
EE	$\geqslant 1$ cluster with energy $\geqslant 10$ GeV contained in $\geqslant 2$ lead–glass blocks and with no one block with >99% of the cluster energy	No. of tracks $\geqslant 1$

Table 4.1: Preselection criteria for an event to be flagged as a possible tagged two-photon event.

4.2 Further Selection

4.2.1 Subdetector Status

Each subdetector in OPAL is given a status codes of 0 to 3 dependent upon its operational status. In table 4.2, the codes and their meanings are given. For events to be pass the second stage of selection, CJ, EB, EE, FD and the track trigger (TT) were required to be at 100% performance. Additionally, events with the candidate tagged electron or positron detected in the SW calorimeter were required to be measured with this calorimeter also at 100% performance.

Subdetector Status	Description
0	Subdetector is dead or off
1	Subdetector is unreliable
2	Subdetector has minor problems
3	Subdetector is at 100%

Table 4.2: Description of the subdetector status codes.

4.2.2 Track Quality Cuts

Tracks found in the central tracking subdetectors are accepted for use in the track–cluster matching and in the final event analysis if they pass selection criteria called "track quality cuts". These cuts are listed below and are made to ensure both that the energy and momentum of the track are accurately measured (cuts 1–5), and that the tracks come from the recorded event rather than from a background or a subdetector artifact (cuts 6-8).

1. the number of hits in central jet chamber, CJ $\geqslant 20$;
2. fraction of total CT hits expected to come from CJ hits $\geqslant 0.1$
3. transverse momentum of track, $p_{\mathrm{t,track}} \geqslant 0.12$ GeV

4. magnitude of momentum, $|p_{\rm track}| \leqslant E_{\rm b} + 6.0\sqrt{(0.02)^2 + (0.0015\ E_{\rm b})^2}$ GeV
5. the polar angle, $\theta_{\rm track}$ is such that, $|\cos\theta_{\rm track}| \leqslant 0.964$;
6. the apparent perpendicular distance from the interaction point in the $x-y$ plane, $|{\rm d_o}| \leqslant 2.0$ cm;
7. the apparent z–coordinate from which the track originated $|{\rm z_o}| \leqslant 30.0$ cm;
8. radial distance of first measured hit, $R1 \leqslant 60.0$ cm

Possible sources of rejected background tracks include beam–wall interactions, beam–gas interactions or back–scatter in the solenoid from particles that have already left the jet chamber or mis–measured track segments.

4.2.3 Electromagnetic and Hadronic Calorimetry Quality Cuts

It is desirable to exclude from the data analysis electromagnetic and hadronic clusters caused by bad calibration of the calorimetry or by noisy electronics. Hence, each cluster from a calorimeter has to satisfy quality cuts to be passed on for subsequent analysis. The first of these quality cuts is a comparison of each calorimeter cluster to a list of known noisy ("hot") clusters. A cluster is not accepted for further use in the analysis if it is known to be hot and has an energy close to that expected from noise. Table 4.3 shows the further quality cuts that must be satisfied for a calorimeter cluster to be used in the analysis.

4.2.4 Track–Cluster Matching

All tracks and calorimeter clusters which pass the quality cuts detailed in sections 4.2.2 and 4.2.3 are input to MT track–cluster matching algorithm [87]. This is used to avoid double counting of particle momentum by the central tracking detectors and the calorimeters. The electromagnetic clusters from the luminosity calorimeters (see section 3.8) are not matched to tracks as these clusters lie outside the region in polar angle for tracks to be passed by the quality cuts. Hence they are remain unchanged by the MT algorithm.

Electromagnetic Calorimetry	
Subdetector	Calorimetry Quality Cut
Electromagnetic Barrel Calorimeter (EB)	Number of adjacent lead–glass blocks in cluster $\geqslant 1$ AND Raw energy of the cluster $\geqslant 0.1$ GeV
Electromagnetic Endcap Calorimeter (EE)	Number of adjacent lead–glass blocks in cluster $\geqslant 2$ AND Raw energy of the cluster $\geqslant 0.25$ GeV
Maryland Forward Calorimeter (FK)	Energy of cluster $\geqslant 1.0$ GeV
Silicon–Tungsten Calorimeter (SW)	Energy of cluster $\geqslant 0.0$ GeV
Hadronic Calorimetry	
Hadronic Barrel Calorimeter (HB)	Number of calorimeter towers $\geqslant 1$ AND Raw energy of the cluster $\geqslant 0.6$ GeV
Hadronic Endcap Calorimeter (HE)	Number of calorimeter towers $\geqslant 1$ AND Raw energy of the cluster $\geqslant 0.6$ GeV
Hadronic Poletip Calorimeter (HP)	Number of calorimeter towers $\geqslant 1$ AND Raw energy of the cluster $\geqslant 2.0$ GeV

Table 4.3: The quality cuts for electromagnetic calorimeter clusters.

The algorithm contains two stages: the first to match tracks and calorimeter clusters, and the second to determine the four momentum of the matched track–cluster system. Fig. 4.1 shows a schematic representation of how the simplest input (one track and one calorimeter cluster) is tested in the algorithm. In the matching stage, the track is extrapolated to obtain polar and azimuthal angles at the inner edge of the calorimeter. The track and the cluster are matched if the track lies within the angular extent of the cluster in **both** polar **and** azimuthal angles to within errors of measurement and extrapolation. If the track and cluster are not matched (Fig. 4.1a), the four momenta measured for the track and the cluster are passed on for analysis unchanged. If the track and cluster are matched in the algorithm, then the expected energy response, f(p), of the calorimeter, along with an energy tolerance $\Delta E(p)$ is calculated for a track of four momentum, p. There are then two possible outcomes dependent upon the measured four momenta of the track and of the cluster, $q = (\mathrm{E_{cl}}, \mathrm{p_{cl}})$:

1. for $\mathrm{E_{cl}} \leq f(p) + \Delta E(p)$, the track–cluster system is given the four momentum of the track, p, (Fig. 4.1b);
2. for $\mathrm{E_{cl}} > f(p) + \Delta E(p)$, the matched track–cluster system is given the four–momentum of the track, p, and an additional cluster remains with four momentum $\frac{[\mathrm{E_{cl}} - \mathrm{f}(p)]}{\mathrm{E_{cl}}} q$ (Fig. 4.1c).

This algorithm is applied for all tracks, electromagnetic and hadronic calorimeter clusters within an event. The output is then used in the final selection (section 4.3).

4.3 Final Selection

The final selection is made by selecting events from the measurement of various events quantities. The event quantities used can be grouped into four categories of selection:

1. the identification and measurement of the tagged electron or positron;
2. an antitag veto to exclude doubly–tagged two–photon events;
3. a minimum number of charged tracks to cut on backgrounds from $\gamma\gamma \rightarrow \mathrm{e^+e^-}$ or $\mu^+\mu^-$;
4. cuts based on quantities calculated from the hadronic final state.

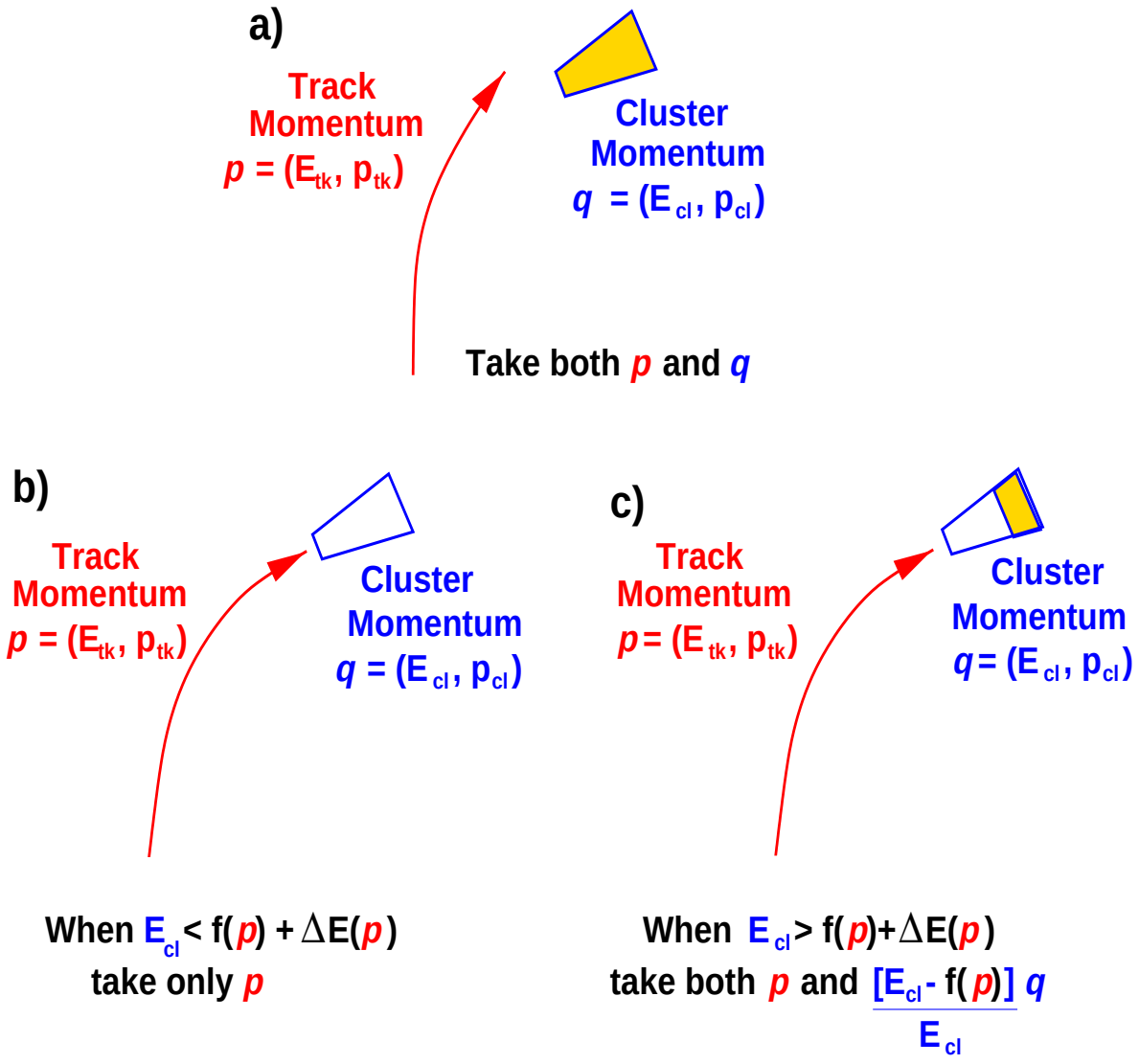

Figure 4.1: Schematic representation of how tracks and clusters are tested for possible matching to the same cause particle using the MT algorithm. In a), the track and cluster are not matched and so are left unchanged by the algorithm. In b), the track and cluster are matched and the energy of the cluster, E_{cl}, is less than or equal to the calculated energy response, $f(p)$, of the calorimeter for a track with four momentum *itp* plus a tolerance energy $\Delta E(p)$. The cluster is removed whilst the track and its four momentum are kept. In c), E_{cl} is larger than expected from the track alone. The track is outputted unchanged along with a cluster of four momentum $\frac{[E_{cl} - f(p)]}{E_{cl}} q$.

Three subdetectors are used to in this analysis to identify tagged electrons: the SW, the FD and the EE calorimeters. The data samples were collected at beam energies of 44.6 – 46.6 GeV (labelled LEP1), 80.5 GeV (labelled LEP2) and 85.0 – 86.0 GeV (also labelled LEP2). The final selection cuts (see sections 4.3.2–4.3.4) used are different for each subdetector used to identify the tag and also between the LEP1 and LEP2 samples due to the changes in the background inherent to increasing the beam energy.

4.3.1 Event Quantities for Final Selection.

The output of tracks and calorimeter clusters from the MT matching algorithm is used to calculate measured quantities for each event. Some of these quantities are used to make a final selection of singly tagged two–photon events from a sample containing signal and background events.

A tagged electron is identified as the highest energy calorimeter cluster in an event. The polar angle of the tag, $\theta_{\rm tag}$, is calculated relative to the nearest beam direction in θ so that $\theta_{\rm tag} < \pi/2$.

An "antitag" condition is imposed to remove doubly–tagged events. A candidate for the other scattered beam particle (the second tag) involved in the event is made by identifying the highest energy cluster in the endcap, forward and silicon–tungsten electromagnetic calorimeters, with energy $E_{\rm a}$, in the hemisphere opposite to the tag, where the division of the hemispheres is defined by the OPAL x–y plane. Fig. 4.2 shows the polar angle, θ_a, of the generated second tag relative to the beam direction for HERWIG and F2GEN Monte Carlo samples. Less than 0.1% of events in either sample are expected to be detected at polar angles large enough to be detected in the central region.

The identifications of the tag and the candidate second tag are made before the track–cluster matching described in section 4.2.4. The Q^2 of the probe photon is calculated from the energy of the tag, $E_{\rm tag}$, and $\theta_{\rm tag}$ using:

$$Q^2 = 2E_{\rm b}E_{\rm tag}(1 - \cos\theta_{\rm tag}) \tag{4.1}$$

where $E_{\rm b}$ is the beam energy. For tags measured in the electromagnetic endcap (EE) calorimeters, the energy, $E_{\rm tag,cone}$, in a cone around the tag excluding the tag energy

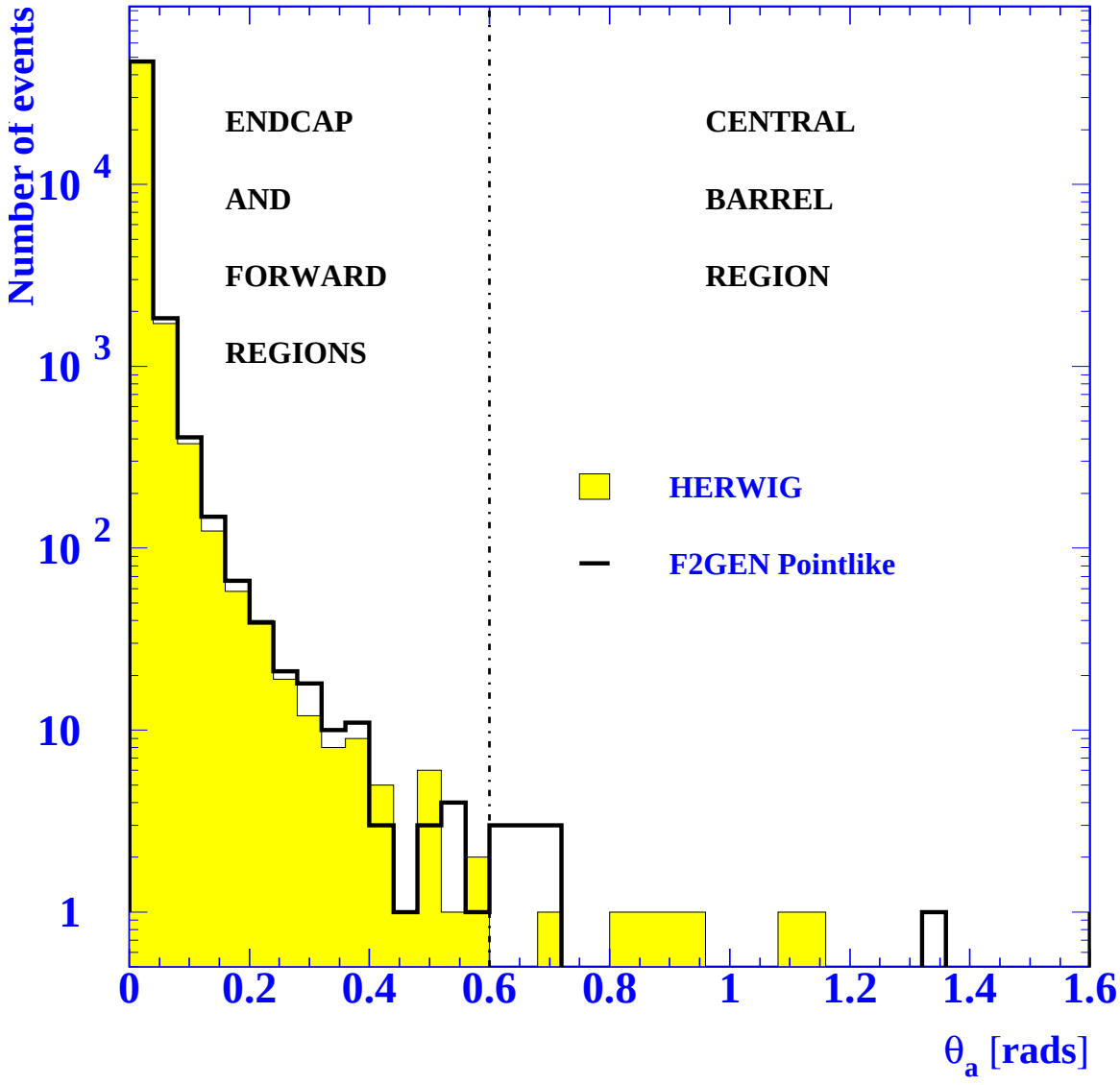

Figure 4.2: The generated polar angle, θ_a, of the antitag electron or positron for HERWIG and F2GEN Pointlike samples. The dot–dashed line marks the boundary in acceptance between the barrel and endcap calorimeters of OPAL.

and the energy, $E_{\mathrm{opp,cone}}$, in a cone around the direction exactly opposite to the tag direction are calculated. The cones are defined to have size $R_{\mathrm{cone}} = 0.5$ in pseudorapidity, $\eta = -\ln\tan\theta/2$, and azimuthal angle, ϕ.

In principle, the invariant mass, $W_{\gamma\gamma^*}$, of the two–photon system in an event could be measured either by using four momenta of the scattered electron and positron beam particles, or by recording the four momenta of all the final state hadrons. However this measurement is not possible since, by definition, only one electron is detected in singly–tagged two–photon events and additionally OPAL is not hermetic in its acceptance of hadrons. Instead, an estimate for $W_{\gamma\gamma^*}$ is obtained by calculating the visible invariant mass, W_{vis}, of all the tracks and clusters (excluding the tagged electron or positron) using:

$$W_{\mathrm{vis}} = \sqrt{\left(\sum_i E_i\right)^2 - \left(\sum_i \vec{p}_i\right)^2} \tag{4.2}$$

and where the sum is performed over all tracks and clusters (excluding double counting). The measurement of W_{vis} is an important quantity as it is used in the final selection cuts. A selection of $W_{\mathrm{vis}} \geq 2.5$ GeV is used to obtain final samples outside the poorly understood resonance region. From W_{vis} and Q^2, it is possible to calculate x_{vis} as a corresponding estimate of the true x of the event using:

$$x_{\mathrm{vis}} = \frac{Q^2}{(Q^2 + W_{\mathrm{vis}}^2)} \tag{4.3}$$

The vectorial sum of the momenta of all tracks and clusters (excluding the tag) is used to define interesting quantities in terms of the net event transverse momentum and the net momentum collinear with the beam axis. Two components of the event transverse momentum are defined and calculated relative to the plane formed by the beam and the tag directions (called the tag–beam plane): the component, $p_{\mathrm{t,in}}$, in the tag–beam plane, and the component, $p_{\mathrm{t,out}}$, out of the tag–beam plane. From the momentum conservation considerations and since efficiency for detecting hadrons is very good except at small polar angles (and hence at small transverse momenta), $p_{\mathrm{t,in}}$ should balance the tag transverse momentum and $p_{\mathrm{t,out}}$ should be small for singly–tagged two–photon events. Hence, the balanced transverse momentum, $p_{\mathrm{t,bal}}$, of the event in the tag–beam plane is defined using the transverse momentum of the tag, $p_{\mathrm{t,tag}}$, as:

$$p_{\mathrm{t,bal}} = p_{\mathrm{t,in}} + p_{\mathrm{t,tag}} \tag{4.4}$$

The net event momentum, $p_{\mathrm{z,event}}$ is used to calculate the missing component, $p_{z,miss}$, of event momentum parallel to the beam axis:

$$p_{z,miss} = p_{\mathrm{z,event}} + p_{\mathrm{z,tag}} + p_{\mathrm{z,a}} \tag{4.5}$$

where $p_{\mathrm{z,tag}}$ is the component of the tag momentum along the beam direction and $p_{\mathrm{z,a}}$ is the component of the untagged electron or positron along the beam direction where it is assumed that it carries the full beam energy and is parallel to the beam axis in the direction opposite to the tag hemisphere.

4.3.2 Final Selection for Tags Found in SW

The final selection cuts for tags found in the SW calorimeters are shown in table 4.4. The cuts are optimised to pass the maximum number of signal two–photon events into the final data sample whilst minimising the number of background events in that sample.

In 1995, LEP was operated in 4+4 bunchtrain mode (see section 3.1.3) with each bunchtrain containing 4 bunchlets. The trigger conditions for OPAL were set up so that the SW calorimeters were read out during the beam–beam crossing of the third bunchlets of each bunchtrain at the centre of the OPAL detector. Due to the difficulty in reconstructing the luminosity for the third bunchlet crossings only, the tags from SW in 1995 have been left out of the LEP1 part of this analysis.

The θ_{tag} cuts are made to make sure the tags are measured within the good acceptance of the SW calorimeters. As described in 3.8.1, at the beginning of 1996, the lower limit in θ of the clear acceptance of the calorimeter increased to 32 mrad.

The other changes in the cuts between LEP1 and LEP2 data samples are due to the changes in backgrounds with the increase in beam energy.

4.3.3 Final Selection for Tags Found in FD

The final selection cuts for tags found in the clean acceptance of the forward luminosity calorimeters (FD) are shown in table 4.5. The data sample for LEP1 is com-

Type of Selection	Selection Criteria	
Tag Selection	$0.775\ E_{\rm b} \leqslant E_{\rm tag} \leqslant 1.2\ E_{\rm b}$	LEP1
	$E_{\rm tag} \geqslant 0.775\ E_{\rm b}$	LEP2
	$31 \leqslant \theta_{\rm tag} \leqslant 55$ mrad	LEP1
	$33 \leqslant \theta_{\rm tag} \leqslant 55$ mrad	LEP2
Antitag Veto	$E_{\rm a} \leqslant 0.25\ E_{\rm b}$	LEP1
	$E_{\rm a} \leqslant 0.08\ E_{\rm b}$	LEP2
Charged Particle Multiplicity	$\mathrm{N}_{\rm tracks} > 2$	LEP1 & LEP2
Hadronic Final state	$2.5 \leqslant W_{\rm vis} \leqslant 40$ GeV	LEP1 & LEP2
	$p_{\rm t,bal} < 3$ GeV	LEP1 only
	$p_{\rm t,out} < 3$ GeV	LEP1 only

Table 4.4: The final selection cuts for singly–tagged two–photon events where the tagged electron or positron is found in one of the silicon tungsten (SW) calorimeters.

prised of data taken from 1994 and 1995 since the data sample for 1995 was unaffected by the change from bunches to bunchtrains.

The cuts on $\theta_{\rm tag}$ were made to accept tags only within the clear acceptance of FD. Below 59 mrad, FD lies in the shadow of SW (see section 3.8, Fig. 3.9).

4.3.4 Final Selection for Tags Found in EE

Table 4.6 shows the final selection for events with tags found in the EE calorimeters. Only events from 1994 and 1995 are used. The cross–section (see table 4.7) prevents an analysis of this high Q^2 region at the LEP2 energies until much

Type of Selection	Selection Criteria	
Tag Selection	$E_{\rm tag} \geqslant 0.775\ E_{\rm b}$	LEP1
	$E_{\rm tag} \geqslant 0.6\ E_{\rm b}$	LEP2
	$60 \leqslant \theta_{\rm tag} \leqslant 120$ mrad	LEP1 & LEP2
Antitag Veto	$E_{\rm a} \leqslant 0.25\ E_{\rm b}$	LEP1
	$E_{\rm a} \leqslant 0.08\ E_{\rm b}$	LEP2
Charged Particle Multiplicity	$N_{\rm tracks} > 2$	LEP1 & LEP2
Hadronic Final state	$2.5 \leqslant W_{\rm vis} \leqslant 40$ GeV	LEP1 & LEP2

Table 4.5: The final selection cuts for singly–tagged two–photon events where the tagged electron or positron is found in one of the forward luminosity (FD) calorimeters.

more data is collected. With the integrated luminosities from the 1996 runs, only a handful of events are observed.

4.3.5 Data Samples after Final Selection

Table. 4.7 shows the number of events passing the final selection criteria for each year during which data was collected and used in this analysis. It can be clearly seen that the cross–section decreases with increasing polar angle of the tagging detector from the beam line.

4.4 Background Estimation

There are many processes that can lead to the faking of signal events. Before conclusions can be drawn from the final data samples, it is necessary to estimate the

Type of Selection	Selection Criteria	
Tag Selection	$0.75\ E_{\rm b} \leqslant E_{\rm tag} \leqslant 1.2\ E_{\rm b}$	LEP1
	$200 \leqslant \theta_{\rm tag} \leqslant 500$ mrad	LEP1
	$E_{\rm tag,cone} < 2$ GeV	LEP1
	$E_{\rm opp,cone} < 1$ GeV	LEP1
Antitag Veto	$E_{\rm a} \leqslant 0.15\ E_{\rm b}$	LEP1
Charged Particle Multiplicity	$\mathrm{N_{tracks}} > 2$	LEP1
Hadronic Final state	$2.5 \leqslant W_{\rm vis} \leqslant 25$ GeV	LEP1
	$p_{\rm t,bal} < 5$ GeV	LEP1
	$p_{\rm t,out} < 4$ GeV	LEP1
	$-0.5\ E_{\rm b} \leqslant p_{\rm z,miss} \leqslant 0.5\ E_{\rm b}$	LEP1

Table 4.6: The final selection cuts for singly–tagged two–photon events where the tagged electron or positron is found in one of the endcap lead–glass electromagnetic calorimeters (EE).

Year	Beam Energy (GeV)	Integrated Luminosity (pb^{-1})	Number of Events Passed Final Selection	Cross–section (pb)
1994	45.6	55.51 ± 0.04	SW : 4253 ± 65.2	102.83 ± 1.17
		58.62 ± 0.05	FD : 1815 ± 42.6	30.96 ± 0.73
			EE : 52 ± 7.2	0.89 ± 0.12
1995	45.6	33.62 ± 0.05	FD : 1153 ± 34.0	34.30 ± 1.01
			EE : 30 ± 5.5	0.89 ± 0.16
1996	80.5	7.21 ± 0.04	SW : 459 ± 21.4	66.29 ± 2.97
		7.22 ± 0.04	FD : 201 ± 14.2	27.85 ± 1.97
1996	86.0	10.02 ± 0.06	SW : 502 ± 22.4	50.10 ± 2.24
		10.03 ± 0.06	FD : 241 ± 15.5	24.03 ± 1.55

Table 4.7: Number of events passing the final selection cuts and the corresponding measured cross–section given in terms of year and beam energy. The errors shown are statistical only.

number of background events that survive the final selection of the data sample. The process of background estimation is an integral part in choosing selection criteria which maximise the number of signal events in the final data sample whilst minimising the background.

The main sources of background for the production of hadrons via multiperipheral two–photon events (Fig. 4.3a) are:

- $e^+e^- \rightarrow Z^0/\gamma^* \rightarrow$ hadrons (Fig. 4.3b);
- $e^+e^- \rightarrow Z^0/\gamma^* \rightarrow \tau^+\tau^-$ (Fig. 4.3c);
- $e^+e^- \rightarrow e^+e^-\gamma\gamma^* \rightarrow e^+e^-\tau^+\tau^-$ (Fig. 4.3d);
- non–multiperipheral $e^+e^- \rightarrow e^+e^-$ + hadrons (Fig. 4.3e–g);
- $e^+e^- \rightarrow e^+e^-\gamma\gamma^* \rightarrow e^+e^-e^+e^-$ (Fig. 4.3h);
- $e^+e^- \rightarrow e^+e^-\gamma\gamma^* \rightarrow e^+e^-\mu^+\mu^-$ (Fig. 4.3i);
- beam gas events

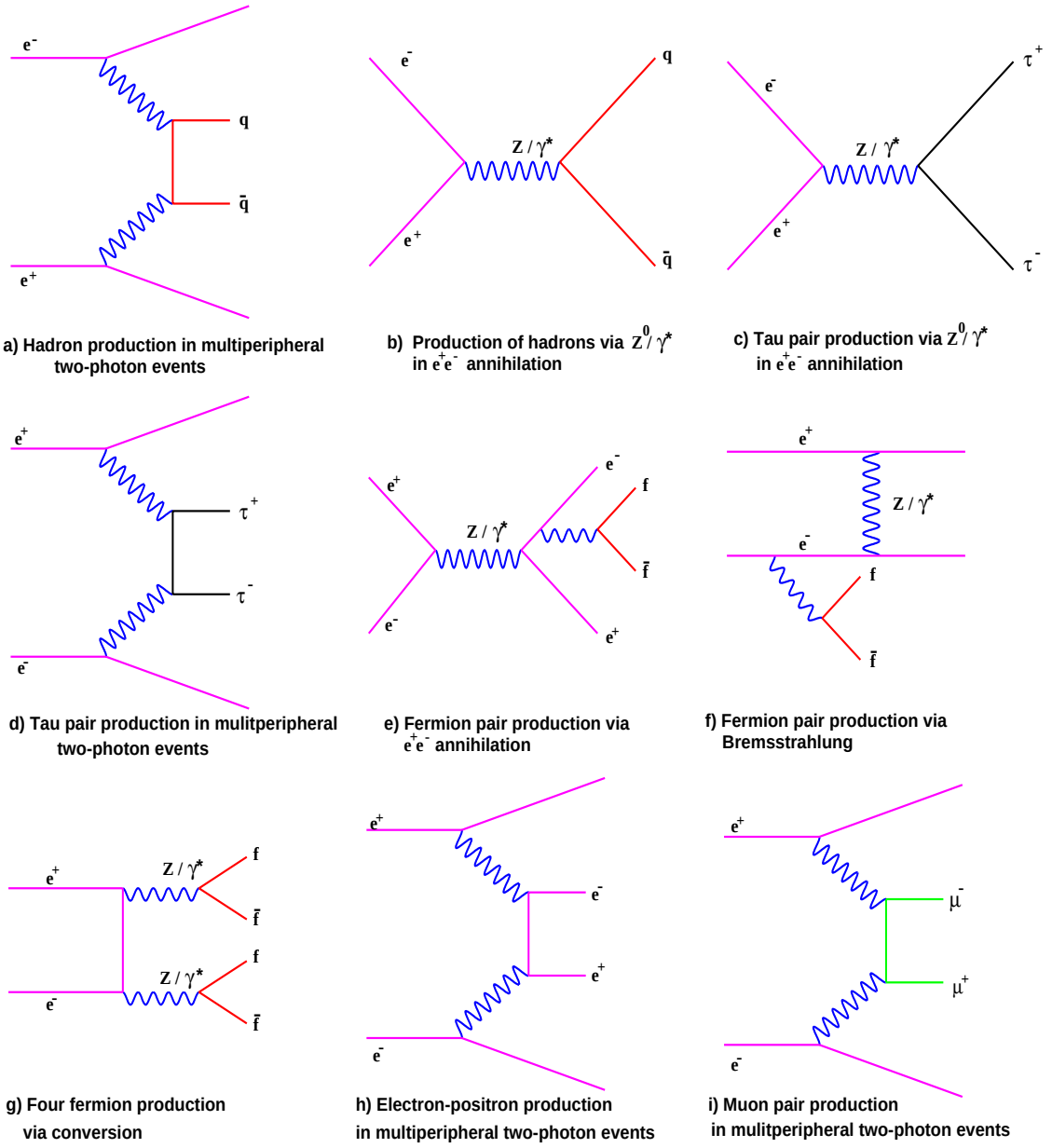

Figure 4.3: Diagrams showing the lowest order contributions to the process $\gamma\gamma \to f\bar{f}f\bar{f}$ as well as background processes to $e^+e^- \to e^+e^-\gamma\gamma \to e^+e^- +$ hadrons. Unlabelled boson lines represent photons only.

Various Monte Carlo generators have been used to simulate these background processes with each event passed through the OPAL detector simulation program [88] so that the background can be compared with, and subtracted from, the data samples on the detector level. Tables 4.8– 4.11 show the luminosities and numbers of events generated to simulate the various sources of background for each data sample, along with the number (both the actual number and the number normalised to the data luminosity) of events that pass the final selection.

4.4.1 Hadron Production from Z^0 Decay

This process (see Fig. 4.3b) involves the annihilation of an electron and a positron into a Z^0 or a virtual photon, γ^*. The Z^0/γ^* then decays into a quark–antiquark pair which into fragment into hadrons.

At LEP1, the colliding beams were created with centre–of–mass energies close to the Z^0 mass and hence this is clearly a very important background source as there are many more Z^0 production events than there are tagged two–photon events (see Fig. 1.3). The final selection criteria have therefore been designed to have a high efficiency for rejecting these events.

An important exploited characteristic of Z^0 events is that the hadronic activity tends to be less peaked at low polar angles than that of tagged two–photon events. This is particularly important for tags found in the SW and FD where the chances of a Z^0 event producing a cluster in either tagging detector is small. Additionally, the chance of producing a fake tag from Z^0 events decreases with the energy of the "tag". As a result, the imposition of a minimum tag energy used on all data samples is extremely effective in cutting down the size of this background source.

For tags found in the EE calorimeters, two further cuts are made on activity around the tag and around the direction opposite to the tag. The first of these cuts is to try to ensure that the candidate tag is isolated, as would be likely for an electron or positron tag but would be unlikely for a tag faked by hadronic activity. The second cut makes use of the fact that the Z^0 decay tends to produce two back–to–back jets of hadrons.

As the beam–beam centre–of–mass energy increases away from the Z^0 mass, the cross–section for this type of event decreases rapidly and so this source of background is much smaller at LEP2 (see tables 4.10 and 4.11).

Several generators were used to simulate this background for each of the three samples at different beam–beam centre–of–mass energies, $\sqrt{s}$. For comparison with the data samples, 4M $Z^0 \rightarrow$ hadrons events were generated using JETSET at $\sqrt{s}$ equal to the Z^0 mass peak, 180k events were generated at $\sqrt{s} = 161$ GeV using PYTHIA, HERWIG and ARIADNE [89], and at $\sqrt{s} = 171 - 172$ GeV, a sample of 300k events was generated using PYTHIA and HERWIG.

4.4.2 Tau Pair Production from Z^0 Decay

In addition to the hadronic decays of the Z^0/γ^* formed in e^+e^- annihilation, it is also possible for the Z^0/γ^* intermediate state to decay to a $\tau^+\tau^-$ pair (Fig 4.3c). The KORALZ [90] generator was used to generate 375k events at $\sqrt{s} = 91.28$ GeV, 100k events at $\sqrt{s} = 161.0$ GeV, and 100k events at $\sqrt{s} = 171.0$ GeV. Tables 4.8- 4.11 show that the final selection is more effective at removing the $Z^0/\gamma^* \rightarrow \tau^*\tau^-$ than the $Z^0/\gamma^* \rightarrow$ hadrons and that the background from the τ pair final state is less than 0.9% in all LEP1 samples and negligible for all LEP2 samples.

4.4.3 Tau Pair Production in Two–Photon Events

τ pair production (Fig. 4.3d) in two–photon interactions is a very important source of background at all $\sqrt{s}$ and for each of the θ_{tag} ranges. The vertices between the beam particles and the radiated photons are identical for two–photon events with τ pair final states and with hadronic final states, so any separation of the two processes relies upon cuts made on final state quantities rather than on tag and antitag criteria. It is extremely difficult, however, to distinguish between the decay products of τ pairs and the final state formed in hadronic two–photon events, and so a significant amount of this type of background passes the final selection. The contamination of the data from $e^+e^- \rightarrow e^+e^-\gamma\gamma^* \rightarrow e^+e^-\tau^+\tau^-$ is estimated using the VERMASEREN generator

described in section 2.8 with the τ pairs decayed using the τ branching ratio tables in JETSET.

For $\sqrt{s}$ = 91.2 GeV, 9221 events were generated for tags in SW and 10k events were generated for FD and EE tags. For the LEP2 data samples, 40k events were generated at $\sqrt{s}$ = 161 GeV and 41k at $\sqrt{s}$ = 171 GeV.

4.4.4 Non–Multiperipheral Processes: 4–Fermion Final States

Fig. 4.3e)-g) show diagrams of processes which give rise to the same final state as the multiperipheral (two–photon) process. The FERMISV [91] Monte Carlo generator is used to estimate the contribution of these processes to the background in the data sample. FERMISV incorporates both Z^0/γ^* exchange diagrams and interference terms, and the Z^0/γ^* decays into either a lepton–antilepton (l^+l^-) pair or a quark–antiquark ($q\bar{q}$) pair.

For the LEP1 background study, 4290, 4170, 5600 and 5550 events were generated for the Z^0/γ^* decays into $q\bar{q}$ ($q = u, d, s, c, b$), $\tau^+\tau^-$, $\mu^+\mu^-$ and e^+e^- respectively. The corresponding numbers of events for the LEP2 samples are 9075, 1460, 4700 and 1000 for $\sqrt{s}$ = 161 GeV, and 8435, 1500, 4500 and 18000 for $\sqrt{s}$ = 171 GeV. At all energies and $\theta_{\rm tag}$ ranges, the number of events that pass the final selection, is less than 0.1% of the size of the data sample and so is neglected.

4.4.5 Muon and Electron Pair Production in Two–Photon Events

In addition to a e^+e^- $\tau^+\tau^-$ final state (section 4.4.3), two–photon interactions at LEP produce $e^+e^-\mu^+\mu^-$ and $e^+e^-e^+e^-$ leptonic final states which need to be estimated in the background. The final selection criteria of more than two charged tracks is effective in reducing the size of this background and samples from the VERMASEREN Monte Carlo generator are used to estimate the number of events remaining after the final selection. 400k $e^+e^-\mu^+\mu^-$ and 400k $e^+e^-e^+e^-$ events at $\sqrt{s}$ = 91.2 GeV, 180k $e^+e^-\mu^+\mu^-$ and 282k $e^+e^-e^+e^-$ events at $\sqrt{s}$ = 161 GeV and 183k $e^+e^-\mu^+\mu^-$ and 300k

$e^+e^-e^+e^-$ events at $\sqrt{s} = 171$ GeV were generated and passed through OPAL simulation. At all energies, the $e^+e^- \rightarrow e^+e^- \mu^+\mu^-$ background is estimated at less than 0.1% of the data sample and is neglected.

4.4.6 W Pair Production

As can be seen in Fig. 1.3, it becomes necessary to estimate the background from the production of W pairs at LEP2 $\sqrt{s}$. The HERWIG, PYTHIA and KORALW [92] Monte Carlo generators were used to generate 240k and 300k events at $\sqrt{s} = 161$ GeV and $\sqrt{s} = 171$ GeV respectively. The contributions to the final data samples from these events is less than 0.05% and so this background source is neglected in the final analysis.

4.5 Beam Gas Events

Residual gas from the beam pipe can interact with particles in the beams. An "off–momentum" electron (or positron) is a beam particle that has lost energy and is scattered into the detector after an interaction of this type. This off–momentum particle can fake a tagged electron (positron). Additionally, if another interaction producing charged particles takes place close to the centre of, and during the same active period of, the detector then the coincidence of these events can fake the signature of a singly–tagged two–photon event.

These type of events provide a major background source within the data sample that is effectively removed by requiring a minimum $E_{\rm tag}/E_{\rm b}$ for a selected event. The effects of this background are clearly visible in Fig. 4.4b) and especially Fig. 4.5a) and c). The peaks are especially prominent for the LEP2 samples with tags in the SW calorimeters. The cut in $E_{\rm tag}/E_{\rm b}$ is set at higher $E_{\rm tag}$ than, and well away from, the peaks in the beam–gas background spectrum at $\sim$50% of $E_{\rm b}$.

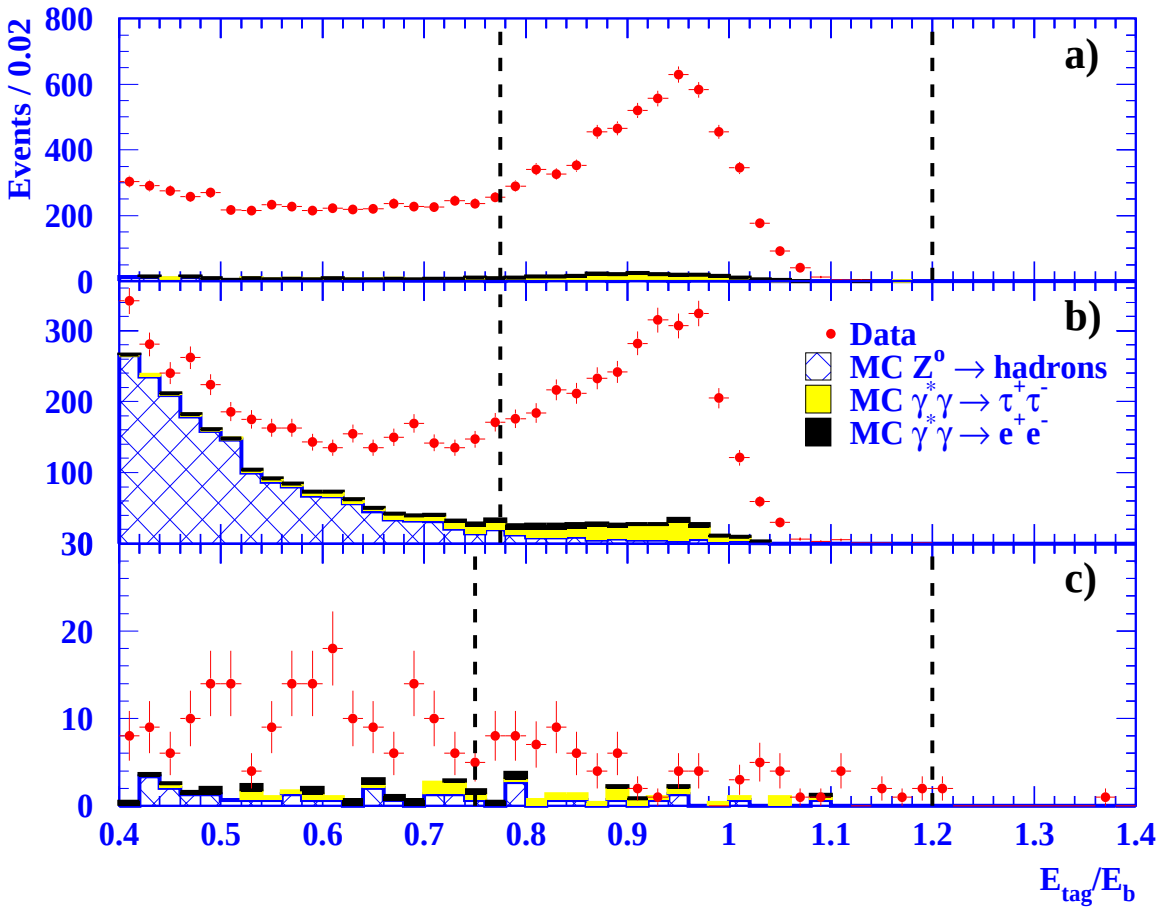

Figure 4.4: Plots showing the estimated contribution of the main background processes to the LEP1 data samples. All of the final selection criteria are applied except the cut on $E_{\rm tag}/E_{\rm b}$. The tagging detectors are a) the SW calorimeters , b) the FD calorimeters and c) the EE calorimeters. Each plot shows the estimates of the background sources $Z^0 \rightarrow$ hadrons, $\gamma\gamma^* \rightarrow e^+e^-$ and $\gamma\gamma^* \rightarrow \tau^+\tau^-$ added together to show the sum of their contributions. The shading for each background sample is different to show their individual contributions. The points are data with statistical errors only.

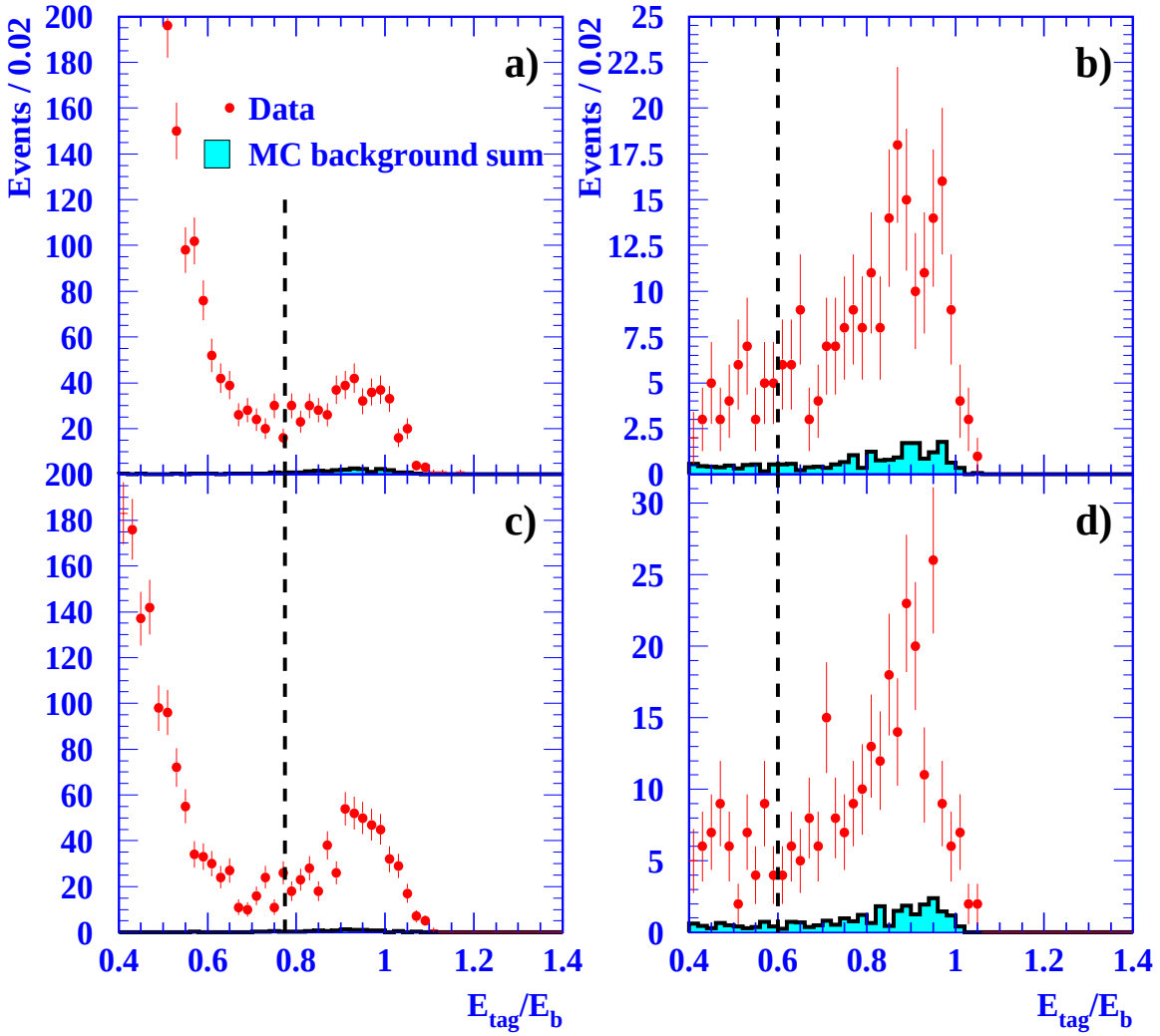

Figure 4.5: Plots showing the estimated contribution of the main background processes to the LEP2 data samples for the ratio of energies $E_{\rm tag}/E_{\rm b}$. All of the final selection criteria are applied except the cut on $E_{\rm tag}/E_{\rm b}$. Plots a) and b) show the data samples at $\sqrt{s} \sim 161$ GeV. Plots c) and d) show the data samples at $\sqrt{s} \sim 171$ GeV. The tagging detectors are a), c) the SW calorimeters and b),d) the FD calorimeters. Each plot shows the estimates of the background sources $Z^0 \rightarrow$ hadrons, $\gamma\gamma^* \rightarrow e^+e^-$ and $\gamma\gamma^* \rightarrow \tau^+\tau^-$ added together to show the sum of their contributions. The points are data with statistical errors only.

Event Generator	Luminosity (pb^{-1})	No of Events Selected	No of Selected Events Normalised to Data
SW TAGS:			
JETSET			
$e^+e^- \to$ hadrons	135.2	31	17.0
FERMISV			
$e^+e^- \to e^+e^- q\bar{q}$	1000.0	0	0.0
$e^+e^- \to e^+e^- e^+e^-$	1000.0	0	0.0
$e^+e^- \to e^+e^- \mu^+\mu^-$	1000.0	0	0.0
$e^+e^- \to e^+e^- \tau^+\tau^-$	1000.0	0	0.0
KORALZ			
$e^+e^- \to Z^0 \to \tau^+\tau^-$	253.1	0	0.6
VERMASEREN			
$e^+e^- \to e^+e^-\gamma\gamma \to e^+e^- \tau^+\tau^-$	151.1	311	114.3
$e^+e^- \to e^+e^-\gamma\gamma \to e^+e^- \mu^+\mu^-$	456.0	8	1.0
$e^+e^- \to e^+e^-\gamma\gamma \to e^+e^- e^+e^-$	392.1	310	43.9
DATA	55.51		4253
TOTAL			177
BACKGROUND			
FD TAGS:			
JETSET			
$e^+e^- \to$ hadrons	135.2	126	86.0
FERMISV			
$e^+e^- \to e^+e^- q\bar{q}$	1000.0	3	0.3
$e^+e^- \to e^+e^- e^+e^-$	1000.0	0	0.0
$e^+e^- \to e^+e^- \mu^+\mu^-$	1000.0	0	0.0
$e^+e^- \to e^+e^- \tau^+\tau^-$	1000.0	1	0.1
KORALZ			
$e^+e^- \to Z^0 \to \tau^+\tau^-$	253.1	8	2.9
VERMASEREN			
$e^+e^- \to e^+e^-\gamma\gamma \to e^+e^- \tau^+\tau^-$	281.1	522	171.3
$e^+e^- \to e^+e^-\gamma\gamma \to e^+e^- \mu^+\mu^-$	456.0	6	1.2
$e^+e^- \to e^+e^-\gamma\gamma \to e^+e^- e^+e^-$	392.1	231	54.3
DATA	92.24		2968
TOTAL			316
BACKGROUND			

Table 4.8: Estimated number of LEP 1 background events for tags found in the SW and FD calorimeters that survive the final selection criteria. The number of events are also shown normalised to the same luminosity as the data.

Event Generator	Luminosity (pb^{-1})	No of Events Selected	No of Selected Events Normalised to Data
EE TAGS:			
JETSET			
$e^+e^- \rightarrow$ hadrons	135.2	9	6.1
FERMISV			
$e^+e^- \rightarrow e^+e^- q\bar{q}$	1000.0	0	0.0
$e^+e^- \rightarrow e^+e^-e^+e^-$	1000.0	0	0.0
$e^+e^- \rightarrow e^+e^-\mu^+\mu^-$	1000.0	0	0.0
$e^+e^- \rightarrow e^+e^-\tau^+\tau^-$	1000.0	0	0.0
KORALZ			
$e^+e^- \rightarrow Z^0 \rightarrow \tau^+\tau^-$	253.1	2	0.7
VERMASEREN			
$e^+e^- \rightarrow e^+e^-\gamma\gamma \rightarrow e^+e^- \tau^+\tau^-$	281.1	24	7.9
$e^+e^- \rightarrow e^+e^-\gamma\gamma \rightarrow e^+e^-\mu^+\mu^-$	456.0	21	4.2
$e^+e^- \rightarrow e^+e^-\gamma\gamma \rightarrow e^+e^-e^+e^-$	392.1	10	2.3
DATA	92.24		82
TOTAL			21
BACKGROUND			

Table 4.9: Estimated number of LEP 1 background events for tags found in the EE calorimeters and which survive the final selection criteria. The number of events are also shown normalised to the same luminosity as the data.

Event Generator	Luminosity (pb^{-1})	No of Events Selected	No of Selected Events Normalised to Data
SW TAGS:			
JETSET			
$e^+e^- \to$ hadrons	407.8	18	0.3
FERMISV			
$e^+e^- \to e^+e^- q\bar{q}$	25000.0	1	0.0
$e^+e^- \to e^+e^-e^+e^-$	5000.0	0	0.0
$e^+e^- \to e^+e^-\mu^+\mu^-$	5000.0	0	0.0
$e^+e^- \to e^+e^-\tau^+\tau^-$	5000.0	0	0.0
KORALZ			
$e^+e^- \to Z^0 \to \tau^+\tau^-$	8159.3	0	0.0
WW			
$e^+e^- \to W^+W^-$ $\to$ all decays	57931.2	1	0.0
VERMASEREN			
$e^+e^- \to e^+e^-\gamma\gamma \to e^+e^-\tau^+\tau^-$	100.0	213	15.4
$e^+e^- \to e^+e^-\gamma\gamma \to e^+e^-\mu^+\mu^-$	94.6	2	0.2
$e^+e^- \to e^+e^-\gamma\gamma \to e^+e^-e^+e^-$	100.0	102	7.4
DATA	7.21		459
TOTAL			23
BACKGROUND			
FD TAGS:			
JETSET			
$e^+e^- \to$ hadrons	407.8	88	1.6
FERMISV			
$e^+e^- \to e^+e^- q\bar{q}$	25000.0	27	0.0
$e^+e^- \to e^+e^-e^+e^-$	5000.0	7	0.0
$e^+e^- \to e^+e^-\mu^+\mu^-$	5000.0	6	0.0
$e^+e^- \to e^+e^-\tau^+\tau^-$	5000.0	7	0.0
KORALZ			
$e^+e^- \to Z^0 \to \tau^+\tau^-$	8159.3	0	0.0
WW			
$e^+e^- \to W^+W^-$ $\to$ all decays	57931.2	1	0.0
VERMASEREN			
$e^+e^- \to e^+e^-\gamma\gamma \to e^+e^-\tau^+\tau^-$	100.0	172	12.4
$e^+e^- \to e^+e^-\gamma\gamma \to e^+e^-\mu^+\mu^-$	94.6	1	0.1
$e^+e^- \to e^+e^-\gamma\gamma \to e^+e^-e^+e^-$	100.0	46	3.3
DATA	7.22		201
TOTAL			17
BACKGROUND			

Table 4.10: Estimated number of LEP 2 ($\sqrt{s} \sim 161$ GeV) background events that survive the final selection criteria. The number of events are also shown normalised to the same luminosity as the data.

Event Generator	Luminosity (pb^{-1})	No of Events Selected	No of Selected Events Normalised to Data
SW TAGS:			
JETSET			
$e^+e^- \to$ hadrons	1056.7	43	0.4
FERMISV			
$e^+e^- \to e^+e^- q\bar{q}$	25747.9	2	0.0
$e^+e^- \to e^+e^-e^+e^-$	5000.0	3	0.0
$e^+e^- \to e^+e^-\mu^+\mu^-$	5000.0	0	0.0
$e^+e^- \to e^+e^-\tau^+\tau^-$	2300.0	0	0.0
KORALZ			
$e^+e^- \to Z^0 \to \tau^+\tau^-$	9345.8	0	0.0
WW			
$e^+e^- \to W^+W^-$ $\to$ all decays	21013.8	1	0.0
VERMASEREN			
$e^+e^- \to e^+e^-\gamma\gamma \to e^+e^-\tau^+\tau^-$	100.0	208	20.9
$e^+e^- \to e^+e^-\gamma\gamma \to e^+e^-\mu^+\mu^-$	100.8	3	0.3
$e^+e^- \to e^+e^-\gamma\gamma \to e^+e^-e^+e^-$	100.0	77	7.7
DATA	10.02		502
TOTAL			29
BACKGROUND			
FD TAGS:			
JETSET			
$e^+e^- \to$ hadrons	1056.7	135	1.3
FERMISV			
$e^+e^- \to e^+e^- q\bar{q}$	25747.9	25	0.0
$e^+e^- \to e^+e^-e^+e^-$	5000.0	3	0.0
$e^+e^- \to e^+e^-\mu^+\mu^-$	5000.0	9	0.0
$e^+e^- \to e^+e^-\tau^+\tau^-$	2300.0	5	0.0
KORALZ			
$e^+e^- \to Z^0 \to \tau^+\tau^-$	9345.8	0	0.0
WW			
$e^+e^- \to W^+W^-$ $\to$ all decays	21013.8	1	0.0
VERMASEREN			
$e^+e^- \to e^+e^-\gamma\gamma \to e^+e^-\tau^+\tau^-$	100.0	158	15.8
$e^+e^- \to e^+e^-\gamma\gamma \to e^+e^-\mu^+\mu^-$	100.8	2	0.2
$e^+e^- \to e^+e^-\gamma\gamma \to e^+e^-e^+e^-$	100.0	46	4.6
DATA	10.03		241
TOTAL			22
BACKGROUND			

Table 4.11: Estimated number of LEP 2 ($\sqrt{s} \sim 171$ GeV) background events that survive the final selection criteria. The number of events are also shown normalised to the same luminosity as the data.

4.6 Trigger Efficiencies

4.6.1 Calculation of Trigger Efficiencies for Events with FD and EE Tags

The trigger efficiencies for FD and EE tags are calculated by the same method employed in [2, 46]. This method relies upon the use of two independent triggers, $\mathcal{T}$ and $\mathcal{H}$. This independence is taken to mean that the likelihood of one of the triggers firing is unaffected by the firing state of the other trigger. Hence, a data sample of N events can be divided into 4 subsamples according to the state of these two triggers:

1. N_{not} events where neither trigger fires,
2. $N_{\mathcal{T}}$ events where trigger $\mathcal{T}$ fires whilst trigger $\mathcal{H}$ does not,
3. $N_{\mathcal{H}}$ events where trigger $\mathcal{T}$ does no fire whilst trigger $\mathcal{H}$ fires, and
4. $N_{\mathcal{TH}}$ events where both triggers fire.

The efficiencies $\epsilon_{\mathcal{T}}$ and $\epsilon_{\mathcal{H}}$ of the triggers $\mathcal{T}$ and $\mathcal{H}$ respectively are calculated using

$$\epsilon_{\mathcal{T}} = \frac{N_{\mathcal{TH}}}{N_{\mathcal{TH}} + N_{\mathcal{H}}} \qquad (4.6)$$
$$\epsilon_{\mathcal{H}} = \frac{N_{\mathcal{TH}}}{N_{\mathcal{TH}} + N_{\mathcal{T}}}$$

Assuming that all events cause at least one of the two triggers to fire, then the estimated total trigger efficiency, ϵ_{TOT}, is:

$$\epsilon_{TOT} = [1 - (1 - \epsilon_{\mathcal{T}})(1 - \epsilon_{\mathcal{H}})] \qquad (4.7)$$

4.6.2 Estimation of Efficiency for Events with FD and EE Tags

For singly–tagged tow–photon events, the event can be trigger–selected by causing the firing of at least one of:

- an FDHIOR trigger (table 3.1) from a tag in one of the FD calorimeters;

- an EEL(R)HI trigger from a tag in the left(right) EE calorimeter;
- a stand alone trigger from a track and/or calorimeter trigger;
- a programmed coincidence of triggers.

Year	E_b(GeV)	N	$N_{\mathcal{T}}$	$N_{\mathcal{H}}$	$N_{\mathcal{TH}}$	$\epsilon_{\mathcal{T}}(\%)$	$\epsilon_{\mathcal{H}}(\%)$	$\epsilon_{TOT}(\%)$
FD Tags								
1994	44.6–46.6	1815	0	683	1132	62.3	100.0	100.0
1995	44.6–46.6	1153	0	592	561	51.3	100.0	100.0
1996	80.5	201	0	4	197	98.0	100.0	100.0
1996	85.0–86.0	241	0	10	231	95.9	100.0	100.0
EE Tags								
1994	44.6–46.6	52	17	0	35	100.0	67.3	100.0
1995	44.6–46.6	30	12	0	18	100.0	60.0	100.0

Table 4.12: Estimated trigger efficiencies for tags found in the FD and EE calorimeters

4.6.3 Calculation of Trigger Efficiencies for Events with SW Tags

No SW trigger condition for tag candidates was set up independent of the triggers for the hadronic final state. Accordingly, the method for calculating the trigger efficiencies for tags found in the SW calorimeters is different from that of section 4.6.1 and is the same as described in [93].

Three sets of triggers (A,B,C) with high efficiencies are chosen. A,B and C can each be any one of:

- a single stand alone trigger;
- a coincidence of triggers;
- a collection of different triggers.

The result, T_A, of a trigger set, A, for an event is defined as:

$$\begin{aligned} T_A &= 0 \quad \text{if triggersetA is not fired} \\ &= 1 \quad \text{if triggersetA is fired} \end{aligned} \tag{4.8}$$

with T_B and T_C defined correspondingly for trigger sets B and C.

The trigger set A is used to define a subset of $N^{'}$ events from the data sample of N events for which $T_A = 1$. The efficiencies for trigger sets B and C are assumed to remain the same for $T_A = 0$ and $T_A = 1$. This data subset of $N^{'}$ events is then used to calculate the correlation, corr^{BC}, between the trigger sets B and C:

$$\text{corr}^{\text{BC}} = \frac{1}{N^{'}} \sum^{N^{'}} \frac{(T_B - \epsilon_B^{'})(T_C - \epsilon_C^{'})}{\sigma_B \sigma_C} \tag{4.9}$$

where $\epsilon_B^{'}$, $\epsilon_C^{'}$ are the trigger efficiencies of B, C defined for the $N^{'}$ events:

$$\begin{aligned} \epsilon_B^{'} &= \frac{1}{N^{'}} \sum^{N^{'}} T_B \\ \epsilon_C^{'} &= \frac{1}{N^{'}} \sum^{N^{'}} T_C \end{aligned} \tag{4.10}$$

and σ_B, σ_C are the standard deviations:

$$\begin{aligned} \sigma_B &= \frac{1}{N^{'}} \sum^{N^{'}} (T_B - \epsilon_B^{'})^2 \\ \sigma_C &= \frac{1}{N^{'}} \sum^{N^{'}} (T_C - \epsilon_C^{'})^2 \end{aligned} \tag{4.11}$$

The triggers B and C are independent if $\text{corr}^{\text{BC}} \approx 0$. The trigger efficiency, ϵ_{TOT} for the whole data set ($T_A = 1$ or 0) is

$$\epsilon_{TOT} = \epsilon_B + \epsilon_C - \epsilon_B \epsilon_C \tag{4.12}$$

where ϵ_B and ϵ_C are calculated using Eqn. 4.10 by performing the sums over all N events.

4.6.4 Estimation of Efficiency for Events with SW Tags

Table 4.13 shows the estimated trigger efficiencies, ϵ_{TOT}, for the LEP 1 and LEP 2 data sets with SW tags. These estimates are lower limits on the true trigger

efficiency since not all triggers with low efficiencies were considered for the formation of independent triggers.

For the LEP 1 and LEP 2 $\sqrt{s} \sim 161$ GeV data samples, the trigger sets chosen are:

trigger A

(TPEML.AND.TPTTR).OR.(TPEMR.AND.TPTTL).OR.
(SWHIOR.AND.(TPEML.OR.TPEMR)).OR.
((TM1.OR.TPT01).AND.(EERLO.OR.EELLO))

trigger B

(SWHIOR.AND.TBM1).OR.(TPTTO.AND.TBEBS)

trigger C

TPTTEM.

Some trigger definitions were changed or removed for the LEP 2 $\sqrt{s} \sim 171$ GeV data taking, and hence the trigger sets for this data sample are:

trigger A

(TPEML.AND.TPTTR).OR.(TPEMR.AND.TPTTL).OR.
(SWHIOR.AND.(TPEML.OR.TPEMR)).OR.
(TM1.AND.(EERLO.OR.EELLO))

trigger B

(SWHIOR.AND.TBM1).OR.(EEPRLR.AND.TBEBS)

trigger C

TPTTEM.

Year	E_{b} (GeV)	ϵ_B (%)	ϵ_C (%)	$\mathrm{corr}^{\mathrm{BC}}$	ϵ_{TOT} (%)
1994	44.6–46.6	91.2	63.1	0.0610	96.8
1996	80.5	86.1	67.3	0.0005	95.4
1996	85.0–86.0	60.8	78.9	0.0338	91.7

Table 4.13: Estimated trigger efficiencies for tags found in the SW calorimeters

Chapter 5

Comparing Data and Monte Carlo Samples

5.1 Monte Carlo Generator Samples

Three Monte Carlo generators were used to simulate singly–tagged two photon events:

- HERWIG [8]
- PYTHIA [9]
- F2GEN [10]

The methods of generation for the HERWIG and PYTHIA multipurpose generators are described in section 2.7 along with a brief description of the F2GEN generator. A fuller description of the algorithm used in the F2GEN program is detailed in chapter 7. The parameterisations used for F_2^γ were GRV (LO) for HERWIG and F2GEN and SaS1D for PYTHIA.

Table 5.1 shows the numbers of events, cross–sections and integrated luminosities for the samples generated using each Monte Carlo program. These samples were generated at e^+e^- beam energies, E_b, of 45.6 GeV, 80.5 GeV and $85.5 - 86.0$ GeV and then passed through the simulation program for the OPAL detector.

Event Generator	Tagging Detector(s)	Beam Energy (GeV)	Number of Events	Cross–section (pb)	Luminosity (pb^{-1})
F2GEN	SW	45.6	49980	721.2	69.3
	FD	45.6	49889	245.6	203.1
	EE	45.6	10000	15.4	649.9
	SW & FD	80.5	50000	994.0	50.3
	SW & FD	85.5	50000	1039.5	48.1
HERWIG	SW	45.6	50000	526.0	95.1
	FD	45.6	49863	275.9	180.7
	EE	45.6	9999	7.4	1353.9
	SW & FD	80.5	100000	960.6	104.1
PYTHIA	SW	45.6	49799	379.9	131.1
	FD	45.6	40000	172.3	232.1
	EE	45.6	10000	6.2	1605.1
	SW & FD	80.5	100000	694.9	143.9
	SW & FD	86.0	100000	722.5	138.4

Table 5.1: The number of events generated, cross–sections and integrated luminosities for the singly–tagged two–photon Monte Carlo samples used for comparison with the data samples.

For all Monte Carlo samples, a cut of $W^2_{\gamma\gamma^*} > 3$ GeV^2 was imposed on generator level. Additionally, a minimum Q^2 cut was set at 1.0 GeV^2 except for the LEP1 HERWIG and PYTHIA samples where it was set at 1.5 GeV^2. Cuts in $\theta_{\rm tag}$ are made in the detector level selection to eliminate discrepancies between the Monte Carlo samples arising from the different minimum Q^2 generator level cuts. In each sample, $n_f = 4$ active quark flavours were used with charm mass $m_c = 1.5$ GeV for HERWIG and F2GEN, and $m_c = 1.3$ GeV for PYTHIA.

5.2 Cross–Sections

Event Sample	Tagging Detector(s)	Number of Events N_{cuts}	Integrated Luminosity $\mathcal{L}$ (pb^{-1})	σ_{cuts} (pb)
Data	SW	4217 $\pm$ 65	55.5	76.0 $\pm$ 1.2
HERWIG	SW	6235 $\pm$ 79	95.1	65.6 $\pm$ 0.8
PYTHIA	SW	8875 $\pm$ 94	131.1	67.7 $\pm$ 0.7
F2GEN Pointlike	SW	5100 $\pm$ 71	69.3	73.6 $\pm$ 1.0
Data	FD	2656 $\pm$ 57	92.2	28.8 $\pm$ 0.6
HERWIG	FD	5134 $\pm$ 72	180.7	28.4 $\pm$ 0.4
PYTHIA	FD	6273 $\pm$ 79	232.1	27.0 $\pm$ 0.3
F2GEN Pointlike	FD	5846 $\pm$ 76	203.1	28.8 $\pm$ 0.4
Data	EE	66 $\pm$ 8	92.2	0.71$\pm$ 0.09
HERWIG	EE	998 $\pm$ 32	1353.9	0.74$\pm$ 0.02
PYTHIA	EE	1065 $\pm$ 33	1605.1	0.66$\pm$ 0.02
F2GEN Pointlike	EE	490 $\pm$ 22	649.9	0.75$\pm$ 0.03

Table 5.2: The number of events passing the final selection criteria, and the corresponding cross–sections, σ_{cuts}, for the LEP1 data and Monte Carlo samples. The numbers for the data sample of events with SW tags are corrected to account for trigger efficiencies. The estimated background is subtracted from each data sample.

Tables 5.2 and 5.3 show the number of events, N_{cuts}, passing the final selection criteria for data and Monte Carlo samples at LEP1 and LEP2 energies. In each of the SW tag data samples, the numbers are corrected to account for the estimated trigger

Event Sample	Tagging Detector(s)	Number of Events N_{cuts}	Integrated Luminosity $\mathcal{L}$ (pb^{-1})	σ_{cuts} (pb)
Data ($\sqrt{s} \sim 161$ GeV)	SW	459 ± 22	7.2	63.8 ± 3.0
HERWIG	SW	4251 ± 65	104.1	40.8 ± 0.6
PYTHIA	SW	5172 ± 72	143.9	35.9 ± 0.5
F2GEN Pointlike	SW	2137 ± 46	50.3	42.5 ± 0.9
Data ($\sqrt{s} \sim 161$ GeV)	FD	184 ± 15	7.2	25.6 ± 2.1
HERWIG	FD	2250 ± 47	104.1	21.6 ± 0.5
PYTHIA	FD	2686 ± 52	143.9	18.7 ± 0.4
F2GEN Pointlike	FD	1099 ± 33	50.3	21.8 ± 0.7
Data ($\sqrt{s} \sim 171$ GeV)	SW	547 ± 23	10.0	54.7 ± 2.3
PYTHIA	SW	4688 ± 68	138.4	33.9 ± 0.5
F2GEN Pointlike	SW	2011 ± 45	48.1	41.8 ± 0.9
Data ($\sqrt{s} \sim 171$ GeV)	FD	219 ± 16	10.0	21.9 ± 1.6
PYTHIA	FD	2333 ± 48	138.4	16.9 ± 0.3
F2GEN Pointlike	FD	959 ± 31	48.1	19.9 ± 0.6

Table 5.3: The number of events, N_{cuts}, passing the final selection criteria, and the corresponding cross–sections, σ_{cuts}, for the LEP2 data and Monte Carlo samples. The numbers for the data samples of events with SW tags are corrected to account for trigger efficiencies.The estimated background is subtracted from each data sample.

efficiencies found in section 4.6. The estimated background is subtracted from the data samples. The cross–sections, σ_{cuts}, are calculated using the integrated luminosities, $\mathcal{L}$, for each sample:

$$\sigma_{cuts} = \frac{N_{cuts}}{\mathcal{L}} \tag{5.1}$$

It can be clearly seen from Tables 5.2 and 5.3 that there are discrepancies in the cross–sections between data and Monte Carlo samples. The largest discrepancies occur at low Q^2 and for LEP2 samples.

From comparisons with the LEP1 data samples, the predictions from the HERWIG generator agree within errors except for the SW tag sample where it is

$\sim 10\%$ lower than the data, the predictions from PYTHIA lie $6 - 8\%$ lower than the data for all samples, whilst the cross–sections for F2GEN are in reasonable agreement with the data for all samples.

During the LEP2 running in 1996, OPAL received significantly higher off–momentum backgrounds than any of the other three LEP experiments. The size of this background was particularly large in LEP running at $\sqrt{s} \sim 161$ GeV and may account in part for the difference between the cross–sections for the SW tag data samples at $\sqrt{s} \sim 161$ GeV and $\sqrt{s} \sim 171$ GeV. This is also reflected in the size of the disagreements in cross–sections between the data and Monte Carlo samples. At $\sqrt{s} \sim 161$ GeV all of the predictions of the cross–sections from the Monte Carlo samples lie $> 15\%$ below the data. At $\sqrt{s} \sim 171$ GeV, the cross–sections for F2GEN and PYTHIA are at least 9% and 23% lower than the data respectively.

5.3 Sources of Discrepancies

Much of the differences in the cross–section at LEP2 is accounted for by the uniquely high backgrounds received by OPAL. However, this is not the only source of differences between data measurements and Monte Carlo predictions. The OPAL LEP1 analysis at low Q^2 [4] showed that the unfolded points for $F_2^\gamma(x, Q^2)$ lie systematically $\sim 10\%$ above the GRV (LO), GRV (HO) and SaS-1D parameterisations (see Fig. 1.4 and 1.6). From Eqn. 1.17, it can be seen that this has an effect upon the cross–sections calculated in generating a sample of events.

It is important to note that this cannot be the only reason for the discrepancies between the measured cross–sections and those predicted using the Monte Carlo generators. The HERWIG and F2GEN samples were all generated using the GRV (LO) parameterisation but disagree upon cross–sections at low Q^2. In addition, Fig. 2.2 shows that there is little difference between the parameterisations for GRV (LO) and SaS-1D of $F_2^\gamma(x, Q^2)$ at low Q^2 but that PYTHIA consistently predicts a smaller cross-section than F2GEN. Much of the discrepancy arises from the different models used in these generators to simulate the hadronic final state and this is provides the major motivating factor for the studies described in the rest of this thesis.

5.4 Tag and Antitag Distributions

Fig. 5.1 to Fig. 5.6 show the distributions from measured tag quantities[1]: the ratio of tag energy $E_{\rm tag}$ over beam energy $E_{\rm b}$, tag polar angle $\theta_{\rm tag}$ and the negative square of the probe photon momentum Q^2. Fig. 5.7 and Fig. 5.8 show the distributions for the ratio of the energy $E_{\rm a}$ of the candidate second tag over the beam energy. The Monte Carlo distributions are shown normalised to the data luminosity. Dashed lines are used to highlight the values of selection cuts made in the plotted variable with arrows indicating the region where events pass the selection.

In all cases, the data distributions are well reproduced by the Monte Carlo samples allowing for systematic discrepancies arising from differences in the cross–sections. This is important as these are measured quantities from the photon–lepton vertices and are modelled using QED. Any discrepancies between measured quantities from the hadronic final state arise from inaccuracies in the modelling of the production and distribution of hadrons from the photon–photon interaction.

In Fig. 5.1 and Fig. 5.2, the distributions of $E_{\rm tag}/E_{\rm b}$ are peaked at about 0.9 $E_{\rm b}$ for the SW and FD tag samples. For the EE tag samples, the peak lies below the minimum $E_{\rm tag}$ cut. The differences between data and Monte Carlo distributions below the minimum $E_{\rm tag}/E_{\rm b}$ cut are caused by hadron production in Z^0 decay (section 4.4.1) and beam gas backgrounds (section 4.5). Fig. 5.3 and Fig. 5.4 show distributions which decrease with increasing $\theta_{\rm tag}$. Fig. 5.5 and Fig. 5.6 show the corresponding Q^2 for the event, calculated by substituting $E_{\rm tag}$ and $\theta_{\rm tag}$ into Eqn. 4.1. The decrease in the cross–section with $\theta_{\rm tag}$ and Q^2 is understood in terms of the flux factor $, _t$ (Eqn. 1.3) for photon emission by a beam electron which peaks a at low Q^2 and z, where z is the fraction of the beam energy carried by the emitted photon.

Fig. 5.7 and Fig. 5.8 show the ratio of energies $E_{\rm a}/E_{\rm b}$ for the candidate opposite tag (see section 4.3.1). The cut on the maximum value of $E_{\rm a}/E_{\rm b}$ is imposed to remove any doubly–tagged events from the data sample and hence so that the probed photon can be considered quasi–real in the analysis. The distribution is highly peaked at low $E_{\rm a}$ as the candidate second tags are final state hadrons with energy much lower than the beam energy.

[1]The distributions for the data samples with tags found in the SW calorimeters have not been corrected for trigger efficiencies.

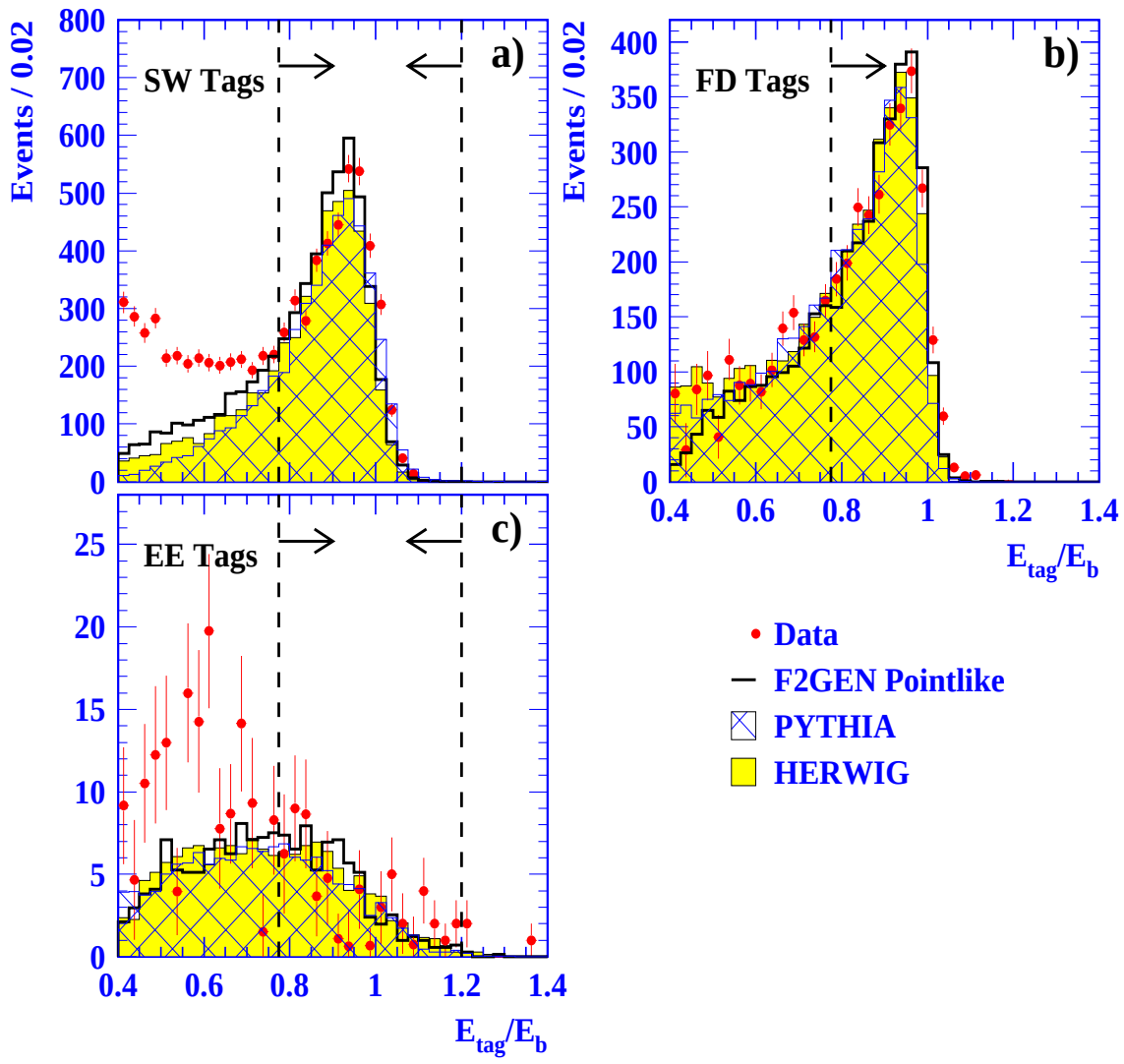

Figure 5.1: The $E_{\rm tag}/E_{\rm b}$ distributions of the LEP1 data and Monte Carlo samples for tags found in the a) SW, b) FD and c) EE calorimeters. The data distributions (dots) are shown with background subtracted whilst the distributions for HERWIG (shaded), PYTHIA (hatched) and F2GEN (open) are plotted normalised to the same luminosity as the data. All cuts have been applied except those made on the ratio $E_{\rm tag}/E_{\rm b}$ (see section 4.3) and these cuts are shown as dashed lines. The arrows indicate the region where the events pass the selection cut. The errors on the data points are statistical only.

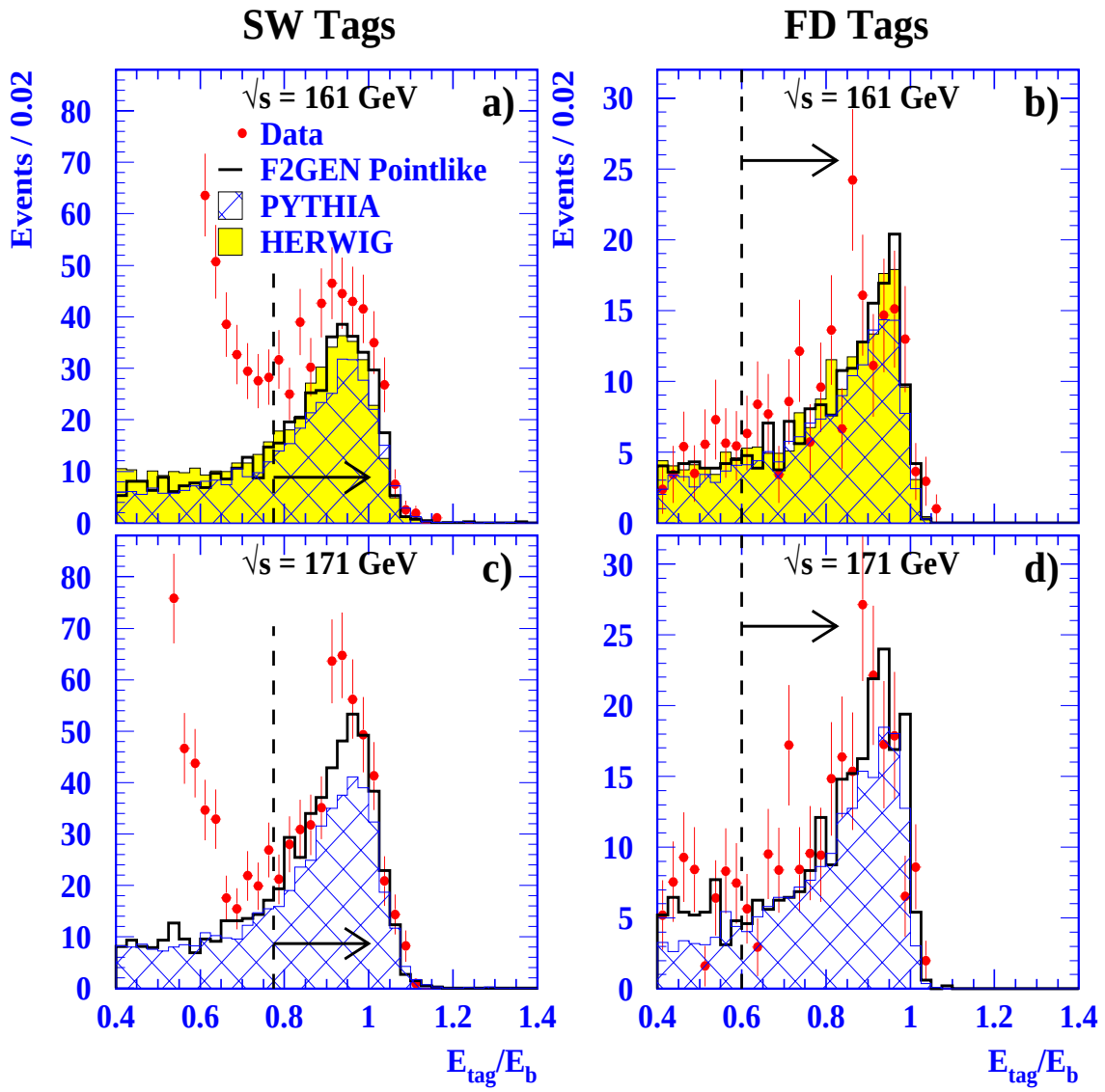

Figure 5.2: The $E_{\rm tag}/E_{\rm b}$ distributions of the LEP2 data and Monte Carlo samples for tags found in the a) & c) SW and b) & d) FD calorimeters. The data distributions (dots) are shown with background subtracted whilst the distributions for HERWIG (shaded), PYTHIA (hatched) and F2GEN (open) are plotted normalised to the same luminosity as the data. All cuts have been applied except those made on the ratio $E_{\rm tag}/E_{\rm b}$ (see section 4.3) and these cuts are shown as dashed lines. The arrows indicate the region where the events pass the selection cut. The errors on the data points are statistical only.

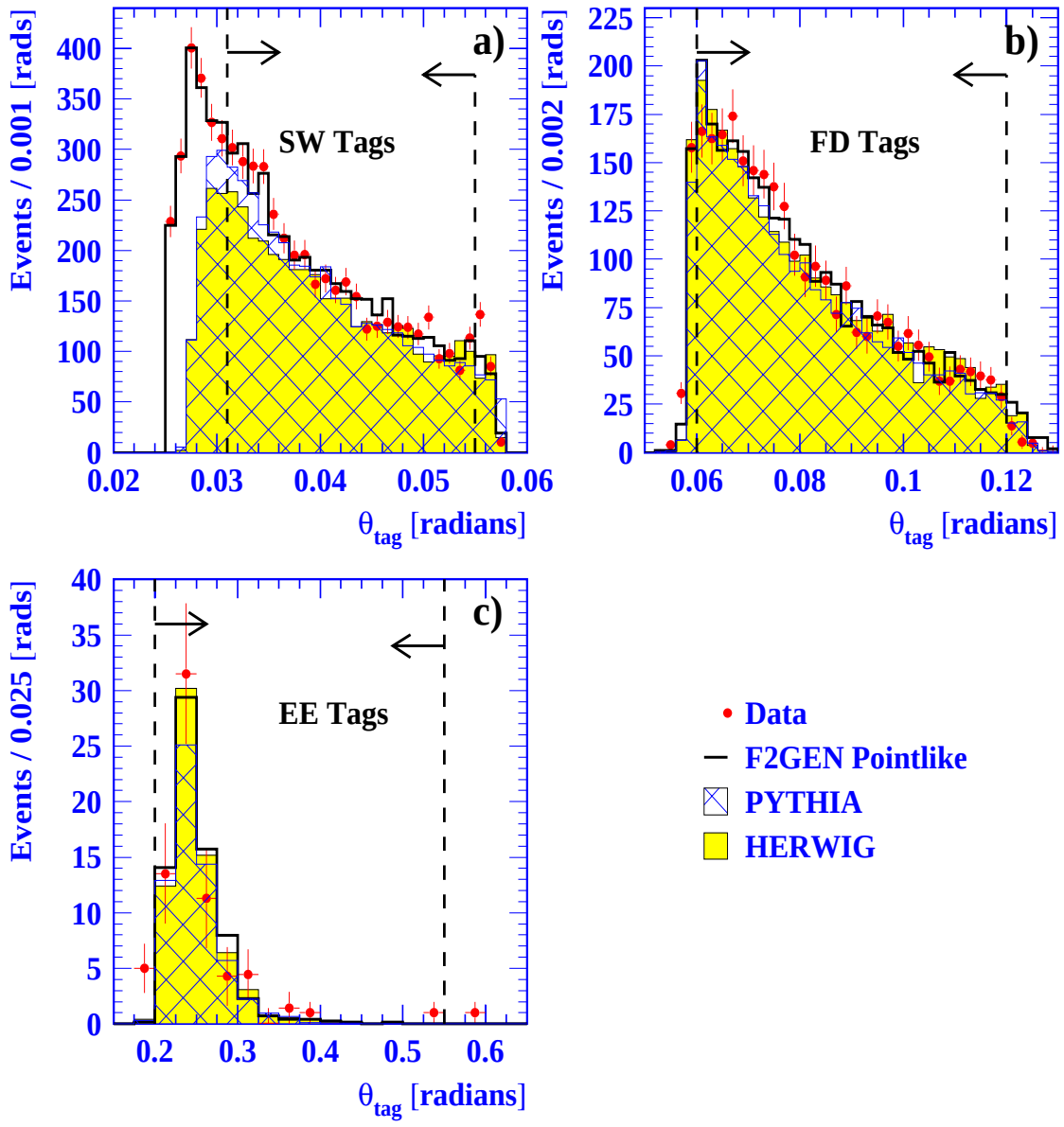

Figure 5.3: The $\theta_{\rm tag}$ distributions of the LEP1 data and Monte Carlo samples for tags found in the a) SW, b) FD and c) EE calorimeters. The data distributions (dots) are shown with background subtracted whilst the distributions for HERWIG (shaded), PYTHIA (hatched) and F2GEN (open) are plotted normalised to the same luminosity as the data. All cuts have been applied except those made on the ratio $\theta_{\rm tag}$ (see section 4.3) and these cuts are shown as dashed lines. The arrows indicate the region where the events pass the selection cut. The errors on the data points are statistical only.

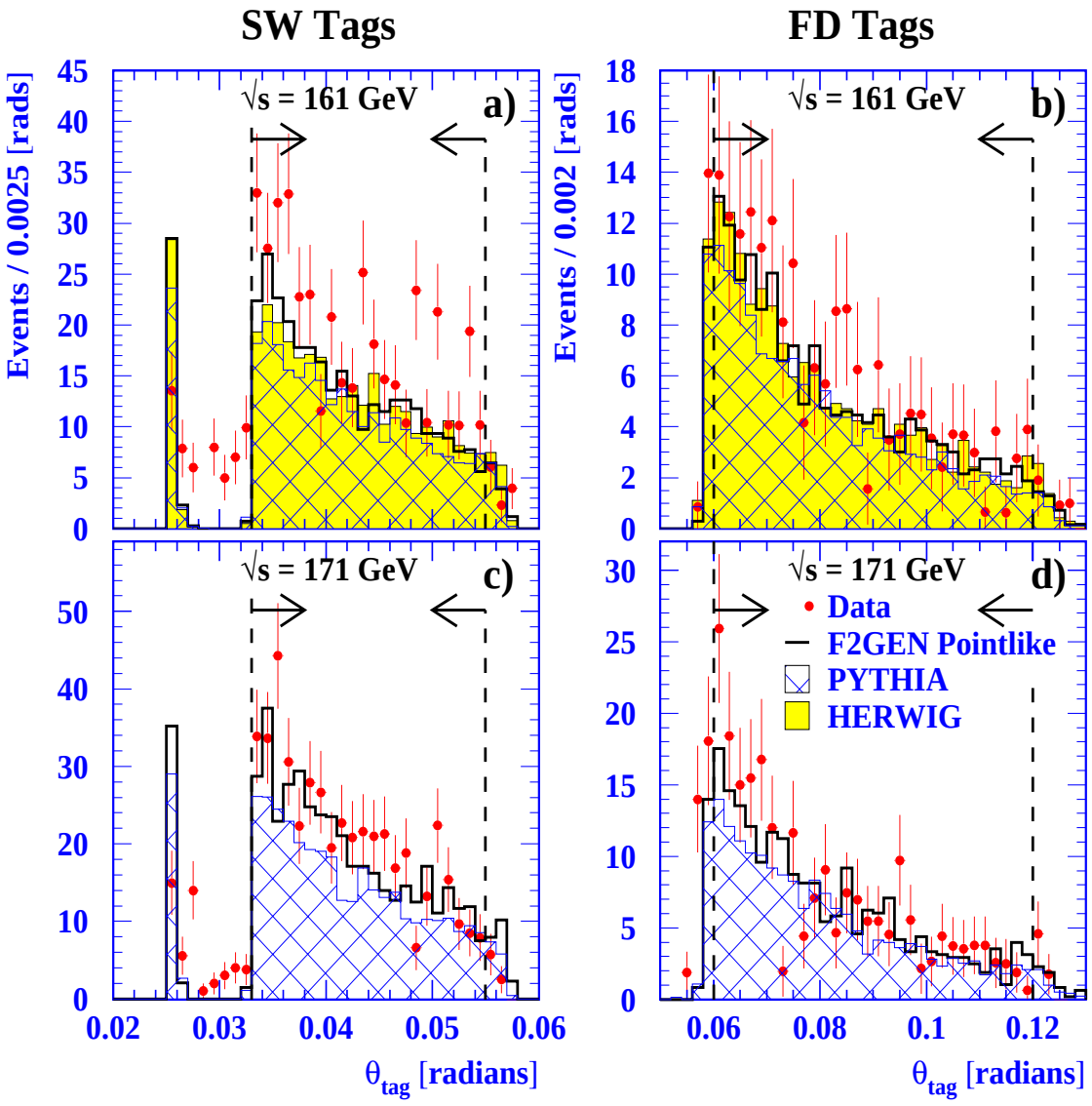

Figure 5.4: The θ_{tag} distributions of the LEP2 data and Monte Carlo samples for tags found in the a) & c) SW and b) & d) FD calorimeters. The data distributions (dots) are shown with background subtracted whilst the distributions for HERWIG (shaded), PYTHIA (hatched) and F2GEN (open) are plotted normalised to the same luminosity as the data. All cuts have been applied except those made on the ratio θ_{tag} (see section 4.3) and these cuts are shown as dashed lines. The arrows indicate the region where the events pass the selection cut. The errors on the data points are statistical only.

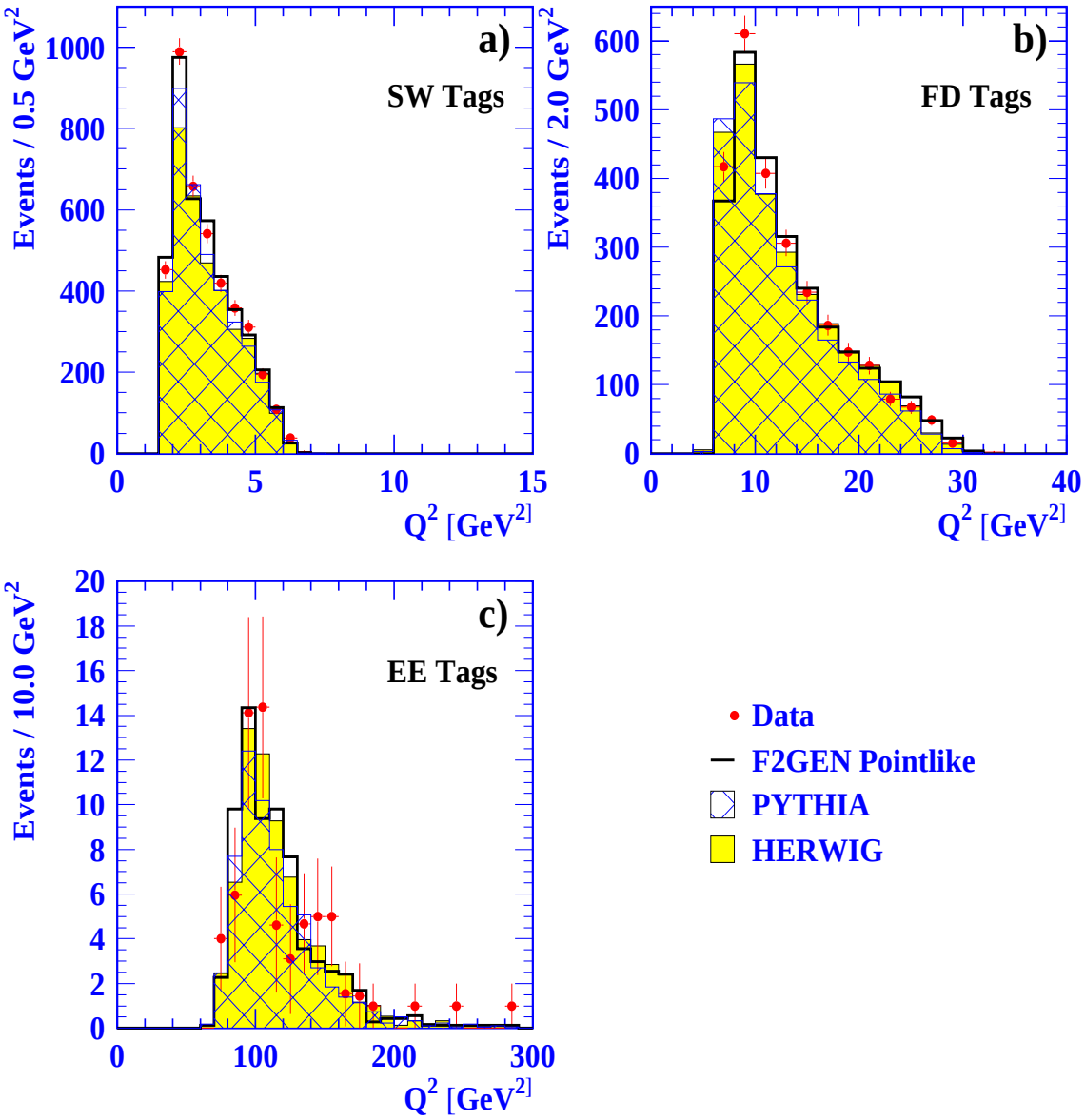

Figure 5.5: The Q^2 distributions of the LEP1 data and Monte Carlo samples for tags found in the a) SW, b) FD and c) EE calorimeters. The data distributions (dots) are shown with background subtracted whilst the distributions for HERWIG (shaded), PYTHIA (hatched) and F2GEN (open) are plotted normalised to the same luminosity as the data. All cuts have been applied (see section 4.3). The errors on the data points are statistical only.

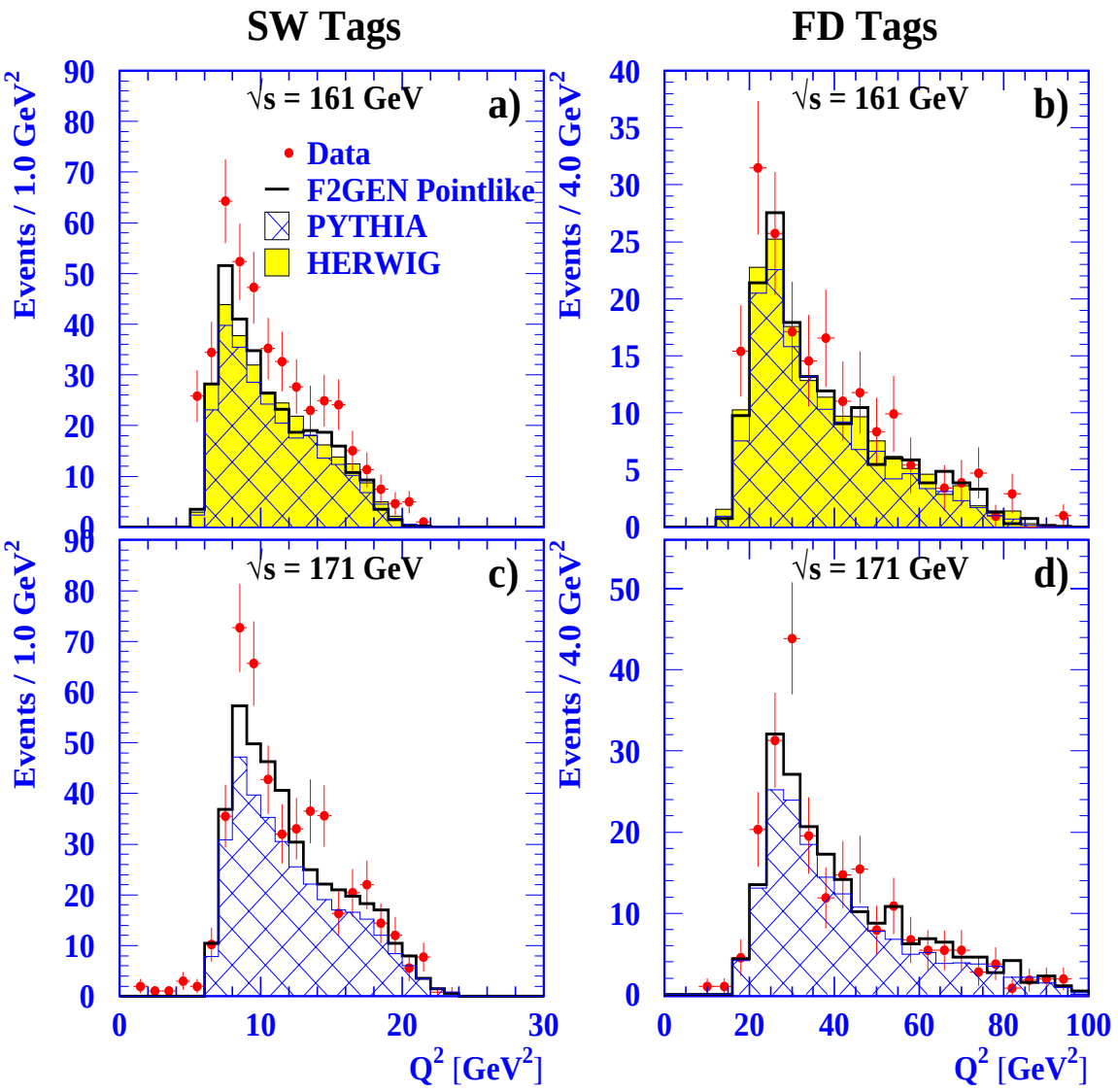

Figure 5.6: The Q^2 distributions of the LEP2 data and Monte Carlo samples for tags found in the a) & c) SW and b) & d) FD calorimeters. The data distributions (dots) are shown with background subtracted whilst the distributions for HERWIG (shaded), PYTHIA (hatched) and F2GEN (open) are plotted normalised to the same luminosity as the data. All cuts have been applied. The errors on the data points are statistical only.

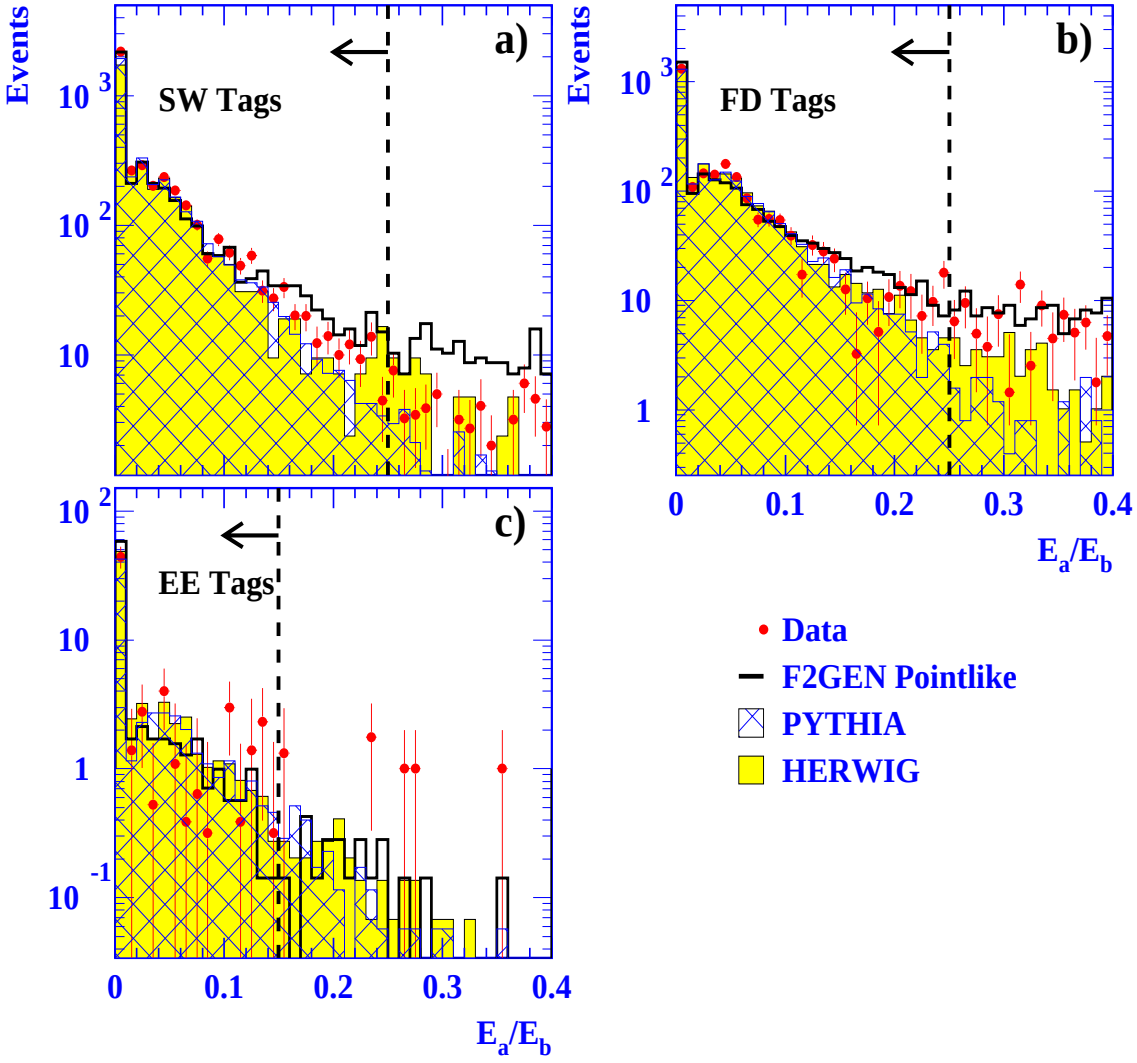

Figure 5.7: The candidate second tag distributions of E_a/E_b for the LEP1 data and Monte Carlo samples with tags found in the a) SW, b) FD and c) EE calorimeters. The data distributions (dots) are shown with background subtracted whilst the distributions for HERWIG (shaded), PYTHIA (hatched) and F2GEN (open) are plotted normalised to the same luminosity as the data. All cuts have been applied except those made on the ratio E_a/E_b (see section 4.3) and these cuts are shown as dashed lines. The arrows indicate the region where the events pass the selection cut. The errors on the data points are statistical only.

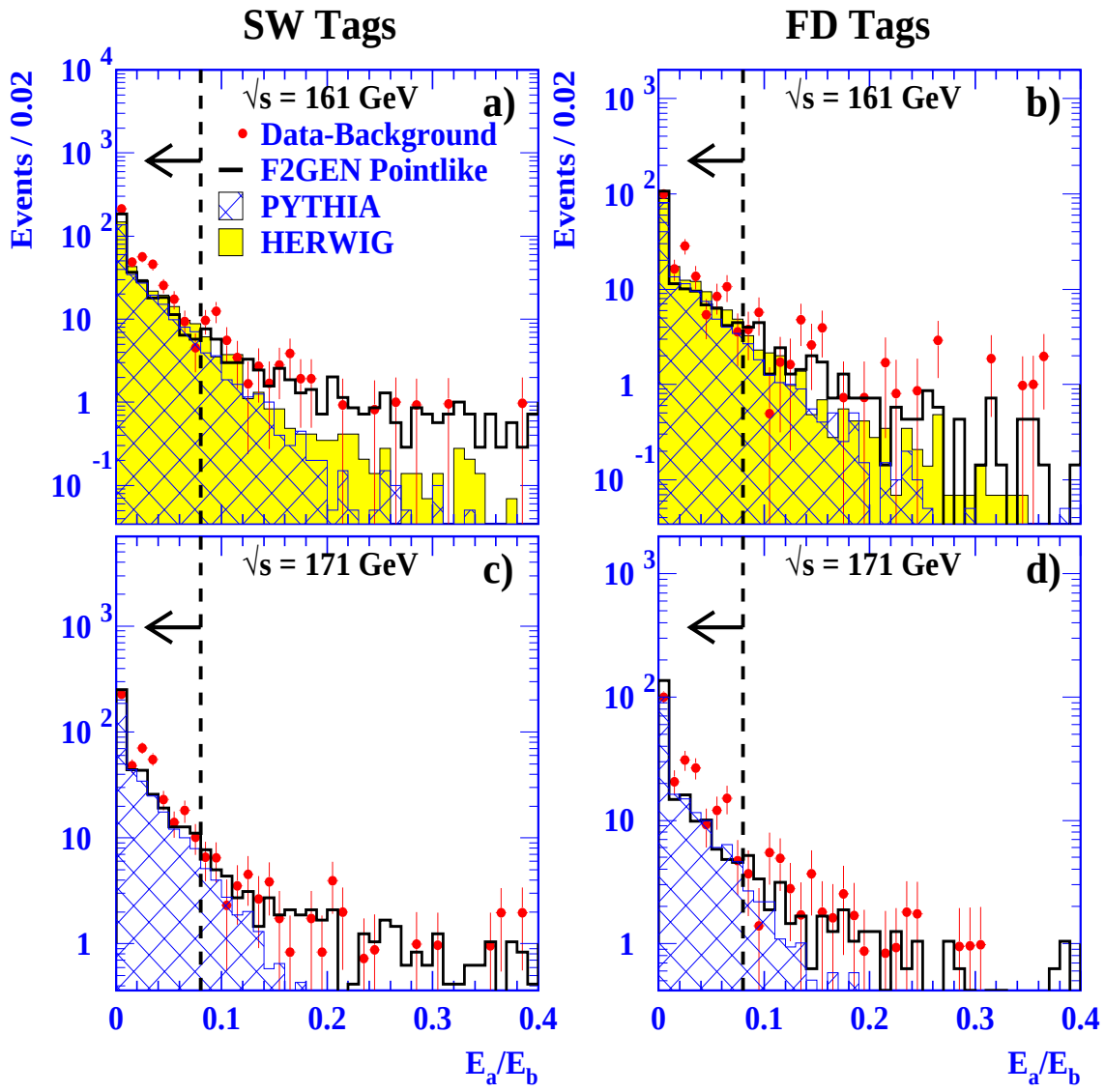

Figure 5.8: The E_a/E_b distributions of the LEP2 data and Monte Carlo samples for tags found in the a) & c) SW and b) & d) FD calorimeters. The data distributions (dots) are shown with background subtracted whilst the distributions for HERWIG (shaded), PYTHIA (hatched) and F2GEN (open) are plotted normalised to the same luminosity as the data. All cuts have been applied except those made on the ratio E_a/E_b (see section 4.3) and these cuts are shown as dashed lines. The arrows indicate the region where the events pass the selection cut. The errors on the data points are statistical only.

5.5 Transverse Momentum Distributions

The transverse momentum variables, $p_{t,bal}$ and $p_{t,out}$, are defined in section 4.3.1 and represent components of the vector sum of the transverse momentum of the event in the tag–beam plane and out of the tag–beam plane respectively. The distributions of $p_{t,bal}$ are shown in Fig. 5.9 and Fig. 5.10 and the distributions of $p_{t,out}$ are shown in Fig. 5.11 and Fig. 5.12. The Monte Carlo distributions are normalised to the corresponding data luminosity.

Taking into account the differences in the cross–sections, the Monte Carlo distributions for both $p_{t,bal}$ and $p_{t,out}$ agree well with the data distributions, of which the F2GEN samples show the best agreement. All of the transverse momentum plots show that both $p_{t,bal}$ and $p_{t,out}$ peak at zero and decrease with increasing transverse momentum component. This suggests that the models for the hadronic final state used in the various Monte Carlo generators balance the transverse momentum of the hadronic final states well and are consistent with the data.

5.6 Charged Track Multiplicity

The definition of a good quality charged track is described in sections 4.1.1 and 4.2.2. The track multiplicity of an event is the number of good quality charged tracks found. Fig. 5.13 and Fig. 5.14 show the track multiplicity, N_{tracks}, distributions. The Monte Carlo distributions are normalised to the corresponding data luminosity.

The selection criteria of at least three good charged tracks is made to confine the analysis to where the Monte Carlo distributions of N_{tracks}, are in reasonable agreement with the data and to get rid of low multiplicity backgrounds such as leptonic two–photon events where either a $\mu^+\mu^-$ pair or an e^+e^- pair is formed in the final state. These low multiplicity events account for the discrepancies between the data and Monte Carlo distributions in the $N_{tracks} = 2$ bin.

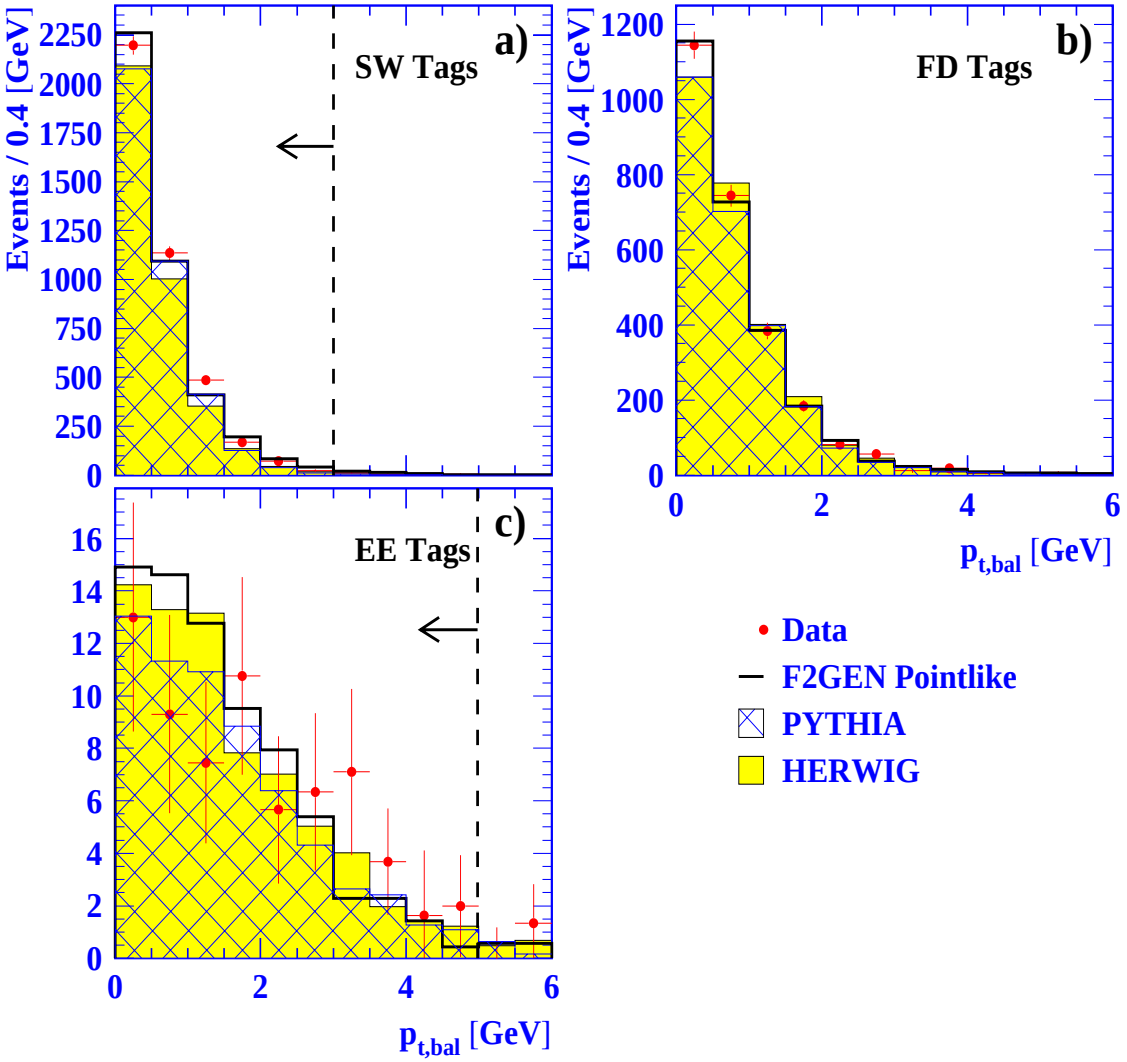

Figure 5.9: The distributions of transverse momentum balance in the tag–beam plane, $p_{t,bal}$, for the LEP1 data and Monte Carlo samples for tags found in the a) SW, b) FD and c) EE calorimeters. The data distributions (dots) are shown with background subtracted whilst the distributions for HERWIG (shaded), PYTHIA (hatched) and F2GEN (open) are plotted normalised to the same luminosity as the data. All cuts have been applied except those made on $p_{t,bal}$ (see section 4.3) and these cuts are shown as dashed lines. The errors on the data points are statistical only.

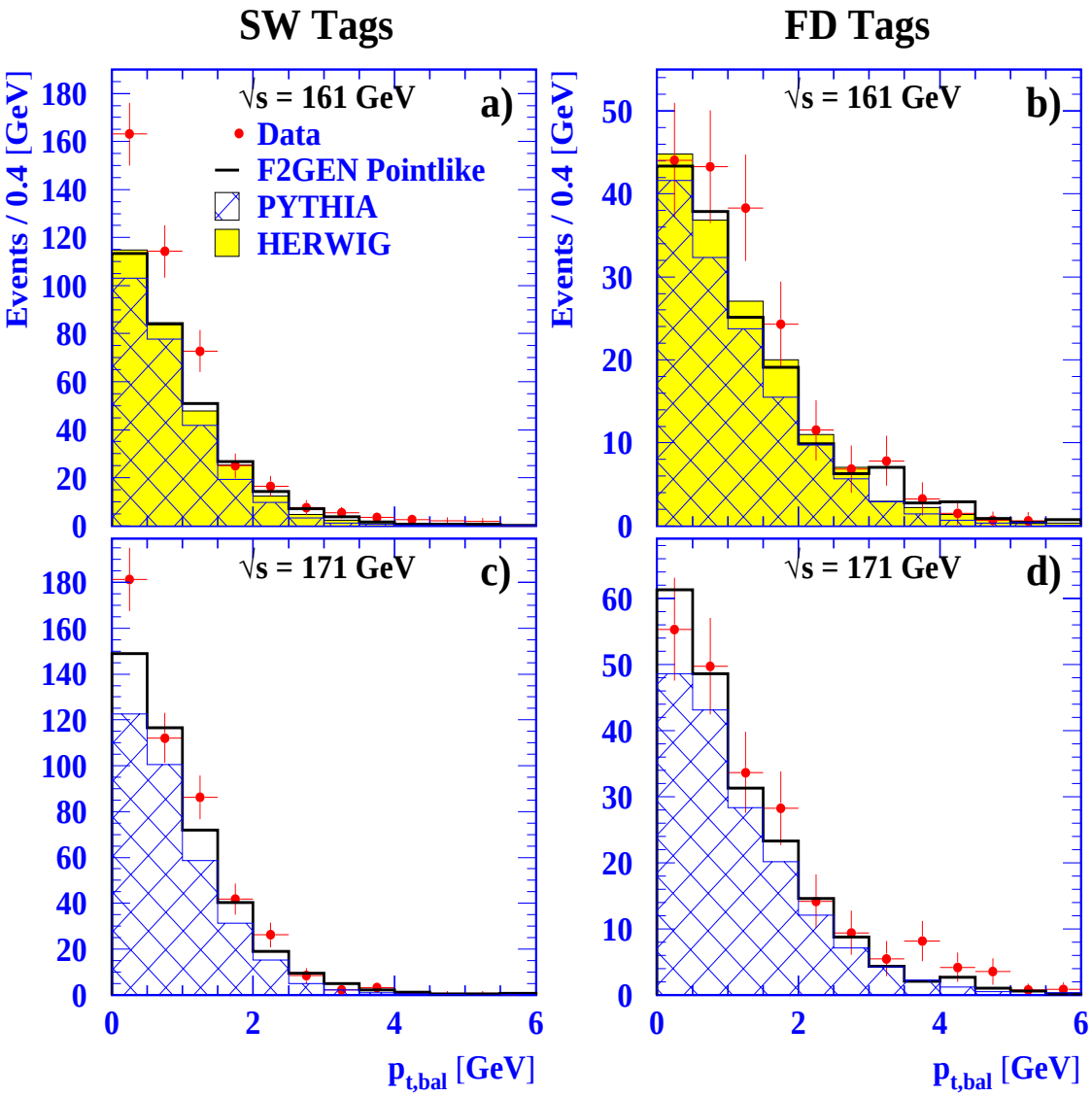

Figure 5.10: The distributions of transverse momentum balance in the tag–beam plane, $p_{t,bal}$, for the LEP2 data and Monte Carlo samples for tags found in the a) & c) SW and b) & d) FD calorimeters. The data distributions (dots) are shown with background subtracted whilst the distributions for HERWIG (shaded), PYTHIA (hatched) and F2GEN (open) are plotted normalised to the same luminosity as the data. All cuts have been applied except those made on $p_{t,bal}$ (see section 4.3) and these cuts are shown as dashed lines. The errors on the data points are statistical only.

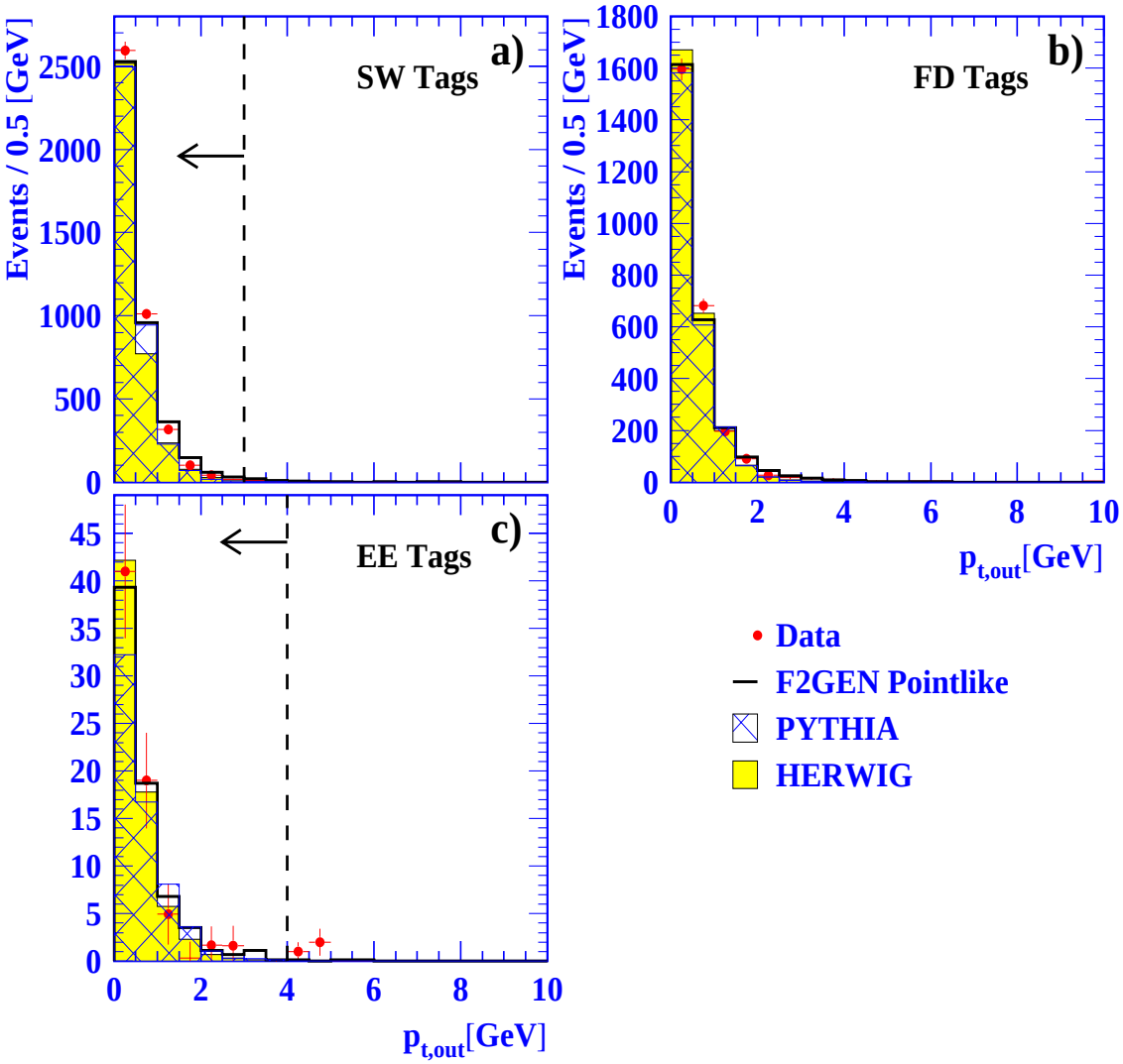

Figure 5.11: The distributions of transverse momentum out of the tag–beam plane, $p_{t,out}$, for the LEP1 data and Monte Carlo samples for tags found in the a) SW, b) FD and c) EE calorimeters. The data distributions (dots) are shown with background subtracted whilst the distributions for HERWIG (shaded), PYTHIA (hatched) and F2GEN (open) are plotted normalised to the same luminosity as the data. All cuts have been applied except those made on $p_{t,out}$ (see section 4.3) and these cuts are shown as dashed lines. The errors on the data points are statistical only.

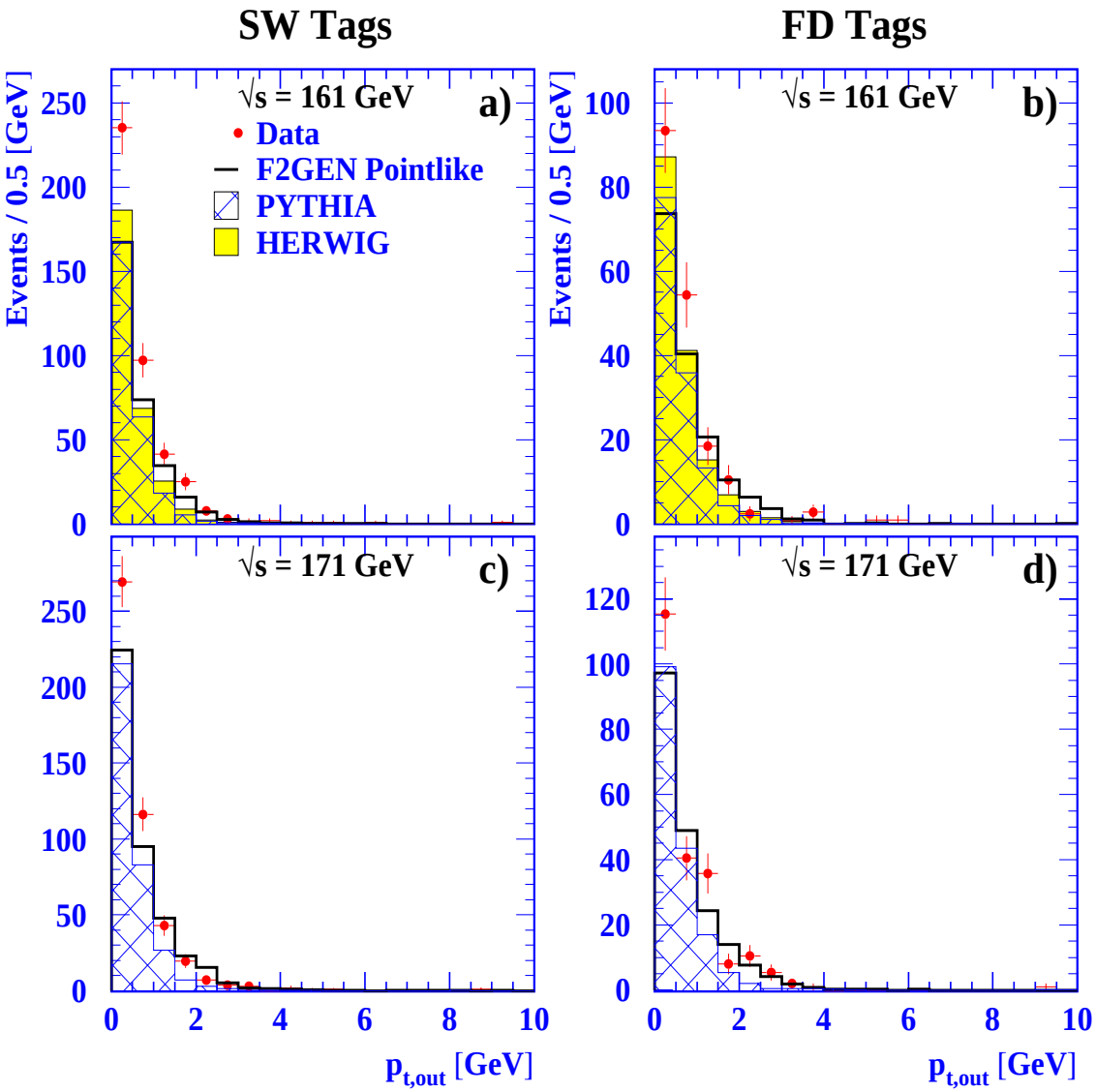

Figure 5.12: The distributions of transverse momentum out of the tag–beam plane, $p_{t,out}$, for the LEP2 data and Monte Carlo samples for tags found in the a) & c) SW and b) & d) FD calorimeters. The data distributions (dots) are shown with background subtracted whilst the distributions for HERWIG (shaded), PYTHIA (hatched) and F2GEN (open) are plotted normalised to the same luminosity as the data. All cuts have been applied except those made on $p_{t,out}$ (see section 4.3) and these cuts are shown as dashed lines. The errors on the data points are statistical only.

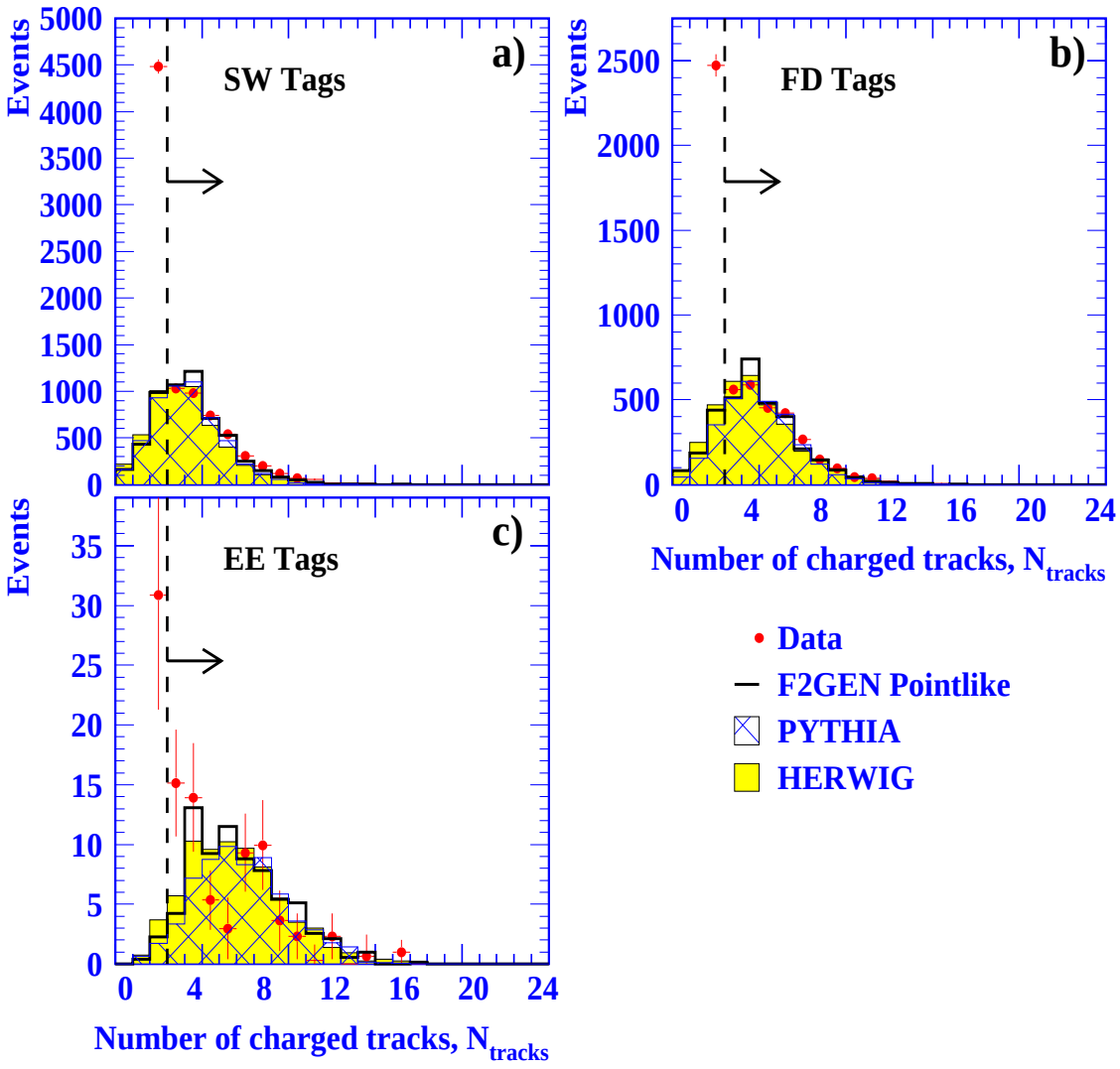

Figure 5.13: The charged track multiplicity, N_{tracks}, for the LEP1 data and Monte Carlo samples for tags found in the a) SW, b) FD and c) EE calorimeters. The data distributions (dots) are shown with background subtracted whilst the distributions for HERWIG (shaded), PYTHIA (hatched) and F2GEN (open) are plotted normalised to the same luminosity as the data. All cuts have been applied except those made on N_{tracks} (see section 4.3) and these cuts are shown as dashed lines. The errors on the data points are statistical only.

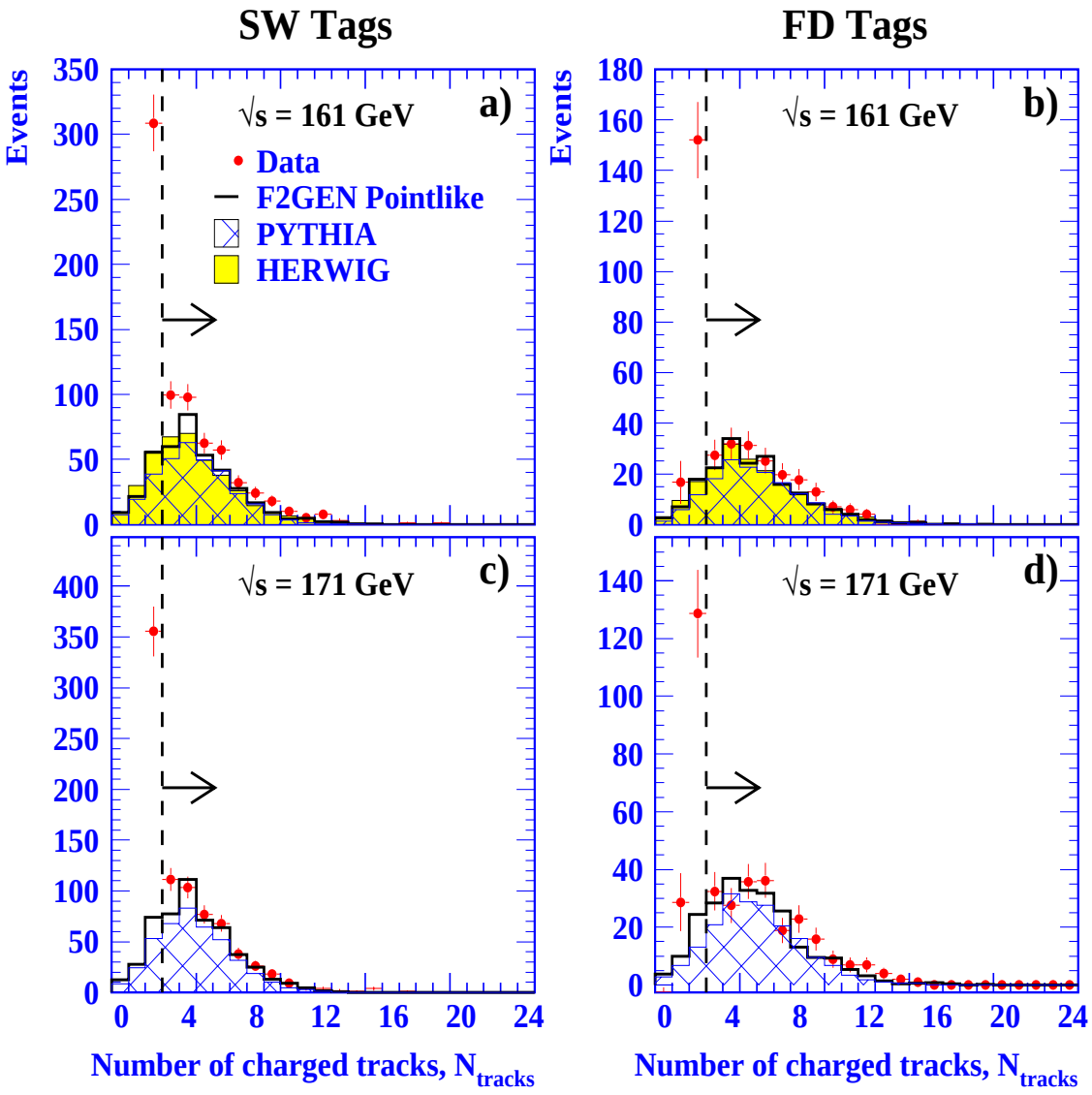

Figure 5.14: The charged track multiplicity, N_{tracks}, for the LEP2 data and Monte Carlo samples for tags found in the a) & c) SW and b) & d) FD calorimeters. The data distributions (dots) are shown with background subtracted whilst the distributions for HERWIG (shaded), PYTHIA (hatched) and F2GEN (open) are plotted normalised to the same luminosity as the data. All cuts have been applied except those made on N_{tracks} (see section 4.3) and these cuts are shown as dashed lines. The errors on the data points are statistical only.

5.7 $W_{\rm vis}$ and $x_{\rm vis}$ Distributions

The variables $W_{\rm vis}$ and $x_{\rm vis}$ are defined in section 4.3.1. The distributions of $W_{\rm vis}$ and $x_{\rm vis}$ (Fig.5.15 to Fig.5.18) are measurements approximating the true distributions for W and x needed to determine $F_2^\gamma(x)$. The Monte Carlo distributions are normalised to the data luminosity.

The Monte Carlo distributions for $W_{\rm vis}$ are in reasonable agreement with the data allowing for the disagreement in the cross–sections (see section 5.3). In the region below the low $W_{\rm vis}$ cut, the data lies well above the predictions of the Monte Carlo generators. This lies in the resonance region of phase space for hadron production and is not modelled for the samples from the three generators.

Given the discrepancies in the cross–sections, the data distributions are reasonably well produced by the Monte Carlo distributions in the mid-range $x_{\rm vis}$. The main differences between data and Monte Carlo distributions occur for $x_{\rm vis} < 0.2$ in all samples and for $x_{\rm vis} > 0.7$ in the EE tag samples. This corresponds to the regions in x where unfoldings of $F_2^\gamma(x, Q^2)$ have produced large systematic errors [2, 3, 4, 5]. The different ways of modelling the hadronic final state clearly give rise to important differences in the predicted distributions from the three Monte Carlo generators. This can be seen between HERWIG and F2GEN samples which were generated with the GRV (LO) parameterisation for $F_2^\gamma(x, Q^2)$. The F2GEN samples contain more events in the range $x < 0.2$ than the HERWIG samples, whilst the converse is true for the high range $x > 0.7$.

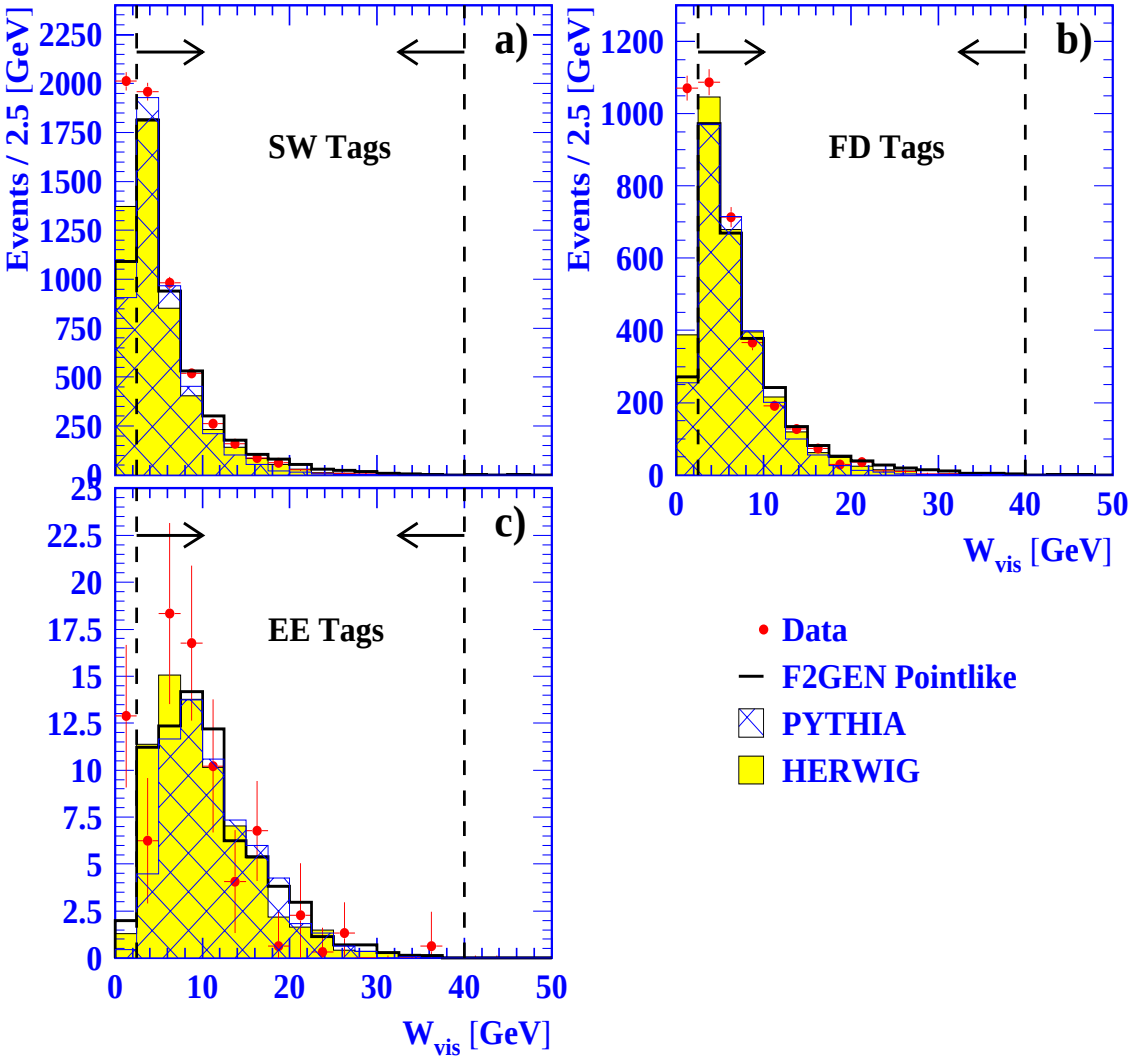

Figure 5.15: The distributions of the measured invariant mass of the hadronic final state $W_{\rm vis}$ for the LEP1 data and Monte Carlo samples for tags found in the a) SW, b) FD and c) EE calorimeters. The data distributions (dots) are shown with background subtracted whilst the distributions for HERWIG (shaded), PYTHIA (hatched) and F2GEN (open) are plotted normalised to the same luminosity as the data. All cuts have been applied except those made on $W_{\rm vis}$ (see section 4.3) and these cuts are shown as dashed lines. The arrows indicate the region where the events pass the selection cut. The errors on the data points are statistical only.

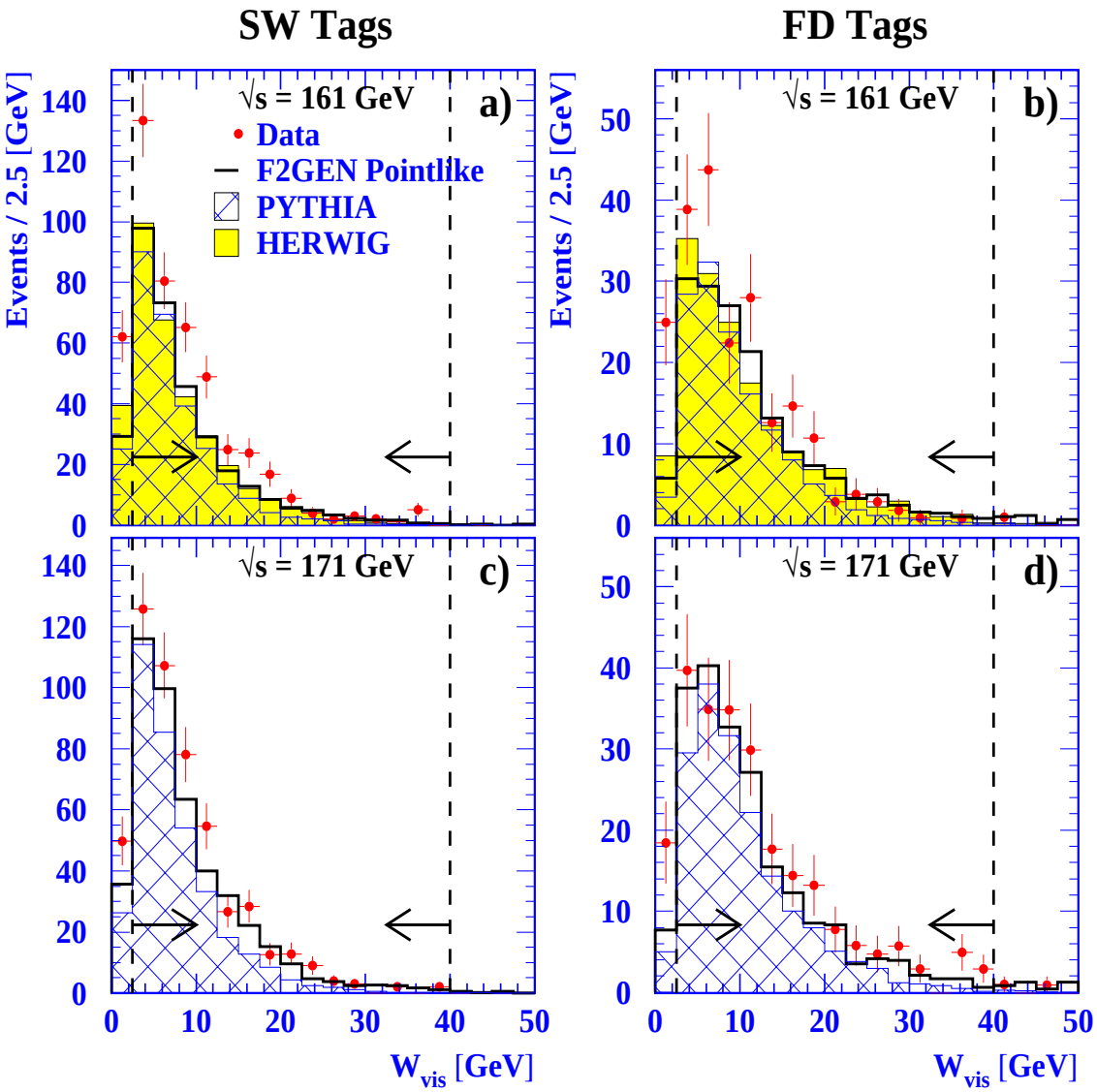

Figure 5.16: The distributions of the measured invariant mass of the hadronic final state $W_{\rm vis}$ for the LEP2 data and Monte Carlo samples for tags found in the a) & c) SW and b) & d) FD calorimeters. The data distributions (dots) are shown with background subtracted whilst the distributions for HERWIG (shaded), PYTHIA (hatched) and F2GEN (open) are plotted normalised to the same luminosity as the data. All cuts have been applied except those made on $W_{\rm vis}$ (see section 4.3) and these cuts are shown as dashed lines. The arrows indicate the region where the events pass the selection cut. The errors on the data points are statistical only.

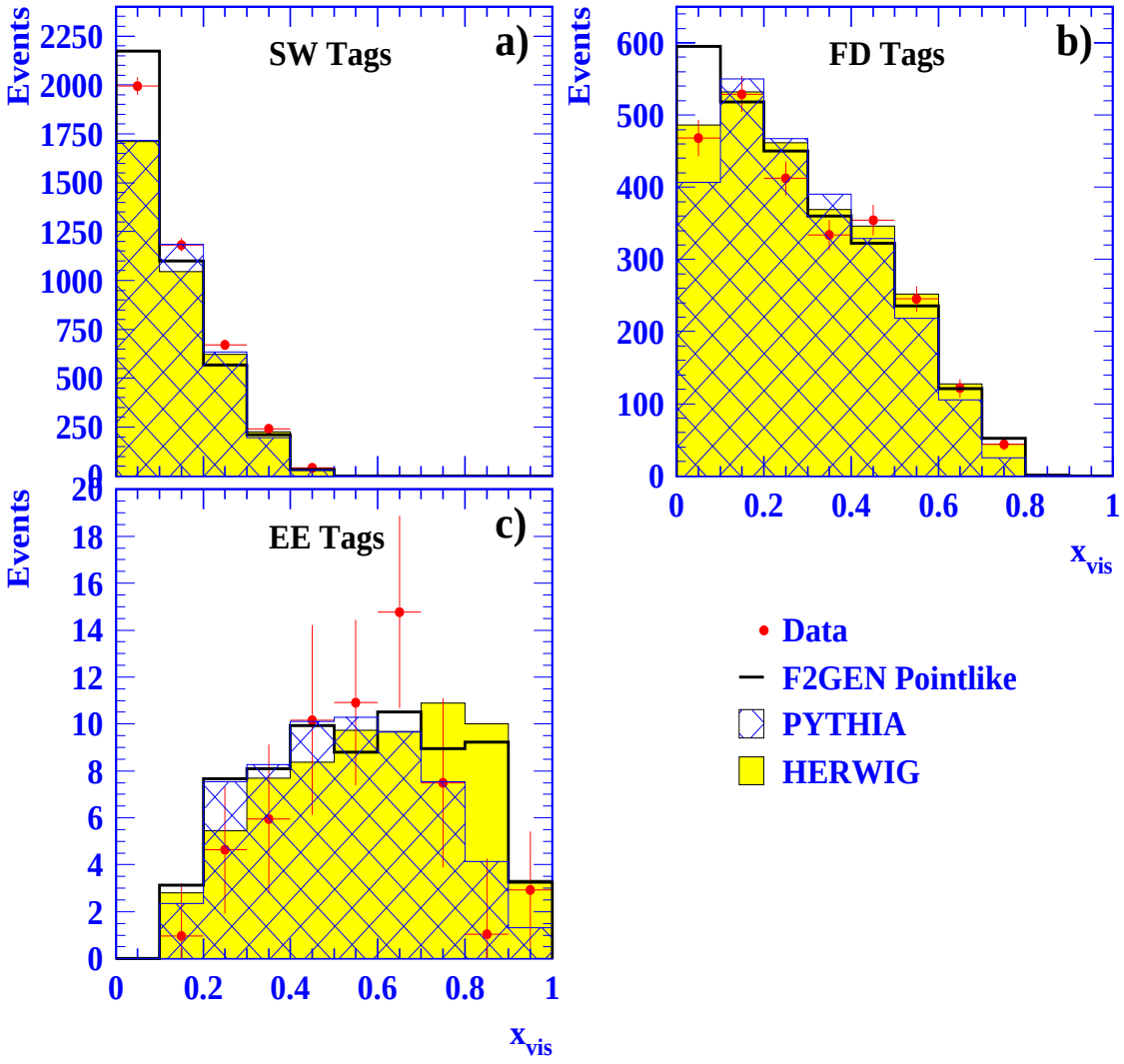

Figure 5.17: The distributions of $x_{\rm vis}$ for the LEP1 data and Monte Carlo samples for tags found in the a) SW, b) FD and c) EE calorimeters. The data distributions (dots) are shown with background subtracted whilst the distributions for HERWIG (shaded), PYTHIA (hatched) and F2GEN (open) are plotted normalised to the same luminosity as the data. All cuts have been applied. The errors on the data points are statistical only.

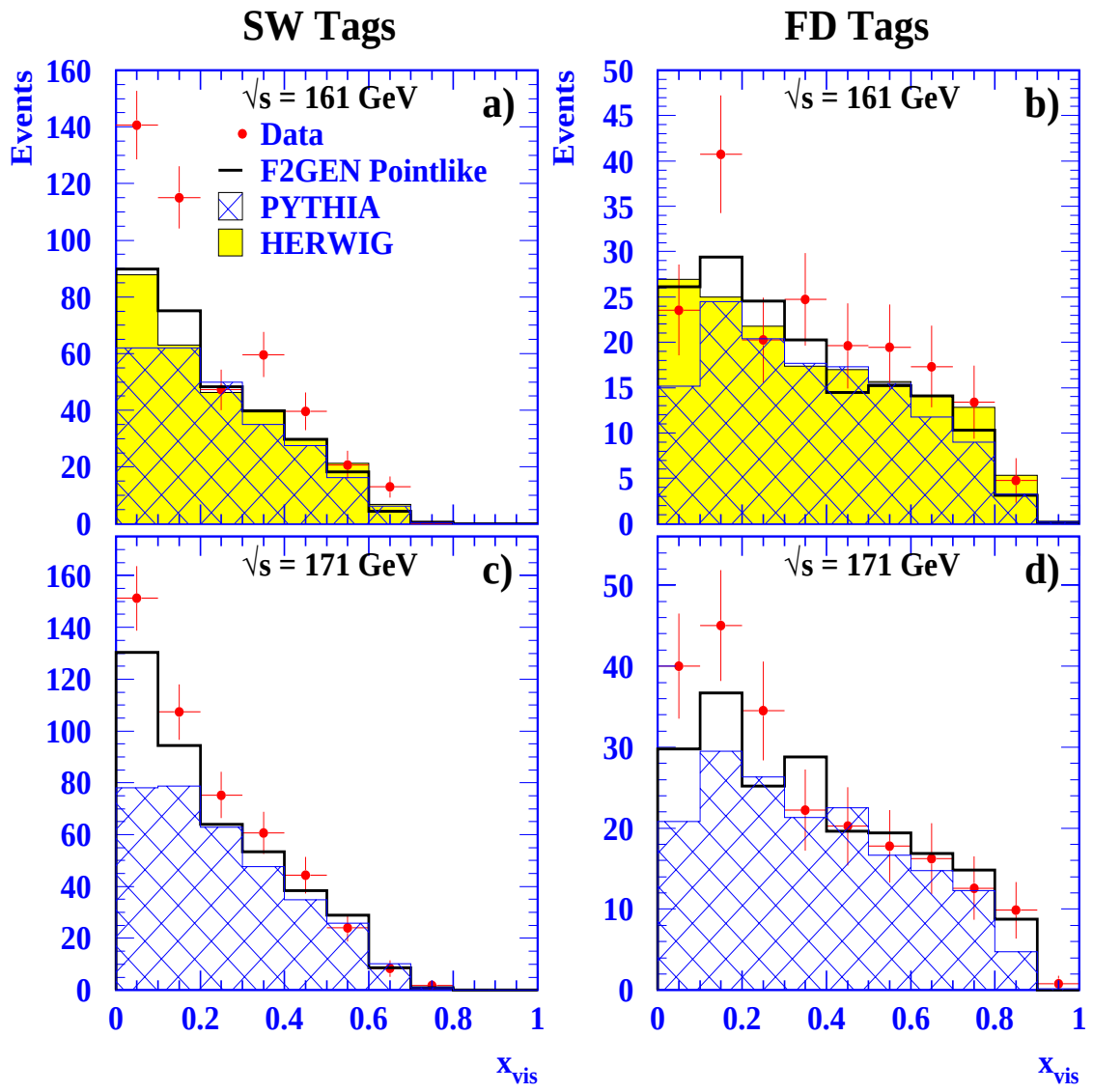

Figure 5.18: The distributions of $x_{\rm vis}$ for the LEP2 data and Monte Carlo samples for tags found in the a) & c) SW and b) & d) FD calorimeters. The data distributions (dots) are shown with background subtracted whilst the distributions for HERWIG (shaded), PYTHIA (hatched) and F2GEN (open) are plotted normalised to the same luminosity as the data. All cuts have been applied. The errors on the data points are statistical only.

Chapter 6

Energy flows and Jet Finding

Motivated by the discrepancies shown in previous OPAL studies [3, 4, 5, 15], Monte Carlo distributions of hadronic energy flow and energy transverse to the plane formed by the tag direction and the beam axis are compared with data distributions. Multiplicities of jets found in each sample using the cone algorithm are compared and used to form subsamples of events with 0 jets, 1 jet and 2 jets found. Further comparisons are made for the subsample hadronic energy flow and transverse energy distributions.

In chapter 5, distributions for the three Monte Carlo generators were compared with three data samples at LEP1 and four data samples at LEP2. In this chapter, the data samples are divided into seven regions of Q^2 with five samples at LEP1 and two at LEP2. At LEP1, the same sample of events with tags found in the EE calorimeters is used whilst each of the SW and FD tag samples is split into two equally–sized subsamples using a division in tag angle at $\theta_{\rm tag} = 40$ milliradians and $\theta_{\rm tag} = 78$ milliradians respectively. At LEP2, the two data samples are formed by combining into one sample each of the data samples with tags found in the SW calorimeters at the two different $\sqrt{s}$, and similarly by combining each of the two FD tag samples.

6.1 The Hadronic Final State Distributions

In [3], two distributions were found to be sensitive to differences between the observed and modelled hadronic final states:

1. the average hadronic energy flow per event as a function of pseudorapidity, where $\eta = -\ln\tan\frac{\theta'}{2}$ and θ' is the polar angle relative to the beam axis recalculated for all hadrons in the event such that the tagged electron is always at $\eta < 0$;

2. the transverse energy, $E_{\mathrm{t,out}}$, out of the tag–beam plane where

$$E_{\mathrm{t,out}} = \sum_{i}^{particles} E_i |\sin\lambda_i|. \tag{6.1}$$

and λ_i is the angle between the particle and the plane formed by the beam axis and the tag direction.

6.1.1 Hadronic Energy Flow

Fig. 6.1 shows the average energy flow per event as a function of pseudorapidity for each of the five LEP1 data samples and the two LEP2 data samples and compared with the samples from the F2GEN pointlike, HERWIG and PYTHIA generators. For a sample of N events, the average energy flow per pseudorapidity bin $d\eta$ is $1/N\ dE/d\eta$, where E is the sum of the energies of all the particles in that bin. The tagged electron was not included in the plots but was defined to be at negative η. The errors on the data points are the average energy per particle in a bin multiplied by the square root of the number of particles in that bin divided by the number of sample events.

As has already been reported [4, 3], none of the available models gives a good representation of the hadronic energy flow. In Fig. 6.1, the data distributions lie below the F2GEN prediction and above the HERWIG and PYTHIA predictions for the energy flow into the region of pseudorapidity $0.0 < \eta < 1.8$ except at $\langle Q^2\rangle = 124$ GeV^2. These differences are particularly marked for $\langle Q^2\rangle = 8.9$ and 17.3 GeV^2. Plots a)–d)

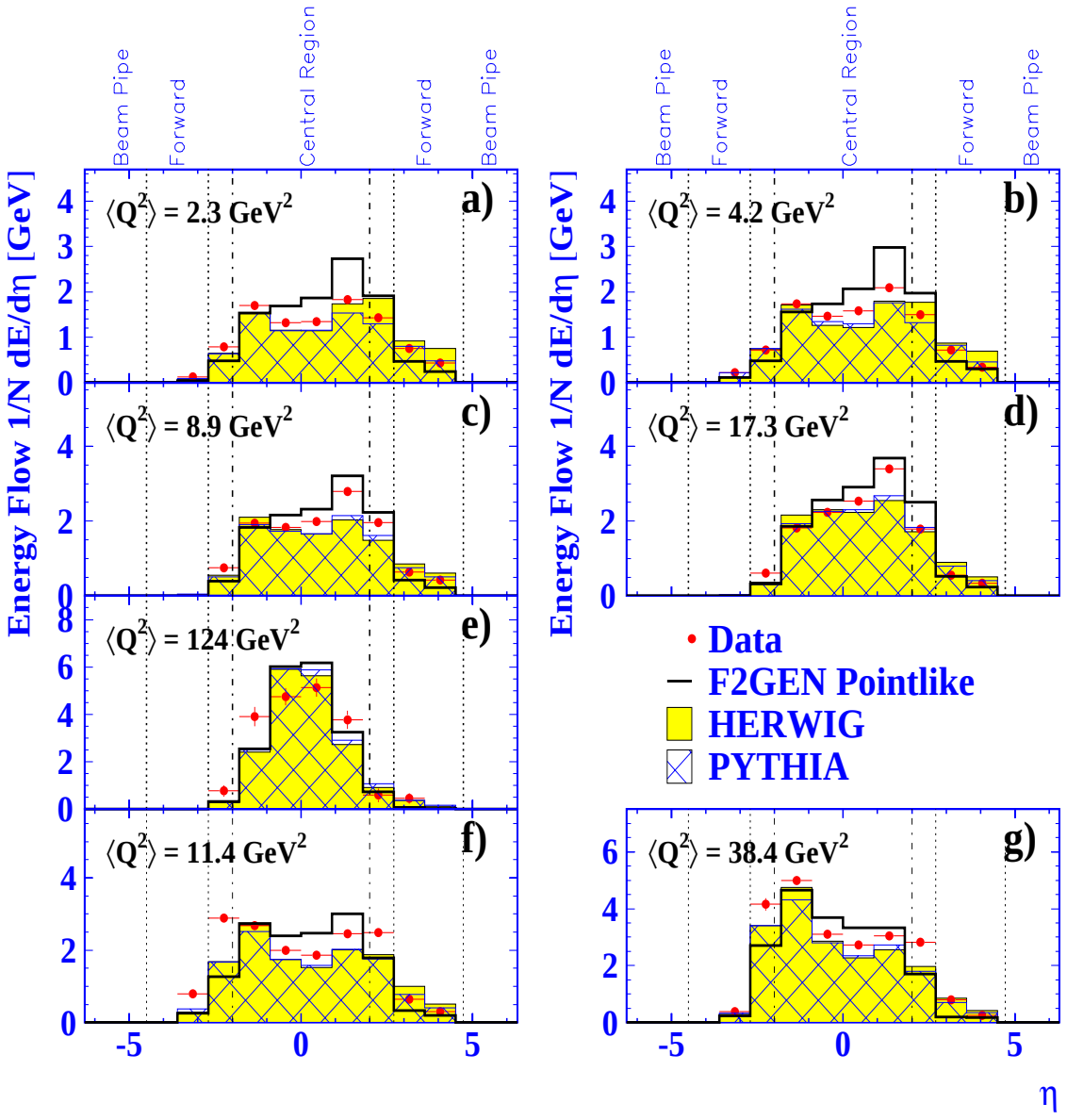

Figure 6.1: The average hadronic energy flow per event in bins of pseudorapidity $\eta = -\ln\tan\theta'/2$. The polar angle, θ', is recalculated for all hadrons relative to the beam axis, such that the tagged electron is always at $\eta < 0$. Plots a) to e) show the distributions for LEP1 data samples and plots f) and g) show the distributions for the LEP2 data samples. The dots represent the data with the estimated background subtracted, whilst the histograms show the corresponding distributions for HERWIG (shaded), PYTHIA (hatched) and F2GEN (open) Monte Carlo samples. The errors shown are statistical only.

show also that the predictions of HERWIG and PYTHIA for this region worsen with increasing $\langle Q^2 \rangle$ whilst the corresponding bins from the F2GEN generator approach the data.

The other major trend shown in these distributions is in the forward region $2.7 < \eta < 4.5$ where both HERWIG and PYTHIA tend to overestimate the amount of energy flow whilst conversely F2GEN tends to underestimate the hadronic energy flow. Plots a)–d) of Fig. 6.1 show that the energy flow into these bins from the F2GEN samples approaches the data points with increasing $\langle Q^2 \rangle$. This is an important area of the distributions as only about 42% of the hadronic energy flow into this forward region is actually measured. This effect is largest at low x (high W) and thus contribute to the large systematic errors at low x in unfoldings of $F_2^\gamma(x, Q^2)$.

6.1.2 Energy Transverse to the Tag–Plane, $E_{\mathrm{t,out}}$

Fig. 6.2 shows the number of events in each data sample as a function of the energy, $E_{\mathrm{t,out}}$, out of the tag–beam plane. The Monte Carlo distributions are normalised to the integrated luminosity of the corresponding data sample.

The disagreements between data and Monte Carlo distributions are clearest at high values of $E_{\mathrm{t,out}}$ except for $\langle Q^2 \rangle = 124$ GeV^2 where the distributions are in agreement within statistical errors. These disagreements begin at $E_{\mathrm{t,out}} \sim 5$ GeV for $\langle Q^2 \rangle = 2.4$ GeV^2 increasing to $E_{\mathrm{t,out}} \sim 8$ GeV for $\langle Q^2 \rangle = 38.4$ GeV^2. The PYTHIA generator does not populate the high regions of $E_{\mathrm{t,out}}$ with the effect worst at lowest $\langle Q^2 \rangle$ and improving inadequately with increasing Q^2. In contrast, the F2GEN generator overestimates the number of events at high $E_{\mathrm{t,out}}$ especially in the lowest $\langle Q^2 \rangle$ sample, with the size of the disagreement decreasing with increasing Q^2 to $\langle Q^2 \rangle = 38.4$ and 124 GeV^2 sample where the differences between the data and F2GEN distributions are small. The HERWIG generator provides the closest prediction to the measured distributions although it underpopulates the high $E_{\mathrm{t,out}}$ region for most $\langle Q^2 \rangle$ samples.

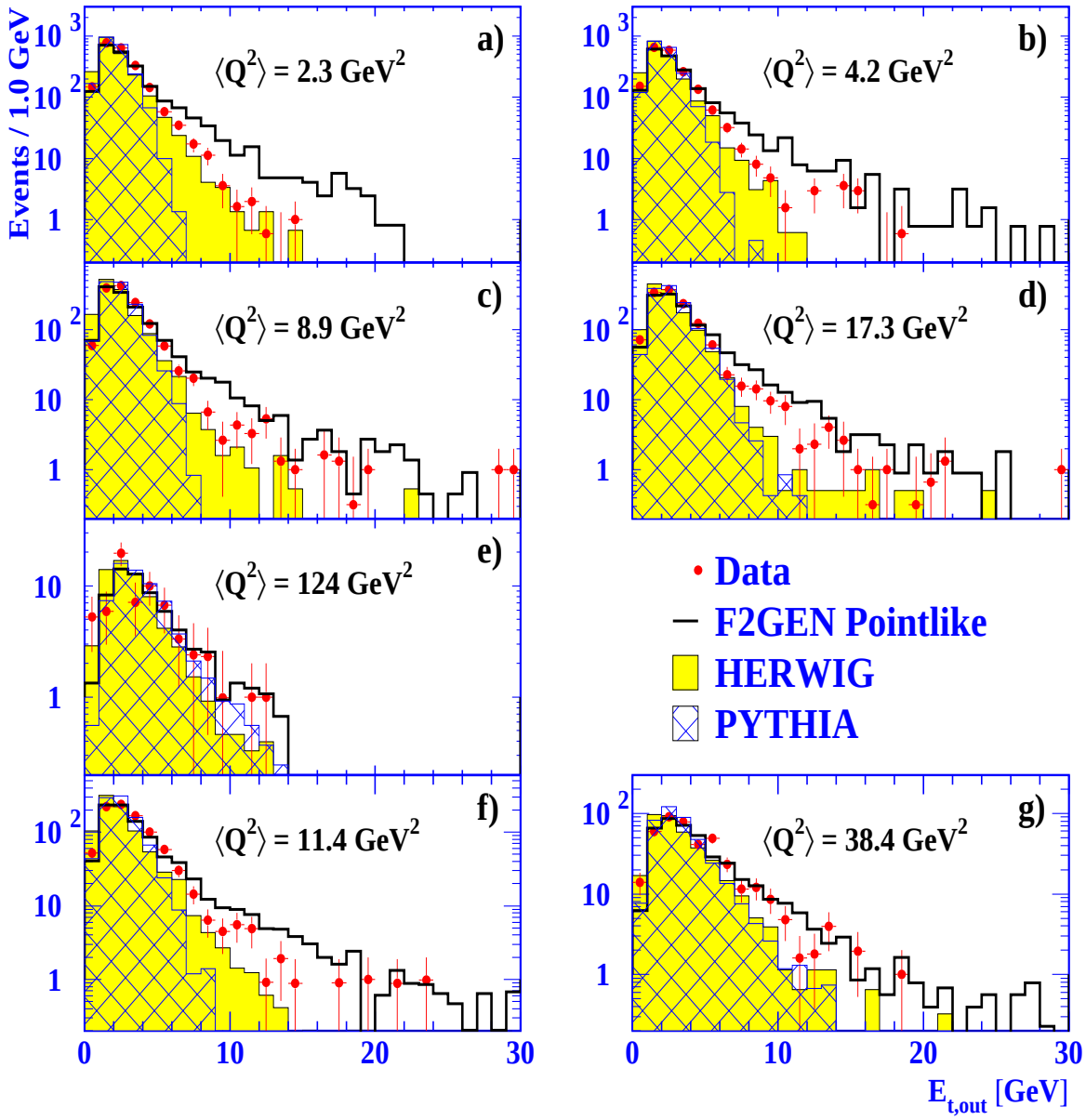

Figure 6.2: The energy, $E_{\mathrm{t,out}}$, out of the plane formed by the tagged electron and the beams. The estimated background has been subtracted from the data distributions (dots) whilst the Monte Carlo distributions for HERWIG (shaded), PYTHIA (hatched) and F2GEN (open) are shown normalised to the data luminosity. The errors shown are statistical only.

6.2 The Cone Jet Finding Algorithm

The same cone jet finding algorithm [13] is used to analyse the hadronic final state of singly–tagged two–photon events as was used to study the hadrons in untagged and singly–tagged two–photon events [15, 16, 94, 95]. A jet is defined as a set of particles contained in a cone with half–angle R (see Fig. 6.3),

$$R = \sqrt{(\Delta\eta)^2 + (\Delta\phi)^2}, \tag{6.2}$$

and where the cone axis is defined by the direction of the momentum sum of the constituent particles. $\Delta\eta$ and $\Delta\phi$ are the differences in the pseudorapidity and the azimuthal angle between the cone axis and the particle direction. A particle is defined in this analysis to be an object whose four–momenta is an output of the MT package described in section 4.2.4, with all final state particles, excluding the tagged electron, input to the algorithm.

The i^{th} particle's values of η_{i}, ϕ_{i}, and transverse energy, $E_{\text{T}_{\text{i}}} = E_{\text{i}}|\sin\theta_{\text{i}}|$, relative to the e^+e^- beam–beam axis are used to define an initial axis and transverse energy for making a jet candidate. The candidate is constructed by iterating over the particles contained inside a cone of size $R = 1$ about the initial axis to form a new transverse energy and jet axis at each iteration:

$$\begin{aligned}
\eta^{\text{jet}}_{\text{new}} &= \eta^{\text{jet}}_{\text{old}} + \frac{E_{\text{T}_{\text{i}}}(\eta_{\text{i}} - \eta^{\text{jet}}_{\text{old}})}{E_{\text{T}_{\text{i}}} + E^{\text{jet}}_{\text{T}_{\text{old}}}} \\
\phi^{\text{jet}}_{\text{new}} &= \phi^{\text{jet}}_{\text{old}} + \frac{E_{\text{T}_{\text{i}}}(\phi_{\text{i}} - \phi^{\text{jet}}_{\text{old}})}{E_{\text{T}_{\text{i}}} + E^{\text{jet}}_{\text{T}_{\text{old}}}} \\
E^{\text{jet}}_{\text{T}_{\text{new}}} &= E_{\text{T}_{\text{i}}} + E^{\text{jet}}_{\text{T}_{\text{old}}}
\end{aligned} \tag{6.3}$$

Two candidate jets are combined if their axes lie within a cone of size R of each other. Any particle assigned to more than one jet is placed in the closest one in η and ϕ, and its contribution to the η^{jet}, ϕ^{jet} and transverse energy of the other jet(s) is removed. Jets are accepted by requiring a minimum transverse energy $E^{\text{jet}}_{\text{T}} = 3.0$ GeV and requiring the pseudorapidity of the jet to be within the central tracking detectors, $|\eta^{jet}| < 2$. These are the same cuts as are used in [15, 16, 95].

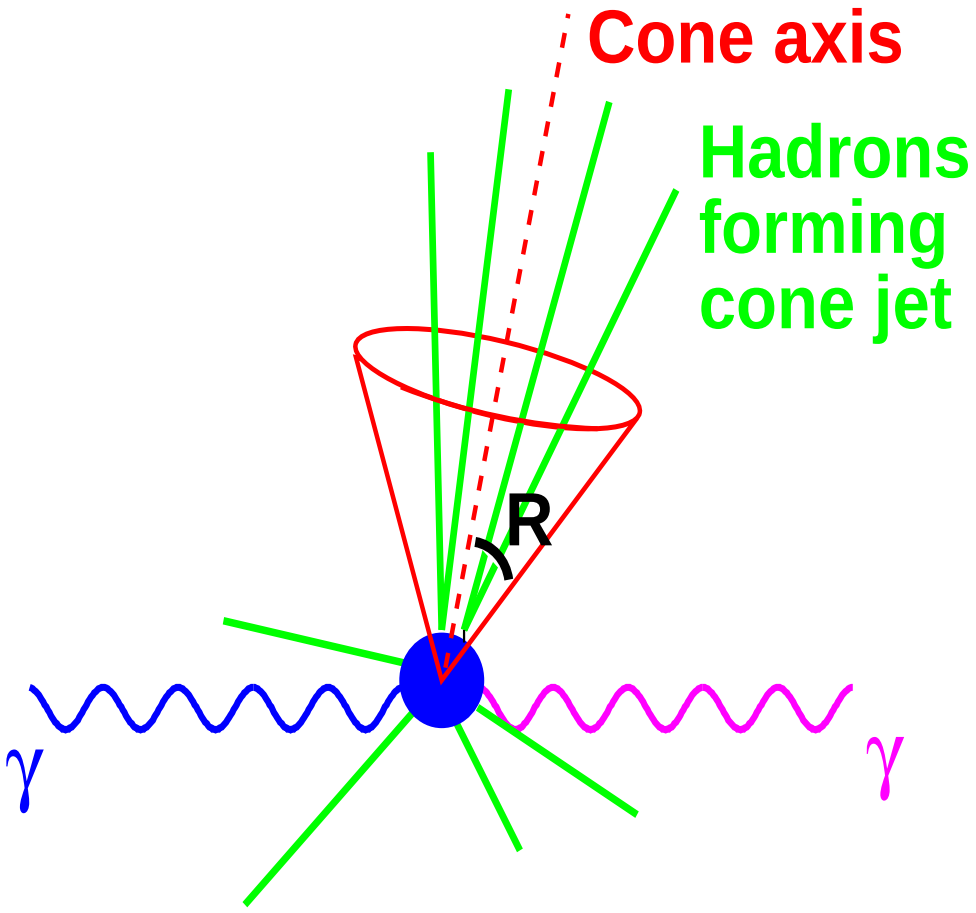

Figure 6.3: A schematic diagram of a cone jet of hadrons formed in the interaction between two photons. The cone jet axis is parallel to direction of the momentum sum of the jet constituents. The size of the cone is defined by the half angle R

6.3 Jet Multiplicities

Fig. 6.4 shows the fraction N_i/N of events in the total sample, N, with $i = 0 - 3$ jets. The estimated background has been subtracted from the data. Fig. 6.5 shows explicitly how these fractions vary with $\langle Q^2 \rangle$ for the subsamples of events with a) 0 jets, b) 1 jet and c) 2 jets found. Tables 6.1 and 6.2 show the number of events in each data and Monte Carlo sample at LEP1 and LEP2 respectively, as well as the number of events with 0, 1 and 2 jets found for each sample. The Monte Carlo samples have been normalised to the same luminosity as the data and the numbers of events with $\geqslant 3$ jets found for each sample are omitted from the tables as they comprise $< 1\%$ of any one sample.

Fig. 6.4 displays clearly the underestimation of number of events found with 2 jets, N_2, by the HERWIG and PYTHIA generators as well as the overestimation of N_2 by the F2GEN generator. Fig. 6.5c) explicitly shows that these differences between Monte Carlo predictions and data measurements are present over the full range of $\langle Q^2 \rangle$ samples, although the error bars on the $\langle Q^2 \rangle = 124$ GeV^2 are too large to exclude agreement of the Monte Carlo samples with the data samples.

Tables 6.1 and 6.2 show that HERWIG predicts $67 - 69\%$ fewer 2 jet events than are found in the data samples at $\langle Q^2 \rangle = 2.3$, 4.2, 8.9 (LEP1) and 11.4 GeV^2 (LEP2). This difference decreases to 31% in the highest Q^2 samples at LEP1 and LEP2. The corresponding predictions from the PYTHIA generator are even lower in the same four lower $\langle Q^2 \rangle$ samples. These predictions from PYTHIA improve relative to both the data and HERWIG samples with increasing $\langle Q^2 \rangle$. At the opposite extreme to PYTHIA, the predictions from F2GEN show considerably more 2 jet events, N_2, than found in the data or predicted in the other two Monte Carlo samples.

Fig. 6.4 and Table 6.1 also show that the number of 1 jet events, N_1 in the $\langle Q^2 \rangle = 2.3$ and 4.2 GeV^2 bins are underestimated by $> 36\%$ in the HERWIG samples and $> 28\%$ in the PYTHIA samples, whilst overestimated by 75% and 21% respectively in the F2GEN samples.

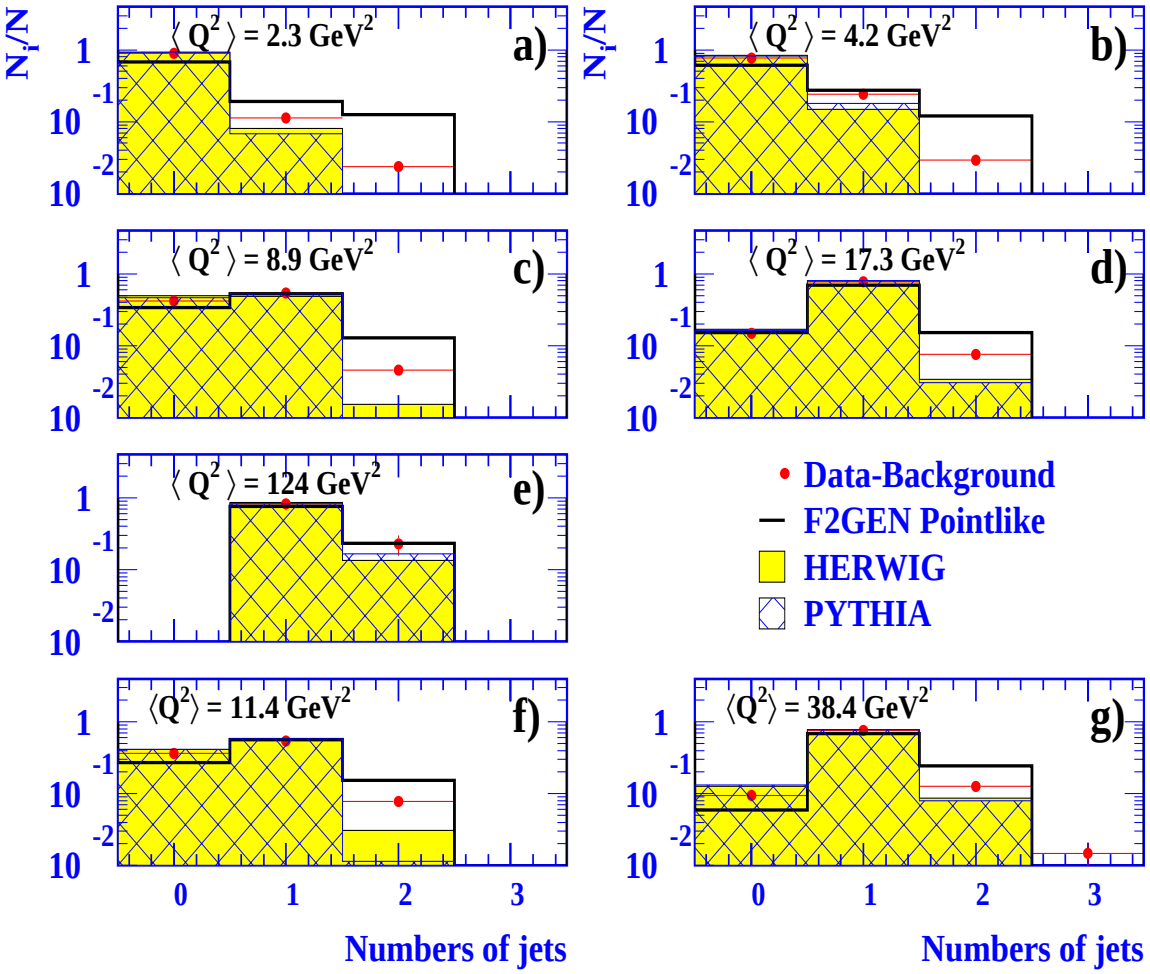

Figure 6.4: Fractions of events with 0–3 jets found for data and Monte Carlo samples using the measured four–momenta of the hadronic final state particles. The data distributions (dots) are plotted with background subtracted whilst the histograms represent the distributions for the HERWIG (shaded), PYTHIA (hatched) and F2GEN (open) Monte Carlo samples. The errors given are purely statistical.

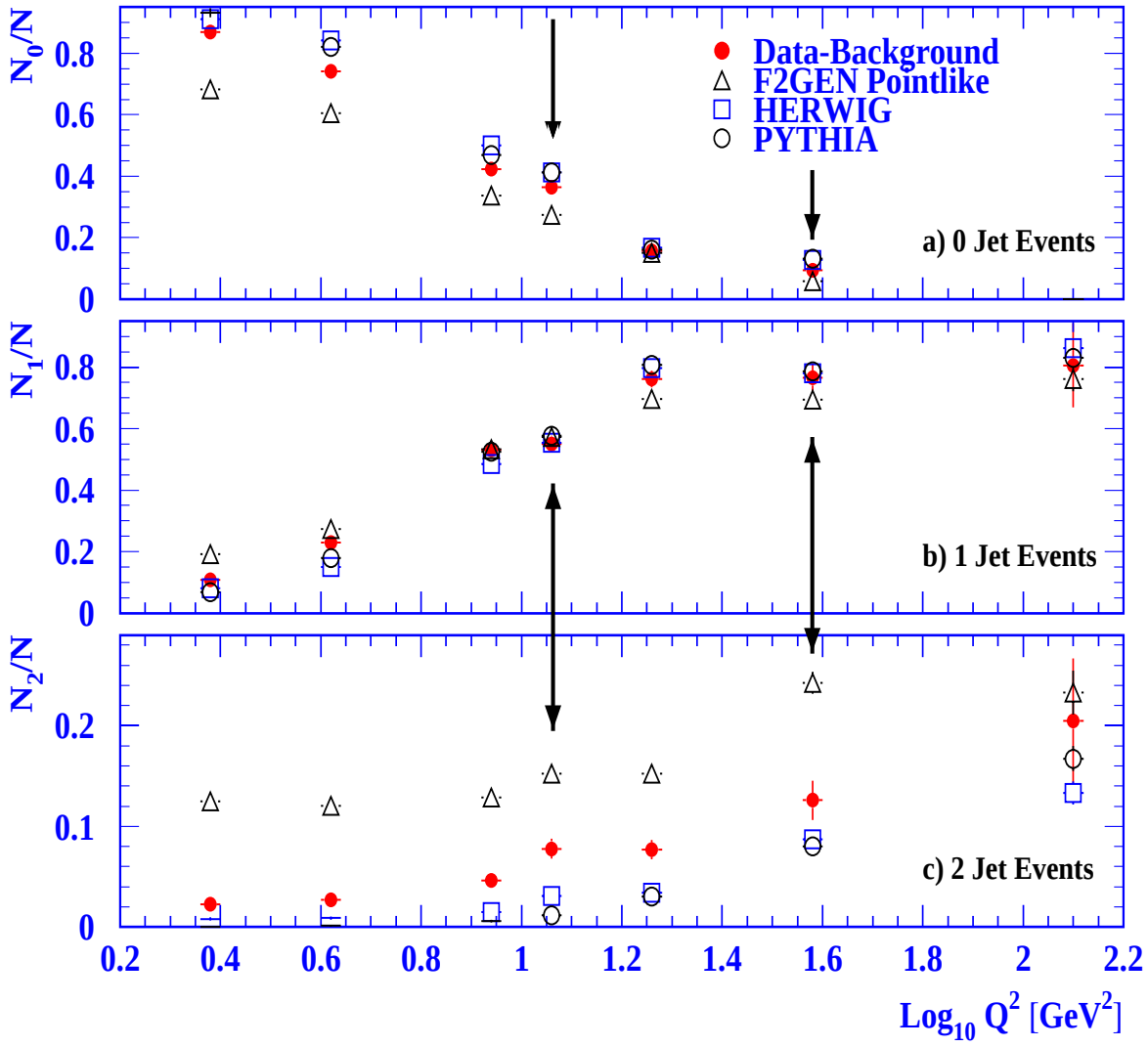

Figure 6.5: The Q^2 dependence of the fractions of events with 0–2 jets found for data and Monte Carlo samples using the measured four–momenta of the hadronic final state particles. The arrows denote the LEP2 samples.

Sample	All Events N	0 jet N_0	1 jet N_1	2 jet N_2
$\langle Q^2 \rangle = 2.3$ GeV^2				
Data	2233 ± 49	1940 ± 45	242 ± 17	50 ± 8
HERWIG	1847 ± 33	1683 ± 31	149 ± 9	15 ± 3
PYTHIA	2002 ± 29	1866 ± 28	136 ± 8	0.4 ± 0.4
F2GEN	2128 ± 41	1452 ± 34	410 ± 18	266 ± 15
$\langle Q^2 \rangle = 4.2$ GeV^2				
Data	1984 ± 47	1471 ± 40	455 ± 23	55 ± 9
HERWIG	1794 ± 32	1510 ± 31	268 ± 13	16 ± 3
PYTHIA	1756 ± 27	1440 ± 25	313 ± 11	3 ± 1
F2GEN	1956 ± 40	1185 ± 31	534 ± 21	235 ± 14
$\langle Q^2 \rangle = 8.9$ GeV^2				
Data	1373 ± 39	580 ± 26	729 ± 28	63 ± 9
HERWIG	1319 ± 26	659 ± 18	640 ± 18	20 ± 3
PYTHIA	1300 ± 23	611 ± 16	682 ± 16	8 ± 2
F2GEN	1368 ± 25	461 ± 15	729 ± 18	176 ± 9
$\langle Q^2 \rangle = 17.3$ GeV^2				
Data	1283 ± 39	202 ± 17	977 ± 33	99 ± 12
HERWIG	1302 ± 26	218 ± 11	1039 ± 23	44 ± 5
PYTHIA	1193 ± 22	193 ± 9	964 ± 20	36 ± 4
F2GEN	1288 ± 24	195 ± 9	897 ± 20	196 ± 9
$\langle Q^2 \rangle = 124$ GeV^2				
Data	66 ± 9	-	53 ± 9	13 ± 4
HERWIG	68 ± 2	-	59 ± 2	9 ± 1
PYTHIA	61 ± 2	-	51 ± 2	10 ± 1
F2GEN	70 ± 3	-	53 ± 3	16 ± 2

Table 6.1: The numbers of events with 0, 1 or 2 jets found for LEP1 data and Monte Carlo samples. The numbers given for the Monte Carlo samples have been normalised to the data luminosity. The estimated background has been subtracted from the data samples and the errors given are statistical.

Sample	All Events N	0 jet N_0	1 jet N_1	2 jet N_2
$\langle Q^2 \rangle = 11.4$ GeV^2				
Data	1006 ± 32	367 ± 19	553 ± 24	80 ± 9
HERWIG	744 ± 8	305 ± 5	415 ± 6	23 ± 1
PYTHIA	598 ± 6	243 ± 4	348 ± 5	7 ± 1
F2GEN	725 ± 11	195 ± 6	419 ± 9	111 ± 4
$\langle Q^2 \rangle = 38.4$ GeV^2				
Data	403 ± 20	38 ± 6	308 ± 18	51 ± 7
HERWIG	400 ± 6	50 ± 2	312 ± 5	35 ± 2
PYTHIA	304 ± 4	40 ± 2	240 ± 4	24 ± 1
F2GEN	358 ± 8	21 ± 2	248 ± 7	88 ± 4

Table 6.2: The numbers of events with 0, 1 or 2 jets found for LEP2 data and Monte Carlo samples. The numbers given for the Monte Carlo samples have been normalised to the data luminosity. The estimated background has been subtracted from the data sample and the errors given are statistical.

Clearly this demonstrates that, for all the Monte Carlo generators, the calculation of the overall cross–sections for a sample cannot be corrected by merely factoring in a simple multiplicative factor, but that the modelling of the relevant subprocesses is imperfect, most particularly in the lower $\langle Q^2 \rangle$ samples. The underestimation of N_2 in the HERWIG and PYTHIA samples, in contrast to the overestimation of N_2 in the pointlike F2GEN samples, suggests that a hard scattering process is underestimated in the HERWIG and PYTHIA generators, especially at low Q^2.

6.4 Hadronic Energy and Jet Subsamples

In this section, each data and Monte Carlo sample is split into subsamples comprised of events with the same number of found jets. Comparisons are made at each $\langle Q^2 \rangle$ between data and Monte Carlo distributions for the three subsamples of events with 0, 1 and 2 jets. No subsamples of events with 3 or more jets were compared due to the low numbers of events with a jet multiplicity higher than 2.

6.4.1 Energy Flows

Fig. 6.6 to 6.9 show the average hadronic energy flow for the subsamples of events at each $\langle Q^2 \rangle$. In Fig. 6.6, 6.7 and 6.9, plots a) and d) show the average energy flow for the subsamples with 0 jets, plots b) and e) for the subsamples with 1 jet and plots c) and f) show the corresponding distributions for the 2 jet subsamples. Fig. 6.8a) and b) show the average energy flow distributions for the subsamples with 1 and 2 jets respectively. The average energy flow is calculated by normalising each distribution to the number, N_i, of events with i jets in each subsample. This allows comparisons of the shapes of the energy flows directly by normalising out the effects due to the different numbers of events in each jet–classified subsample.

None of the Monte Carlo distributions reproduce the shapes of the data distributions well. This is apparent in the $0.9 < \eta < 1.8$ bin for events with 1 jet, especially for the subsample at $\langle Q^2 \rangle = 8.9$ GeV^2. The PYTHIA generator underestimates the energy flow into this bin for all subsamples except at $\langle Q^2 \rangle = 124$ GeV^2. The HERWIG distributions also show an underestimation of flow into this bin for the subsamples at $\langle Q^2 \rangle = 8.9$, 11.4, 17.3 and 38.4 GeV^2.

The energy flow distributions for events with 2 jets are more highly peaked than those for events with 0 or 1 jets. These peaks occur in the range in the region $0 < \eta < 1.8$ and are 2–3 times higher than those in the 0 jet and 1 jet distributions. This and the bad description of the region $0.9 < \eta < 1.8$ for 1 jet events form the major contributing factors to the discrepancies shown in Fig. 6.1 in the region $0 < \eta < 1.8$.

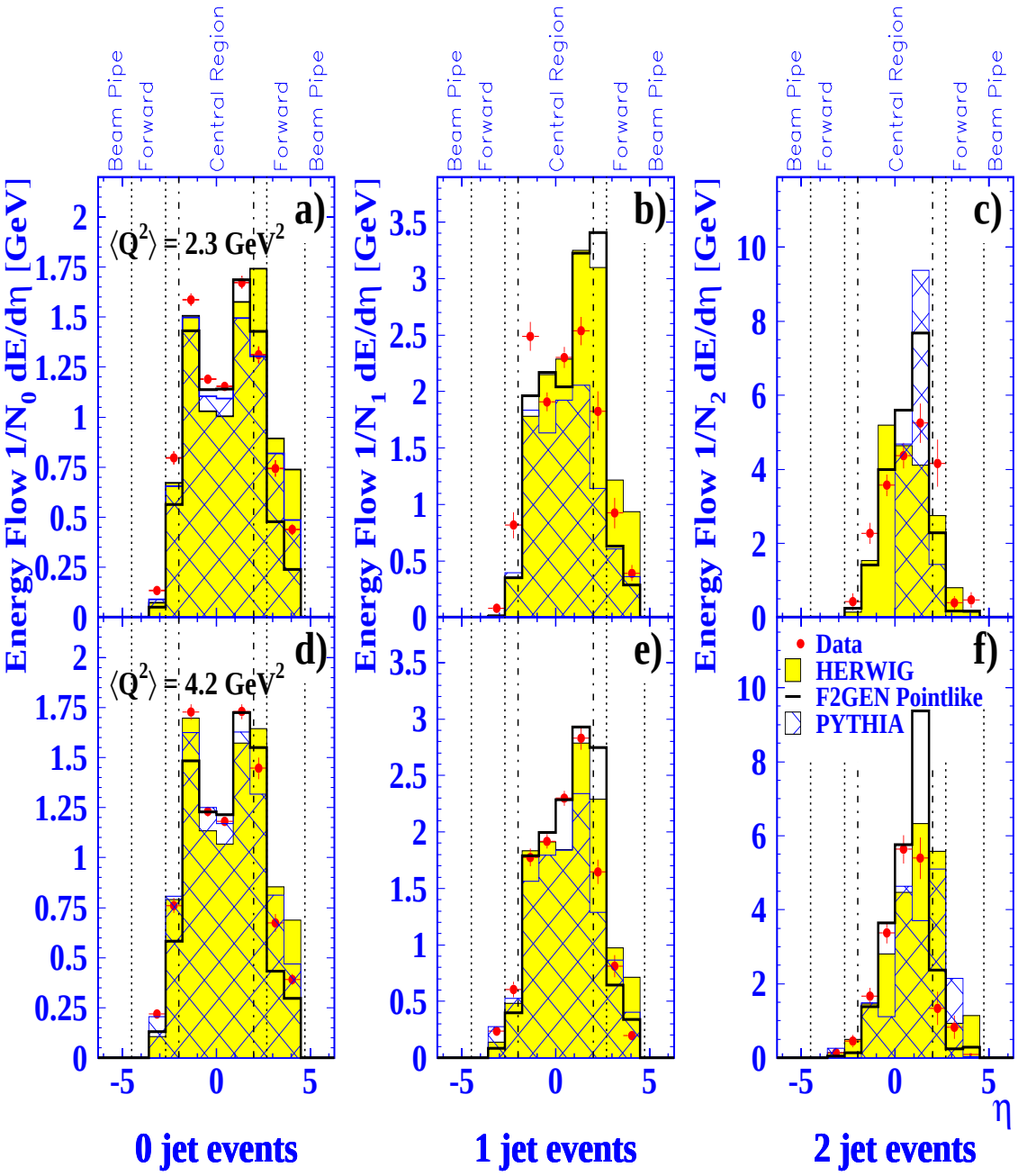

Figure 6.6: The average hadronic energy flow per event in bins of pseudorapidity $\eta = -\ln\tan\theta'/2$. The polar angle, θ', is recalculated for all hadrons relative to the beam axis, such that the tagged electron is always at $\eta < 0$. Plots a) and d) show the average energy flow for events with 0 jet, plots b) and e) for events with 1 jet, and plots c) and f) for events with 2 jets. The dots represent the data with the estimated background subtracted, whilst the histograms show the corresponding distributions for HERWIG (shaded), PYTHIA (hatched) and F2GEN (open) Monte Carlo samples. The errors shown are statistical only.

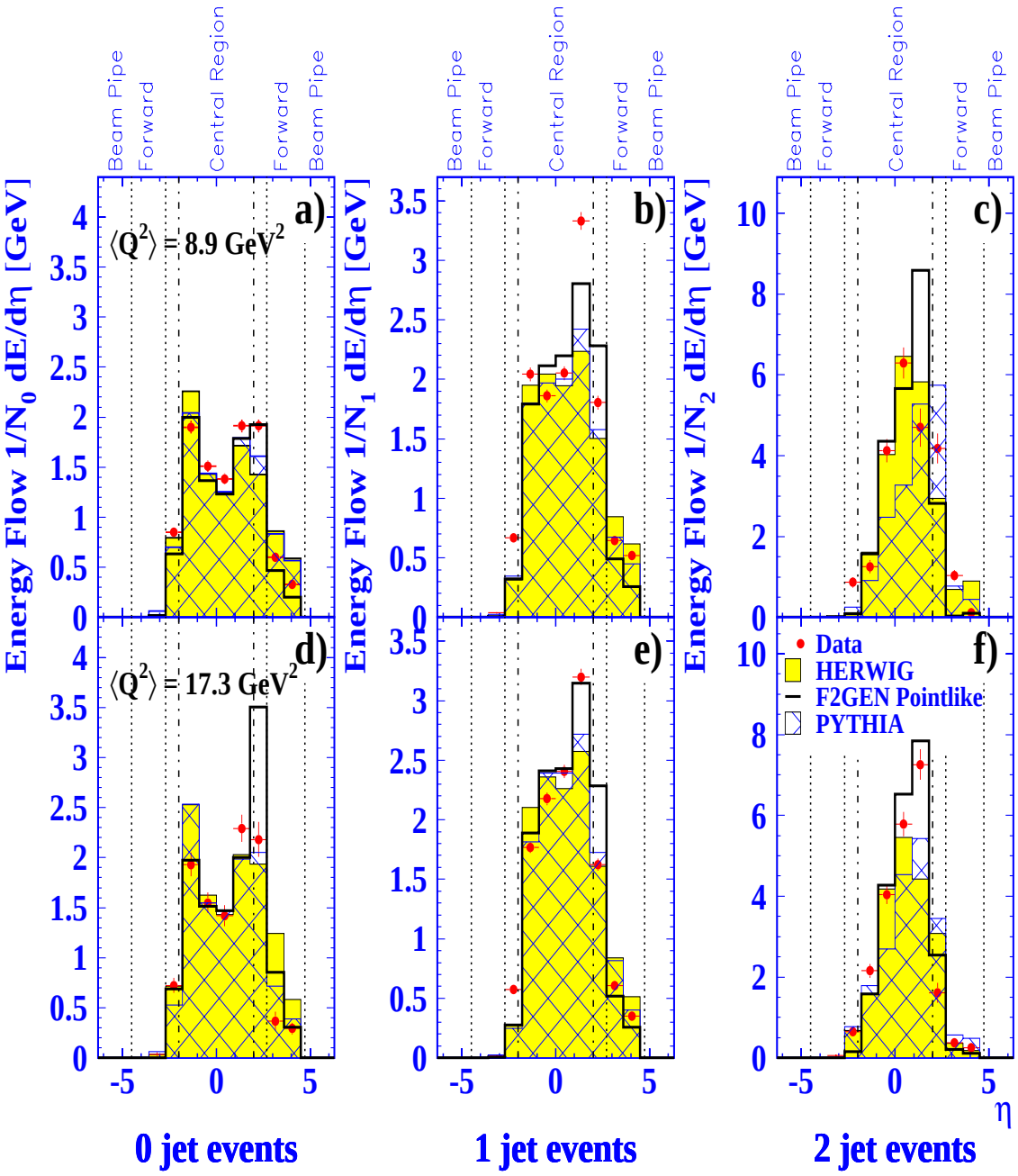

Figure 6.7: The average hadronic energy flow per event in bins of pseudorapidity $\eta = -\ln\tan\theta'/2$. The polar angle, θ', is recalculated for all hadrons relative to the beam axis, such that the tagged electron is always at $\eta < 0$. Plots a) and d) show the average energy flow for events with 0 jet, plots b) and e) for events with 1 jet, and plots c) and f) for events with 2 jets. The dots represent the data with the estimated background subtracted, whilst the histograms show the corresponding distributions for HERWIG (shaded), PYTHIA (hatched) and F2GEN (open) Monte Carlo samples. The errors shown are statistical only.

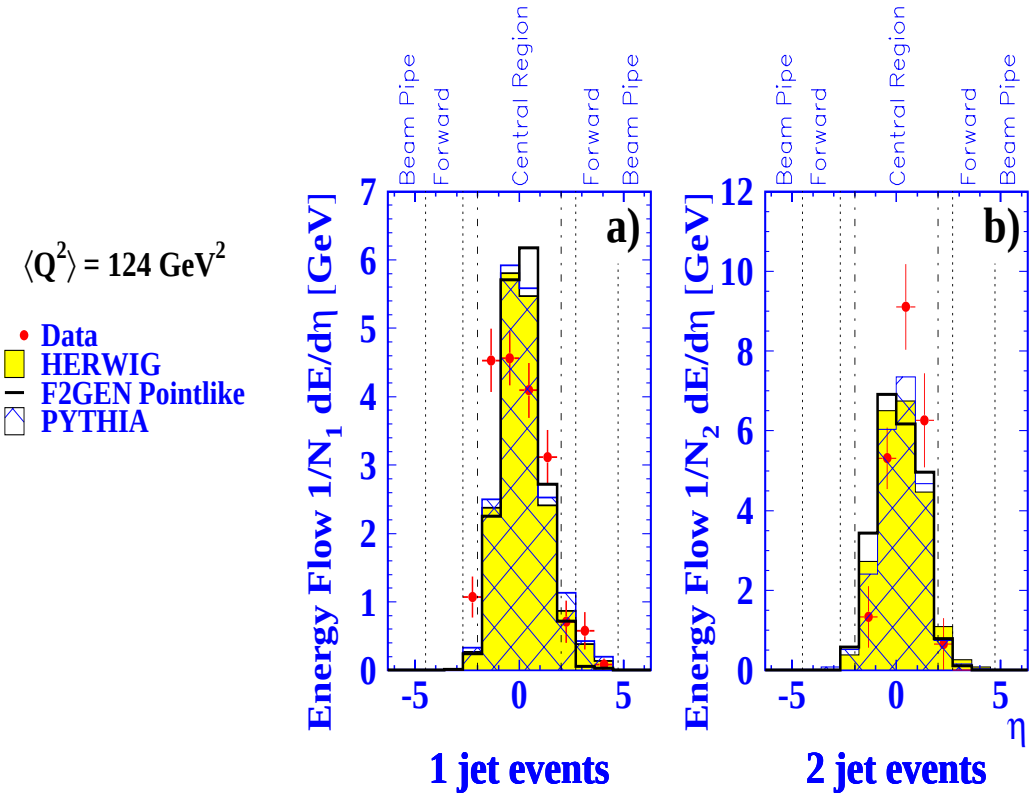

Figure 6.8: The average hadronic energy flow per event in bins of pseudorapidity $\eta = -\ln\tan\theta'/2$. The polar angle, θ', is recalculated for all hadrons relative to the beam axis, such that the tagged electron is always at $\eta < 0$. Plot a) shows the average energy flow for events with 1 jet and plot b) for events with 2 jets. The dots represent the data with the estimated background subtracted, whilst the histograms show the corresponding distributions for HERWIG (shaded), PYTHIA (hatched) and F2GEN (open) Monte Carlo samples. The errors shown are statistical only.

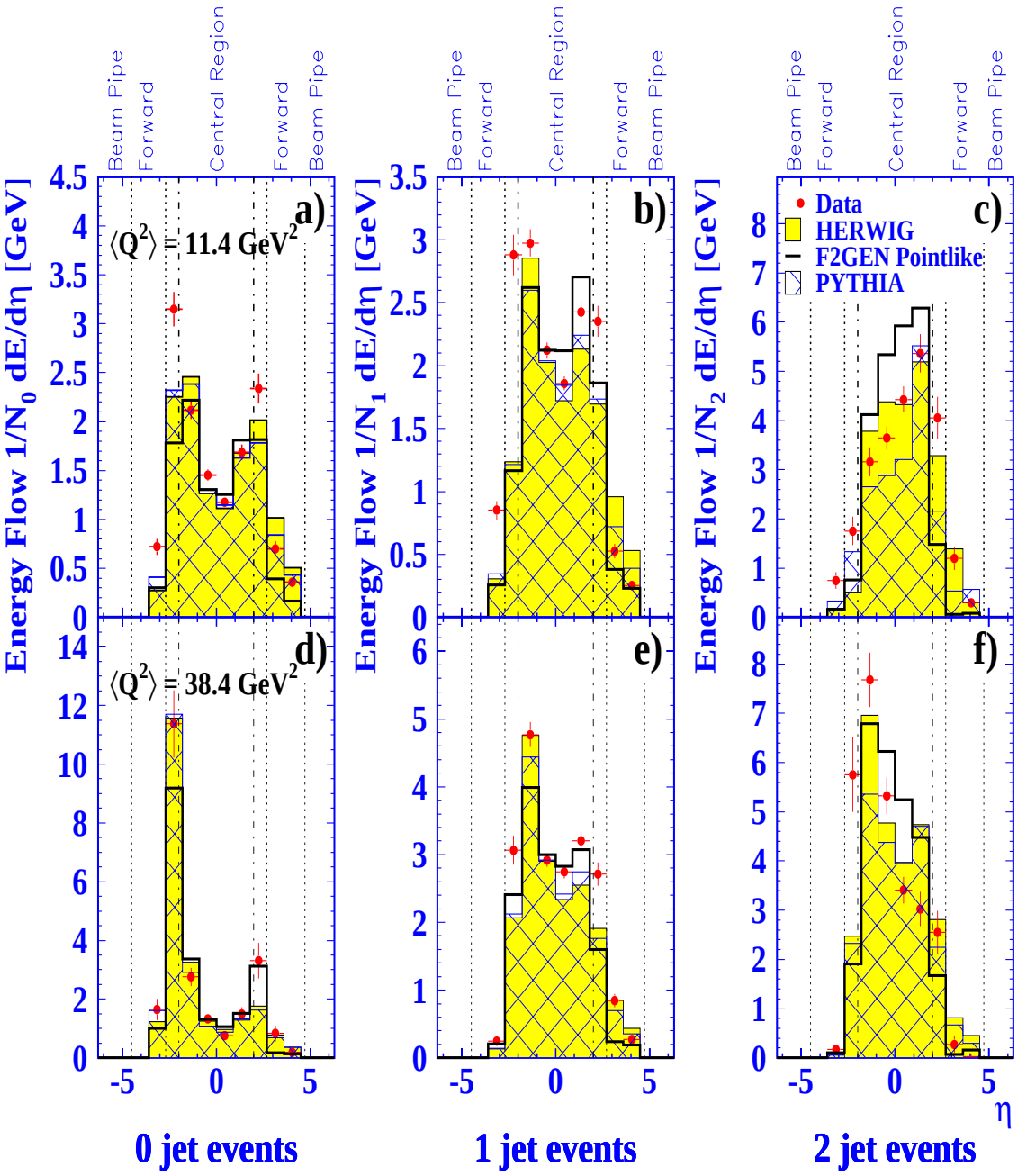

Figure 6.9: The average hadronic energy flow per event in bins of pseudorapidity $\eta = -\ln\tan\theta'/2$. The polar angle, θ', is recalculated for all hadrons relative to the beam axis, such that the tagged electron is always at $\eta < 0$. Plots a) and d) show the average energy flow for events with 0 jet, plots b) and e) for events with 1 jet, and plots c) and f) for events with 2 jets. The dots represent the data with the estimated background subtracted, whilst the histograms show the corresponding distributions for HERWIG (shaded), PYTHIA (hatched) and F2GEN (open) Monte Carlo samples. The errors shown are statistical only.

The poor description of the energy flow into the region $2.7 < \eta < 4.5$ in Fig. 6.1 by the Monte Carlo samples is also shown in Fig. 6.6, 6.7 and 6.9. The flow into this region is overestimated for 0 jet and 1 jet subsamples by the PYTHIA generator and especially by the HERWIG generator at $\langle Q^2 \rangle = 2.3$, 4.2, 8.9, 11.4 and 17.3 GeV^2. In contrast, the energy flow into these η bins is mostly underestimated by the pointlike F2GEN generator for all 0, 1 and 2 jet subsamples, except at $\langle Q^2 \rangle = 124$ GeV^2.

6.4.2 Energy Transverse to the Tag–Beam Plane, $E_{\mathrm{t,out}}$

Fig. 6.10 to 6.13 show the distributions of $E_{\mathrm{t,out}}$ for the subsamples at each $\langle Q^2 \rangle$. Each Monte Carlo distribution is normalised to the integrated luminosity of the data.

These diagrams show that the discrepancies observed at high $E_{\mathrm{t,out}}$ in Fig. 6.2 between the data and Monte Carlo samples can be understood mainly in terms of the poor predictions of the number of 2 jet events by all of the Monte Carlo generators. There are also significant discrepancies for the 1 jet events, especially between the data and PYTHIA distributions.

The effects of the overestimation of the 2 jet rate by the F2GEN pointlike generator, and the corresponding underestimation by the HERWIG and PYTHIA generators, can be clearly seen in the plots c) and f) of Fig. 6.10 and 6.11 and in plot c) of Fig. 6.13. It is also noticeable that these distributions are shifted to higher $E_{\mathrm{t,out}}$ than those of 0 and 1 jet events and that nearly all events with $E_{\mathrm{t,out}} > 10$ GeV are 2 jet events.

The cut–off in generation of high $E_{\mathrm{t,out}}$ events by PYTHIA is apparent in the distributions for events 1 jet and for events with 2 jets, with the cut–off most noticeable at $\langle Q^2 \rangle = 2.3$ GeV^2. The PYTHIA distributions approach the HERWIG distributions with increasing $\langle Q^2 \rangle$ and the difference between them negligible for $\langle Q^2 \rangle =$ 38.4 and 124 GeV^2. The HERWIG distributions for 0 jet and for 1 jet events show reasonable agreement with the data distributions for all $\langle Q^2 \rangle$.

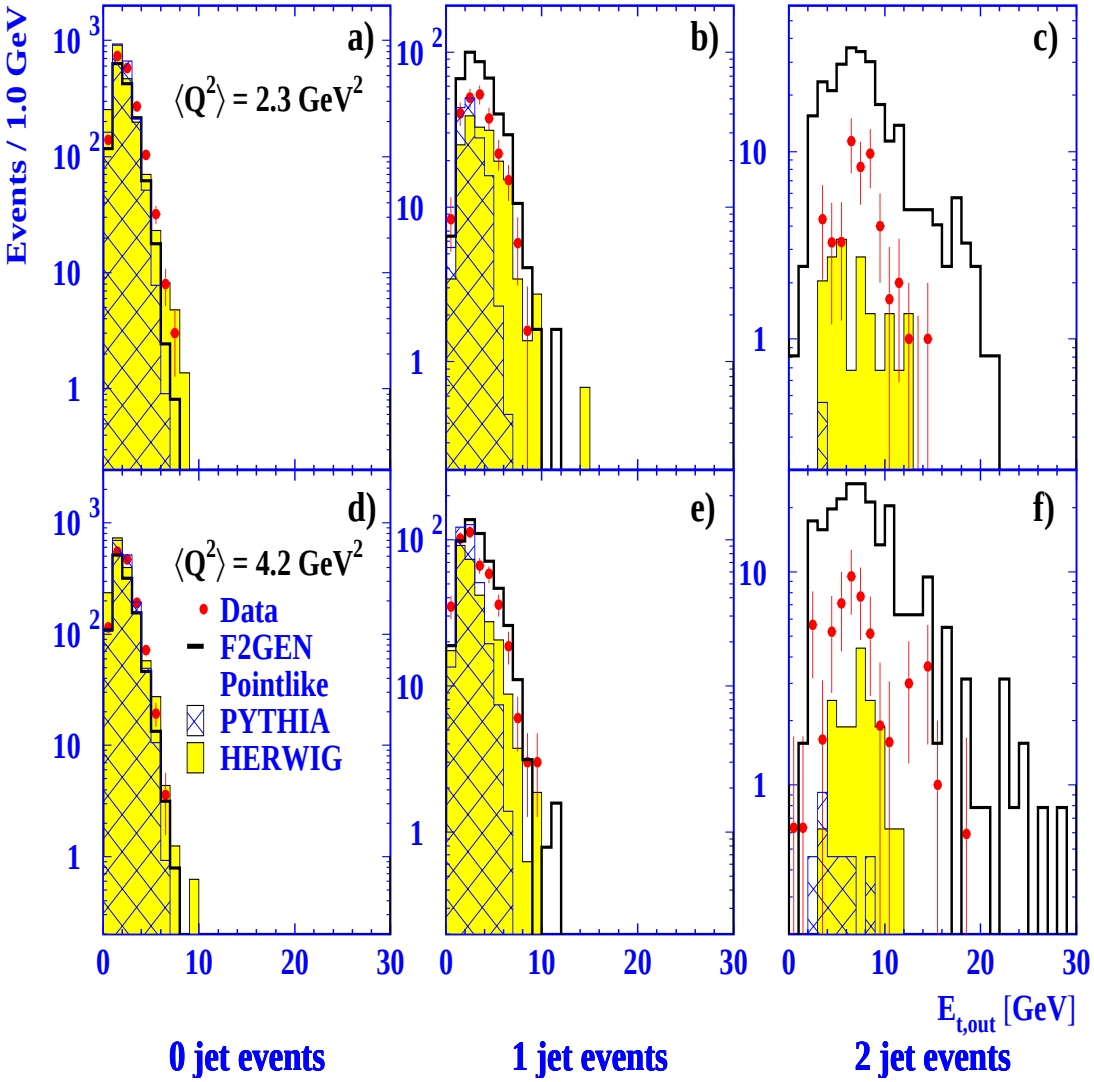

Figure 6.10: The transverse energy out of the plane formed by the tagged electron and the beams, $E_{t,out}$. For the data distributions (dots) are shown with the estimated background subtracted. Plots a) and d) show the numbers of events with 0 jets, plots b) and e) the numbers of events with 1 jet, and plots c) and f) the numbers of events with 2 jets. The histograms show the distributions for the HERWIG (shaded), PYTHIA (hatched) and F2GEN (open) samples respectively and are normalised to the same luminosity as the data. The errors shown for the data distributions are statistical only.

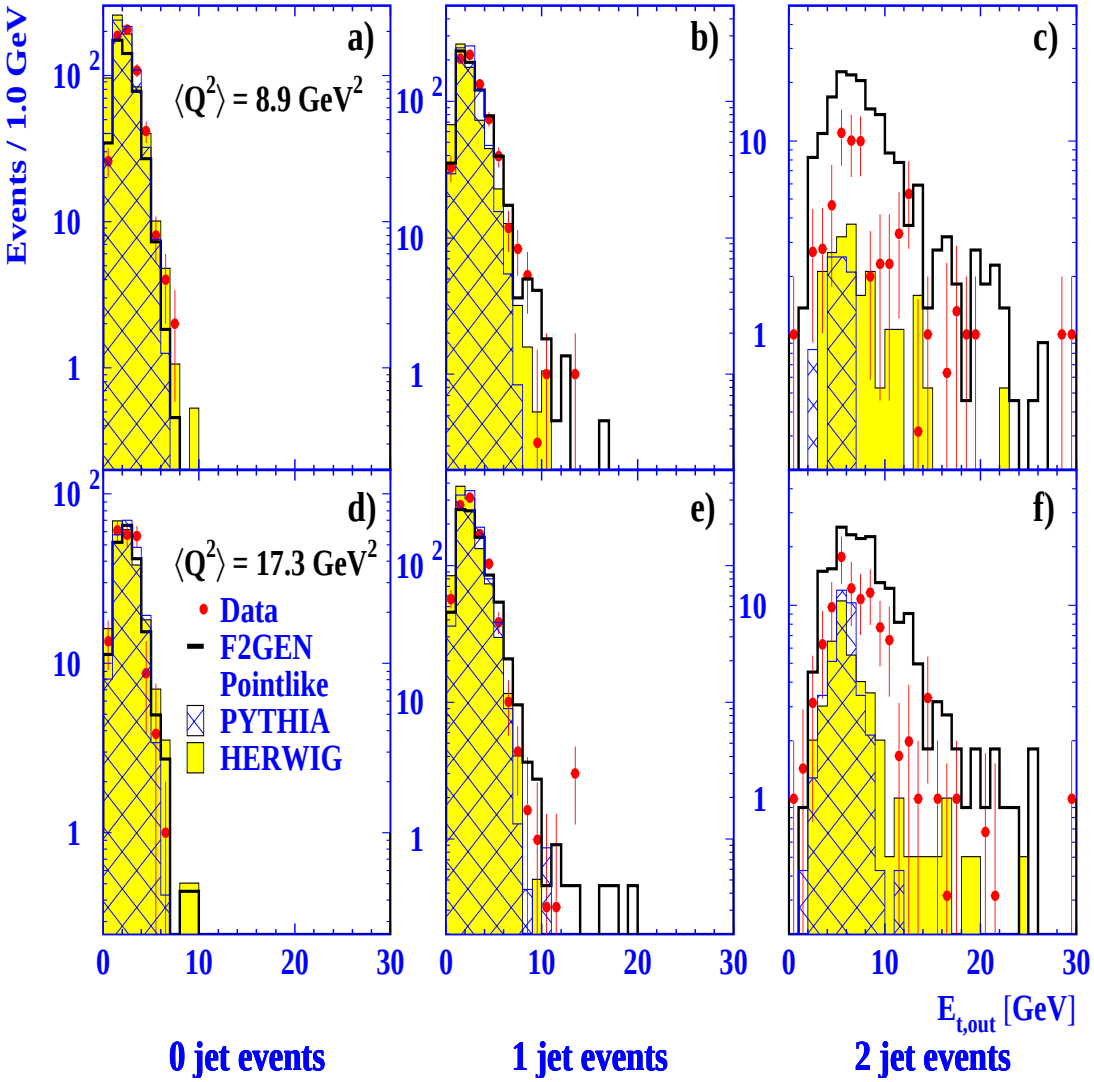

Figure 6.11: The transverse energy out of the plane formed by the tagged electron and the beams, $E_{t,out}$. For the data distributions (dots) are shown with the estimated background subtracted. Plots a) and d) show the numbers of events with 0 jets, plots b) and e) the numbers of events with 1 jet, and plots c) and f) the numbers of events with 2 jets. The histograms show the distributions for the HERWIG (shaded), PYTHIA (hatched) and F2GEN (open) samples respectively and are normalised to the same luminosity as the data. The errors shown for the data distributions are statistical only.

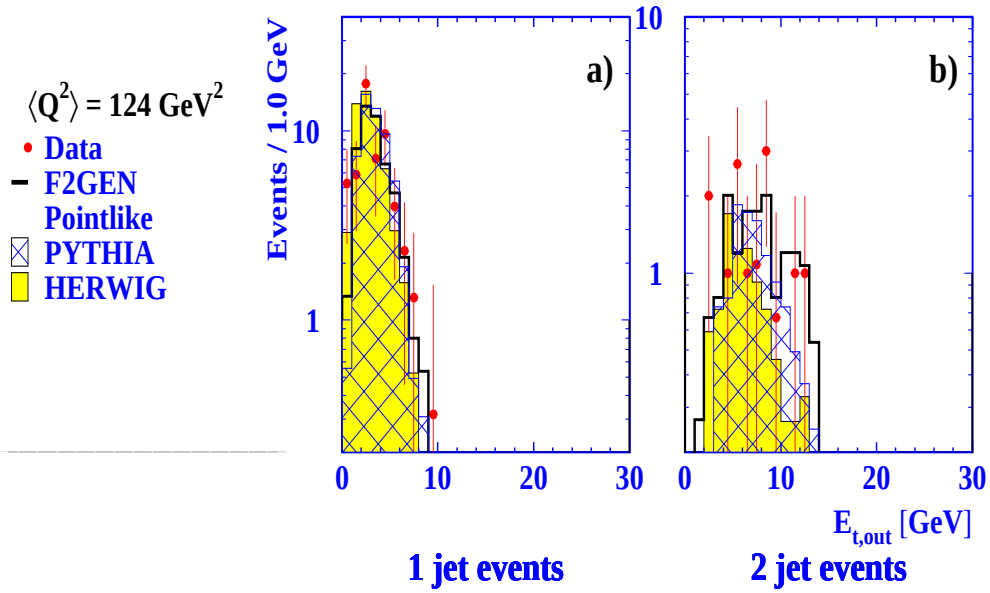

Figure 6.12: The transverse energy out of the plane formed by the tagged electron and the beams, $E_{t,out}$. For the data distributions (dots) are shown with the estimated background subtracted. Plot a) shows the numbers of events with 1 jets and plot b) the numbers of events with 2 jets. The histograms show the distributions for the HERWIG (shaded), PYTHIA (hatched) and F2GEN (open) samples respectively and are normalised to the same luminosity as the data. The errors shown for the data distributions are statistical only.

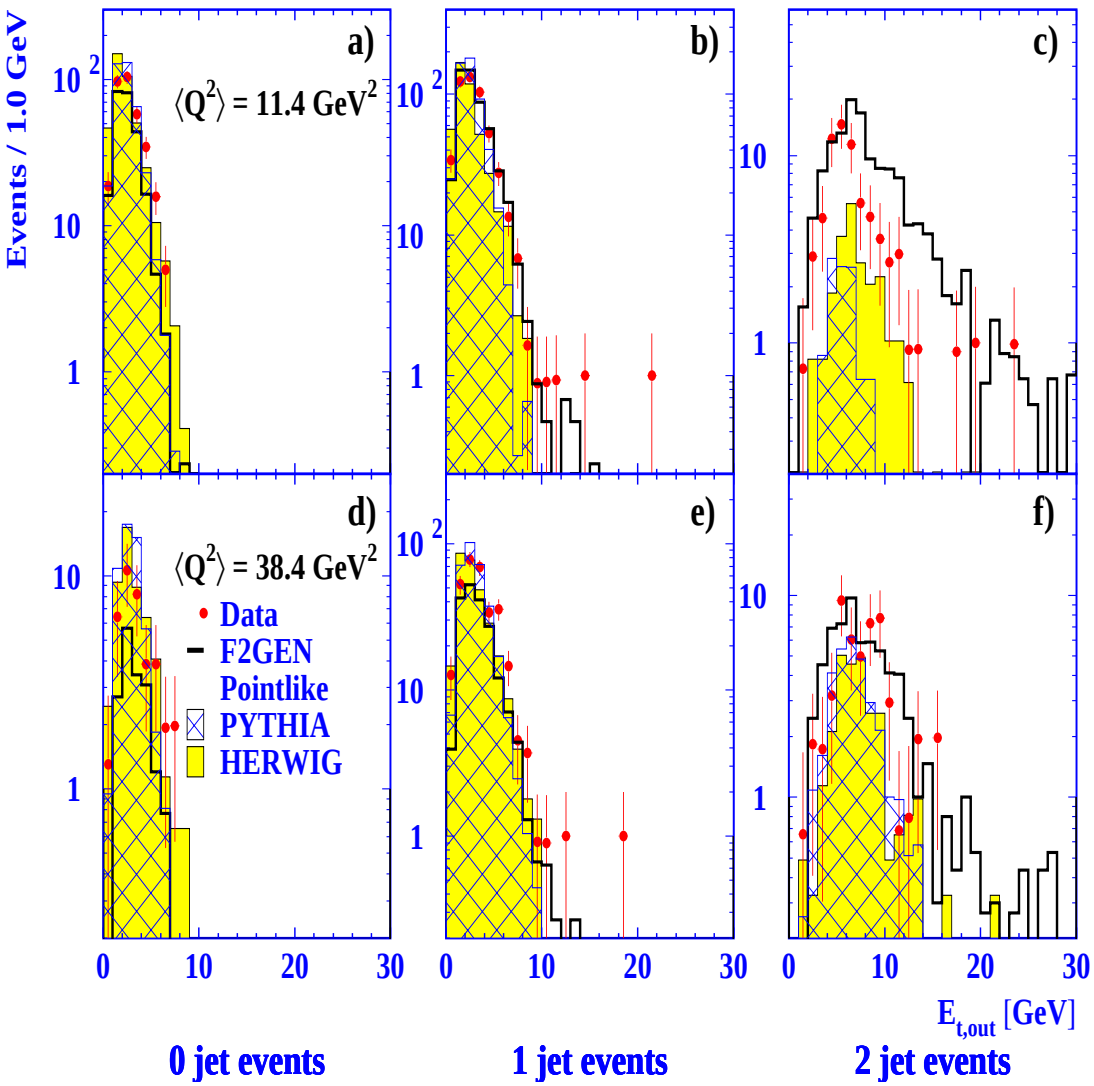

Figure 6.13: The transverse energy out of the plane formed by the tagged electron and the beams, $E_{t,out}$. For the data distributions (dots) are shown with the estimated background subtracted. Plots a) and d) show the numbers of events with 0 jets, plots b) and e) the numbers of events with 1 jet, and plots c) and f) the numbers of events with 2 jets. The histograms show the distributions for the HERWIG (shaded), PYTHIA (hatched) and F2GEN (open) samples respectively and are normalised to the same luminosity as the data. The errors shown for the data distributions are statistical only.

6.5 Interpretation of Jet Multiplicity Subsamples

In section 6.1, it is shown that the HERWIG and PYTHIA generators underestimate:

1. the average energy flow into the region $0 < \eta < 1.8$
2. the number of events in a sample with $E_{\mathrm{t,out}} > 5 - 8$ GeV

In section 6.3, the HERWIG and PYTHIA generators also underestimate the 2 jet rate. In contrast, the F2GEN pointlike generator overestimates all of these quantities.

The definition of subsamples of events by jet multiplicity shows that the poor descriptions of the average energy flow (Fig. 6.1) and $E_{\mathrm{t,out}}$ (Fig. 6.2) distributions are sensitive to the numbers of events with 2 jets in the total sample.

It is important that the underestimation of 2 jet rates, energy flow and transverse energy, $E_{\mathrm{t,out}}$, by the PYTHIA generator is significantly worse than that of the HERWIG generator, and that these differences are largest at low Q^2. For instance, the number of 2 jet events predicted by the PYTHIA generator is just under 40 times lower than that of the HERWIG generator in the $\langle Q^2 \rangle = 2.3$ GeV^2 samples but the corresponding 2 jet rates are comparable for the $\langle Q^2 \rangle = 124$ GeV^2 PYTHIA and HERWIG samples. These differences may be due to differences between the generators in the modelling of the parton evolutions. As discussed in section 2.7.2, the parton shower models used in HERWIG and PYTHIA generators best describe soft emissions in the parton evolution. These models do not extend into all regions of emission phase space, particularly the region where harder emissions of partons occur. However, the HERWIG generator uses first order α_s matrix elements to model these harder parton emissions whereas the PYTHIA generator does not attempt to model this region. The differences between the HERWIG and PYTHIA generators shown in this chapter suggest that the region of hard parton emission is important, particularly in low Q^2 events.

The results for the F2GEN generator with the pointlike scattering model also suggest that the HERWIG and PYTHIA generators do not incorporate hard scattering

processes correctly when generating samples of events. It is therefore useful to try to understand further the effects of hard parton emission in a sample of events. In the following chapter, one of the possible hard subprocesses, photon–gluon fusion, is investigated using the F2GEN generator.

Chapter 7

F2GEN And Photon–Gluon Fusion

7.1 F2GEN Monte Carlo Algorithm

The generator F2GEN is used to generate singly–tagged, two–photon events and was developed from the TWOGEN program [10] as a tool for use in OPAL measurements of the hadronic photon structure function, $F_2^\gamma(x, Q^2)$ [47]. The assumption made in the method of generation is that the cross–section can be factorised into two parts:

$$\sigma(\mathrm{e^+e^-} \to \mathrm{e^+e^-X}) = \mathcal{L}_{\gamma\gamma}(\mathrm{e^+e^-} \to \mathrm{e^+e^-}\gamma_1^*\gamma_2^*)\sigma(\gamma_1^*\gamma_2^* \to \mathrm{X}) \qquad (7.1)$$

where $\mathcal{L}_{\gamma\gamma}(\mathrm{e^+e^-} \to \mathrm{e^+e^-}\gamma_1^*\gamma_2^*)$ is the $(\gamma^*\gamma^*)$ luminosity function [96] and $\sigma(\gamma_1^*\gamma_2^* \to \mathrm{X})$ is the cross–section for hadronic production from two photons. Fig. 7.1 shows a flow diagram of the stages of event generation in F2GEN and which are described below. Fig. 7.2 shows definitions of the kinematic variables used to describe the generation.

7.1.1 Generating the Two Photons

Stage 1 in Fig. 7.1 is the generation of the four–momenta ($q_i = (\overline{q_i}, \omega_i)$, $i = 1, 2$) of the two photons, and these four-momenta are used to calculate the four momenta ($p_i^{'} = (\overline{p_i^{'}}, E_i^{'})$) of the two scattered beam particles.

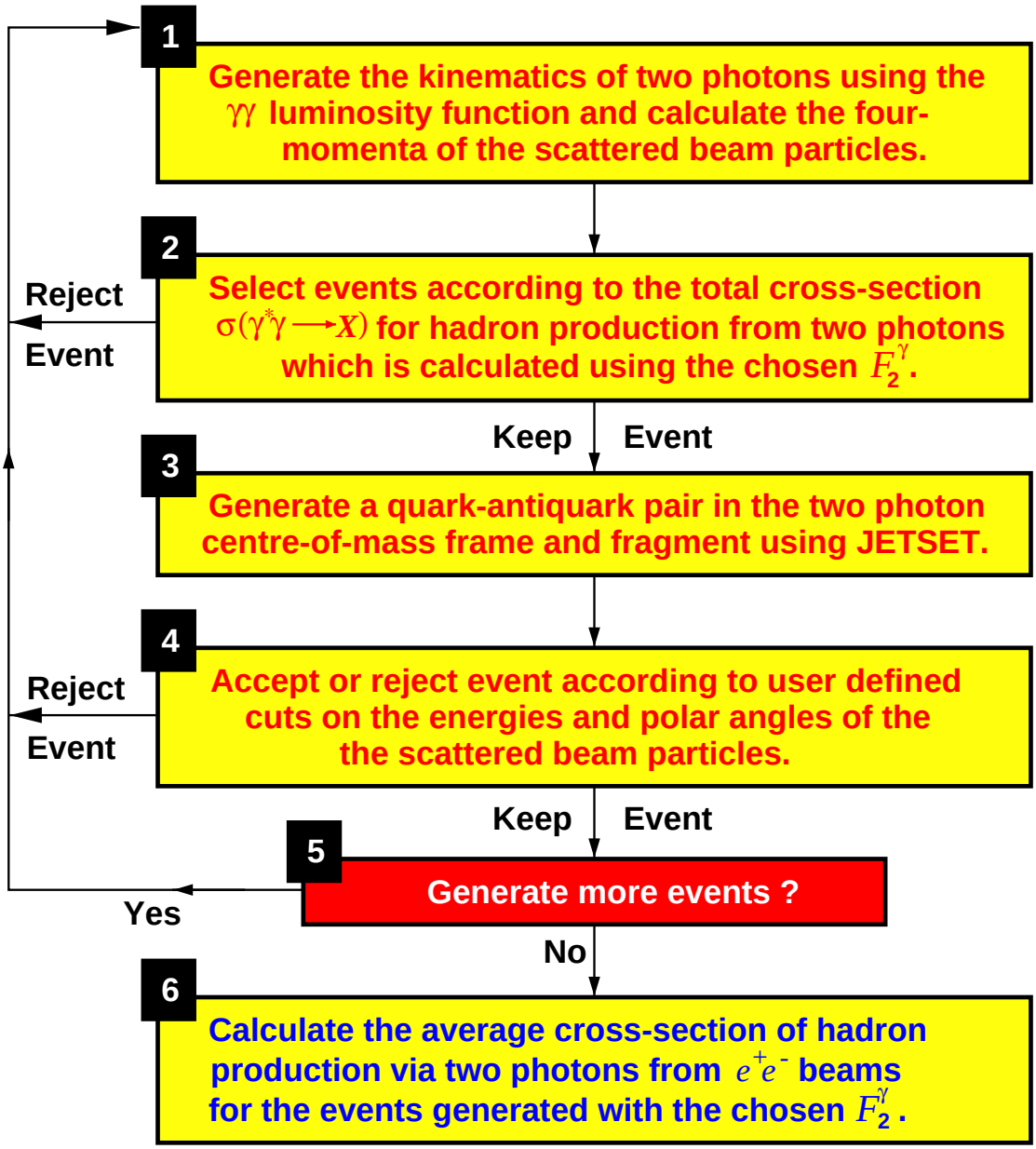

Figure 7.1: Flow chart of the sequence of generation for hadronic two–photon events in F2GEN.

The expression for the differential cross–section $\mathrm{d}\sigma(\mathrm{e^+e^-} \to \mathrm{e^+e^-X})$ involves the cross–sections σ_{TT}, σ_{TL}, σ_{LT} and σ_{LL} corresponding to all the possible combinations of transverse (T) and longitudinal (L) photon polarisation, with only σ_{TT} non–zero for real photons. In F2GEN, it is assumed that the two photons generated are quasi–real so that σ_{TL}, σ_{LT} and σ_{LL} are negligible and hence that $\mathcal{L}_{\gamma\gamma}$ is approximated to by the transverse photon luminosity function $\mathcal{L}^{\mathrm{TT}}_{\gamma\gamma}$. The differential form of the luminosity function sampled is:

$$\frac{\mathrm{d}^6\mathcal{L}^{\mathrm{TT}}_{\gamma\gamma}}{\mathrm{d}\omega_1\mathrm{d}\omega_2\mathrm{d}\theta_1\mathrm{d}\theta_2\mathrm{d}\phi} = \frac{\alpha^2 E_1' E_2'}{8\pi^4 E^2}\frac{\sin\theta_1\sin\theta_2}{q_1^2 q_2^2}\sqrt{X}\rho_1^{++}\rho_2^{++} \tag{7.2}$$

where E_i, E_i', ω_i are the energies and θ_i polar angles defined in Fig. 7.2; ρ_i^{++} are the density matrix elements:

$$\rho_1^{++} = \frac{(k - 4E\omega_2 q_2^2)^2}{2X} + \frac{1}{2} + 2\frac{\mathrm{m}_e^2}{q_1^2}; \tag{7.3}$$

$$\rho_2^{++} = \frac{(k - 4E\omega_1 q_1^2)^2}{2X} + \frac{1}{2} + 2\frac{\mathrm{m}_e^2}{q_2^2}; \tag{7.4}$$

$$k = \frac{1}{2}(W^2 - q_1^2 - q_2^2); \tag{7.5}$$

$$X = k^2 - q_1^2 q_2^2 \tag{7.6}$$

and $W_{\gamma\gamma}$ is the invariant mass of the two photons. The photon generated with the largest value of $Q^2 = -q_i^2$ $(i = 1, 2)$ is called the probe photon, whilst the other photon (with $P^2 = -q_j^2 \ll Q^2, j = 1, 2 \neq i$) is called the target photon.

7.1.2 Sampling the Cross–Section for $\gamma\gamma \to$ hadrons

In stage **2**, events are sampled according to the cross–section for production of hadrons (X) from two photons, $\sigma(\gamma^*\gamma \to q\bar{q} \to X)$. In F2GEN, the structure function $F_2^\gamma(x, Q^2)$ is used to estimate $\sigma(\gamma^*\gamma \to q\bar{q} \to X)$ (Eqn. 2.38). The generated kinematical variables of the two–photon system $W_{\gamma\gamma}^2$, P^2 and Q^2 are used to calculate Björken x:

$$x = \frac{Q^2}{2(q_1.q_2)} = \frac{Q^2}{W_{\gamma\gamma}^2 + Q^2 + P^2}. \tag{7.7}$$

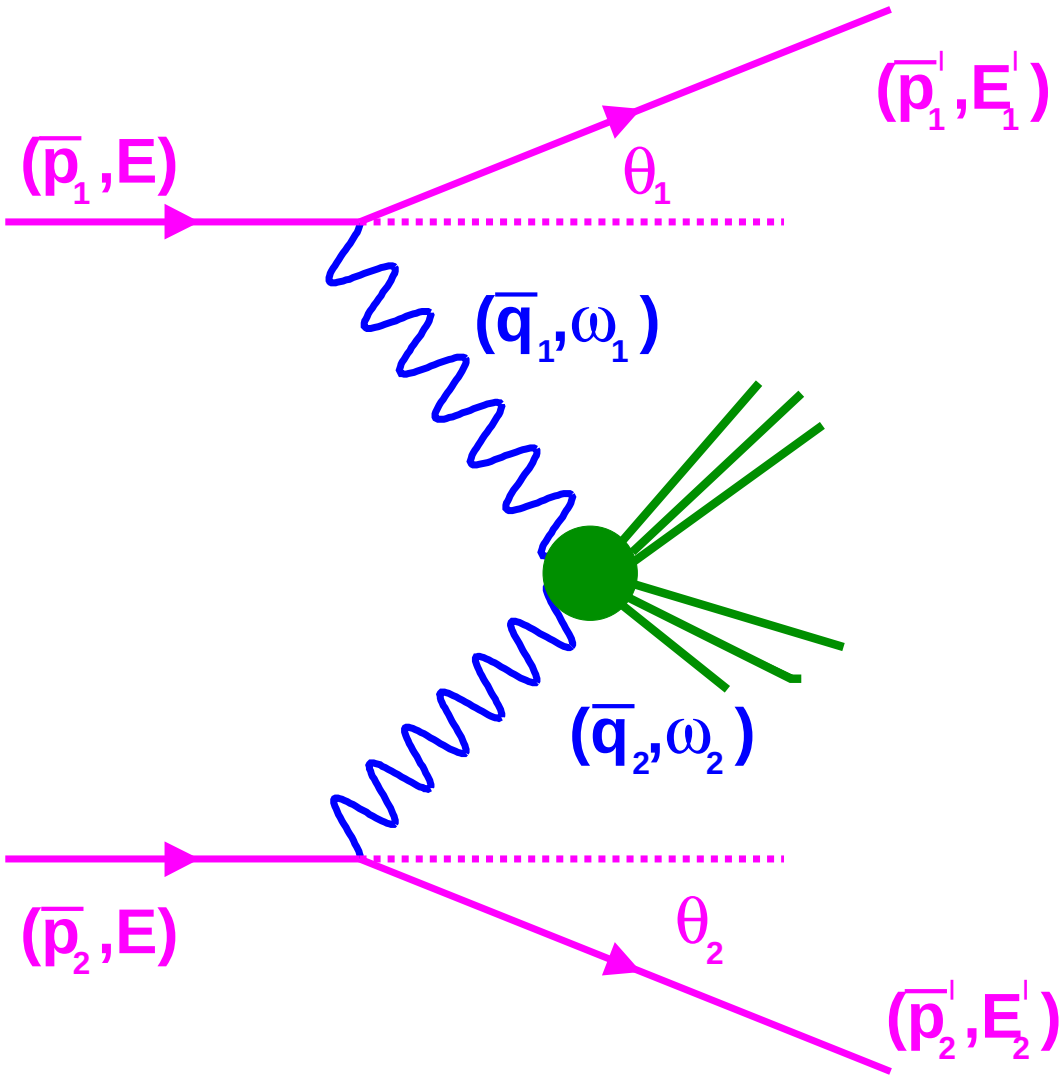

Figure 7.2: Definition of kinematical variables used in F2GEN.

7.1.3 Generating the Hadronic Final State in F2GEN

In stage 3, a quark–antiquark pair is generated in the two–photon centre–of–mass system, with angular distribution chosen using either "pointlike" or "peripheral" models or a combination of the two (such as the "perimiss" model), and are then fragmented to hadrons using the JETSET string fragmentation algorithm. The index "*" is used to label kinematic variables in the two–photon centre–of–mass frame.

The Pointlike Angular Distribution

The "pointlike" model generates the quark–antiquark final state in the $\gamma^*\gamma$ centre–of–mass using the same angular distribution as for generation of a lepton–antilepton pair [96]:

$$\frac{\mathrm{d}\sigma(\gamma\gamma \to l^+l^-)}{\mathrm{d}\Omega^*} = \frac{\alpha^2}{W_{\gamma\gamma}}\beta^* \frac{2\beta^{*2}\sin^2\theta^* - \beta^{*4}\sin^4\theta^* + 1 - \beta^{*4}}{(1-\beta^{*2}\cos^2\theta^*)^2} \tag{7.8}$$

where

$$\beta^* = \sqrt{1 - \frac{4m_l^2}{W_{\gamma\gamma}^2}} \tag{7.9}$$

and θ^* is the angle of the lepton relative to the two–photon axis and m_l is the lepton mass. To form the corresponding distribution for a quark–antiquark pair, the lepton mass is replaced by the quark mass, m_q, the distribution is pre-multiplied by the fourth power of the fractional electric charge of the quark, e_q^4, and a sum is performed over the allowed quark flavours (only the four quark flavours u, d, s and c are considered):

$$\frac{\mathrm{d}\sigma(\gamma\gamma \to q\bar{q})}{\mathrm{d}\Omega^*} = \frac{\alpha^2}{W_{\gamma\gamma}} \sum_q e_q^4 \beta_q^* \frac{2\beta_q^{*2}\sin^2\theta^* - \beta_q^{*4}\sin^4\theta^* + 1 - \beta_q^{*4}}{(1-\beta_q^{*2}\cos^2\theta^*)^2} \tag{7.10}$$

$$\beta_q^* = \sqrt{1 - \frac{4m_q^2}{W_{\gamma\gamma}^2}} \tag{7.11}$$

This distribution is purely QED based with no QCD terms arising either from hard final state QCD radiation or from a hadron–like component of the photon.

An implicit assumption of Eqn. 7.8 is that both photons are real. The angular distribution of a massless quark–antiquark pair in the two–photon centre–of–mass

where one photon is real ($P^2 \equiv 0$) and the other photon is virtual ($Q^2 > 0$) can be obtained from Eqn. 4.35 and Eqn. 10.38 of [97]:

$$\frac{d\sigma(\gamma^*\gamma \to q\bar{q})}{d\Omega^*} = \sum_q \frac{3e_q^4\alpha^2}{(W_{\gamma\gamma^*}^2 + Q^2)\sin^2\theta^*}\left[(1+\cos^2\theta^*) - \frac{4Q^2W_{\gamma\gamma^*}^2}{({W_{\gamma\gamma^*}}^4 + Q^4 + 2Q^2W_{\gamma\gamma^*}^2)}\right] \quad (7.12)$$

Like Eqn. 7.10, Eqn. 7.12 is purely QED based and contains no QCD terms.

The distributions of $\cos\theta^*$ are shown in Fig. 7.3 for events where the θ^* is generated using Eqn. 7.10 and using Eqn. 7.12. The effect of the photon virtuality is clearly important in the two–photon centre–of–mass frame where the distributions for $\gamma\gamma \to \mathrm{q\overline{q}}$ are more strongly peaked towards $\cos\theta^* \sim 1$ than those for $\gamma^*\gamma \to \mathrm{q\overline{q}}$. However, the effect of this difference is small due to smearing effects in the boost back to the $\mathrm{e^+e^-}$ centre–of–mass frame and the hadronisation of the quark and antiquark.

The Peripheral Angular Distribution

Clearly it is unphysical to model the angular distribution of every generated quark–antiquark pair in the two–photon centre–of–mass without any allowance for effects from processes involving QCD terms (low x behaviour) or the hadron–like component (VMD) of the photon. These processes give rise to smaller transverse momenta, p_t, for the quark–antiquark pair than are obtained using a pointlike model.

The "peripheral" model is used to generate a limited p_t for the quark–antiquark pair by sampling a Gaussian distribution with mean zero and half–width of 0.3 GeV. This scale was chosen to represent the average transverse momentum of a quark in a meson. This model therefore represents an attempt to model the target photon as a meson and is the opposite extreme from the pointlike model.

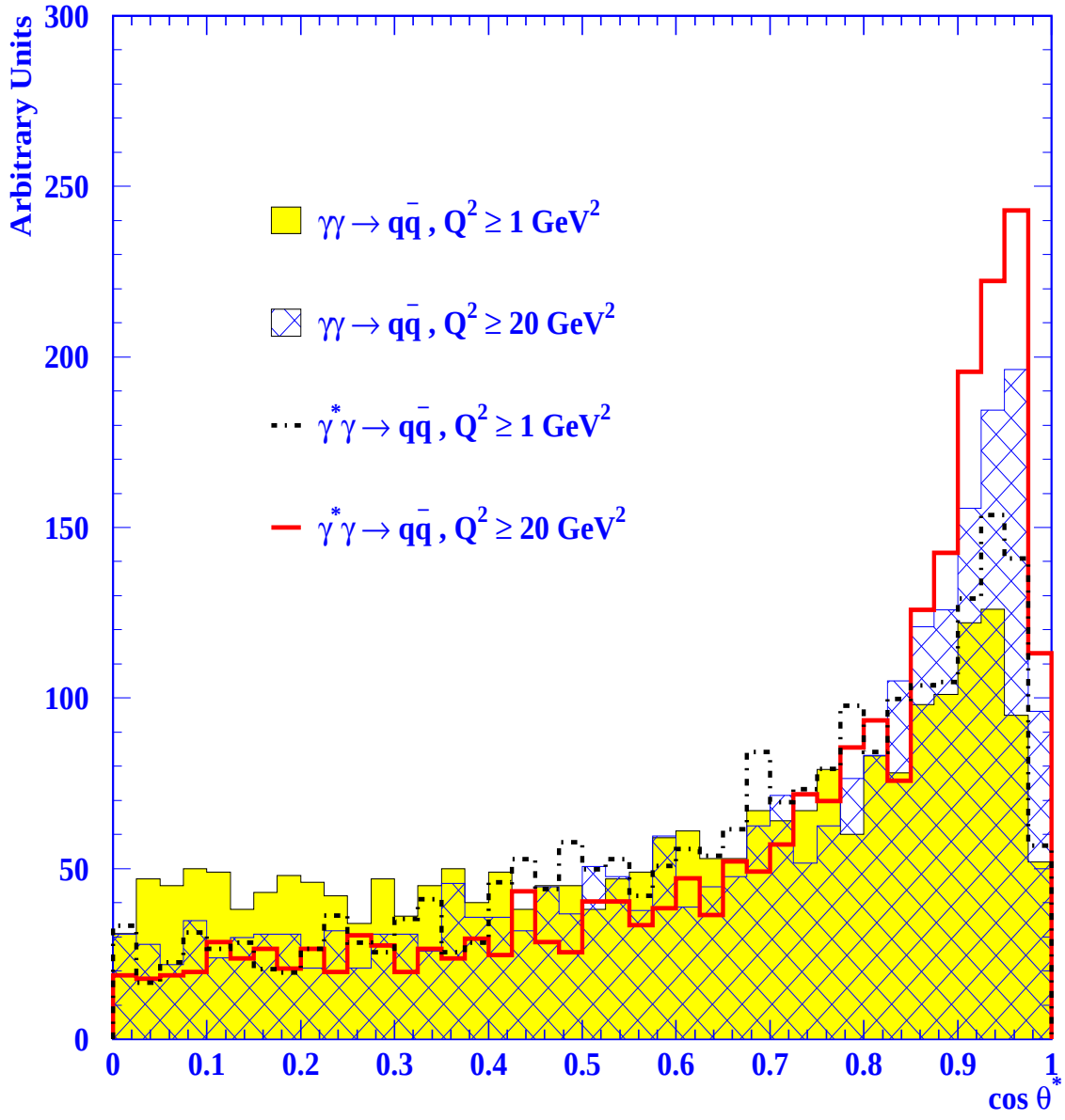

Figure 7.3: Distributions of $\cos\theta^*$ for the quark in the $\gamma\gamma$ centre–of–mass system. The polar angle θ^* is generated using Eqn. 7.10 (shaded and hatched histograms) or using Eqn. 7.12 (solid and dotted lines). This angle is measured between the $\gamma\gamma$ axis and the direction of the quark momentum. The histograms are all normalised to the same area.

The Perimiss Angular Distribution

The "perimiss" model of the angular distribution is a mixture of the pointlike and peripheral models such that the peripheral model is used to describe the low x and VMD behaviour of the final state whilst the pointlike model is used to describe all other cases.

A small value x_o is set as the point in x below which only the peripheral model is used to determine θ^*. For an event generated with $x > x_o$, a random number, $\mathcal{R}$, is generated and compared with the ratio $F_2^\gamma(x,Q^2)/F_{2,\mathrm{VMD}}^\gamma(x,Q^2)$ to decide which of the peripheral or the pointlike models is used:

- **EITHER**

  $\mathcal{R} > F_2^\gamma/F_{2,\mathrm{VMD}}^\gamma$ then the pointlike model is chosen;

- **OR**

  $\mathcal{R} \leqslant F_2^\gamma/F_{2,\mathrm{VMD}}^\gamma$ then the peripheral model is chosen.

F_2^γ is the chosen parameterisation being used in F2GEN to generate the event and $F_{2,\mathrm{VMD}}^\gamma$ is the TPC/2γ fit given in Eqn. 2.12.

Samples of events have been generated using this model in previous OPAL analyses [2, 3]. The distributions of hadronic final state variables such as energy flow and transverse energy, $E_{\mathrm{t,out}}$, were found to be similar to those of HERWIG.

7.1.4 Selection of the Final Sample of Events

Stage 4 in the generation of a sample of events involves the selection of events generated according to user defined cuts upon the energies and polar angles of the scattered beam particles. A check is made (stage 5) after every event passing these selection criteria comparing the number of events in the selected sample with the desired number of events. The average cross–section for the generated sample is then calculated (stage 6) from the integrated luminosity factor $\mathcal{L}^{\mathrm{TT}}$ (section 7.1.1) and the cross–section $\sigma(\gamma^*\gamma \to X)$ (section 7.1.2).

7.2 Comparison of VERMASEREN and F2GEN

In order to check that the homegrown F2GEN generator can be trusted in calculating a well-defined process (pointlike QPM), it was compared with the exact LO QED/QPM model in the VERMASEREN generator. N_{gen} events were generated for $u\bar{u}$ pair final states using both F2GEN and VERMASEREN generators and satisfying the following loose cuts:

- $E_{\rm tag} \geq 20$ GeV
- $W_{\rm vis} > 2$ GeV
- $Q^2 > 1.0$ GeV^2
- $20 \leq \theta_{\rm tag} \leq 650$ milliradians

The numbers of events, N_{cuts}, were found for each sample satisfying the tighter cuts:

- $E_{\rm tag} \geq 0.6\ E_{\rm b}$
- $W_{\rm vis} \geq 2.5$ GeV
- $\theta_a \leq 50$ milliradians

together with a cut on the tag angle, $\theta_{\rm tag}$, of

- $25 \leq \theta_{\rm tag} \leq 55$ milliradians for $N_{cuts} = N_{SW}$
- $60 \leq \theta_{\rm tag} \leq 120$ milliradians for $N_{cuts} = N_{FD}$
- $200 \leq \theta_{\rm tag} \leq 500$ milliradians for $N_{cuts} = N_{EE}$

All the samples (see Table 7.1) agree well within errors except for those events with $25 \leq \theta_{\rm tag} \leq 55$ milliradians (N_{SW}) at $E_{\rm b} = 45.6$ GeV. The cross–section for the F2GEN sample in this region lies $2.8 \pm 1.0\%$ lower than the corresponding cross–section for the VERMASEREN sample. The F2GEN samples generated with $E_{\rm b} > 45.6$ GeV have cross–sections systematically 1 to 3 % higher than the corresponding VERMASEREN samples. For the purposes of this thesis, the agreement between the generators is tolerable.

Generator	E_b(GeV)	N_{gen}	σ_{gen}	N_{cuts}		σ_{cuts}
F2GEN	45.6	115938	213.09	N_{SW}	44980	82.6 ± 0.4
				N_{FD}	14930	27.4 ± 0.2
				N_{EE}	1138	2.1 ± 0.1
VERMASEREN		779343	1805.24	N_{SW}	36700	85.0 ± 0.4
				N_{FD}	11907	27.6 ± 0.3
				N_{EE}	938	2.2 ± 0.1
F2GEN	80.5	172406	286.12	N_{SW}	41377	68.7 ± 0.3
				N_{FD}	9048	15.0 ± 0.2
VERMASEREN		1429786	2446.69	N_{SW}	39609	67.8 ± 0.3
				N_{FD}	8568	14.7 ± 0.2
F2GEN	85.5	185566	294.27	N_{SW}	41336	65.6 ± 0.3
				N_{FD}	8775	13.9 ± 0.1
VERMASEREN		1546710	2519.89	N_{SW}	39743	64.7 ± 0.3
				N_{FD}	8267	13.5 ± 0.2

Table 7.1: Comparisons of cross–sections for F2GEN and VERMASEREN generators. The errors quoted on σ_{cuts} are the fraction $(N_{cuts})^{-1/2}$ of σ_{cuts}.

7.3 Photon–Gluon Fusion in F2GEN

One of the limitations of the algorithm described in section 7.1 is that it does not model interactions between the probe photon and a gluon in the target photon. I have added a new package to the F2GEN program to investigate events generated using a simple model of this subprocess.

The simulation of photon–gluon fusion events in F2GEN involves the simulation of four subprocesses which are shown schematically in Fig. 7.4. The algorithm used is the same as that shown in Fig. 7.1 with the addition of the generation of the gluon and photon remnant (Fig 7.4b) between stages 2 and 3. The generation of two photons, Fig. 7.4a), is the only stage in the algorithm that is unchanged from the original algorithm. All the other stages required some adaptation to allow for the additional subprocess.

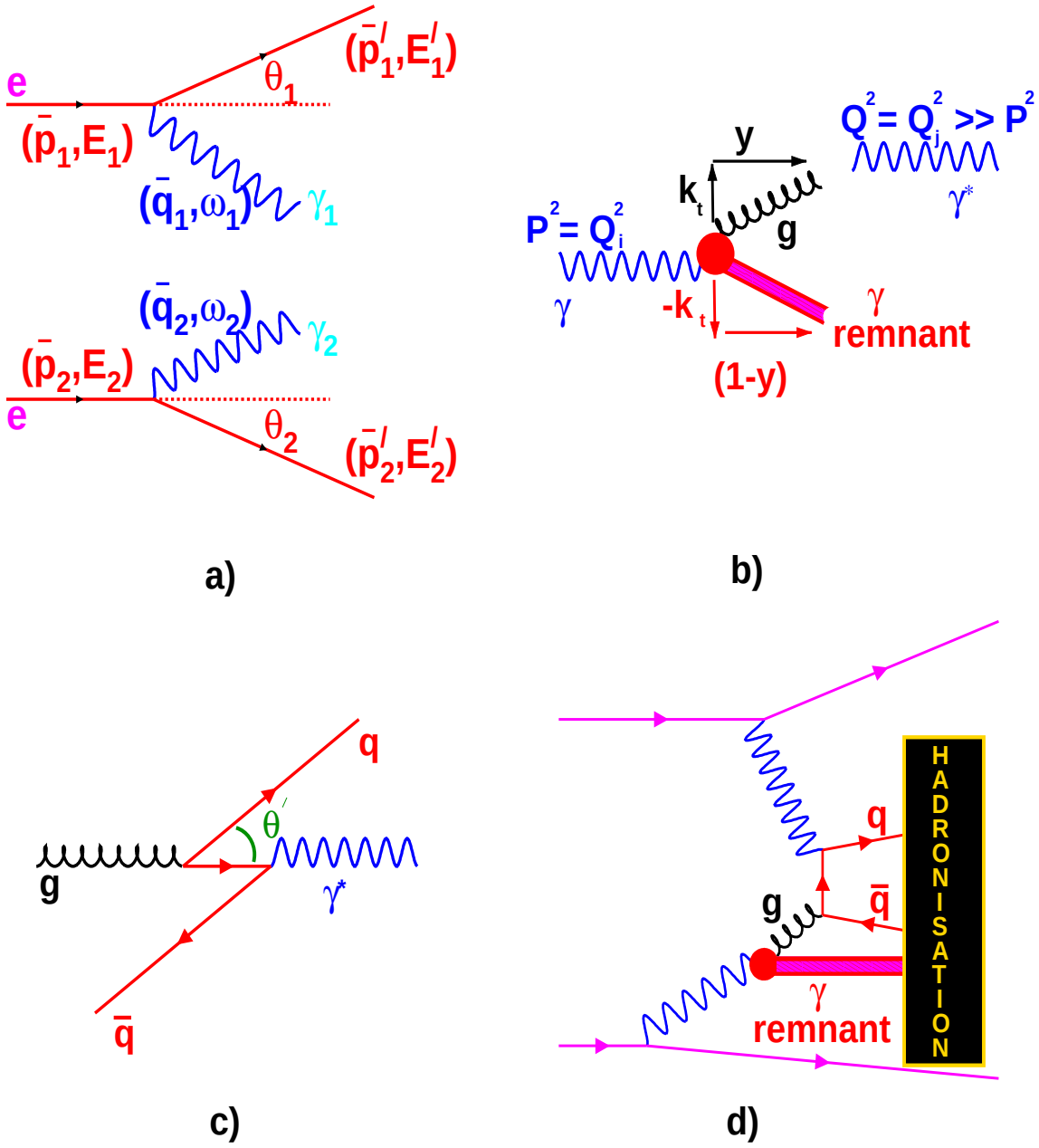

Figure 7.4: The four main subprocesses simulated in the F2GEN generator to model photon–gluon fusion events.

7.3.1 Sampling the Cross–Section for Photon–Gluon Fusion Events

The sampling of the cross–section for photon–gluon events is performed by an adaptation of stage **2**. Eqn. 2.38 relates the cross–section $\sigma(\gamma^*\gamma \rightarrow q\bar{q})$ to the structure function $F_2^\gamma(x,Q^2)$. In the original algorithm, only the subprocess $\gamma^*\gamma \rightarrow q\bar{q}$ is used in the calculation of $F_2^\gamma(x,Q^2)$. As part of the generation of photon–gluon fusion events, the cross–section is calculated using en 2.38 for subprocesses $\gamma^*\gamma \rightarrow q\bar{q}$ and $\gamma^* g \rightarrow q\bar{q}$ and where the input $F_2^\gamma(x,Q^2)$ is

$$F_2^\gamma(x,Q^2) = F_2^\gamma(x,Q^2)|_{\gamma^*\gamma\rightarrow q\bar{q}} + F_2^\gamma(x,Q^2)|_{\gamma^* g\rightarrow q\bar{q}}. \tag{7.13}$$

$F_2^\gamma(x,Q^2)|_{\gamma^* g\rightarrow q\bar{q}}$ is given by [97]:

$$\left.\frac{F_2^\gamma(x,Q^2)}{x}\right|_{\gamma^* g\rightarrow q\bar{q}} = \sum_q e_q^2 \int_x^1 \frac{dy}{y} g(y,Q^2) \frac{\alpha_s}{2\pi} P_{qg}\Big(\frac{x}{y}\Big) \log\frac{Q^2}{\mu^2} \tag{7.14}$$

where $g(y,Q^2)$ is the gluon density in the target photon and

$$P_{qg}\Big(\frac{x}{y}\Big) = \frac{1}{2}\Big(\frac{x^2}{y^2} + (1-\frac{x}{y})^2\Big) \tag{7.15}$$

is the probability that a gluon annihilates into a $q\bar{q}$ pair such that the quark has a fraction $\frac{x}{y}$ of the gluon momentum. The variable y denotes the fraction of the target photon momentum that the gluon carries parallel to the direction of the target photon momentum in the $\gamma^*\gamma$ centre–of–mass frame.

7.3.2 Generating a Gluon and Photon Remnant from the Target Photon

The four–momentum of the gluon is constructed by choosing a fraction y for the three–momentum component of the gluon in a direction parallel to the target photon momentum in the $\gamma^*\gamma$ centre–of–mass frame, and by generation of a transverse momentum, k_t, for the gluon relative to the target photon momentum. The three–momenta of the target and probe photons in this frame are taken to lie parallel to the z–axis.

The HISRAN algorithm [98] is used to generate a random value for y from a histogram of the $\frac{1}{y}G(y,Q^2)P_{qg}\left(\frac{x}{y}\right)$ distribution for the x and Q^2 of the event. Fig. 7.5a) shows $P_{qg}\left(\frac{x}{y}\right)$ as a function of y for different values of x. Fig. 7.5b)–d) shows plots of $\frac{1}{y}G(y,Q^2)P_{qg}\left(\frac{x}{y}\right)$ from the GRV leading order parameterisation with $x = 0.001$, $x = 0.1$, $x = 0.5$ for Q^2 values of 5 GeV^2 and 45 GeV^2, and with $\mu^2 = 0.25$ GeV^2.

The selection of the transverse momentum k_t for the gluon is performed using the RNORML algorithm to generate random numbers in a Gaussian distribution about 0. The direction of the k_t is set by sampling a uniform distribution of random numbers in the range $[0, 2\pi]$. Maximum and minimum values for k_t are left as free parameters to be set by the user.

The three–momenta of the photon remnant is constructed by assuming that it carries a fraction $(1 - y)$ of the target photon three–momentum parallel to the z–axis whilst the momenta of the gluon and the remnant are balanced in the transverse plane. The energies of the gluon and remnant are then calculated assuming that they are massless.

Generating a $q\overline{q}$ Pair in the $\gamma^* g$ Centre–of–Mass Frame

The generation of the $q\overline{q}$ pair is performed in the same way as described for $\gamma\gamma^* \rightarrow q\overline{q}$ generation in section 7.1.3 except the target photon is replaced by the gluon. The angle of the quark, θ', relative to the $\gamma^* g$ axis (see Fig. 7.4c) is obtained by sampling the angular distribution:

$$\frac{d\sigma(\gamma^* g \rightarrow q\overline{q})}{d\Omega'} = \sum_q \frac{3e_q^4\alpha^2}{(W^2_{\gamma^* g} + Q^2)\sin^2\theta'} \left[(1+\cos^2\theta') - \frac{4Q^2 W^2_{\gamma^* g}}{(W^4_{\gamma^* g} + Q^4 + 2Q^2 W^2_{\gamma^* g})}\right] \tag{7.16}$$

where primed quantities are in the $g\gamma^*$ centre–of–mass frame. The polar angle, ϕ', in the $\gamma^* g$ frame is chosen using random numbers in a uniform distribution over the full 2π range. From θ', ϕ' and $W_{\gamma^* g}$, the four–momentum of the $q\overline{q}$ pair are calculated assuming massless quarks.

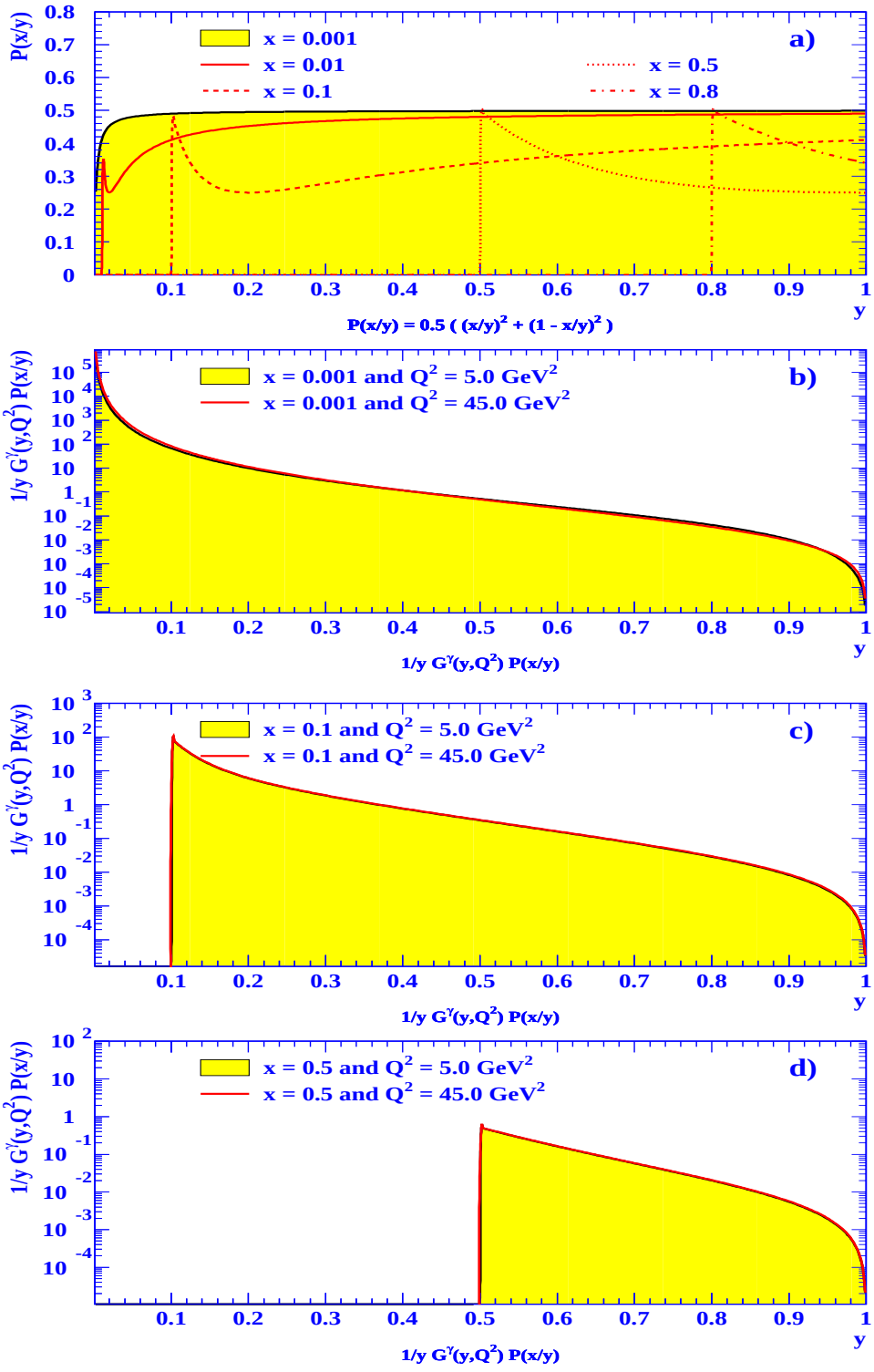

Figure 7.5: Plots showing a) $P_{qg}\left(\frac{x}{y}\right)$ and b)–d) $\frac{1}{y}G(y,Q^2)P_{qg}\left(\frac{x}{y}\right)$ as a function of y for various values of x and Q^2.

Hadronisation of the $q\overline{q}$ Pair and the Photon Remnant

The four–momenta of the $q\overline{q}$ pair are boosted back into the $\gamma\gamma^*$ centre–of–mass frame, and the invariant mass, $W_{q\overline{q},rem}$, of the quark, antiquark and photon remnant system is calculated. The model for the generation of the gluon transverse momentum k_t means that energy is not conserved and hence $W_{q\overline{q},rem} > W_{\gamma\gamma^*}$. To prevent this, the four–momenta of each of the quark, antiquark and remnant are rescaled using the ratio $W_{\gamma\gamma^*}/W_{q\overline{q},rem}$.

Finally, hadronisation of these three objects is performed using the JETSET string model. Since the gluon from the target photon is a coloured object, the photon remnant must also be coloured and is treated as a gluon.

7.4 Photon–Gluon Fusion Events

To compare with each of the data samples except the sample with $\langle Q^2 \rangle = 124$ GeV^2, two additional pairs of samples of singly–tagged two–photon events were generated at each $\langle Q^2 \rangle$ region using F2GEN with the photon–gluon fusion subprocess model described in section 7.3. One of each of these pairs of samples was generated with a minimum gluon transverse momentum, k_t, in the two–photon centre–of–mass frame of 10 MeV. For the other samples in each pair, this minimum k_t was set at 500 MeV to estimate the effects high and low k_t's would give in the final state. The GRV (LO) parameterisations of F_2^γ and $G(y, Q^2)$ were used for this generation.

7.4.1 Jet Multiplicity

Fig. 7.6 shows the fraction, N_i/N of events in the total sample, N, with $i = 0 - 3$ jets for the F2GEN samples compared with the data. It can be seen that there is little difference between the pairs of photon–gluon fusion samples for all $\langle Q^2 \rangle$.

The plots show that the photon–gluon fusion provides a simple model for generating relatively high numbers of events with 2 jets compared to the total sample, N. In the high $\langle Q^2 \rangle$, the ratio N_2/N is higher for the photon–gluon fusion samples than even the original F2GEN pointlike samples. High numbers of events with 1 jet are found at $\langle Q^2 \rangle = 2.3$ GeV^2 where the HERWIG and PYTHIA distributions (Fig. 6.1 6.2 and 6.4) show deficiencies compared with the data.

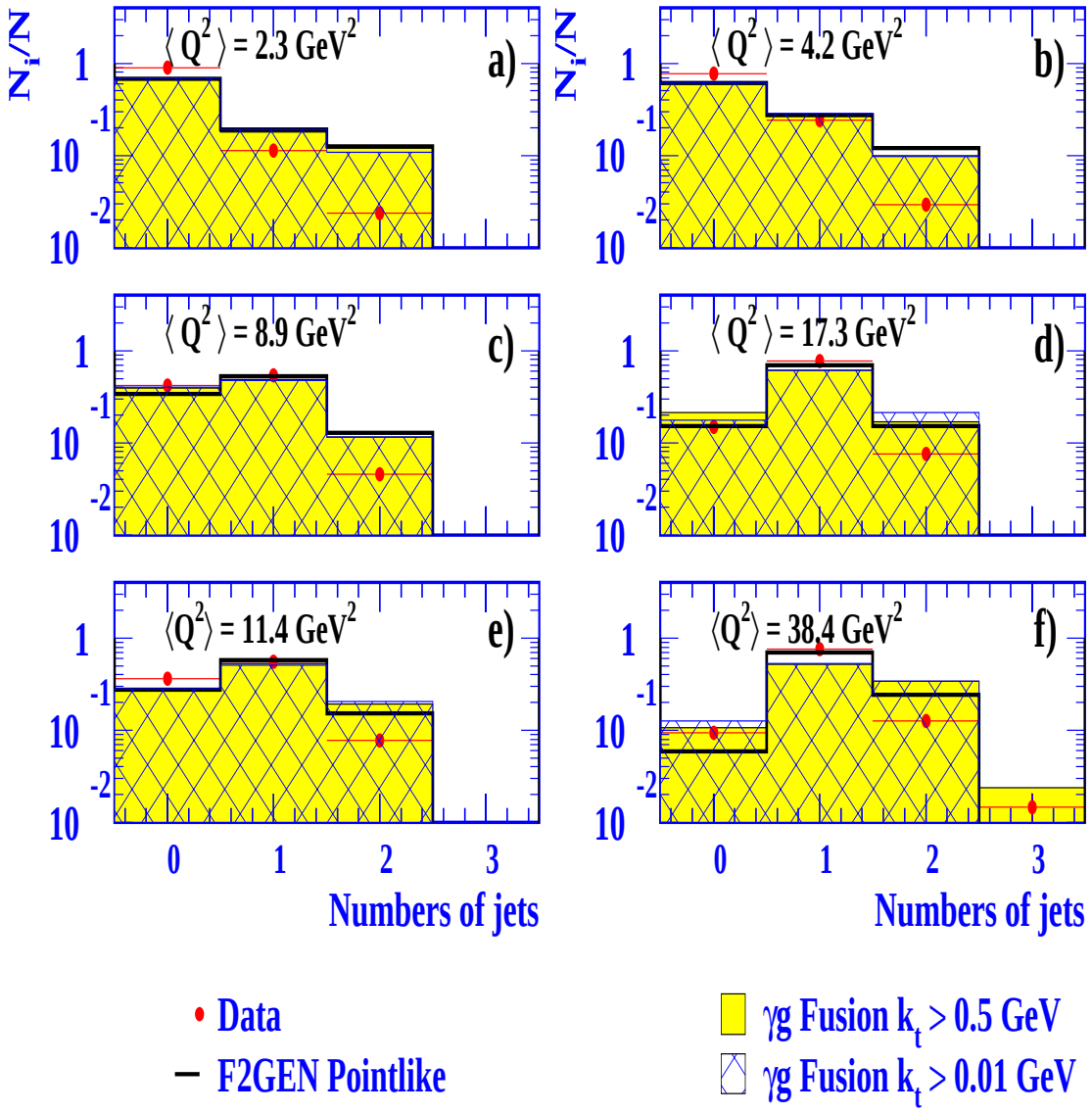

Figure 7.6: Fractions of events with 0–3 jets found for data and F2GEN Monte Carlo samples using the measured four–momenta of the hadronic final state particles. The data distributions (dots) are plotted with background subtracted whilst the histograms represent the distributions for the F2GEN photon–gluon fusion and pointlike Monte Carlo samples. The errors given are purely statistical.

7.4.2 Energy Flows

Fig. 7.7 shows the average hadronic energy flow per event using the same definitions as in Fig. 6.1. The photon–gluon fusion distributions do not agree with those of the data as expected. It is noticeable that these distributions show more energy flow into the region $0 < \eta < 1.8$ than for the data samples, and even more than the F2GEN pointlike samples for the three highest $\langle Q^2 \rangle$ regions. Additionally, for the three lowest $\langle Q^2 \rangle$ samples, the energy flow into the forward region $2.7 < \eta < 4.7$ is lower or the same as the data, whereas for the three higher $\langle Q^2 \rangle$ samples is more than seen in the data.

7.4.3 Energy Transverse to the Tag–Beam Plane, $E_{\mathrm{t,out}}$

Fig. 7.8 shows the distributions of $E_{\mathrm{t,out}}$ for each of the full samples of N events. They show that the photon–gluon fusion samples populate the high $E_{\mathrm{t,out}}$ regions of phase space, again where HERWIG and particularly PYTHIA samples are too low. The distributions even show that in the highest $\langle Q^2 \rangle$ region, the photon–gluon fusion samples appear to be in slight excess of the F2GEN pointlike distributions in the high $E_{\mathrm{t,out}}$ region.

7.5 Combination of HERWIG and Photon–Gluon Fusion Results

In the previous two sections, samples of two–photon events generated using the F2GEN program with the photon–gluon fusion process are compared directly to the data and F2GEN pointlike samples. The results show that this process, or others similar to it, could provide a mechanism for generating more events in the regions of phase space where the HERWIG and PYTHIA Monte Carlo samples show deficits. However, this process should be one of many subprocesses included in the Monte Carlo program. It is not easy to calculate the correct contribution that a hard subprocess such as photon–gluon fusion should make to the generated cross–section. Instead, a much simpler approach is adopted here to estimate this. In each of the HERWIG samples, 25% of events are removed from the sample and replaced with the equivalent number of events from the samples of photon–gluon fusion events. This choice was

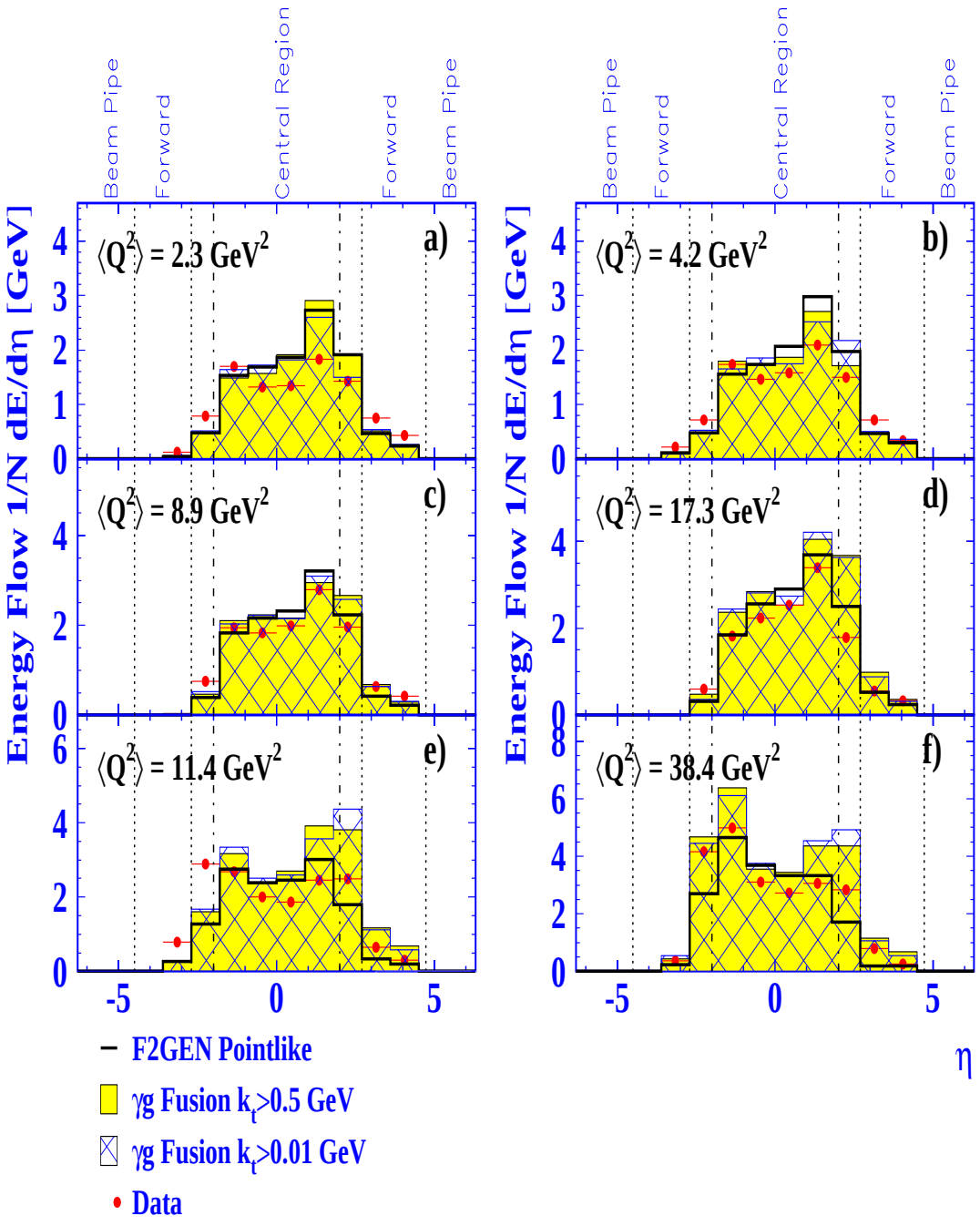

Figure 7.7: The average hadronic energy flow per event in bins of pseudorapidity $\eta = -\ln\tan\theta'/2$. The polar angle, θ', is recalculated for all hadrons relative to the beam axis, such that the tagged electron is always at $\eta < 0$. The dots represent the data with the estimated background subtracted, whilst the histograms show the corresponding distributions the F2GEN Monte Carlo samples. The errors shown are statistical only.

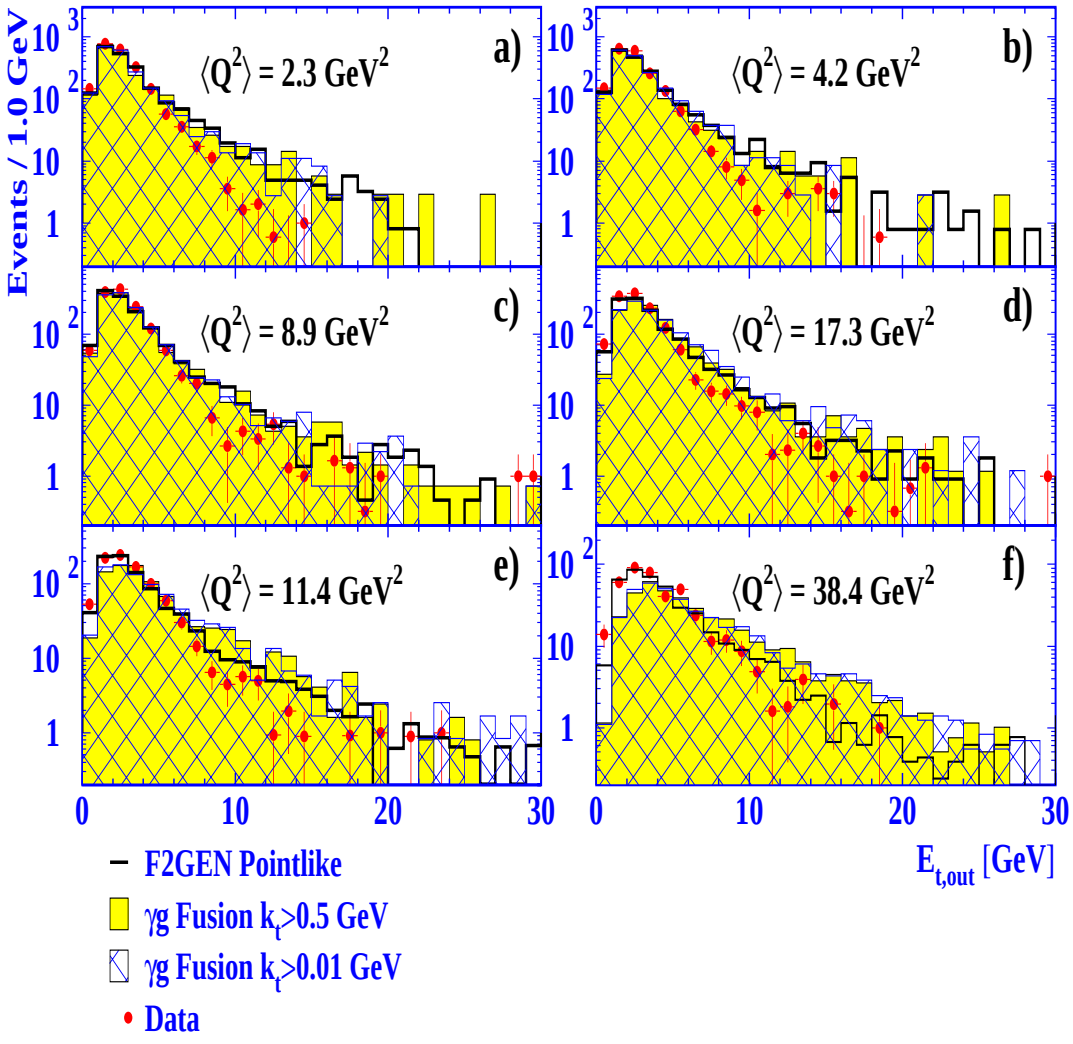

Figure 7.8: The transverse energy out of the plane formed by the tagged electron and the beams, $E_{\mathrm{t,out}}$. The histograms show the distributions for the F2GEN Monte Carlo samples. These histograms are normalised to the data luminosity. The errors shown for the data–background distributions are statistical only.

made to obtain the best fit to the data jet rates in Fig. 7.9. Since there is little difference between the results from the two types of photon–gluon fusion events, only the combined sample of 75% HERWIG and 25% photon–gluon fusion ($k_t > 0.01$ GeV) are shown here.

Fig. 7.9 shows the fraction N_i/N of events with $i = 0 - 3$ jets for the data samples compared with F2GEN pointlike, HERWIG and HERWIG+F2GEN photon–gluon fusion samples. This shows that the combined sample of events gives a much better description of the 2 jet rate than the HERWIG sample alone, and similarly for the 1 jet rate at $\langle Q^2 \rangle = 2.3$ and 4.2 GeV^2.

Fig. 7.10 shows the average energy flow per event for the samples in Fig 7.9. The central region, $0 < \eta < 1.8$, is better described by the combined sample than by the HERWIG sample, although the combined sample still underestimates the flow into this region for the $\langle Q^2 \rangle = 8.9$ and 17.3 GeV^2 samples. In the forward region $2.7 < \eta < 4.5$, there is little difference between the purely HERWIG samples and the HERWIG+photon–gluon fusion samples, all of which overestimate the energy into this region except at $\langle Q^2 \rangle = 38.4$ GeV^2.

Fig. 7.11 shows the distributions of $E_{\mathrm{t,out}}$ for these samples with the samples normalised to the integrated luminosity of the data. For the combined sample, the estimated luminosity of the pure HERWIG samples was used to normalise the distributions to the data luminosity. The combined samples show good agreement with the data distributions for all $\langle Q^2 \rangle$ and match the data distribution better than the pure HERWIG samples, both in the high $E_{\mathrm{t,out}}$ regions where HERWIG and PYTHIA fall short of the data as well as the very low $E_{\mathrm{t,out}}$ bins where they consistently overshoot the data.

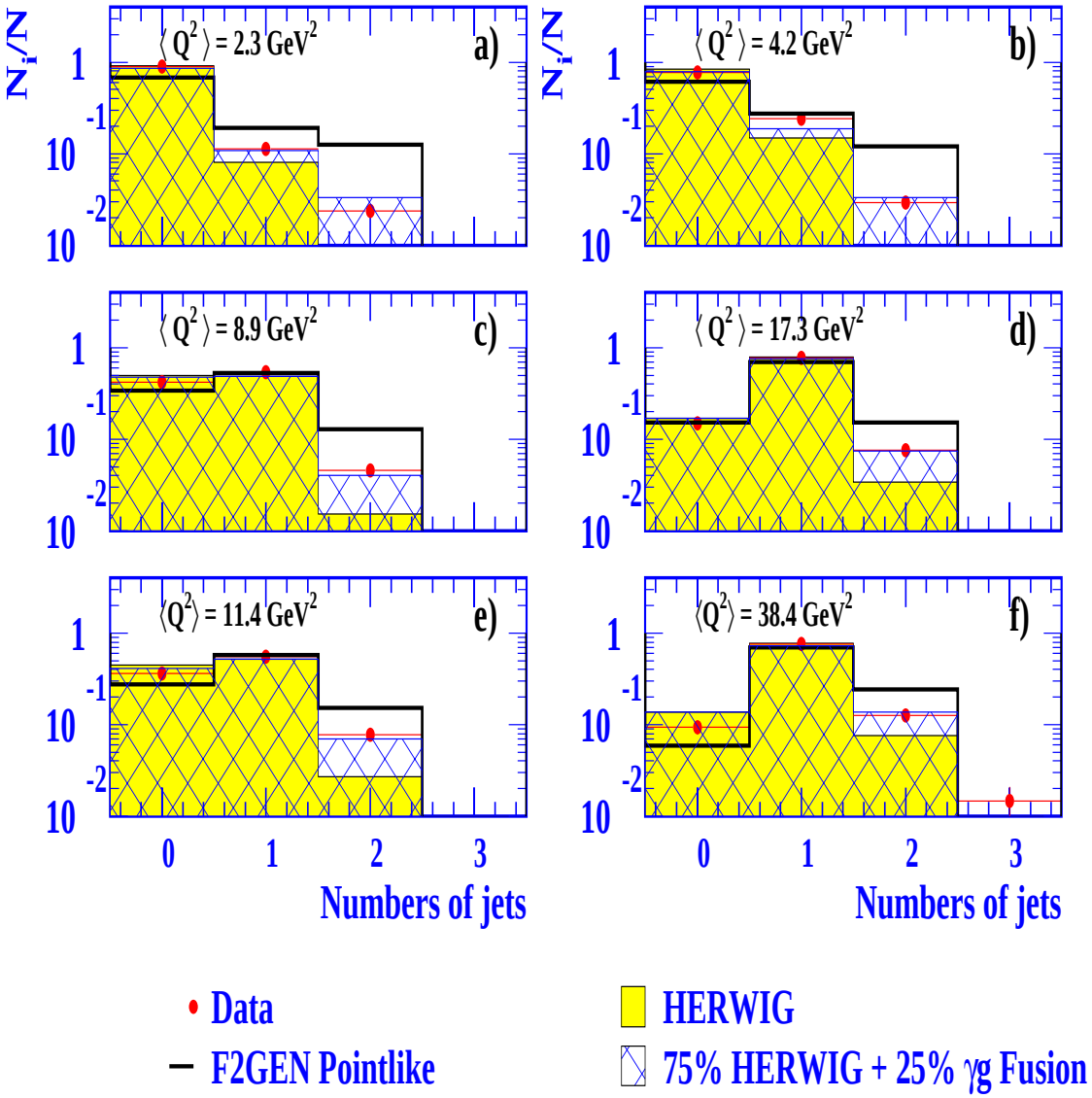

Figure 7.9: Fractions of events with 0–3 jets found for data The errors given are purely statistical.

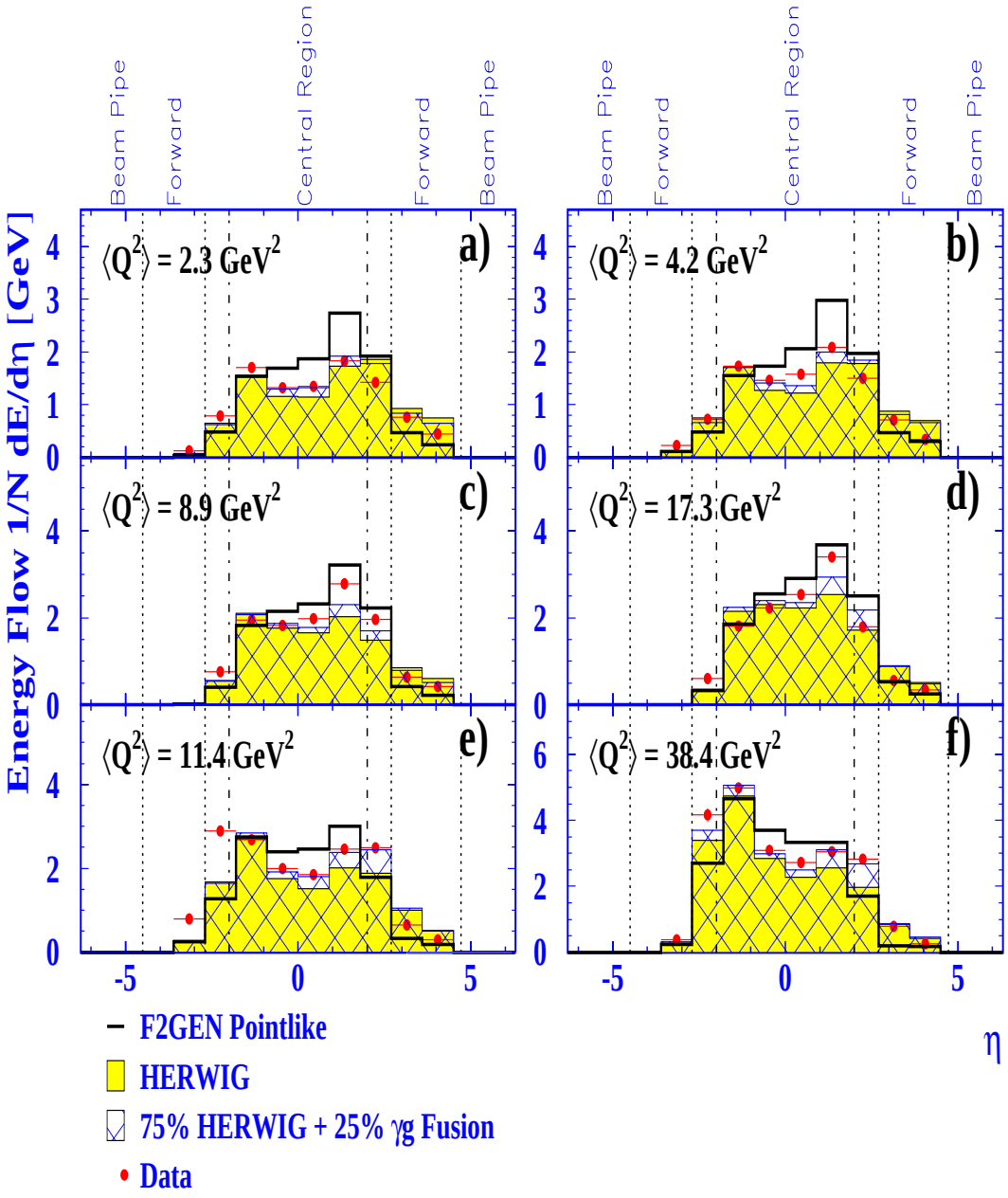

Figure 7.10: The average hadronic energy flow per event in bins of pseudorapidity $\eta = -\ln\tan\theta'/2$ for the data samples The polar angle, θ', is recalculated for all hadrons relative to the beam axis, such that the tagged electron is always at $\eta < 0$. The dots represent the data whilst the histograms show the corresponding distributions . The errors shown are statistical only.

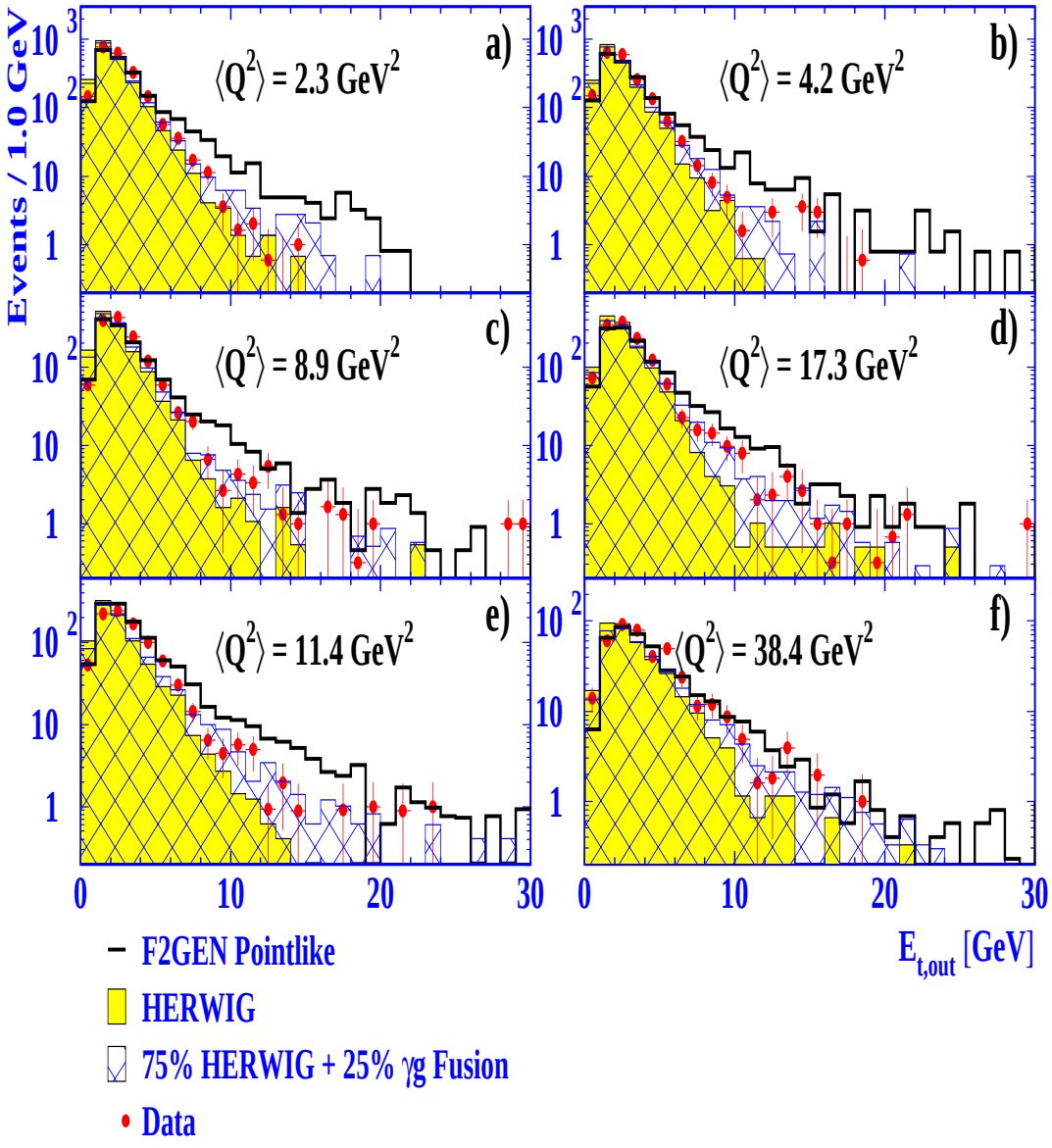

Figure 7.11: The transverse energy out of the plane formed by the tagged electron and the beams, $E_{t,out}$. The errors shown for the data distributions are statistical only.

Chapter 8

Discussion and Conclusions

8.1 Interpretation

The simple model used in the F2GEN program to generate photon–gluon fusion events is successful in generating relatively high numbers of events with 2 jets and high $E_{\mathrm{t,out}}$, and generating more hadronic energy flow into the region $0 < \eta < 1.8$. These correspond to the areas underestimated by the HERWIG and PYTHIA generators compared to the data samples (see sections 6.1 and 6.3).

Good agreement with the data is achieved for the jet multiplicity and $E_{\mathrm{t,out}}$ distributions (Fig. 7.9 and 7.11) of the hybrid "HERWIG+F2GEN photon–gluon fusion" samples created by replacing 25% of HERWIG randomly–selected events with the same number of randomly–selected events from the photon–gluon fusion samples. The corresponding energy flow distributions (Fig. 7.10) show that the hybrid samples describe the data better than the pure HERWIG samples but still underestimate the energy flow into the region $0 < \eta < 1.8$ for $\langle Q^2 \rangle = 8.9$ and 17.3 GeV^2.

These results provide further evidence to the conclusion that the HERWIG and PYTHIA Monte Carlo generators underestimate hard scattering processes. In chapter 6, it is suggested that the main source of the disagreements between the PYTHIA and HERWIG distributions for jet multiplicities is in the modelling of parton evolution. The parton showering models do not cover the full region of emission

phase space described by the full matrix element predictions. This unsampled region corresponds to the emission of hard partons and where the parton shower method is not guaranteed to give a good description of the parton evolution. In the HERWIG program, this region is sampled using first order α_s matrix elements and accounts for $\sim 10\%$ of events with variations in Q^2.

The results of the photon–gluon fusion process samples, in conjunction with those from Chapter 6, suggest that these matrix elements need to be included within the event generation of the PYTHIA program, and also that matrix elements may be needed to describe a larger area of the emission phase space. A free parameter may become available in future versions of the HERWIG generator [99] to be able to vary the relative coverage of the emission phase space by matrix element and parton showering methods. Another possible addition to future versions of the HERWIG generator is the ability to generate events where partons in the evolution may be allowed to have greater virtuality than the probe photon. These changes would provide an interesting line of future investigation, especially at low Q^2, and would require a re–examination of the LEP1 data samples.

The investigation performed by Lauber, Lönnbald and Seymour [16] showed that it is possible to "tune" the HERWIG and PYTHIA generators to give better results. They found that the 2 jet rate, energy flow and transverse energy, $E_{\mathrm{t,out}}$, distributions are sensitive to the intrinsic transverse momentum, k_T, of the target photon in non–perturbative (hadronic) events. The distinction between hadronic events and perturbative (anomalous) events is made differently for both HERWIG and PYTHIA generators. In HERWIG, the classification is made dynamically at the termination of the backward evolution to the target photon. In PYTHIA, the classification is made in the chosen parton density function. By choosing a power–like transverse momentum distribution of the form $dk_T^2/(k_T^2 + k_0^2)$, they obtained better agreement with the data for HERWIG and PYTHIA hadronic final state distributions, although the 2 jet rate for the "tuned" PYTHIA generator was still not high enough.

In the HERWIG generator, if the backward evolution is chosen to terminate in a gluon, the program is forced to perform an extra parton evolution back to the target photon, with the emitted partons given transverse momenta in a similar way to the generation of the intrinsic transverse momentum of the target photon in hadronic

events. It would be interesting to see what the effects would be for the events using the same type of ad hoc change used in [16].

8.2 Summary of Conclusions

In this thesis, comparisons are made over the range $Q^2 = 1 - 200$ GeV^2 between data samples of singly–tagged two–photon events and predictions from the QCD–based Monte Carlo generators, HERWIG and PYTHIA, as well as from the single–purpose generator, F2GEN. The focus has been to highlight the inaccuracies of the modelling of the hadronic final state by HERWIG and PYTHIA, and to propose changes and refinements to this modelling. The nature of the discrepancies provide evidence that the HERWIG and PYTHIA generators underestimate the contribution of hard processes to a generated sample. These deficiencies will need to be corrected if the generators are to be used to give unfolded photon structure functions in which the systematic errors do not dominate the statistical errors

The largest discrepancies between the data and the unmodified Monte Carlo samples are found in comparisons of the distributions of:

- the cone jet multiplicities (Chapter 6, my own work),
- the average hadronic energy flow per event (Chapter 6, extension of the published OPAL analyses [4, 3, 5, 15]),
- the transverse energy, $E_{\mathrm{t,out}}$, out of the tag–beam plane (Chapter 6, extension of the published OPAL analyses).

A new model for the photon–gluon fusion subprocess was added to the F2GEN generator and samples of events generated using this model were compared with the data, HERWIG and original F2GEN samples. This simple model provides a mechanism of generating relatively large numbers of events compared to the data samples in the same regions of distributions underestimated by the HERWIG and PYTHIA generators. A naive replacement of 25% of HERWIG events with the same number of F2GEN photon–gluon fusion events gives a much improved description of the data

distributions than do the HERWIG samples alone. This reinforces the conclusion that hard processes are underestimated by HERWIG and PYTHIA.

These results show very specifically that hard subprocesses must be treated properly by a good Monte Carlo model of singly–tagged deep inelastic $e\gamma$ scattering events. Several suggestions for ways of improving the current models in the HERWIG and PYTHIA generators are given in section 8.1. With improvemed modelling of the hadronic final state in HERWIG and PYTHIA, further analyses of the low-x and high-x region of the photon structure function, $F_2^\gamma(x, Q^2)$, should show smaller systematic errors and with it, our knowledge and understanding of the photon will increase.

Bibliography

[1] "Two Photon Physics at e^+e^- Storage Rings", H. Kolanoski, Springer–Verlag, Berlin (1984).

[2] "A Study of Photon Structure with Special Attention to the Low–x Region" J. J. Ward, Ph. D. Thesis, RAL-TH-96-014.

[3] K. Ackerstaff et al., OPAL Coll., Z. Phys. **C74** (1997) 33.

[4] K. Ackerstaff et al., OPAL Coll., Phys. Lett. **B412** (1997) 225.

[5] K. Ackerstaff et al., OPAL Coll., Phys. Lett. **B411** (1997) 387.

[6] "A Measurement of the Photon Structure Function $F_2^\gamma(x, Q^2)$ Using the ALEPH Detector", G. C. Crawford, Ph. D. Thesis, RAL-TH-97-005.

[7] $\gamma\gamma$ *Event Generators* , L. Lönnblad and M. H. Seymour (convenors) in *Physics at LEP2*, eds. G. Altarelli, T. Sjöstrand and F. Zwirner, CERN 96–01, Vol. 2. (1996) 187.

[8] G. Marchesini et al., Comp.Phys. Comm. **67** (1992) 465–508.

[9] T. Sjöstrand, Comp. Phys. Comm. **39** (1986) 347;
T. Sjöstrand and M. Bengtsson, Comp. Phys. Comm. **43** (1987) 367;
T. Sjöstrand, Comp. Phys. Comm. **82** (1994) 74.

[10] A. Buijs, W. G. Langeveld, M. H. Lehto and D. J. Miller, Comp. Phys. Comm. **79** (1994) 523.

[11] K. Ahmet et al., OPAL Coll. , Nucl. Instr. and Meth. A305 (1991) 275.

[12] European Committee for Future Accelerators. 'General Meeting on LEP', CERN Publications Group, 1981.

[13] R. Akers et al., OPAL Coll., Z. Phys. **C63** (1994) 197.

[14] "Measurement of the inclusive one–jet and two–jet cross–sections in two–photon interactions at $\sqrt{s}$91 GeV", W. M. Newton, Ph.D. Thesis, Submitted August 1997.

[15] A. M. Rooke (for the OPAL Coll.), *Proceedings of the Photon '97 Conference*, Egmond aan Zee, 10–15 May 1997, eds A. Buijs and F. C. Erné, World Scientific (Singapore) 1998; hep-ph/9707003.
"A Study of Energy Flows Based on Jet Classification in Deep Inelastic Electron–Photon Scattering "', J. A. Lauber, D. J. Miller and A. M. Rooke, OPAL internal publication (PN-293), May 1997.

[16] J. A. Lauber, L. Lönnblad and M. H.Seymour, *Proceedings of the Photon '97 Conference*, Egmond aan Zee, 10–15 May 1997, eds A. Buijs and F. C. Erné, World Scientific (Singapore) 1998; hep-ph/9707002.

[17] G. A. Schuler and T. Sjöstrand, *Proceedings of the Workshop on Two–Photon Physics from DAPNE to LEP 200 and Beyond*, College de France, Paris, 2–4 February 1994, eds. F. Kapusta and J. Parisi, World Scientific (Singapore) 1994, p163.

[18] L. N. Hand, Phys. Rev. **129** (1963) 1834.

[19] Ch. Berger and W. Wagner, Phys. Rep. **146** (1987) 1.

[20] H. J. Behrend et al., CELLO Coll., Phys. Lett. **B126** (1983) 384.

[21] M. P. Cain et al., TPC/2γ Coll., Phys. Lett. **B147** (1984) 232.

[22] C. Berger et al., PLUTO Coll., Z. Phys. **C27** (1985) 249.

[23] R. Akers et al., OPAL Coll., Z. Phys. **C60** (1993) 593.

[24] I. Naraghi, F. Kapusta and V. Pozdnyakov (for the DELPHI Coll.), *Proceedings of the Photon '95 Conference*, Sheffield, 8–13 April 1995, eds. D. J. Miller, S. L. Cartwright and V. Khoze, World Scientific (Singapore) 1995. P. Abreu et al., DELPHI Coll., Z. Phys. **C69** (1996) 223.

[25] K. Ackerstaff et al., OPAL Coll., Z. Phys. **C74** (1997) 49.

[26] C. Brew, S. Cartwright and M. Lehto (for the ALEPH Coll.), *Proceedings of the Photon '97 Conference*, Egmond aan Zee, 10–15 May 1997, eds A. Buijs and F. C. Erné, World Scientific (Singapore) 1998.

[27] R. Nisius (for the LEP Collaborations), to be published in *Proceedings of the International Europhysics Conference on High Energy Physics*, Jerusalem, 19–26 August 1997; hep-ex/97-12012.

[28] C. Peterson, T. F. Walsh and P. M. Zerwas, Nucl. Phys. **B229** (1983) 301.

[29] F. Lehner, a talk presented at the *The Lake Louise Winter Institute*, Lake Louise, Alberta, Canada, 15–21 February 1998.

[30] M. Derrick et al., ZEUS Coll., Phys. Lett. **B316** (1993) 412;
I. Abt et al., H1 Coll., Nucl. Phys **B407** (1993) 515.

[31] Yu. L. Dokshitzer, Sov. Phys. JETP **46** (1977) 641;
L. N.Lipatov, Sov. J. Nucl. Phys. **20** (1975) 95;
V. N.Gribov and L. N.Lipatov, Sov. J. Nucl. Phys. **15** (1972) 438;
G. Altarelli, Phys. Rep. **81** (1982) 1.

[32] E. A. Kuraev, L. N. Lipatov and V. S. Fadin, Phys. Lett. **60B** (1975) 50;
Ya. Ya. Balitsky and L. N. Lipatov, Sov. J. Nucl. Phys. **28** (1978) 822.

[33] "Unfolding Methods In High Energy Physics Experiments"
V. Blobel From *Proceedings Of The CERN School Of Computing*, Aiguablanca CERN 85-09 (1985).

[34] A. Höcker and V. Kartvelishvili, MC-TH/95–15 ; LAL/95–55 ; hep–ph/9509307.

[35] $\gamma\gamma$ *Physics*, P. Aurenche and G. A. Schuler (convenors) in *Physics at LEP2*, eds. G. Altarelli, T. Sjöstrand and F. Zwirner, CERN 96–01, Vol. 1. (1996) 297.

[36] C. Berger et al., PLUTO Coll., Phys. Lett. **B142** (1984) 111.

[37] C. Berger et al., PLUTO Coll., Phys. Lett. **B281** (1987) 365.

[38] M. Althoff et al., TASSO Coll., Z. Phys. **C31** (1986) 527.

[39] W. Bartel et al., JADE Coll., Z. Phys. **C24** (1984) 231.

[40] H. Aihara et al., TPC/2γ Coll., Z. Phys. **C34** (1987) 1.

[41] J. S. Steinman et al., TPC/2γ Coll., UCLA preprint, UCLA-HEP-88-004 (1988).

[42] T. Sasaki et al., AMY Coll., Phys. Lett. **B252** (1990) 491.

[43] S. K. Sahu et al., AMY Coll., Phys. Lett. **B346** (1995) 208.

[44] K. Muramatsu et al., TOPAZ Coll., Phys. Lett. **B332** (1994) 477.

[45] D. J. Miller, "Proceedings of the XVI International Symposium on Lepton and Photon Interactions", Ithaca, NY, August 1993, eds. P. Drell and D. Rubin, AIP Press, 1994.

[46] "A Measurement of the Photon Structure Function $F_2(x)$"
M. H. Lehto, Ph. D. Thesis, University College London, 1993.

[47] R. Akers et al., OPAL Coll., Z. Phys. **C61** (1994) 199.

[48] I. Kronkvist, F. Kapusta and V. Pozdnyakov (for the DELPHI Coll.), *Proceedings of the Photon '95 Conference*, Sheffield, 8–13 April 1995, eds. D. J. Miller, S. L. Cartwright and V. Khoze, World Scientific (Singapore) 1995; CERN–PPE/95–87.

[49] I. Tyapkin (for the DELPHI Coll.), *Proceedings of the Photon '97 Conference*, Egmond aan Zee, 10–15 May 1997, eds A. Buijs and F. C. Erné, World Scientific (Singapore) 1998.

[50] E. Laenen, S. Riemersma, J. Smith and W. L. van Neerven, Phys. Rev. **D49** (1994) 5753.

[51] W. A. Bardeen and A. J. Buras, Phys. Rev. **D20** (1979) 166;
Phys. Rev. **D21** (1980) 2041(E).

[52] M. Glück, E. Reya and A. Vogt, Phys. Rev. **D45** (1992) 3986.

[53] T. H. Bauer, F. M. Pipkin, R. D. Spital and D. R. Yennie, Rev. Mod. Phys. **50** (1978) 261.

[54] J. Badier et al., the NA3 Collab., Z. Phys. **C18** (1983) 281.

[55] M. Glück, E. Reya and A. Vogt, Phys. Rev **D46** (1992) 1973.

[56] M. Glück, E. Reya and A. Vogt, Z. Phys. **C53** (1992) 651.

[57] G. A. Schuler and T. Sjöstrand, *Proceedings of the Photon '95 Conference*, Sheffield, 8–13 April 1995, eds. D. J. Miller, S. L. Cartwright and V. Khoze, World Scientific (Singapore) 1995; hep-ph/9506279.

[58] C. T. Hill and G. G. Ross, Nucl. Phys. **B148** (1979) 373.

[59] E. Witten, Nucl. Phys. **B120** (1977) 189.

[60] C. H. Lewellyn–SMith, Phys. Lett. **B79** (1978) 83.

[61] W. R. Frazer and J. F. Gunion, Phys. Rev. **D20** (1979) 147.

[62] J. H. Field, F. Kapusta and L. Poggioli, Phys. Lett. **B181** (1986) 362;
J. H. Field, F. Kapusta and L. Poggioli, Z. Phys. **C36** (1987) 121.

[63] G. A. Schuler and T. Sjöstrand, Z. Phys. **C68** (1995) 607.

[64] K. Hadiwara, M. Tanaka, I. Watanabe and T. Izubuchi, Phys. Rev. **D51** (1995) 3197.

[65] L. E. Storrow and J. K. Storrow, Z. Phys. **C56** (1992) 307.

[66] M. Drees and K. Grassie, Z. Phys. **C28** (1985) 451.

[67] P.Aurenche et al., Z. Phys. **C56** (1992) 589.

[68] H. Abramowicz, K. Charchula and A. Levy, Phys. Lett. **B269** (1991) 458.

[69] R. J. De Witt et al., Phys. Rev. **D19** (1979) 2046.

[70] A. Vogt, *Proceedings of the Photon '97 Conference*, Egmond aan Zee, 10–15 May 1997, eds A. Buijs and F. C. Erné, World Scientific (Singapore) 1998; hep-ph/9709345.

[71] G. Altarelli and G. Parisi, Nucl. Phys. **B126** (1977) 298.

[72] M. Glück, E. Hoffmann and E. Reya, Z. Phys. **C13** (1982) 119.

[73] V. Budnev et al., Phys. Rep. **C15** (1975) 182.

[74] E. Gotsman, A. Levy and U. Maor, Z. Phys. **C40** (1988) 117.

[75] "QCD and Collider Physics", R. K. Ellis, W. J. Stirling and B. R. Webber, Cambridge University Press (1996).

[76] A. H. Mueller, Nucl. Phys. **B415** (1994) 373.

[77] M. Glück, E. Reya and A. Vogt, Z. Phys. **C53** (1992) 127.

[78] J. F. Field, *Proceedings of the VIII Int. Workshop on Photon–Photon Collisions*, Shoresh, Isreal, 1988, ed. U. Karshon, World Scientific, (Singapore) 1988.

[79] A. Vogt, *Proceedings of the workshop on Two–Photon Physics at LEP and HERA*, Lund, 26–28 May 1994, eds. G. Jarlskog and L. Jönsson, Lund University 1994.

[80] P. Kessler, *Proceedings of the workshop on Two–Photon Physics at LEP and HERA*, Lund, 26–28 May 1994, eds. G. Jarlskog and L. Jönsson, Lund University 1994.

[81] M. Seymour., Comp. Phys. Comm. **90** (1995) 95;
M. Seymour., Contribution gls0258 to the "27 International Conference on High Energy Physics", Glasgow, U.K., 20 – 27^{th} July 1994.

[82] J. André and T. Sjöstrand, Phys. Rev **D57** (1998) 5767.

[83] B. R. Webber, Nucl Phys. **B238** (1984) 492.

[84] X. Arttu and G. Mennessier, Nucl. Phys. **B70** (1974) 93;
M. G. Bowler, Z. Phys **C11** (1981) 169;
B. Andersson, G. Gustafson and B. Söderberg, Z. Phys. **C20** (1983) 317;
B. Andersson, G. Gustafson and B. Söderberg, Nucl. Phys. **B264** (1986) 29.

[85] R. Bhattacharya, G. Grammer Jnr, and J. Smith, Phys. Rev. **D15** (1977) 3267;
G. Grammer Jnr, J. Smith, J. A. M. Vermaseren, Phys. Rev. **D15** (1977) 3280;
G. Grammer Jnr, J. Smith, J. A. M. Vermaseren, Phys. Rev. **D19** (1979) 137.

[86] "ROPE User's Guide",
C. Hawkes et al., OPAL internal publication.

[87] "A Matching Algorithm: MT package",
T. Omori et al., OPAL internal publication.

[88] J. Allison et al., Nucl. Instr. and Meth. **A317** (1992) 47.

[89] L. Lönnblad, Comp. Phys. Comm. **71** (1992) 15,
http://www.nordita.dk/ leif/ariadne/index.html.

[90] S. Jadach, B. F. L. Ward and Z. Was, Comp. Phys. Comm. **79** (1994) 503–522.

[91] F. Le Diberder, J. Hilgart and R. Kleiss, Comp. Phys. Comm. **75** (1993) 191–218.

[92] M. Skrzypek, S. Jadach, M. Martinez, W. Placzek and Z. Was, Phys. Lett. **B372** (1996) 289-298.

[93] "Trigger Efficiency for Untagged Inclusive Two–Photon Events at $\sqrt{s_{ee}}$ = 161 and 172 GeV", R. Bürgin, OPAL internal publication (TN-496), July 1997.

[94] K. Ackerstaff et al., OPAL Coll., Z. Phys. **C73** (1997) 433.

[95] R. Bürgin, *Proceedings of the Photon '97 Conference*, Egmond aan Zee, 10–15 May 1997, eds A. Buijs and F. C. Erné, World Scientific (Singapore) 1998; hep-ex/9706007.

[96] "Pion and Kaon Pair–Production In Photon–Photon Collisions",
W. G. Langeveld, Ph.D. Thesis, University of Utrecht, 1985.

[97] "Quarks and Leptons: An Introductory Course in Modern Particle Physics",
F. Halzen and A. D. Martin, Wiley (1984).

[98] "CERNLIB – Short Writeups",
CERN Computing and Networks Division Internal Publication.

[99] M. Seymour, private communication.